INVESTIGATIONS ON FUNCTIONAL MATERIALS FOR HYBRID SULFUR CYCLE FOR THERMOCHEMICAL HYDROGEN PRODUCTION

By

ASHISH NATARAJAN NADAR

CHEM01201304013

Bhabha Atomic Research Centre, Mumbai, India

A thesis submitted to the

Board of Studies in Chemical Sciences

In partial fulfillment of requirements

for the Degree of

DOCTOR OF PHILOSOPHY

of

HOMI BHABHA NATIONAL INSTITUTE

December, 2017

Homi Bhabha National Institute

Recommendations of the Viva Voce Committee

As members of the Viva Voce Committee, we certify that we have read the dissertation prepared by **Ashish Natarajan Nadar** entitled **"Investigations on functional materials for hybrid sulfur cycle for thermochemical hydrogen production"** and recommend that it may be accepted as fulfilling the thesis requirement for the award of Degree of Doctor of Philosophy.

Chairman - Dr. R. K. Vatsa RKVatsa **Date:** 23/5/2018

Guide / Convener - Dr. A. K. Tripathi Tripathi **Date:** 23/05/2018

Examiner - Prof. Sreedevi Upadhyayula **Date:** 23/05/2018

Member 1- Dr. P. A. Hassan **Date:** 23/05/2018

Member 2- Dr. V. Sudarsan Sudarsan. V **Date:** 23/5/2018

Member 3- Dr. S. C. Parida **Date:** 23.05/2018

Member 4- Dr. (Smt.) M. R. Pai **Date:** 23/05/2018

Final approval and acceptance of this thesis is contingent upon the candidate's submission of the final copies of the thesis to HBNI.

I/We hereby certify that I/we have read this thesis prepared under my/our direction and recommend that it may be accepted as fulfilling the thesis requirement.

Date: May 23, 2018

Place: Mumbai

Tripathi

Dr. A. K. Tripathi

Guide

STATEMENT BY AUTHOR

This dissertation has been submitted in partial fulfillment of requirements for an advanced degree at Homi Bhabha National Institute (HBNI) and is deposited in the Library to be made available to borrowers under rules of the HBNI.

Brief quotations from this dissertation are allowable without special permission, provided that accurate acknowledgement of source is made. Requests for permission for extended quotation from or reproduction of this manuscript in whole or in part may be granted by the Competent Authority of HBNI when in his or her judgment the proposed use of the material is in the interests of scholarship. In all other instances, however, permission must be obtained from the author.

Ashish

Ashish Natarajan Nadar

DECLARATION

I, hereby declare that the investigation presented in the thesis has been carried out by me. The work is original and has not been submitted earlier as a whole or in part for a degree / diploma at this or any other Institution / University.

Ashish

Ashish Natarajan Nadar

List of publications arising from the thesis

Journal

1. "Catalytic Properties of Dispersed Iron Oxides Fe_2O_3/MO_2 (M = Zr, Ce, Ti and Si) for Sulfuric Acid Decomposition Reaction: Role of Support." Ashish Nadar, A. M. Banerjee, M. R. Pai, S. S. Meena, R. Tewari, Pai R.V. A. K. Tripathi, *Int. J. Hyd. Energy* **2018,** *43*, 37-52.
2. "Nanostructured Fe_2O_3 Dispersed on SiO_2 as Catalyst for High Temperature Sulfuric Acid Decomposition - Structural and Morphological Modifications on Catalytic Use and Relevance of Fe_2O_3-SiO_2 Interactions", A. Nadar, A. M. Banerjee, M. R. Pai, S. S. Meena, R. V. Pai, R. Tewari, S. M. Yusuf, A. K. Tripathi and S. R. Bharadwaj, *App. Catal. B: Env.* **2017,** *217,* 154-168.
3. Performance Evaluation of Dispersed Molybdenum Carbide for Hydrogen Evolution Reaction, Ashish Nadar, Atindra Mohan Banerjee, Mrinal R. Pai, Rajini P. Antony, A. K. Tripathi, *Int. J. Hyd. Energy (under revision)*
4. "Catalytic activity of Fe_2O_3 dispersed on SiO_2 support for sulfuric acid decomposition reaction: Effect of preparation method Ashish Nadar, A. M. Banerjee, M. R. Pai and A. K. Tripathi,*(to be communicated)*
5. "Investigations on SO_2 aqueous electrolysis in PEM based electrolyser: Evaluation of Pt based electrocatalyst" Ashish Nadar, A. M. Banerjee, M. R. Pai and A.K. Tripathi,*(to be communicated)*

Conferences

1. Ashish Nadar, A. M. Banerjee, M. R. Pai, R. V. Pai, A. K. Tripathi and S.R. Bharadwaj "Preparation & Characterization of Dispersed Fe_2O_3/SiO_2 Catalysts for use in Sulfuric Acid

Decomposition Reaction", 19th National Symposium & Workshop on Thermal Analysis (THERMANS-2013) in TSH, BARC Mumbai, Dec 19-23, 2013 (Oral presentation)

2. Ashish Nadar, A. M. Banerjee, M. R. Pai, R. V. Pai, A. K. Tripathi and S.R. Bharadwaj, "Preparation, Characterization and Catalytic activity Evaluation of Fe_2O_3/SiO_2 Catalyst for Sulfuric Acid Decomposition Reaction.", 5th Interdisciplinary Symposium on Material Chemistry (ISMC-2014) in TSH, BARC Mumbai, Dec 9-13, 2014, (Received Best Poster award)
3. Ashish Nadar, A. M. Banerjee, S. Ravichandran, M. R. Pai, S. Vasudevan, D. Jonas Davidson, G. Sozhan, A. K. Tripathi and S. R. Bharadwaj "Aqueous SO_2 Electro-oxidation on Pt/Nafion prepared by in-situ Impregnation-Reduction Method", 22nd National Symposium on Catalysis (CATSYMP22) CSIR-Central Salt and Marine Chemicals Research Institute (CSIR-CSMCRI), Bhavnagar, Jan 7-9, 2015 (Poster presentation)
4. Ashish Nadar, A. M. Banerjee, M. R. Pai, A. K. Tripathi and S. R. Bharadwaj,"Comparative Evaluation of Pd/C electrocatalyst Prepared by Polyol and Chemical Reduction Method for Hydrogen Evolution Reaction" International Conference on Sustainable Chemistry & Engineering (SusChemE 2015), Hotel Lalit, Mumbai, Oct 8-9, 2015 (Oral presentation)

5. S. S. Meena, A. Nadar, A. M. Banerjee, M. R. Pai, A. K. Tripathi, S. R. Bharadwaj, Pramod Bhatt, S. M. Yusuf, "Effect of Calcination Temperature on Phase Formations in Nanocomposites $x\mathrm{Fe_2O_3/SiO_2}$: A Mössbauer Study", 60th Solid State Physics Symposium 2015, Amity University UP, Noida Uttar Pradesh, Dec 21-25, 2015 (Poster presentation)

6. Ashish Nadar, A. M. Banerjee, M. R. Pai, A. K. Tripathi and S.R. Bharadwaj "Studies on Supported Fe_2O_3 Catalysts for Sulfuric Acid Decomposition Reaction", International Conference on Frontiers at the Chemistry-Allied Sciences Interface (FCASI-2016), Department of Chemistry, University of Rajasthan, Jaipur, April 25-26, 2016 (Received Best Poster Award)

7. Ashish Nadar, A. M. Banerjee, M. R. Pai, A. K. Tripathi and S.R. Bharadwaj Presented poster "Comparative Study of Pt/C Electrocatalyst Prepared by Polyol and Chemical Reduction Method for Hydrogen Evolution Reaction" 6th Interdisciplinary Symposium on Material Chemistry (ISMC-2016), TSH, BARC Mumbai, Dec 6-10, 2016 (Poster presentation)
8. A. M. Banerjee, Ashish Nadar , M. R. Pai, A. K. Tripathi and S. R. Bharadwaj "Design, Fabrication and Testing of a Quartz Solar Reactor for Decomposition of Sulfuric Acid as part of Solar Thermochemical Hydrogen Production"6th Interdisciplinary Symposium on Material Chemistry (ISMC-2016), TSH, BARC Mumbai, Dec 6-10, 2016 (Poster presentation)
9. Ashish Nadar, A. M. Banerjee, M. R. Pai and A. K. Tripathi, "Catalytic activity of Fe_2O_3 dispersed on SiO_2 support for sulfuric acid decomposition reaction: Effect of method of preparation", 7th Asia-Pacific Congress on Catalysis (APCAT-7), Hotel Lalit, Mumbai, Jan 17-21, 2017 (Poster presentation)
10. Ashish Nadar, A. K. Tripathi "Investigations on Functional Materials for Hybrid Sulfur Cycle for Thermochemical Hydrogen Production", Research Scholar Meet (RSM-2017), St. Xavier's College, Mumbai, Feb 17-18, 2017 (Oral presentation)

11. Ashish Nadar, A. M. Banerjee, M. R. Pai, R. P. Antony, A. K. Tripathi, “Molybdenum Carbide Dispersed on Carbon: A Viable Nanoelectrocatalyst for Hydrogen Evolution Reaction, University of Aveiro, Portugal, July 19-21, 2017.(Oral presentation)

Ashish

Ashish Natarajan Nadar

Dedicated to

Mom,

My beloved Family and Friends

ACKNOWLEDGEMENTS

Words are inferior to express my gratitude to each and everyone who had been the pillars during the PhD programme. I am blessed to be associated with such wonderful people for not only being supportive for the programme but even beyond the scientific discussions.

I really feel fortunate to work under the guidance of two great inspiring scientists. I sincerely thank Dr. A. K. Tripathi for providing constant support and encouragement. His efforts for bringing about the precision and accuracy in every aspect really helped me a lot and indeed taught a lot of skill to help me in the long run. I am highly obliged to Dr. (Ms) Shyamala R Bharadwaj, Former Head, FCM&CS who had initially roped me for this PhD programme and still extends her support and care even after her retirement till present. It was an auspicious experience while working with such a respectable personality.

Appreciation to Dr. Atindra Mohan Banerjee will be never ending, who as a friend, mentored me at each and every step right from the day one. It was really stimulating to work with such an inspiring, humble, cool, persona.

I express gratitude to Dr. (Ms.) Mrinal R Pai who had not only supported me during the mini project of the course work but even extended her advice and guidance till the end of this programme.

I sincerely acknowledge for the support towards my research given by former Chemistry Group Directors, Dr. T. Mukherjee, Dr. B. N. Jagatap, present Chemistry Group Director Dr. P.D Naik and former Chemistry Division Heads, Dr. D. Das, Dr. V. K. Jain and present Chemistry Division Head, Dr. K. Indira Priyadarsini.

I would like to acknowledge DST and B.A.R.C. for funding during the PhD programme.

I earnestly thank Dr. R. K. Vatsa (Chairman), Dr. P. A. Hassan, Dr. V. Sudarsan, Dr. S. C. Parida, Dr. (Ms) M. R. Pai, the Doctoral Committee members for assessing my work and providing valuable suggestions during the progress review and pre-synopsis viva voce.

It gives me pleasure to place on record my genuine thanks to Analytical Chemistry Division for carrying out ICP-OES, ED-XRF, TG-EGA. Thanks are also due to Dr. S. Kolay (ChD, B.A.R.C.) for TG-DTA, Shri. S. S. Meena (SSPD, B.A.R.C.) for Mossbauer Spectroscopy, Dr. K. Bhattacharaya and Dr. D. Tyagi (ChD, B.A.R.C.) for XPS analysis, Shri Asheesh Kumar (ChD, B.A.R.C.) for SEM and EDAX analysis, Dr. R.V.Pai (FCD, B.A.R.C.) for TPR studies, Ms. Rashmi Singh (RRCAT,Indore) for N_2 BET surface area analysis and TPR studies, Dr. R. Tewari (MSD, B.A.R.C.) for TEM analysis and Dr. S. Rao (CTD, B.A.R.C.) for allowing to carry out the aqueous SO_2 electrolysis experiment in the closed glass loop setup.

I owe my sincere thanks to Dr. S. Ravichandran (CSIR-CECRI, Karaikuddi, Tamil Nadu, India) for giving me an opportunity to work in his lab which helped me a lot in understanding the basics of electrochemistry.

I take this opportunity to thank all the office staff, administrative officers, the members of Hydrogen Energy and Catalysis Section for providing a cordial environment. I am very much grateful to Shri G. S. Mane for providing the technical support while handling several setups. I express thanks to Dr. (Ms.) Rajini P.Antony for giving invaluable advice. I am also thankful to my friend Ms. Sushma Rawool, who always being so helpful.

I express my thankfulness to my mom for her unceasing support and encouragement that helped me to achieve the present situation. At last I would like to thank my loving family and friends whose love and appreciation always trigger me to work harder.

Table of content

Page No.

Chapter 2: Experimental methods 24-70

SYNOPSIS

In view of ever-increasing worldwide energy demands, depleting fossil resources and growing concern about global warming issues, hydrogen being a clean and renewable energy carrier, has emerged as a promising alternative to the fossil fuels, particularly for the transport applications using fuel cell technology. Presently used method for large-scale production of hydrogen involves steam methane reforming but the process suffers from a major drawback i.e. generation of CO_2, a greenhouse gas, as a by-product. More recently, thermochemical splitting of water has shown great potential towards efficient production of hydrogen on an industrial scale.

Present thesis deals with the development of functional materials such as catalysts and electrocatalysts for the two steps of Hybrid-sulfur cycle namely (i) sulfuric acid decomposition and (ii) aqueous SO_2 electrolysis with an objective to improve the reaction kinetics and efficiency of the process. The thesis is divided into seven chapters. A brief description of various chapters is given below.

Chapter 1 - Introduction:

This chapter will focus on the prospect of hydrogen as an alternative energy carrier, thermochemical cycles, hybrid sulfur cycle, catalyst and electrocatalyst requirements for the cycle and their current international status. Considering the gross calorific value of hydrogen fuel (141.8 MJ/Kg, 3 times of gasoline) and with enabling production, storage and utilization technologies, it has the potential to replace fossil fuels in the global transportation sector. Among the hydrogen generation technologies, thermochemical cycles hold enormous promise by virtue of the larger scale of production. Thermochemical cycles consist of a series of reactions which can produce hydrogen using nuclear or solar heat at much lower temperatures than that required for direct splitting of water.[1] The efficiency of the hybrid sulfur thermochemical cycle is potentially high (~ 40 %) and it has the advantage of being an all fluid process. Moreover, the possibility of coupling to high temperature nuclear reactor exists due to similar operating temperature of the coolant and the high temperature step of the cycle. The Hybrid-Sulfur Cycle consists of the following steps:

Step 1 : Sulfuric acid decomposition reaction:

$H_2SO_{4(l)} = SO_{2(g)} + 0.5\ O_{2(g)} + H_2O_{(l)}$ (800-900 °C) (1.1)

Step 2: Aqueous SO_2 electrolysis

$SO_{2(g)} + H_2O_{(l)} = H_2SO_{4(l)} + H_{2(g)}$ (RT, $E^o = 0.158$ V) (1.2)

Net reaction: (Water splitting) $H_2O_{(l)} = H_{2(g)} + 0.5\ O_{2(g)}$ (1.3)

Sulfuric acid decomposition is the highest temperature step in hybrid-sulfur cycle.[2]In this thesis, studies have been carried out on dispersed iron oxide based catalyst for sulfuric acid decomposition (equation 1.1). Further, investigations have also been carried out on electrocatalyst for aqueous SO_2 electrolysis (equation 1.2) along with design and development of a PEM based cell for the above reaction.

Chapter 2 - Experimental methods

This chapter will deal with the experimental techniques employed for the synthesis, characterization of materials and evaluation of the catalytic along with electrocatalytic properties. Various techniques were used for the characterization of the materials during the present work, which includes X-Ray Diffraction (XRD), Fourier Transform Infrared Spectroscopy (FTIR), N_2-adsorption-desorption isotherm studies, X-Ray Photoelectron Spectroscopy (XPS), Scanning Electron Microscopy (SEM), Energy Dispersive X-ray (EDX), Transmission Electron Microscopy (TEM), Mössbauer Spectroscopy, Temperature Programmed Desorption/Reduction/Oxidation (TPD/R/O), Thermogravimetry-Differential Thermal Analysis-Evolved Gas Analysis (TG-DTA-EGA). To evaluate the performance of catalysts quartz catalytic reactors were used for the study related to sulfuric acid decomposition reaction. Three electrode configuration, as well as PEM type cell, were employed to assess the electrocatalytic properties.

Chapter 3 - Comparative evaluation of iron oxide dispersed on different metal oxide supports for sulfuric acid decomposition reaction

Details will be presented regarding the synthesis, characterization and catalytic activities of a set of iron oxide[3] based catalysts Fe_2O_3 (15 wt.%)/MO_2 (M = Zr, Ce, Ti and Si) prepared from iron acetylacetonate as iron precursor and commercial supports by an equilibrium-adsorption method. The synthesized catalysts were characterized by N_2-adsorption-desorption isotherm, powder X-ray diffraction (XRD), Mössbauer spectroscopy, Fourier transform infrared spectroscopy (FTIR), diffuse reflectance UV-visible spectroscopy (DRUV-VIS), X-ray photoelectron spectroscopy (XPS) and transmission electron microscopy (TEM). Structural analysis by powder XRD and Mössbauer revealed that α-Fe_2O_3 was dispersed over the support in ZrO_2 and CeO_2, ε-Fe_2O_3 crystallized as major phase over SiO_2 support while evolution of Fe_2TiO_5 phase was evident in the case for TiO_2. XPS spectra revealed that in all cases iron was in Fe^{3+} state while O1s peak could be deconvoluted into three peaks – the lowest binding energy peak due to O^{2-} in the dispersed phase, the major central peak owing to oxoanion in the metal oxide supports, while the highest binding energy peak arising out of chemisorbed oxygen/hydroxyl species. The TEM images indicated that Fe_2O_3 was homogeneously distributed over SiO_2 support but non-uniformly spread over $CeO_2$and no proper dispersion over ZrO_2while Fe_2TiO_5 particles formed aggregates in the case of Fe_2O_3/TiO_2. The order of catalytic activity at a low temperature of ~ 750 °C was observed to follow the order $Fe_2O_3/SiO_2 > Fe_2O_3/TiO_2 > Fe_2O_3/ZrO_2 > Fe_2O_3/CeO_2$.

Chapter 4 - Investigations on sulfuric acid decomposition reaction over silica-supported iron oxide catalysts: Effect of preparation methodology and loading

Further studies were carried out with Fe_2O_3/SiO_2 system to find out the optimum loading of Fe_2O_3 in SiO_2. Comparative evaluation of iron oxide (Fe_2O_3) dispersed in various amounts on SiO_2 support (5, 10, 15 and 20 weight percent of Fe_2O_3 in SiO_2) were attempted and will be discussed in this chapter[4]. Structural investigations with XRD and Mössbauer revealed that the 1000 °C calcined samples contained ε-Fe_2O_3 as the major phase in addition to minor α and γ-Fe_2O_3 phases. Analysis of surface features by N_2-BET surface area, pore size distribution, pore volume and XPS indicated that the majority of Fe_2O_3 was encapsulated within the mesoporous structure of SiO_2 till 15 wt. % dispersion, beyond which Fe_2O_3 was deposited outside the pores in a much larger quantity. The extent of reducibility measured via TPR increased with increasing loading[5] and was found to be maximum for the 15 wt.% dispersed samples. The multiple TPR cycles of the samples exhibited a progressively increasing peak area for reduction of Fe_2O_3 in successive cycles establishing the presence of iron oxide silica interactions, as it inhibited Fe_2O_3complete reduction. The catalytic activity of the Fe_2O_3/SiO_2 catalyst for sulfuric acid decomposition reaction was investigated in a flow-through quartz catalytic reactor at a WHSV of ~ 27 g acid g^{-1}cat h^{-1} and it was found to increase with an increase in loading of active Fe_2O_3 phase upto a maximum of 15 wt.

% and then decreased for 20 wt. %. Further evaluation of the 15 wt. % sample revealed the long term stability (100 h) and practical applicability of the composition. The major physical and chemical changes of the Fe_2O_3 (15 wt. %)/SiO_2 catalyst on prolonged use included iron sulfate formation, amorphisation and agglomeration[6].

In order to prepare dispersed iron oxide catalyst with improved performance, several other synthesis techniques were employed and the results are also presented in this chapter. Fe_2O_3 (15 wt. %)/SiO_2 catalyst was also prepared by different methods[7] such as polyol method, wet impregnation method and hydrothermal method and their catalytic activities for sulfuric acid decomposition was compared with that of 15% wt. iron oxide dispersed on silica catalyst which was initially prepared by equilibrium adsorption method. The samples were characterized by XRD, N_2 - BET, FTIR, XPS and TPR. Nature of iron oxide phase of the catalyst was found to depend on the method of preparation. Sample prepared via polyol route contained only α-Fe_2O_3 (ICSD No. 15840) whereas those prepared via wet impregnation and hydrothermal routes contained ε-Fe_2O_3 (ICSD No. 415250) as a minor phase along with α-Fe_2O_3. The catalytic activity for sulfuric acid decomposition reaction was evaluated with 20-45(A.S.T.M) mesh fraction of the catalyst in the temperature range 500-900°C in a flow-through quartz catalytic reactor. The order of catalytic activity at 800 °C followed the order: polyol > equilibrium adsorption > hydrothermal > wet impregnation. This study suggested that polyol method is the most suitable to prepare dispersed iron oxide catalysts.

Chapter 5- Studies on electrocatalyst for SO_2 aqueous electrolysis and its evaluation in PEM based electrolyser

This chapter deals with studies on SO_2 aqueous electrolysis[8] (Eqn. 1.2, chapter 1) carried out in a PEM (Proton Exchange Membrane) based electrolyser, where oxidation of aqueous SO_2 occurs in the anodic compartment to produce sulfuric acid which is recycled in the decomposition step (Eqn. 1.1, chapter 1) and hydrogen evolution reaction (HER) occurs in the cathodic compartment. Varying content of Pt (5, 10, 20 and 40 wt. %) w.r.t. commercial Vulcan carbon was deposited and half-cell reaction for aqueous SO_2 oxidation was studied. Further, platinum catalyst was deposited on Nafion-117 membrane by impregnation-reduction method and tested for aqueous SO_2 electrooxidation. The Pt/Nafion membrane electrode assembly exhibited onset of electro-oxidation of aqueous SO_2 at ~ 0.6 V in a single PEM type cell having area 4 cm^2. All the above progress will be presented in details in this chapter.

To investigate an alternate electrocatalyst to Pt, Mo_2C dispersed on carbon with varying Mo loadings for hydrogen evolution reaction was studies and will also be presented in this chapter. It involved synthesis by carburization[9] of Vulcan carbon (XC 72R) supported ammonium molybdate, characterization by powder XRD, FTIR, SEM, cyclic voltammetry and finally evaluation of their electrocatalytic activities for hydrogen evolution reaction. All the samples were active for electrochemical hydrogen evolution reaction. The 30% Mo_2C/VC proved to be the most active amongst the synthesized catalyst suggesting an optimum loading of the Mo_2C on the carbon support.

Chapter 6- Demonstration of solar thermochemical sulfuric acid decomposition in a cavity type reactor

This chapter presents work done towards utilization of solar heat for sulfuric acid decomposition reaction, the heat extraction step in the solar hybrid-sulfur cycle. A cavity type solar thermal reactor[10] was developed in quartz for carrying out sulfuric acid decomposition as part of solar thermochemical hydrogen production using hybrid sulfur cycle. Maximum SO_2 yield of ~ 38 % was obtained at a WHSV of 28 g acid/gcat/h in the solar receiver-reactor utilizing concentrated heat from a 1.8 m diameter solar dish and employing $Fe_{1.8}Cr_{0.2}O_3$ as catalyst.

Chapter 7- Conclusion and scope of future work

This chapter discusses the summary and outcome of the present thesis and also the scope for the future work. In-depth investigations have been carried out on dispersed iron oxide catalysts for sulfuric acid decomposition delineating the role of active dispersed phase and role of support. Further, detailed synthesis procedure of nanoparticulate iron oxide, their characterization along with mechanistic understanding for sulfuric acid decomposition will be helpful in the design and development of future catalytic systems. The work with solar thermochemical sulfuric acid decomposition was attempted which showed the initial promise and this work can be extended in future with improved reactors for efficient heat extraction. Exploring the aqueous SO_2 electrolysis in PEM based electrolyzer exhibited the promise of coupling of solar thermochemical sulfuric acid decomposition with the electrolyzer for a complete closed cycle demonstration of hybrid-sulfur cycle.

References:

1. L. C. Brown, J. F. Funk, S.K. Showalter, GA-A23373 report (2000).

2. V. Barbarossa, S. Brutti, M. Diamanti, S. Sau, G. De Maria, Int. J. Hyd. Energy31 (2006) 883-890.

3. A. M. Banerjee, A. R. Shirole, M. R. Pai, A. K. Tripathi, S. R. Bharadwaj, D. Das and P. K. Sinha, *Appl. Catal. B: Environ.,* 2012, **127**, 36-46.

4. A. Gervasini, C. Messi, P. Carniti, A. Ponti, N. Ravasio, F. Zaccheria, J. Catal. 262 (2009) 224–234.

5. A.M. Banerjee, M.R. Pai, Jagannath, S.R. Bharadwaj, Thermochim. Acta 516 (2011) 40–45.

6. N. J. Divins, I. Angurell, C. Escudero, V. Pérez-Dieste, J. Llorca, Science 346 (2014) 602-607.

7. J. A. Schwarz, C. Contescu, A. Contescu, Chem. Rev. 95 (1995), 477-510

8. J. A. O'Brien, J.T. Hinkley, S. W. Donne, S-E Lindquist, Electrochemica Acta 55 (2010) 573-591.

9. W. F. Chen, C. H. Wang, K. Sasaki, N. Marinkovic, W. Xu, J. T. Muckerman, Y. Zhu, R. R. Adzic Energy Env. Sci., 6 (2013) 943-951.

10. T. Melchiora, C. Perkins, A. W. Weimer, A. Steinfeld,Int. J. of Thermal Sci. 47 (2008) 1496–1503.

List of Figures

List of Tables

Chapter 1: Introduction

1.1 World Energy Outlook

In the current scenario apart from the basic requirements, energy has become one of the fundamental necessities and is also one of the important factors for economic progress. The demand for energy seems to be ever increasing with time, due to the ever-increasing global population. Since the last 300 years, there has been extensive reliance upon fossil fuels (coal, oil and gas) for industrialization and urbanization [1]. World is therefore heavily dependent on fossil fuels for its energy requirements in improving the standard of living and for transportation needs. However, the fossil fuels are gradually depleting and there is an urgent need to find alternate sources to meet the increasing energy demands.

1.2 Green House Effect

While propelling the economic progress, extensive uses of fossil fuels has also contributed to the environmental pollution causing significant changes in the global climate. The climate of globe keeps on changing throughout the history [2]. Inclement weather conditions like stern droughts, floods, hurricanes, and tremendous heat turn out to be the modern phenomenon. Human actions such as deforestation and widespread uses of fossil fuels for transportation results in emission of carbon dioxide, a greenhouse gas causing global warming [3]. In addition coal and oil-based power generation plants contribute significantly to the CO_2 emissions. Global CO_2emissions in the year 2014 were around 35.9 gigatonnes (Gt).Among various nations, India appears at twentieth position with respect to per capita CO_2 emissions per annum [4].

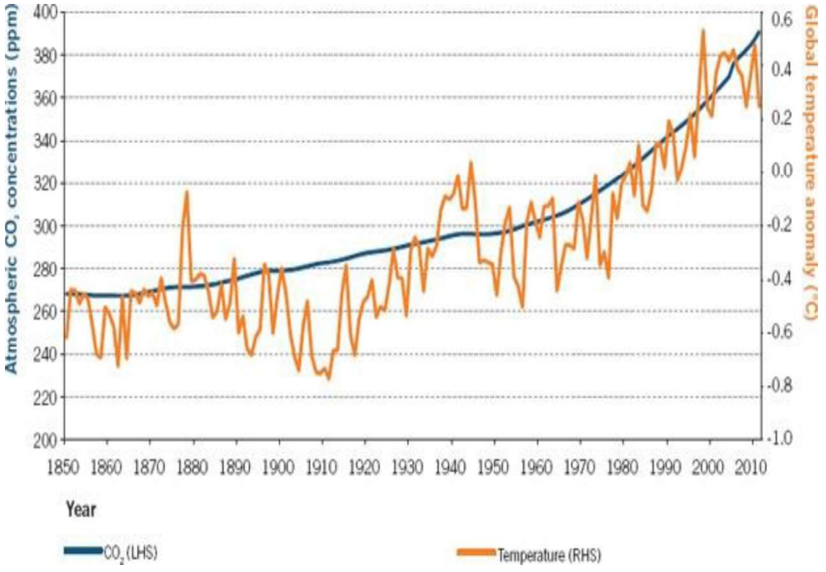

Figure 1.1: Global CO_2 atmospheric concentrations and temperature

(Source:https://hub.globalccsinstitute.com)

Figure 1.1 portrays that over the past 150 years or so, amount of atmospheric CO_2 concentrations has increased significantly leading to substantial rise in average global temperatures. This trend became more predominant from 1950 onwards and can be mainly attributed to human activity and industrial revolution.

In view of increasing energy requirements and growing concern about the global warming issues, the world is in need of an alternative energy source. Some of the resources that can provide clean renewable energy by replacing fossil fuels include solar, wind, biomass, geothermal and hydel energy. For energy security in India "A National Renewable Energy Act" that came in to effect in 2015, strongly recommended energy production via renewable energy sources, so that not only the dependence on fossil fuels can be reduced but also CO_2 emission levels can be decreased [4].

1.3 Hydrogen: An Alternate Energy Carrier

Exploration of alternate energy resources has attained greater significance in recent times due to depleting fossil resources and alarming global warming conditions caused by the emission of greenhouse gases. For many applications like in transport sector, usages of a clean and sustainable/renewable energy-carrier/fuel is in great demand today. As combustion of hydrogen produces only water, it has a great potential as a clean and renewable energy carrier (like electricity) and a promising alternative to the fossil fuels, particularly for the transport applications using fuel cell technology. It can also be deployed for applications such as heating and power generation in areas which are either remote or away from the electrical grid. In some cases, transporting hydrogen by pipeline is even cheaper than transmission of electricity over long distances. Liquid hydrogen is widely used as a fuel in the rockets/space shuttle, whereas hydrogen fuel cell generates power for the electrical systems and produces pure water for the crew members. Hydrogen fuel cells produce power more efficiently than the conventional combustion technologies in a pollution free manner and can feed power to any portable systems that uses batteries such as car, trucks, bus etc. Thus, hydrogen, in future, can play a lead role as an alternate energy carrier reducing our dependency on oil and in overcoming the global warming issues.

1.4 Methods for Hydrogen Production

Although hydrogen is most abundant element, it does not occur in free-state on the earth and is predominantly present as water, fossil fuels and biomass. Production of hydrogen from these sources is energy intensive as it involves breaking of O-H/C-H bonds. Most of the hydrogen, at present, is produced from fossil resources, where contributions from hydrocarbons, coal and oil is ~ 48%, 30% and 18%, respectively [5,6]. Steam reforming of hydrocarbons such as steam methane reforming (SMR) is a widely used process globally for hydrogen production but it suffers from a major drawback such as emission of CO_2, a greenhouse gas. Water electrolysis accounts for ~ 4% of global hydrogen production without any greenhouse gas emission [7].

Hydrogen can be considered as a renewable fuel provided it is generated directly from water (abundant source of hydrogen) using solar or nuclear energy or indirectly through electricity via a renewable source, e.g. wind power or hydro power. Thermolysis of water requires temperatures beyond 2500 K [8]. Electrolysis of water utilizing electricity from renewable energy sources has been studied for a long time and the H_2 generated by this process is very pure. In general, the production of hydrogen through electrolysis of water is a highly energy intensive process (4.5-6.5 kWh/Nm^3). High energy consumption coupled with high capital investment is the reason, why water electrolysis technology is not preferred for commercial purposes [9]. Other processes for hydrogen generation from water include photocatalytic, photoelectrochemical and photobiological but these are at research level.

1.5 Thermochemical Water Splitting

Alternative routes to produce hydrogen from water are by thermochemical water splitting cycles. Thermochemical water splitting processes use high-temperature heat (500–2000°C) derived from either a solar or a nuclear source to drive a series of chemical reactions where hydrogen and oxygen are the final products as shown in Figure 1.2. The chemicals used in the process are recycled creating a closed loop. Hybrid thermochemical process involves a combination of heat and electrolysis step.

The hydrogen produced from fossil fuels does possess minor contaminants (CO, S etc.) that are disadvantageous to fuel cells but thermochemical hydrogen will not contain such contaminants. Also the products i.e. oxygen and hydrogen in thermochemical cycles are produced in different stages therefore issues about their separation may not arise. Thus the hydrogen generated from thermochemical cycle is more compatible with the fuel cells.

The evaluation and screening of thermochemical processes are generally conducted with an objective to couple it with an advanced high-temperature nuclear reactor HTGR (e.g. helium gas cooled reactor; operating at ~ 900 °C) as the primary energy source [5–7]. In the case of solar thermochemical cycle, the focusing of direct solar radiations can be attained by sun-tracking mirrors referred as collectors or heliostats [8-12] and depending upon the design of the solar concentrators the maximum temperatures can exceed 1500 °C. In general, the thermochemical processes are not very compatible with the solar concentrators due to frequent thermal transitions caused by inconsistent solar radiation reaching on earth's surface. Hence, adaptation of such processes to solar heat is necessary.

The general classification of thermochemical cycles includes multi-step thermochemical cycles and metal oxide redox pair-based cycles. The former type of cycles is defined on the basis of compounds which are generally composed of sulfur, chlorine, bromine etc. These components go through a series of reactions to produce hydrogen and oxygen in different stages of the reaction via water splitting. In the case of later type cycles, the redox material produces oxygen and hydrogen by cyclic reduction-oxidation reactions, respectively. These are further categorized as volatile or non-volatile cycles based on type of the redox material employed [13].

Thermochemical water-splitting cycles have been studied since the past five decades and numerous (~300) thermochemical cycles have been investigated for hydrogen production [9]. Some of these cycles are included in Table 1 [13, 14]. However, the technical issues such as material of construction, operating conditions, availability of heat source (nuclear reactor, solar concentrator), process efficiency and economic criteria have delayed the commercial exploitation of thermochemical cycles. Amongst several cycles sulfur based thermochemical cycles such as Sulfur- Iodine and Hybrid Sulfur cycle are most preferably studied due to several advantages which are highlighted in the following sub-sections.

Table 1.1 List of few thermochemical cycles [13, 14] (* Electrochemical step)

S. No.	**Name of the cycle**	**Reactions Involved**	**T_{max} (°C)**
1.	GA Sulfur-Iodine	$2H_2SO_4(g) = 2SO_2(g) + 2H_2O(g) + O_2(g)$	850
		$2HI = I_2(g) + H_2(g)$	300
		$I_2 + SO_2(g) + 2H_2O = 2HI(l) + H_2SO_4(l)$	100
2.	Hybrid Sulfur	$2H_2SO_4(g) = 2SO_2(g) + 2H_2O(g) + O_2(g)$	850
		$SO_2(g) + 2H_2O(l) = H_2SO_4(l) + H_2(g)$	77*
3.	Copper Chlorine	$2Cu(s) + 2HCl(g) = 2CuCl(l) + H_2(g)$	~450
		$2CuCl(s) = 2CuCl(aq) = CuCl_2(aq) + Cu(s)$	25*
		$CuCl_2(aq) = CuCl_2(s)$	>100
		$2CuCl_2(s) + H_2O(g) = CuO.CuCl_2(s) + 2HCl(g)$	400
		$CuO.CuCl_2(s) = 2CuCl(l) + 1/2O_2(g)$	500
4.	Hybrid Copper Chlorine	$2Cu(s) + 2HCl(g) = H_2 + 2CuCl(s)$	425
		$4CuCl(s) = 2Cu(s) + 2CuCl_2(s)$	25*
		$2CuCl_2(s) + H_2O = Cu_2OCl_2(s) + 2HCl(g)$	325
		$Cu_2OCl_2(s) = 2CuCl(s) + 1/2O_2$	550
5.	Ispra Mark 13	$2H_2SO_4(g) = 2SO_2(g) + 2H_2O(g) + O_2(g)$	850
		$2HBr(l) = Br_2(g) + H_2(g)$	77*
		$Br_2(l) + SO_2(g) + 2H_2O(l) = 2HBr(g) + H_2SO_4(l)$	77
6.	UT-3 Univ. of Tokyo	$2Br_2(g) + 2CaO = 2CaBr_2 + O_2(g)$	600
		$3FeBr_2 + 4H_2O = Fe_3O_4 + 6HBr + H_2(g)$	600
		$CaBr_2 + H_2O = CaO + 2HBr$	750
		$Fe_3O_4 + 8HBr = Br_2 + 3FeBr_2 + 4H_2O$	300
7.	JulichCenter EOS	$2Fe_3O_4 + 6FeSO_4 = 6Fe_2O_3 + 6SO_2 + O_2(g)$	800
		$3FeO + H_2O = Fe_3O_4 + H_2(g)$	700
		$Fe_2O_3 + SO_2 = FeO + FeSO_4$	200
8.	Hallett Air Products 1965	$2Cl_2(g) + 2H_2O(g) = 4HCl(g) + O_2(g)$	800
		$2HCl = Cl_2(g) + H_2(g)$	25*

9.	Gaz de France	$2K + 2KOH = 2K_2O + H_2(g)$ $2K_2O = 2K + K_2O_2$ $2K_2O_2 + 2H_2O = 4KOH + O_2(g)$	725 825 125
10.	Aachen UnivJulich 1972	$2Cl_2(g) + 2H_2O(g) = 4HCl(g) + O_2(g)$ $2CrCl_2 + 2HCl = 2CrCl_3 + H_2(g)$ $2CrCl_3 = 2CrCl_2 + Cl_2(g)$	850 170 800
11.	Ispra Mark 1C	$2CuBr_2 + Ca(OH)_2 = 2CuO + 2CaBr_2 + H_2O$ $4CuO(s) = 2Cu_2O(s) + O_2(g)$	100 900
12.	Ispra Mark 8	$3MnCl_2 + 4H_2O = Mn_3O_4 + 6HCl + H_2(g)$ $3MnO_2 = Mn_3O_4 + O_2(g)$ $4HCl + Mn_3O_4 = 2MnCl_2(a) + MnO_2 + 2H_2O$	700 900 100
13.	Ispra Mark 6	$2Cl_2(g) + 2H_2O(g) = 4HCl(g) + O_2(g)$ $2CrCl_2 + 2HCl = 2CrCl_3 + H_2(g)$ $2CrCl_3 + 2FeCl_2 = 2CrCl_2 + 2FeCl_3$ $2FeCl_3 = Cl_2(g) + 2FeCl_2$	850 170 200 420
14.	Ispra Mark 4	$2Cl_2(g) + 2H_2O(g) = 4HCl(g) + O_2(g)$ $2FeCl_2 + 2HCl + S = 2FeCl_3 + H_2S$ $2FeCl_3 = Cl_2(g) + 2FeCl_2$ $H_2S = S + H_2(g)$	850 100 420 800
15.	Ispra Mark 3	$2Cl_2(g) + 2H_2O(g) = 4HCl(g) + O_2(g)$ $2VOCl_2 + 2HCl = 2VOCl_3 + H_2(g)$ $2VOCl_3 = Cl_2(g) + 2VOCl_2$	850 170 200
16.	Ispra Mark 2 (1972)	$Na_2O.MnO_2 + H_2O = 2NaOH(a) + MnO_2$ $4MnO2(s) = 2Mn_2O_3(s) + O_2(g)$ $Mn_2O_3 + 4NaOH = 2Na_2O.MnO_2 + H_2(g) + H_2O$	100 487 800
17.	Ispra Mark 7B	$2Fe_2O_3 + 6Cl_2(g) = 4FeCl_3 + 3O_2(g)$ $2FeCl_3 = Cl_2(g) + 2FeCl_2$ $3FeCl_2 + 4H_2O = Fe_3O_4 + 6HCl + H_2(g)$ $4Fe_3O_4 + O_2(g) = 6Fe_2O_3$ $4HCl + O_2(g) = 2Cl_2(g) + 2H_2O$	1000 420 650 350 400

18.	Vanadium Chloride	$2Cl_2(g) + 2H_2O(g) = 4HCl(g) + O_2(g)$ $2HCl + 2VCl_2 = 2VCl_3 + H_2(g)$ $2VCl_3 = VCl_4 + VCl_2$ $2VCl_4 = Cl_2(g) + 2VCl_3$	850 25 700 25
19.	US - Chlorine	$2Cl_2(g) + 2H_2O(g) = 4HCl(g) + O_2(g)$ $2CuCl + 2HCl = 2CuCl_2 + H_2(g)$ $2CuCl_2 = 2CuCl + Cl_2(g)$	850 200 500
20.	ZnO/Zn	$ZnO = Zn + 1/2\,O_2$ $Zn + H_2O = ZnO + H_2$	2000 1100
21.	Fe_3O_4/FeO	$Fe_3O_4 = 3\,FeO + 1/2\,O_2$ $3FeO + H_2O = Fe_3O_4 + H_2$	1300 900

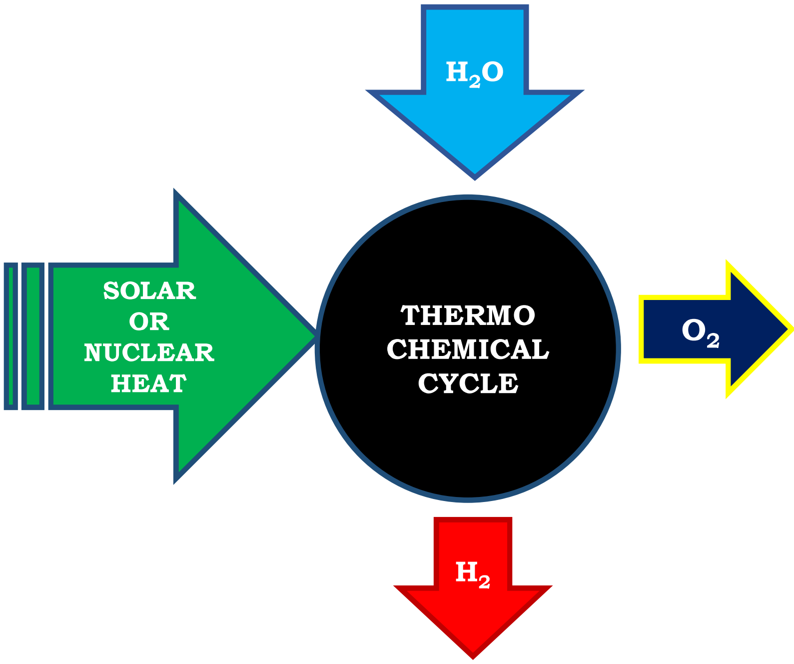

Figure 1.2: Thermochemical Cycle

1.6 Sulfur based Thermochemical Cycle: Strongest Contender

1.6.1 Sulfur Iodine Cycle

The sulfur-iodine(S-I) cycle (Figure 1.3) is considered to be as one of the most favorable and competent thermo-chemical water splitting technologies for the large-scale production of hydrogen and can play an important role in hydrogen-based economy [10-11]. India holds the 5th position globally in developing this process after USA (1980), Japan (2004), South Korea (2009) and China (2010). In the 1970s, the S–I thermochemical cycle was invented at General Atomics[12].Japan Atomic Energy Agency (JAEA) has conducted extensive R&D on S-I process for hydrogen production from water and a test facility producing 32 L/h hydrogen has been demonstrated [12].A successfully closed loop operation of S-I process in glass/quartz has been achieved in the Bhabha Atomic Research Centre, India. The ONGC Energy Centre (OEC) is also working on thermochemical hydrogen generation via Copper -Chlorine and Sulfur-Iodine processes[4].

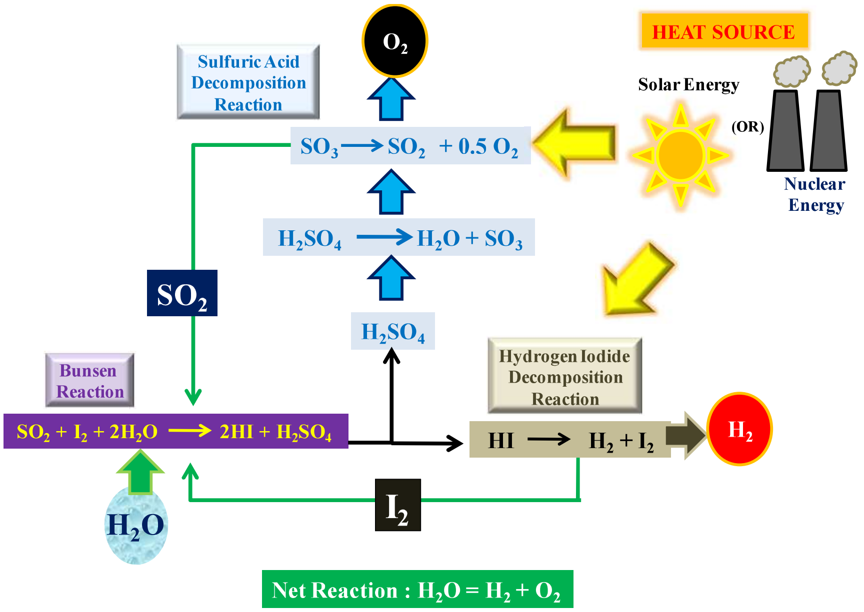

Figure 1.3: Schematics of Sulfur-Iodine thermochemical Cycle

The Sulfur–Iodine cycle comprises of three steps where water is the only net reactant and hydrogen and oxygen are the net products. The additional chemicals are recycled back in subsequent steps [15,16]. This process however, requires high-grade heat from either nuclear or solar source. The reactions involved in this S-I cycle are as follows:

$I_2 + SO_2 + 2\,H_2O \rightarrow 2\,HI + H_2SO_4$ (Bunsen reaction)------------------------(1.1)

$H_2SO_4 \rightarrow SO_2 + H_2O + 1/2O_2$ (Sulfuric Acid Decomposition) -------------------- (1.2)

$2\,HI \rightarrow I_2 + H_2$ (450 °C) (Hydriodic Acid Decomposition)-----------------(1.3)

Net reaction: $2\,H_2O \rightarrow 2\,H_2 + O_2$--------------------- (1.4)

There are many advantages of the S–I process such as

a. It is an all fluid (liquids, gases) process, thus its well capable for continuous operation;

b. S-I cycle is compatible with nuclear, solar sources of heat;

c. This cycle is more efficient (~56%) than the other thermochemical processes

Though having several advantages it still requires substantial development for large scale continuous operation. The process equipment requires superior materials, which could withstand the corrosive reaction environment caused due to iodine, sulfur dioxide, hydroiodic acid and sulfuric acid. Various materials reported to be compatible for the process include refractory metals, reactive metals, superalloys, ceramics, polymers, and coatings such as tantalum alloys, niobium alloys, mullite, silicon carbide (SiC), noble metals, high-silicon steels nickel-based superalloys, glass, silicon nitride (Si_3N_4),etc. [17].

1.6.2 Hybrid Sulfur Cycle

The Hybrid Sulfur (HyS) cycle is two-step process involving SO_2 aqueous electrolysis and thermochemical sulfuric acid decomposition as depicted in Figure 1.4. It is also referred to as the Westinghouse cycle [16] or Ispra Mark 11 cycle, first proposed by Westinghouse Electric Corporation in 1970s. The two reaction steps, as shown below, involve fluid reactants hence this cycle is one of the most desirable and simplest thermochemical processes.

$H_2SO_4 \rightarrow SO_2 + 1/2\ O_2 + H_2O$ (thermal decomposition) -------------(1.5)

$2H_2O + SO_2 \rightarrow H_2SO_4 + H_2$ (electrolysis) ------------------------------(1.6)

Net reaction: $2\ H_2O \rightarrow 2\ H_2 + O_2$--------------------- -------(1.4)

In the HyS cycle, electrolysis of sulfur dioxide and water mixture at low temperature produces hydrogen and sulfuric acid. The sulfuric acid is decomposed at high temperature to oxygen and sulfur dioxide. SO_2 produced is recycled back into the electrolyzer. Thus, the net reaction is production of hydrogen and oxygen via water splitting. The theoretical voltage for splitting of pure water by electrolysis is 1.23 V at room temperature while the aqueous SO_2 electrolysis requires only 0.158 V at unit activity for reactants and products. In hybrid-sulfur process, sulfuric acid is the only feedstock so, the requirement of chemical stock in the hydrogen plant is comparatively lower than that required for the S-I process. Further, the complications involved with the hydroiodic acid section are also avoided. Thus, the hybrid process has prospective advantages with regard to both pure electrolysis and pure thermochemical processes [19].

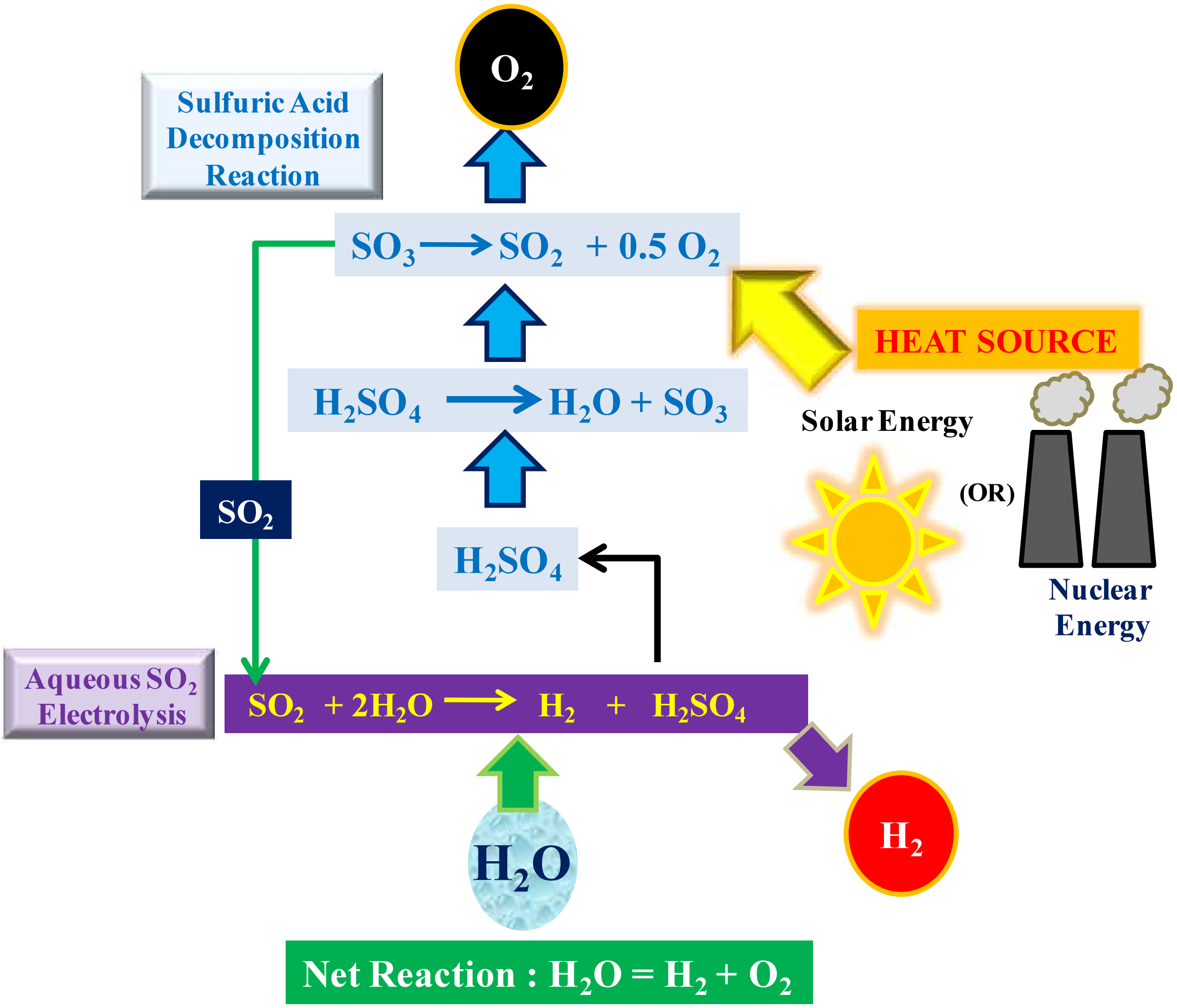

Figure 1.4: Schematics of Hybrid Sulfur thermochemical Cycle

There are four major subsystems in this cycle: concentrator, decomposer, separator, and electrolyzer. Sulfuric acid is obtained in the anodic compartment of the electrolyzer by oxidizing SO_2 and hydrogen is generated at the cathode. The sulfuric acid is concentrated, dehydrated and decomposed to generate SO_2 and O_2 which is separated in the separator before SO_2 recycling for closed loop operation. The process efficiency for the HyS cycle is reported to be ~50 % @ 10 bar and 927 °C [13-21].

1.7 Sulfuric Acid Decomposition: The most Endothermic Step in S-I and HyS Cycle:

In both S-I and HyS cycles, the most energy demanding step is sulfuric acid decomposition reaction. The conversion of H_2SO_4 to SO_2 as described by the Equation 1.2, essentially takes place in two successive steps:

Step one is a non-catalytic thermal dehydration of sulfuric acid to sulfur trioxide and water vapor.

$$H_2SO_{4(l)} \rightarrow SO_{3(g)} + H_2O_{(g)} \text{---------------------------------} (1.7)$$

The equilibrium constant of this reaction computed with the help of the thermodynamic data of pure components is found to be above 1 at 400 °C and increases rapidly. It is an endothermic process $\Delta H_{298^\circ} = 97.54$ kJ/mol, [22] however, the equilibrium constant is above 1.

The succeeding step involves catalytic decomposition of sulfur trioxide into sulfur dioxide and oxygen,

$$SO_{3(g)} \rightarrow SO_{2(g)} + 1/2O_{2(g)} \text{--------------------------------} (1.8)$$

This is also an endothermic process having $\Delta H_{298^\circ} = 98.92$ kJ/mol, the equilibrium constant for this reaction is more than 1 at temperatures above 777°C [23]. Hence this reaction is generally studied in the temperature range above 750°C.

Dehydration reaction of sulfuric acid occurs faster than the SO_3 decomposition step. Thus, the complete rate of the process is governed by rate of SO_3 conversion to SO_2 and is also important for the thermochemical cycle efficiency [24-25]. The catalyst must comply with two crucial conditions: firstly it should have adequate activity for catalyzing the reduction of sulfur trioxide to sulfur dioxide and secondly to remain stable and active for an extensive period of time under harsh reaction conditions (corrosive environment and high temperature).

Another important factor is the operating temperature since it has a major impact on the reduction kinetics of SO_3 to SO_2 [23].The reaction rate along with the thermodynamic equilibrium are influenced by temperature and pressure [26]. High conversions of SO_3 to SO_2 are achieved at low pressures and high temperatures [27-29].

Studies on catalytic reduction step are generally performed at laboratory level, in a tubular quartz reactor, heated by an electric furnace. Whereas, at pilot plant scale, fabrication of reactors from materials resistant to high temperatures and corrosive environment is necessary. Most considered materials for this purpose are: *special alloy*, such as Hastelloy C-276 [29], Incolloy 800H; *ceramic materials*, such as SiC, SiSiC, Si_3N_4 [29]; different ceramic materials supported on the special alloy, such as: SiC/Hastelloy X [30], SiC/Inconel 800H, SiC/Inconel 690 [31].

1.8 Role of Catalyst for Sulfuric Acid Decomposition

As it is evident, amongst the two elementary steps of sulfuric acid decomposition reaction, the second step i.e. the decomposition of SO_3 is the catalytic step. Wide range of catalysts has been studied for the decomposition of SO_3. These can be broadly divided into two groups: noble metals and metal oxides.

1.8.1 Noble Metals

The noble metal catalyst dispersed on a stable support like metal oxides such as Al_2O_3, ZrO_2, TiO_2 and even carbides such as SiC have been widely reported for sulfuric acid decomposition reaction [32].Out of these, platinum metal is the most preferred one. The reported systems are Pt supported on alumina, titania and zirconia [33], Pt dispersed on rutile TiO_2 [34], and Pt/$BaSO_4$ [35].The reaction mechanism on supported Pt involves adsorption and dissociation of SO_3 at the surface active sites which involves formation of intermediate adduct [SO_2.O] on the noble metal active centre. Few studies on supported metal particles such as Palladium, Platinum, Rhodium, Iridium, and Ruthenium have also been reported [36].

1.8.2 Metal Oxides

Besides their higher cost, supported noble metal catalysts suffer problems such as leaching, sintering, oxidation during prolonged use for sulfuric acid decomposition reaction [30]. Sulfation of support during acid decomposition also causes deactivation of supported noble metal catalysts as reported by Norman et al [37].

Thus, there is a necessity for more economic, active and stable catalyst for the above reaction. These requirements can be accomplished through metal oxides. Fe_2O_3 was highlighted as best catalyst amongst the series of metal oxide studied as a catalyst for sulfuric acid decomposition reaction [16]. The order of activity of variable catalyst studied for a fixed bed reactor were reported as: $Pt \approx Cr_2O_3 > Fe_2O_3 > CeO_2 > NiO > Al_2O_3$ [16]. The consequence on dissociation efficiency of Fe_2O_3 and Pd-Ag alloy has been studied [16]. Though simple metal oxides are suitable substituent catalysts for the supported noble metals but there are few aspects such as instability at high temperature and agglomeration issues on repetitive usage, preclude them from serving for the purpose. Thus exploration of new catalysts is highly desirable to overcome these issues.

Multi-metal oxides were found to be superior to the simple oxides due to their better chemical and thermal stability and also due to their improved catalytic properties. Still, efforts to investigate mixed metal oxide systems for the H_2SO_4 decomposition reaction are very scarce.

$ZnFe_2O_4$ and $NiFe_2O_4$ were reported as excellent mixed metal oxide for SO_3 decomposition [38]. Iron-based mixed metal oxide catalysts were explored as catalysts and its performance augmented with Fe content, suggesting that the iron would be the active component. Iron titanate, manganese titanate, nickel ferrite, copper ferrite, nickel chromate, copper oxide and iron oxide were also reported for H_2SO_4 decomposition [39]. Although substituted metal oxides and multi-metal oxides were explored as catalyst for sulfuric acid decomposition reaction, issues related to sintering and agglomeration on prolonged use are still persistent. One way of overcoming these could be by dispersing the active component on a stable support, so as to avoid the active component- active component interaction.

1.9 Aqueous SO_2 Electrolysis

Cell with two compartments separated by a proton exchange membrane (PEM) was the original SO_2 depolarized electrolyzer design, conceptualized by Westinghouse as shown in Figure 1.5 [18-19]. The SO_2 saturated sulfuric acid was used as the anolyte while catholyte comprised of sulfuric acid only. The cathode reaction in sulfur dioxide depolarized electrolysis (SDE) is hydrogen evolution (equation 1.10), while the anode reaction (equation1.9) is the electro-oxidation of dissolved sulfur dioxide gas, which occurs at much lower anodic potentials in comparison to water electrolysis.

Positive Electrode: Oxidation of Sulfur dioxide $SO_2 + 2H_2O \rightarrow H_2SO_4 + 2H^+ + 2e^-$-----(1.9)

Negative Electrode: Production of Hydrogen $2H^+ + 2e^- \rightarrow H_2$ -----------(1.10)

The overall cell reaction is:

$$SO_2\ (aq) + 2H_2O \rightarrow H_2SO_4\ (aq) + H_2\ (g);\ E^0 = +0.158\ V \text{ ---------(1.6)}$$

Modern electrolyzer involves Membrane Electrode Assembly wherein the cell resistance is reduced to a greater extent. The schematic of such electrolyzer has been shown in Figure 1.6.

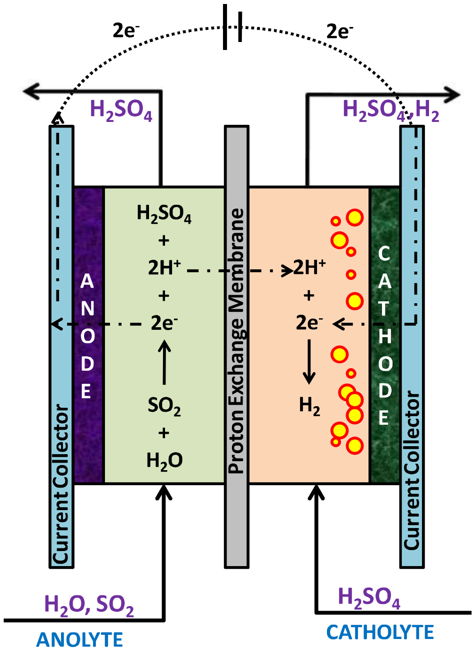

Figure 1.5 Schematic of the original Westinghouse electrolyzer

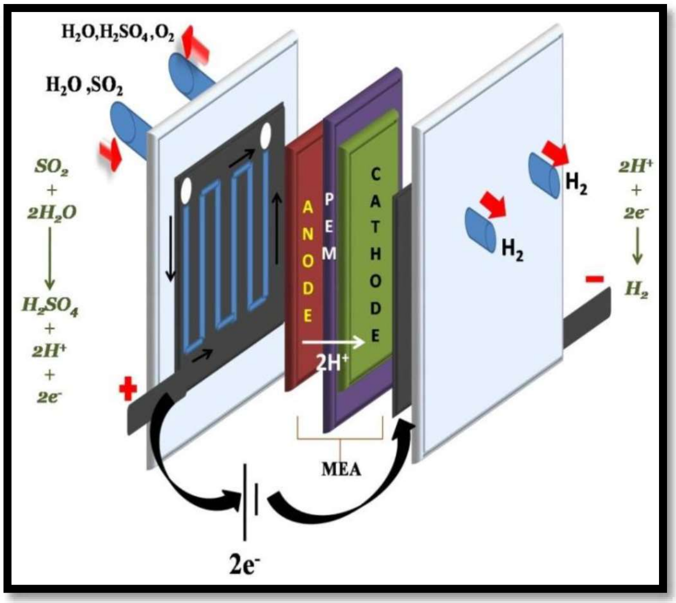

Figure 1.6 Schematic of Membrane Electrode Assembly based Electrolyzer set up

In this electrolyzer, sulfur dioxide saturated water is pumped into the anodic compartment of the cell where sulfur dioxide is oxidized at the positive anode forming sulfuric acid (equation 1.9). The generated protons migrate towards the negative cathode via the membrane and combine with an electron at cathode to form a hydrogen molecule (equation 1.10).Designing and developing the electrolyzer and its components are the most essential part in determining the cell efficiency.

The standard reversible voltage, E^0 for SDE process (1.6) is only 0.158 V, which is much lower than that required for the conventional water electrolysis($E^0 = 1.23$ V) [40]. In lab-scale experiments, the observed cell voltage of SDE has been in the range 0.5-1.2 V, based on the current density and other working conditions [41-43],compared to that of commercial alkaline water electrolyzers [44] (1.8-2.0 V). Thus, SDE requires comparatively lower electrical energy (25-60 %) than for the conventional water electrolysis [41,42].

To avoid reduction of SO_2 on the negative electrode, the anolyte and the catholyte are well separated. Initially, diaphragm-type separators were used in the cells [43], subsequently these were modified and substituted by membranes. Numerous sophisticated membranes, initially developed and utilized in fuel cells were also tested for SDE [42,45,46]. The protons permeate through the separator along with some water, but the membrane doesn't allow passage of any other species or electrons. Generally graphitic bipolar plates and platinum were used as the electrocatalyst for the anode and the cathode.

Variation in models for the SDE and its principle components have thoroughly been devised and studied [40,45,47]. In one of the modeled SDE cell, SO_2 gas was fed to the anode [42] whereas the reaction on the positive side of the cell depended on the water supply from the cathodic compartment. In this case where H_2O and H^+ fluxes inside the membrane act in reverse directions does not allow high current densities [48]. Most of the electrolyzer designs have liquid-fed catholyte and anolyte compartments [40,43,47].

1.10 Electrocatalysts for SDE Step of HyS Cycle

The main aspects related for creation and working of the electrolyzer are mostly interrelated to cell over potential, SO_2 cross over, mass transfer issues, materials of construction, catalyst expense and reliability during prolonged uses. Sulfur dioxide cross-over is associated with the tricky streaming of SO_2 gas from the anodic compartment to the cathodic compartment through the membrane where it undergoes reduction reaction to form elemental sulfur. Another interesting factor is the anodic overpotential where it comprises most of the requisite electrolyzer input voltage for a current density of 200 $mAcm^{-2}$ with a net input voltage of 0.85 V [47].Even with noble metal electrodes [43,49] the over potential issue is quite remarkable at the onset of the oxidation reaction, and is still not fully understood. Aqueous SO_2 electrolysis comprises protons (equation 1.9), hence it is anticipated likely that the half-cell potential of the reaction is dependent on concentration of the acid i.e. due to the varying activity of protons present in the solution media. Also, it has been reported that the initiation of oxidation is shifts to elevated potentials when concentration of H_2SO_4 solutions were increased [49]. The concentration of sulfuric acid also affects the kinematics of the reaction along with the mechanistic aspects of the reaction. The direct proportionality between observed open circuit potential (OCP) and H_2SO_4 strength was also reported [50].Struck et al. specified that there is a decrease in the current density from $25mAcm^{-2}$ to $0mAcm^{-2}$ at a potential of 0.7 V vs. SHE with varying concentration of H_2SO_4 from 5 – 80 wt% [51].

The criterion for selection of electrode materials for efficient operation of the electrolyzer are long-term steadiness, good electrical conductivity, high specific surface area, minimized gas bubble problems, low cost and large availability, better mechanical properties, efficient catalytic properties [41].

1.10.1 Noble Metals

Various kinds of base materials were evaluated for use as an anodic electrode in extremely concentrated H_2SO_4 [43,49]. It was also highlighted that carbon materials such as graphite, carbides are catalytically inactive for the reaction. Activated carbon and carbon black were found to have intermediate performance [49]. The oxidation behavior of porous catalyzed carbon was also investigated by for aqueous SO_2 oxidation [41]. Palladium was found to be the best performing and in addition to this, the formation of palladium oxide on the electrode also promoted the electrocatalytic activity [43]. However, activity of palladium in comparison to platinum was found to be inferior as reported [50]. The studies on electrode activity using Pt and Pd dispersed on carbon support shown that Pt possessed lower activation energy and thus exhibited higher current densities. Repeated experiments highlighted the issues with dissolution of the palladium electrocatalyst, which got hastened by increment in temperature and acid concentration. Also, electrocorrosion of Pd is prominent due to polarization at high potentials in H_2SO_4 solution, further suggested its non-suitability as an electrode material. Bimetallic aluminum and platinum alloy was also investigated for the oxidation of aqueous sulfur dioxide [52]. Gold (Au) was found to have interesting features as an electrode material and performed well kinetically. In reality, it has been observed that Au is having higher activity for the oxidation reaction than Pt due to a dissimilarity in the oxidation mechanism by Quijada and Vazquez [53]. Regardless of this study, carbon cloth/paper/foam electrodes are more commonly used in membrane electrode assemblies, often as a support for a Pt catalyst.

1.10.2 Novel Compounds

A cheaper Fe–N–C catalyst was prepared by disposing and pyrolyzing the raw materials of porous carbon BP2000, nitrogen source imidazole and iron source $FeCl_3$ and employed for SO_2 electrooxidation. Investigations reflected that the pyridinic N, Fe– N and carbides act vital roles on SO_2 electrooxidation [54-55].

1.11 Objective of the Present Study

The present research work has been initiated with an objective to develop suitable functional materials such as catalysts for sulfuric acid decomposition reaction and electrocatalysts for aqueous SO_2 electrolysis steps of hybrid-sulfur cycle. For the purpose following strategy was adapted:

(a) ***Development of Catalyst for Sulfuric Acid Decomposition Reaction:***

The issues such as sintering and grain growth encountered during prolonged uses of sulfuric acid decomposition at 800 °C will be addressed by dispersing the active iron oxide species over stable oxide supports viz., silica, titania, zirconia and ceria. In addition, several preparation methods were employed to optimize the dispersion. Redox behavior of the dispersed iron oxide catalysts were evaluated to correlate with their catalytic activity. Detailed characterizations of both fresh and spent catalysts were carried out to investigate the mechanistic aspects of the acid decomposition process. Efforts were also made to utilize solar heat for sulfuric acid decomposition reaction [56]. For this purpose, a 1.8 m diameter solar dish was employed and a suitable cavity type quartz reactor was designed, fabricated and tested.

(b) ***Development of Electrocatalysts for Aqueous SO_2 Electrolysis***

Detailed studies were carried out to optimize the noble metal loading in the electrocatalyst for the aqueous SO_2 electrolysis. A PEM based electrolyzer comprising of Nafion-117 membrane electrode assembly was also developed for this purpose. Prior to uses in aqueous SO_2 electrolyser, the developed electrocatalysts were evaluated for hydrogen evolution reaction. In addition, efforts were made to develop a non-noble metal electrocatalyst.

Chapter 2: Experimental methods

2.1 Introduction:

The methodologies used for the synthesis of the catalyst along with their characterization and the catalytic activity for sulfuric acid decomposition as well as the electrocatalysts developed for aqueous SO_2 electrolysis and hydrogen evolution reaction are being described in this chapter. The dispersed catalysts were prepared by various routes such as equilibrium adsorption method, polyol method, wet impregnation method, solvothermal method whereas the electrocatalyst were prepared by *insitu* chemical reduction method and polyol method. To investigate the physicochemical properties of the fresh and spent catalyst, number of characterization technique such as X-ray diffraction study (XRD), N_2-BET (Brunauer-Emmett-Teller) surface area, Fourier Transform Infrared Spectroscopy (FTIR), Mössbauer Spectroscopy, X-ray Photoelectron spectroscopy(XPS), Inductively Coupled Plasma Optical Emission Spectroscopy (ICP-OES), X-ray Fluorescence Spectroscopy (XRF), Temperature Programmed Reduction (TPR), Temperature Programmed Oxidation (TPO), Scanning Electron Microscopy (SEM), Transmission Electron Microscopy (TEM), Evolved Gas Analysis (EGA), Differential Thermal Analysis (DTA) etc. were employed. The electrochemical properties of the developed electrocatalysts were evaluated by Cyclic Voltammetry (CV), Linear Sweep Voltammetry (LSV), Chronopotentiometry and Potentiostatic Electrochemical Impedance Spectroscopy (PEIS). The general principles of these techniques are discussed in this chapter concisely. The design of the reactor used for studying the catalytic activity for sulfuric acid decomposition reaction is also illustrated.

2.2 Preparation methods of the catalyst:

In this thesis, the various synthetic routes employed for catalyst preparation are described in brief. The general description of the preparative methods is expressed. However, the detailed procedures for preparation of individual catalyst are mentioned in the respective chapter.

2.2.1 Equilibrium Adsorption Method:

Preparation of the metal oxides by this synthesis method involves immersion of solid supports in the precursor solution for a longer period of time. The governing driving forces for this particular method are the concentration gradient and electrostatic interactions. Supports usually bear a net positive or negative electrical charge on their surface which then attracts the oppositely charged ions in the aqueous solutions. The development of the charges on the oxides depends on the pH of the solution and on the point of zero charge (pzc) of oxides. If pH is greater than pzc then deprotonation of surface hydroxyl takes place results in development of negative charge which attracts cationic species. Similarly for pH lesser than pzc protonates the hydroxyl group which causes adsorption of anionic species. Thus the surface oxide loading can be controlled by just modifying the difference between pH and pzc. Due to chemisorption there is more uniform dispersion of the active species over the support, hence this technique is considered better than the simple wet impregnation method [57]. The iron oxide (Fe_2O_3) was dispersed on different supports such as TiO_2, CeO_2, ZrO_2 and SiO_2 support by equilibrium adsorption method and Fe_2O_3 in various loading composition (5, 10, 15 and 20 wt.%) on SiO_2 support was also prepared; the detailed explanation is mentioned in the chapter 3 and 4 respectively.

2.2.2 Polyol Method:

There are several chemical, physical, or electrochemical methods for nanoparticle synthesis amongst which the polyol-mediated synthesis of inorganic nanoparticles appears as an easier and versatile route [58]. A polyol is high-boiling alcohol containing multiple hydroxyl groups [59].The polyol method is basically a liquid phase synthesis method especially used for preparation of nanoparticles. Ethylene glycol (EG) as its basic representative of the polyols. Depending upon the ethylene glycol, two different series can be ideally observed (i) ethylene glycol, triethylene glycol, tetraethylene glycol, upto polyethylene glycol and secondly (ii) propanediol, butanediol, etc. Fievet, Lagier and Figlarz initially described the preparation of very fine particles using polyols, also coined the term “polyol process” or “polyol synthesis”. Their initial work was based on preparation of cobalt, nickel, copper, and platinum particles and later continued to other metals, intermetallics and alloys [60]. In this reaction the polyol at first acts as a solvent for the reactants because of the high dielectric constant. Later, ethylene glycol reduces the species in the liquid phase, in which nucleation and growth of the metallic phase occur. Thus, ethylene glycol also acts as a crystal growth medium for the metal particles. In addition to the colloidal stabilization, the high boiling points of polyols permit preparation to be carried out in the temperature range of 473-593 K without any need for an autoclaves or high pressure. The polyols are also ideal for the preparation of oxide nanoparticles because of their water-comparable and the chelating characteristics. The solvent immediately coordinates to the as-synthesized particle nuclei which allocates for exceptional control on growth of the particles. For the formation of oxides, water component is crucial and can be modified by means of the inherent condensation of the polyols itself, by using hydrates as the starting materials. The polyol synthesis allows preparing variable compositions, and composite hetero-structures. Also this method is well known for obtaining nanomaterials with definite shapes, which are nearly all kinds of polyhedra and morphologies. Fe_2O_3 was dispersed on SiO_2 by polyol method and it is illustrated in chapter 4 and 6.

2.2.3 Wet Impregnation Method:

Impregnation technique to prepare supported solid nanoparticles, involves linking a solid support with a solution comprising of the active component to be dispersed on the supporting material. During this method several diverse steps occur with different pace such as specific adsorption of species due to coulombic forces, Van der Waals forces or H-bonds; exchange of ions between the charged surface and the electrolyte; polymerization/depolymerization of the species (molecules, ions) attached to the surface; partial dissolution of the surface of the solid. The kind of product is dependent on the nature of both reactants as well as the reaction parameters. The major conditions influencing the solution are the pH, the type of the solvent and the dissolved species. The key properties of the solid support are the stability, the nature of functional groups, the exchangeable ions present in it, and its reactivity. While considering wet impregnation method following points must be considered:

- There is difference in the properties of the liquid in the pores than those observed in the bulk.
- The liquid and solid equilibrates very slowly and also allocation of attached species inside the pores is tough to achieve.
- Deposition comprises diverse kind of interactions [61].

Impregnation could be performed by eight various techniques, such as soaking technique, dry or pore volume impregnation, incipient wetness impregnation, deposition by selective reaction with the surface of the support, impregnation by percolation, co-impregnation, successive impregnation and precipitation-deposition.

In our study catalyst was prepared by soaking method. In this method additional liquid is removed by evaporation or by draining. The loading of the active component by this method is never quantitative and depends upon ratio of the solid to liquid components. Deposition is time-consuming and may require several hours or days. It may also result in extensive restructuring of the surface. Nevertheless, the scheme allows the controlled distribution of the species and high dispersions could also be achieved. This method is more efficient, when there is better ion/solid interactions being involved [61].The detailed description of preparation of the dispersed iron oxide catalyst supported on silica is explained in the chapter 4.

2.2.4 Solvothermal Method:

A solvothermal process can be described as a procedure in a closed reaction vessel inducing a decomposition or a chemical reaction(s) between precursor(s) in the presence of a solvent at a temperature more than the boiling point of the used solvent [62].The method employs the solvent under moderate to elevated pressure (~ 1-10,000 atmosphere) and temperature (100- 1000°C) that allows the interaction of precursors during preparation. The pressure can be autogenous where the pressure value depends on the filling of the reaction vessel else it can be imposed in which the pressure is more than 1 atm. at the starting point of the experiment that could be brought about by the compressing the reaction medium. The solvothermal system can be heterogeneous or homogeneous and in subcritical or supercritical conditions, which are determined by the experimental conditions such as pressure and temperature [57]. Originally this process was studied with water, and was known as "hydrothermal synthesis." In the case of hydrothermal method, it is normally carried out below the supercritical temperature of water (647 K). Solvothermal technique can synthesize samples in many forms such as thin films, powders, single crystals, and nanocrystals. In addition, the morphology (sphere (3D), rod (2D), or wire (1D)) of the crystals formed can be manipulated by altering the solvent supersaturation, concentration of chemical substances, and kinetic control. Through this technique, stable novel materials which could not be easily formed from other synthetic routes can also be prepared. In recent years, many studies on solvothermal synthesis have been devoted on nanocrystals of a range of materials such as metals, metal oxides, ceramics, and polymers. The solvothermal equipment is generally made of steel, which is closed at one end and screw cap with gasket on the other end to provide proper seal. The equipment commonly referred as autoclave which can also be directly connected to an independent pressure source in that case it is known to be as cold seal method. The starting materials and along with the solvent are then placed in the autoclave. After proper sealing it is then placed inside the oven at the requisite temperature [63].

The dispersed iron oxide on silica support was also synthesized by solvothermal method, during the study of effect of method preparation and is explained in detail in chapter 4.

2.2.5 Chemical Reduction Method:

Chemical reduction is one of the most commonly utilized methods for the preparation of metal nanoparticles as stable, colloidal dispersions in water or organic solvents. The reduction of metal cations in aqueous solution generally yields colloidal metal with particle diameters of several nanometers. The precursors are generally the corresponding metal salt of interest and the most commonly used reducing agents are sodium tetrahydroborate, sodium citrate, hydrogen, citric acid, carbon monoxide, methanol, formaldehyde, hydrogen peroxide. Depending upon the type of the reducing agent the size of metallic colloids differs extensively. A strong reducing agent brings about a fast reduction reaction, and if the reaction is fast, generally small nanoparticles are formed. On the other hand, a weak reducing agent induces a slow reaction and usually large particles are formed [64]. A strong reducing agent generates an abrupt surge of the concentration of the growth species resulting in a very high supersaturation. Consequently, a very large number of nuclei are formed initially. For a given concentration of the metal precursor, the formation of a large number of nuclei results in small size of the nanoparticles. Inorder to prevent the aggregation of the nanoparticles polymeric stabilizer can be used along with the reducing agent which forms a monolayer on the surface, thus depriving the agglomeration. The polymeric stabilizer is also referred as a capping agent. The monolayer of the polymer, however, can affect the growth process significantly. If the growth sites are occupied by the polymer, the rate of growth of nanoparticles may be reduced. If the polymeric stabilizer completely covers the surface of the growing particle, it may hinder the diffusion of the growth species from the surrounding solution to the surface of the particle. The shape of the nanoparticles can be modified with different amounts of the polymeric stabilizer [64]. The Vulcan carbon supported Pt catalysts in different loadings (10, 20, and 40 wt.%) were prepared by chemical reduction, the description regarding its synthesis is mentioned in chapter 5.

2.2.6 Carburization Method:

Metal carbides are metal compounds containing carbon in the interstices of the metal grid. Transition metal carbides are traditionally synthesized by carburization of metal oxides. Successful carburizing performance depends on the effective control of the three principal variables: temperature, time and the carburizing atmosphere. Carburization can be achieved several different ways such as, for example, carbothermal reduction, electrochemical synthesis, arc melting with graphite, thermal decomposition of diethylenetriamine oxometal compounds, and reduction of oxides by H_2 or mixtures of a hydrocarbon gas such as methane as the carburizing gas. Also, in few cases propane instead of methane mixed with H_2 gas are used to obtain metal carbides. Metal carbides can be prepared upon heating metal precursors in the absence of hydrocarbons along with carbon in an inert environment. This process can be used for preparation of any metal carbide [65].

A series of carbon supported Mo_2C samples were synthesized by carburization method and the detailed procedure is included in the chapter 5.

2.2.7 Membrane Electrode Assembly Preparation Methods:

Membrane Electrode Assembly preparation method would be successful if it satisfies with conditions of optimal accessibility, stability and number of three-phase boundaries (The three-dimensional interfaces where catalyst, ionomer and reactant assemble to meet the entire required clause).The method to produce MEA is generally classified into two categories:

(i) Application of the catalyst directly on the proton conducting membrane

(ii) Application of the catalyst directly on the electrically conductive supports.

The catalyst can be applied in either of the surfaces either in the solid form or in the form of emulsion or in the vapor state or by electrochemical process or in the form of aerosol or by using the component in the precursor state. The catalyst in the solid form can be applied by dry spraying or decal method. A range of techniques have been classified for applying the catalyst in the form of an emulsion which involves preparation of an ink and then smearing it over the membrane of gas diffusion layer by brush coating or spraying technique. Catalyst can also be applied in the form of vapor by physical vapor deposition (PVD; e.g., magnetron sputtering) and chemical vapor deposition (CVD). Here the catalyst is deposited as a metal on the membrane or GDL from its vapor phase. Catalyst coated by electrochemical methods involves electrodeposition, electrospraying, etc. which is very similar to vacuum deposition technique with an advantage of preparing very fine catalyst layer. The catalyst in the precursor form can be applied by electron beam reduction or impregnation reduction. The precursor is reduced to obtain a catalyst layer in metallic state due to the occurrence of reduction reaction. The catalyst in the aerosol form can be used by utilizing spraying gun or sonicated spraying. In spraying gun technique, the catalyst ink is sprayed using an air-brush onto the membrane or GDL using a pressurized stream of inert gas such as argon or nitrogen [66].The Pt/C catalyst was coated on the GDL using the painting method by preparing an ink of the catalyst in an emulsion form. The preparation details of the MEA are discussed in chapter 5.

2.3 Characterisation Techniques

2.3.1 X-Ray Diffraction

Diffraction occurs on scattering of light by a periodic array with long-range order, resulting in constructive interference at definite angles (Figure 2.1).The atoms in a crystal being arranged periodically could diffract light. The distances between atoms are similar to the wavelength of X-ray, and Powder X-ray Diffraction (PXRD) technique uses this principle to explain the crystallinity of any materials. When the X-rays are scattered from atoms, it produces a diffraction pattern. This pattern may provide an insight to the atomic arrangement in a crystal and can also be used for identification. Amorphous materials do not possess any periodical arrangement of atoms in it, hence cannot produce any significant peak in diffraction pattern. The spacings (or distances) between these planes have nearly the same magnitude as the wavelength of X-rays (0.5 to 2 Å) and hence, crystal planes act as diffraction gratings. Due to interaction of X-rays reflected by a set of parallel planes satisfies Bragg's condition leads to constructive interference only at a particular angle [63].

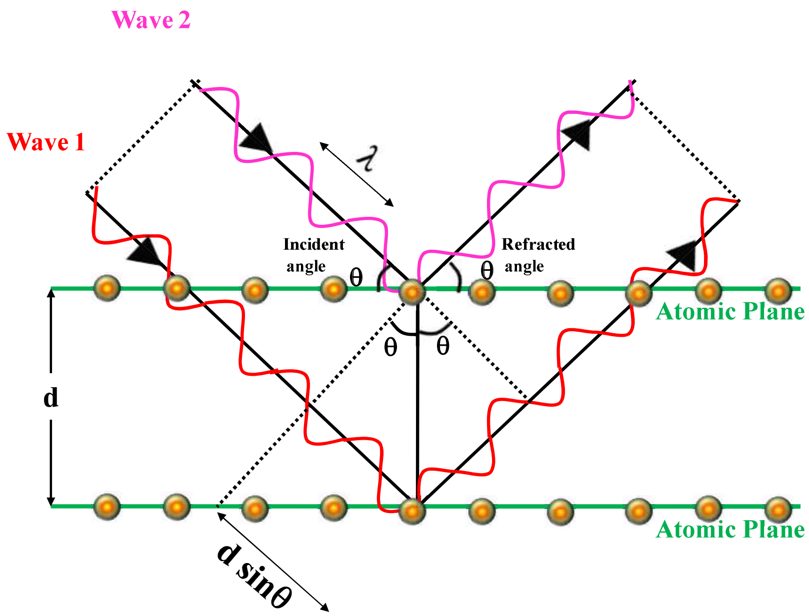

Figure 2.1: Schematic representation of the Bragg's diffraction of X rays by the atomic planes.

The Bragg condition for leading to such diffraction can be written as:

$$\boldsymbol{n\lambda = 2d\ \sin\theta} \text{---------} \ (2.1)$$

where, λ is wavelength of X-rays, θ is the glancing angle (called as Bragg's angle), d is inter-planar separations and n is the order of diffraction.

A typical classical powder X-ray diffractometer comprises a source of X-ray and a detector for the detecting the diffracted X-rays. Common diffractometer geometries are based on the Bragg-Brentano (θ-2θ) geometry shown in Figure 2.2. A block diagram of a typical powder X ray diffractometer is shown in the Figure 2.3. The conventional diffractometer employs a sealed tube X-ray source in which, bombardment of high-speed electrons on a metal target produces the X-rays. A part of the electron energy is spent in producing X-ray beam, a combination of a continuous radiation having wavelength in the range of particular shortest value and several intense spikes, which are characteristic of the target elements (called characteristic radiation).

The monochromatic wavelength radiations are usually preferred for the diffraction experiments (angle dispersive). The X-rays produced in multi-direction are allowed to escape from a particular direction in a diffractometer usually through a Be window. β-filters are used for filtering off the background and β-radiations i.e. if target metal has atomic number Z then the filter should be (Z-1).The beam of X-rays is then allowed to pass through the soller and divergence slits and later on the sample.

The powder sample is normally smeared consistently over a rectangular area of a glass slide either using binders like collodion or grease or wax. The scattered X-rays which are diffracted from the sample are collected by a film or counters. In a diffractometer, the diffracted beam from the sample is passed through the soller slits and divergence and receiving slits, monochromator and the detector. The commonly used detectors for X-rays are gas-filled tube (proportional counter or Geiger-Muller counter) or scintillation counters. The detector detects the diffracted rays when swept from one angle to another. A sharp rise in the intensity of detector signal appears as a peak when the angle where the Bragg's law is satisfied for a particular plane, due to the occurrence of constructive interference among the diffracted X-rays from that plane. Thus, the counts of the X-ray photon are measured at different angles and the output is obtained as a plot of the intensity or counts of diffracted X-rays (Y-axis) *vs* angle (X-axis).

The peaks or reflections observed in the plot correspond to a set of parallel planes with inter-planar spacing d_{hkl}. The d-values are calculated from the position of the peaks by using the relation between angle and d-value according to Equation 2.1. The peak positions relates with the unit cell parameters of the lattice and a particular sample reflects a characteristic set of d-values, which hence used for qualitative analysis i.e. identification of the materials.

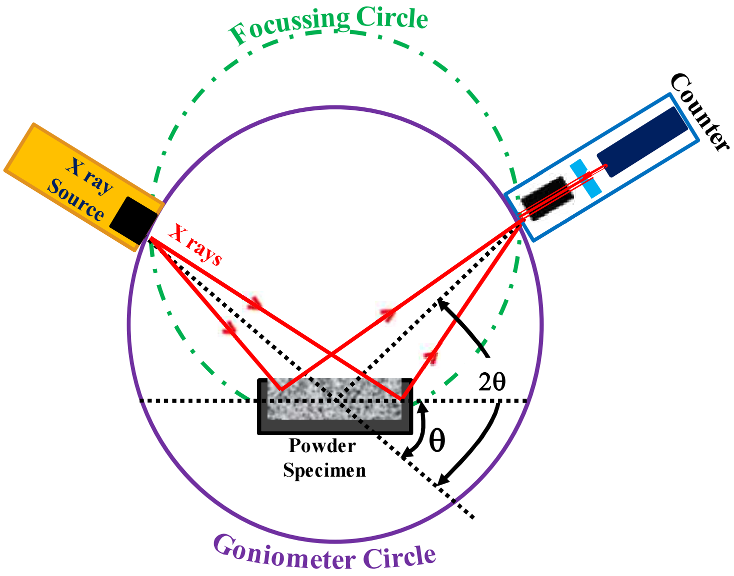

Figure 2.2: Bragg-Brentano geometry

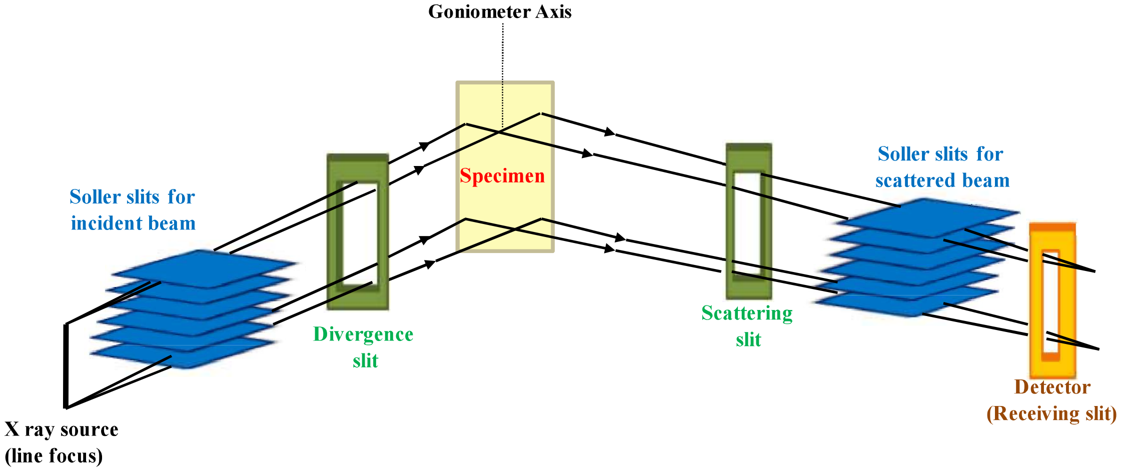

Figure 2.3: Ray diagram of a typical X-ray diffractometer

The intensity distribution of the reflections depends on the nature and kind of distribution of atoms in the unit cell. The absolute intensities of the reflections is dependent of the source intensity and counting time, in addition to the nature and kind of distribution of atoms in the unit cell. In the current work, a Philips 1729 diffractometer was mostly used for the characterization of the samples. Philips-1729 diffractometer is based on the Bragg-Brentano reflection geometry. The Cu Kα emissions from sealed tube are used as the incident beam. The Philips (PW-1729) diffractometer was equipped with an Argon gas filled proportional counter for detection of X-rays. The X-ray tube rating was maintained at 30 kV and 20 mA in the Philips unit.

The data collection procedure often depends on the specific purpose of the data collections. In common practise a short time scan in the two-theta (2θ) range of 10 ° to 80 ° is sufficient for the identification of a well crystalline inorganic powder material. However, low symmetry samples and samples with poor crystallinity necessitate a slow scan. In most cases, data were collected in the 2θ ranges of 10 ° to 70 ° with a step width of 0.02 ° and time 1.25 sec. For calibrating the instrument before analysis, silicon was used followed by assessment of the sample. By comparing the observed diffraction pattern with JCPDS (Joint Committee on Powder Diffraction Standards) data available for reported crystalline samples, fingerprinting of sample materials was carried out. The X-ray peak broadens due to smaller crystallite size or lattice strains from displacements of the unit cells about their normal positions. We briefly describe the two aspects below.

The approximate size of a crystal can be estimated from broadening of the X-ray peak by the Scherer's equation, if the crystal thickness is less than ~ 2000 Å. Thus the approximate crystallite sizes of the synthesized dispersed iron oxides and carbon supported platinum samples were estimated using the Scherer's formula given as follows:

$$\mathbf{B(2\theta)} = \frac{\mathbf{K\lambda}}{\mathbf{L\cos\theta}} \text{---} (2.2)$$

where, L is the thickness of the crystal (in angstroms), λ the X-ray wavelength measured in angstrom (Å) units and θ (in radians) the Bragg angle, K is the Scherrer constant, generally taken as 0.9 for spherical crystals with cubic symmetry. The line broadening, B (2θ), is measured from the full width at half maxima (FWHM) of the peak. Its square is obtained from the difference between the square of the measured peak width of the sample and the square of the measured peak width of a peak of a standard material [67-69]. Using this concept of broadening of the XRD peak for the crystalline sample, the approximate crystallite size of the powders was estimated and described in chapter 3, 4 and 5.

2.3.2 Surface Area Analysis

Heterogeneous catalysis is a surface phenomenon so the surface area of a solid oxide catalyst is an important property from the catalytic point of view. The gas adsorption-desorption techniques are preferred to measure surface area of solid materials. BET method [70] (Brunauer, Emmett and Teller), is the most commonly used analytical technique for determination of surface area, by using the following equation also known as BET equation:

$$\frac{p}{v(p_o-p)} = \frac{1}{v_m C} + \frac{C-1}{v_m C}\left(\frac{p}{p_o}\right)\text{-----------------}(2.3)$$

Where,

p = Adsorption equilibrium pressure

p_0 = Saturation vapours pressure of adsorbate at the adsorption temperature

v_m = Volume of adsorbate required for mono layer coverage

v = Volume of adsorbate adsorbed at equilibrium pressure p

C = Constant which relates to the heat of adsorption in the first layer (q_1) and heat of liquefaction of adsorbate (q_L); $C = e^{(q_1-q_L)/RT}$

The constant C influences the shape of the isotherm. The higher the value of C, the more the isotherm tends to type-II, which is desirable for accurate determination of surface area. A plot of $p/(p_o\text{-}p)v$ against relative pressure p/p_o yields a straight line and from the slope s = (C-1) / v_mC and intercept I = 1/v_mC, v_m can be calculated as follows.

$$v_m = \frac{1}{S+I} \quad \text{------------------(2.4)}$$

Thus the values of the specific surface area of sample can be derived by realizing the monolayer cross-sectional area of adsorbate molecule and from slope and intercept, as described above. Thus, surface area is evaluated as,

$$S = \frac{v_m N_A A_m}{W \times 22414} \times 10^{-20}(m^2/g) \text{------------------(2.5)}$$

where, S is the Specific Surface Area, N_A is Avogadro's number, v_m is Monolayer volume in ml at STP, W is Weight of the catalyst sample (g), A_m is Mean cross sectional area occupied by adsorbate molecule which is 16.2 Å^2 for nitrogen at 77 K.

For many practical purposes, the BET heterogeneous catalysis is a surface phenomenon so the surface area of a solid oxide catalyst is an important property from the catalytic point of view. The BET equation is generally fitted to the data over a range p/p_o = 0.05 - 0.3 as at higher p/p_o values complexity associated with multilayer adsorption and pore condensation may arise. In our study, Micromeretics ASAP-2020 surface area analyzer was used for measuring the N_2-BET surface area, pore size distribution and pore volume from the N_2-adsorption-desorption isotherms. Prior to surface area determination, catalysts were subjected to a pre-treatment at 300°C for ~ 2-3 h under vacuum with a liquid N_2 trap so as to remove impurities such as moisture.

An adsorption isotherm is obtained when the amount of adsorbate on a surface is analysed over a wide-ranging relative pressures at constant temperature. The adsorption is measured at every point by admitting to the adsorbent, consecutive definite volumes of adsorbate, by assessing the equilibrium pressure. Similarly, desorption isotherms can be obtained by measuring the quantities of gas removed from the sample as the relative pressure is lowered. Adsorption isotherms are classified into five types as shown in Figure 2.4. Type I or Langmuir isotherm is concave to the P/P_0 axis and the quantity of adsorbate advances to a limiting value as P/P_0 approximates one. This type is generally observed in the case of by microporous solids with comparatively minute external surfaces, such as activated carbons and zeolites. The limitation in uptake of adsorbate is because of the available micropore volume and not due to the internal surface area.

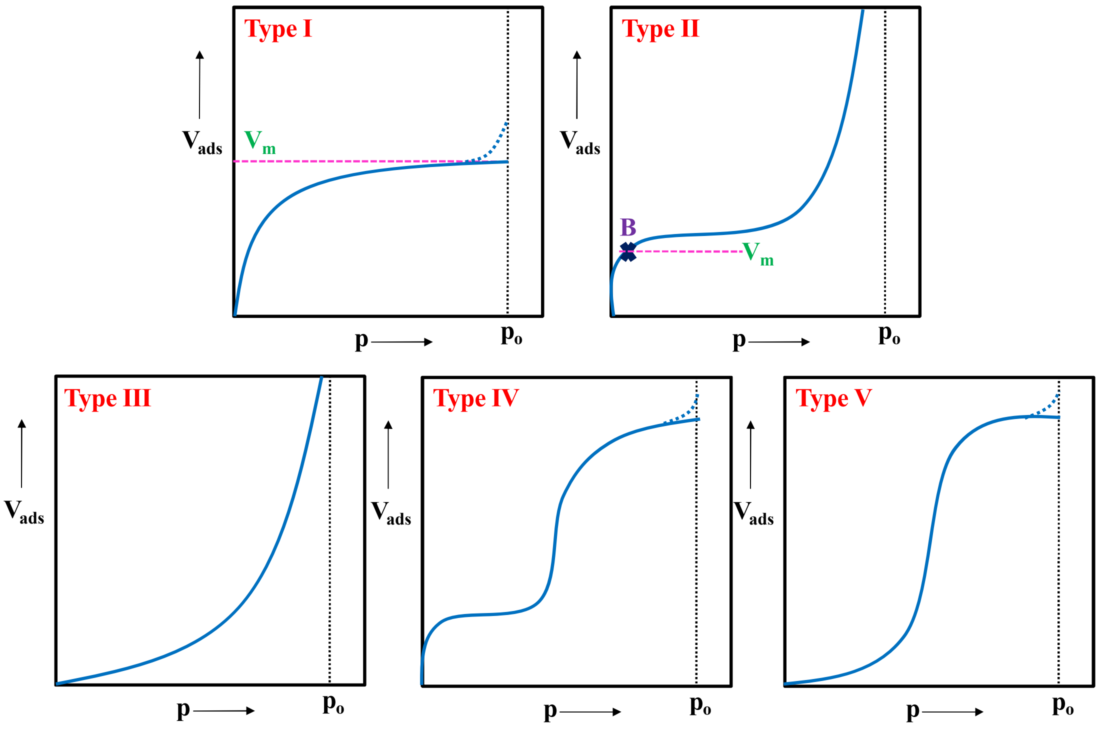

Figure 2.4: Different Adsorption Isotherms (TYPE I to V)

Type II isotherm is the usual one observed in case of a nonporous or macroporous adsorbent. This type of isotherm signifies unrestricted monolayer-multilayer adsorption. Point B, represents the relative pressure at which there is completion of monolayer coverage.

Type III isotherm is convex to the P/Po axis over its entire range. Type III isotherm are hardly observed. A familiar example is the adsorption of water vapor on nonporous carbons. The absence of a distinct point B on type III isotherm is due to stronger adsorbate-adsorbate than adsorbate-adsorbent interactions.

Type IV isotherm is related to the capillary condensation in mesopore structure, specified by the sharp slope at elevated relative pressures. The preliminary part of the type IV isotherm resemble as that of type II.

Type V isotherm is rarely observed, corresponding to the type III, except that pores in the mesopore range are present.

The BET surface area of dispersed iron oxide catalysts were evaluated for the comparative analysis and are explained in the chapters 3 and 4.

2.3.3 Mössbauer Spectroscopy

Mössbauer effect is the phenomenon of recoilless emission and resonance absorption of γ-rays by identical nuclei bound in solid. Rudolph Mössbauer, a noble laureate, discovered Mössbauer Effect in 1957 in ^{191}Ir. Mössbauer found that if the atoms are within a *solid matrix* then their effective mass of the nucleus is very high. The recoiling mass is now efficiently the mass of the entire system, so if the γ-ray energy is small then the recoil of the nucleus is so less that it cannot be transmitted as a phonon and thus the entire system recoils, creating the recoil energy almost zero: a *recoil-free event*. The relative number of recoil-free events mainly depends on the energy of γ-radiation and secondly this effect is only observed in isotopes having low lying excited states. Also the lifetime of the excited state affects the resolution. These two aspects restrict the number of isotopes to be used effectively for Mössbauer spectroscopy. ^{57}Fe is widely used isotope due to its low γ-ray energy and long-lived excited state. Figure 2.5 shows a schematic of Mössbauer effect and spectrum from identical source and absorber [71-72].

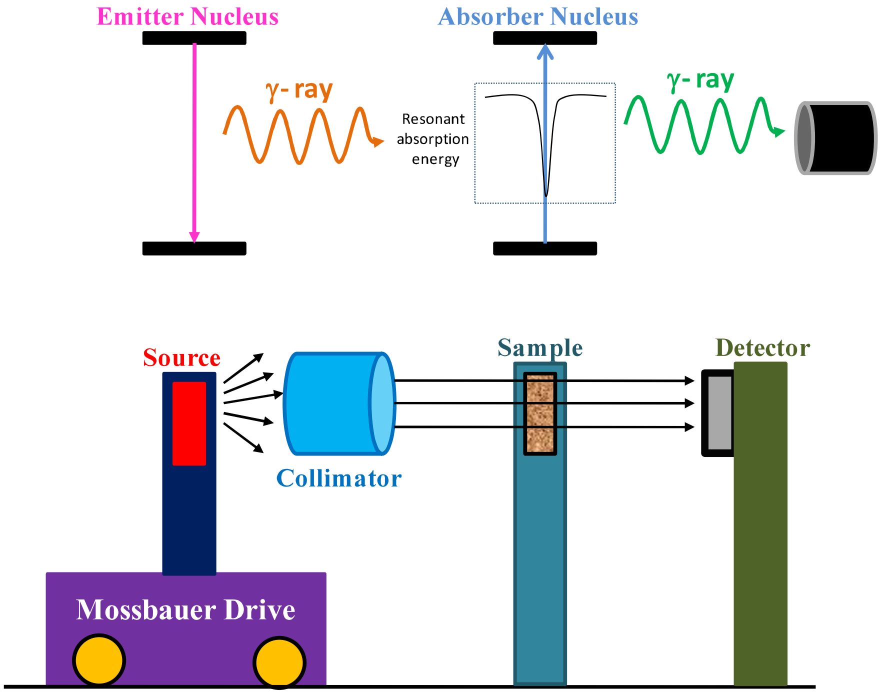

Figure 2.5: Schematic of the Mossbauer Effect

Isomer shift occurs due to different chemical environments at the emitting and absorbing nuclei. The isomer shift results due to the non-zero volume of the nucleus and the electron charge density due to s-electrons within it, causing a Coulombic interaction to shift the nuclear energy levels. Thus, any difference in the s-electron environment between the source and absorber produces a shift in the resonance energy of the transition. This causes the whole spectrum to shift positively or negatively depending upon the s-electron density and establishing the centroid of the spectrum. Since the shift cannot be measured directly isomer shift is normally quoted relative to a known absorber.

$$Isomer\ Shift = \delta = \frac{4\pi}{5} Ze^2 R^2 \frac{\Delta R}{R} [|\Psi(0)|^2_{abs} - |\Psi(0)|^2_{sou}] \text{------------------} (2.6)$$

Here Ze is the positive charge of the nucleus, the term ΔR/R is the fractional change in the nuclear charge radius on the excitation and ΔR is the difference in the radii of the nuclear excited and ground states.

The isomer shift is helpful in evaluating the oxidation number, co-ordination number, shielding effect and the electronegativity of ligands. Even equivalent sites with different number of hydrogen neighbors and geometrical arrangements could be distinguished by their different IS values.

Nucleus with an angular momentum quantum number I>1/2 possess a non-spherical charge distribution causing a nuclear quadrupole moment. Due to the presence of an asymmetrical electric field splitting of the nuclear energy levels occurs. For example, an isotope with a I=3/2 excited state, such as ^{57}Fe or ^{119}Sn, the excited state is split into two substates m_I=±1/2 and m_I=±3/2. This is shown in Figure 2.6, giving a two lines spectrum or 'doublet'. The extent of the splitting depends on the electron charge asymmetry

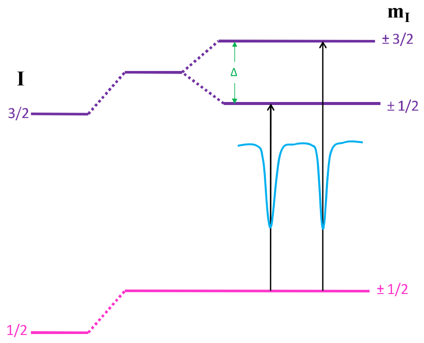

Figure 2.6: Quadrupole splitting for a 3/2 to 1/2 transition

For ^{57}Fe the magnitude of the quadrupole splitting is given by

$$QS = \frac{1}{2}(e^2 q_{zz} Q)(1 + \frac{\eta^2}{3})^{\frac{1}{2}}\text{------------------------}(2.7)$$

where q_{ZZ} is the principal component of the electric field gradient, η is asymmetry parameter = $(q_{ZZ} - q_{YY})/q_{ZZ}$. QS is highly sensitive function of charge state (high spin and low spin) as well as the nearest neighbor environment of the probe atom.

In the presence of a magnetic field, Zeeman splitting is observed. There are many causes of magnetic fields which could be felt by the nucleus. The resultant magnetic field at the nucleus, H_{eff} is represented by:

$$H_{eff} = (H_{contact} + H_{orbital} + H_{dipolar}) + B_{applied}\text{-------------------}(2.8)$$

All these terms $H_{contact}$ (spin on such e^- which polarizes the spin density at the nucleus), $H_{orbital}$ (orbital moment on e^-) $H_{dipolar}$ (dipolar field caused because of e^- spin) are effect of atoms's own partially filled orbitals. This magnetic field removes degeneracy of the nucleus and splitting of the nuclear levels from spin of I into (2I+1) substates, so that the m_I levels have energies given by

$$E_{ml} = -g_n \beta_n m_I H_{eff}\text{------------}(2.9)$$

Where g_n is the electronic g factor or gyromagnetic ratio, β_n is the nuclear Bohr magneton and m_I is the component of nuclear spin I. If m_I changes by 0 or 1 then there could be transitions between the excited state and ground state, which gives rise to six possible transitions for a 3/2 to 1/2 transition (a sextet) as shown in Figure 2.7, with the line spacing being proportional to H_{eff}.

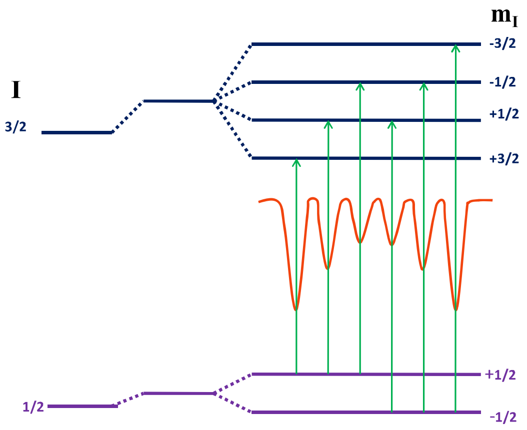

Figure 2.7: Magnetic splitting of the nuclear energy levels

The line positions are associated with the splitting of the energy levels, but intensity of these lines relates to the angle between the Mössbauer gamma-ray and the nuclear spin moment. Thus a purely polycrystalline Fe-metal gives a symmetric six line spectrum (sextet), with intensities in the ratio 3:2:1:1:2:3 and the line separation gives a measure of hyperfine field at the nucleus. Thus, Isomer Shift, Quadrupole Splitting and Magnetic Splitting, alone or altogether are the main features of many Mössbauer spectra.

In the present study ^{57}Co source embedded in the Rh matrix is used as a monochromatic source of γ-ray. Room temperature ^{57}Fe Mössbauer spectra were recorded using the 14.4 keV gamma ray energy, emitted from ^{57}Fe (produced from ^{57}Co by electron capture process), which is modulated by Doppler motion provided by constant acceleration mode. The spectrometer was calibrated with α-Fe and the isomer shift values given in this work are with respect to α-Fe. The experimental data were fitted by least square curve-fitting program.

The Mössbauer spectra were recorded for the dispersed iron oxide samples to understand about the distribution of Fe^{+3} among the octahedral and tetrahedral sites in iron oxide (Chapter 3 & 4).

2.3.4 Fourier Transform Infrared Spectroscopy (FTIR)

The infrared region of the electromagnetic spectrum includes radiation with wavelengths ranging from 1 to 1000 microns. From the point of view of both application and instrumentation, the IR range is is split as; Near IR (12500 – 4000 cm^{-1}), Mid IR (4000 – 200 cm^{-1}) and Far IR (200 – 10 cm^{-1}) [73]. The majority of analytical applications are confined to a portion of the middle region extending from 4000 to 400 cm^{-1} or 2.5 to 25 μm. The absorption spectra in the infrared region originate from the transitions between vibrational (along with rotational) levels of a molecule present in its ground electronic state upon irradiation with infrared radiation.

The atoms in a molecule are never stationary and a good approximation is to treat them as a combination of point masses held together by Hooke's law of forces. By classical mechanics it can be shown that the displacements of the masses from their mean positions are always the sum of the displacements due to a particular set of vibrations. If in these set of vibrations the masses are in phase and the motion of all the nuclei involved are such that the centre of gravity of the molecule remains unaltered, then such vibrations are known as the fundamental modes of vibration the molecule. Mostly, a normal mode is localized largely to a group within the molecule and hence corresponds to stretching or bending of one or few bonds only and hence associated with that particular functional group. Whether for the functional group or the entire molecule, the vibrations are universally classified either as stretching or as bending types. Stretching vibrations, which correspond to the oscillations leading to change in bond lengths, can be further sub-divided into symmetric or asymmetric stretching vibrations. Bending vibrations are characterized by continuously changing angle between the bonds and is further sub classified as wagging, rocking, twisting, or scissoring. Apart from fundamental modes a large number of vibrational absorptions overtones (multiple of fundamental modes, 2ν or 3ν etc), combination tones ($\nu_1 + \nu_2$, $\nu_3 + \nu_4$ etc.)

and difference tones (ν_1 - ν_2, $\nu_5 - \nu_6$ etc.) can also be observed in a typical infrared absorbance spectrum of a molecule [74].

One of the primary requirements for vibrating molecules to interact with the oscillating electric field of the incident radiation and to undergo a transition between two vibrational energy levels is that the molecular dipole moment must change during the vibration. The intensity of the absorption is determined by the magnitude of this dipole moment change. Due to symmetry, some of the vibrations in a molecule may not induce a change in dipole moment and hence are transparent to infrared radiations i.e. IR inactive.

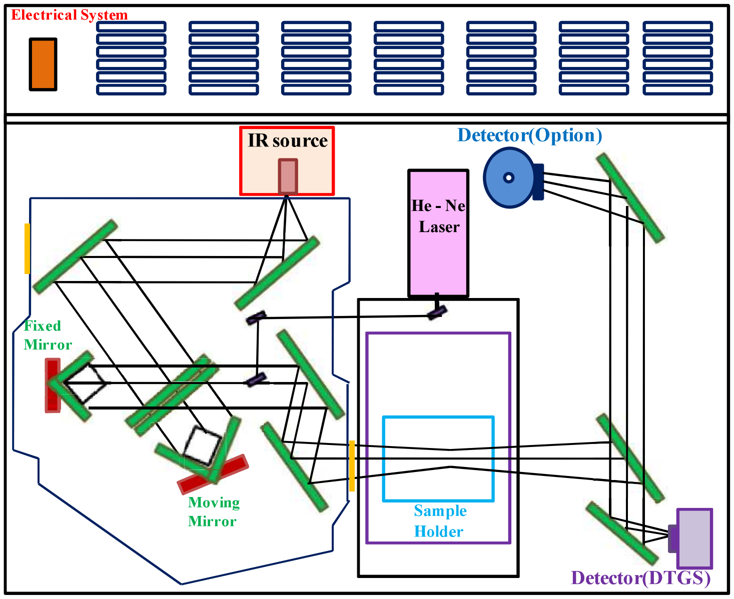

Figure 2.8: Schematic representation of the FT/IR – 1600 instrument (JASCO make)

The instrument used in the present study was FT/IR – 600 model Fourier transform infrared spectrometer of JASCO (Japan). Figure 2.8 depicts a typical ray diagram of this instrument. In this instrument, the light from a ceramic source (SiC) is collimated by a collimator mirror and introduced into the Michelson interferometer, consisting of a beam splitter, fixed mirror and moving mirror. The beam splitter splits the beam into two equal parts – one part goes to the fixed mirror and the other towards the moving one. The movement of the moving mirror introduces a path difference between two beams and hence generates different interferograms consisting of different combination of wavelengths. The movement of the mirror is very precise and its speed decides the scan time and the resolution. The light passing through the interferometer is focused on the sample (placed in a holder) and the transmitted light is focused onto the detector. The detector used in current studies was DTGS (deuterated triglyceride sulphate) type. One complete scan gives an interferogram in terms of intensity with respect to time (in terms of the mirror movement). This interferogram, which is in time domain, is converted into frequency domain by a complicated mathematical treatment called as Fourier Transformation, hence yielding a spectrum of intensity change with respect to wavenumber. The function of the He-Ne laser is to provide alignment, measure precisely the optical path difference. 100 such scans were recorded for each sample to obtain spectra of low signal to noise ratio.

FT-IR spectra of the all the samples were recorded in the mid IR region (4000-400 cm^{-1}). For the purpose, 0.1 g of dry potassium bromide was blended with ~3 mg of the sample and well-grounded in a mortar pestle for homogenization. The mixture was then hard-pressed into a clear, thin pellet at 5000 kg/cm^2 and employed for IR analysis.

FTIR analysis was carried out for uncalcined and calcined dispersed iron oxide catalyst and even for the spent catalyst after evaluation for sulfuric acid decomposition reaction as described in the chapters 3 and 4.

2.3.5 X-Ray Photoelectron Spectroscopy (XPS)

XPS is a surface sensitive semi-quantitative spectroscopic technique, which evaluates the elemental composition, empirical formula and oxidation state of the elements present in the sample. XPS can be applied to a broad range of materials and provides valuable quantitative and chemical state information from the surface of the material being studied. XPS spectra are obtained by irradiating a material with a beam of aluminium or magnesium X-rays and simultaneously measuring the kinetic energy (KE) along with the total electrons, which could escape from the top surface layer (1 to 10 nm) of the material. This technique needs ultra-high vacuum (UHV) conditions. XPS which is generally referred as ESCA is an acronym for Electron Spectroscopy for Chemical Analysis. XPS technique can detect all elements with an atomic number (Z) of 3 (lithium) and above [75]. Which limits in detection of hydrogen (Z=1) or helium (Z=2).

A typical XPS spectrum is a plot of the number of electrons detected (Y-axis) versus the binding energy of the electrons detected (X-axis). A particular element produces a typical set of XPS peaks at specific binding energy values, which confirms the state of elements present on the surface of the material under analysis. These characteristic peaks reflect the electron configuration of the electrons within the atoms. The count of electrons detected in each of the characteristic peaks correlate to the concentration of elements within the irradiation area [76]. It is imperative that XPS is able to detect electrons which could reach into the vacuum of the instrument. The photo-emitted electrons that have escaped into the vacuum of the instrument are the one that originated from the uppermost 10 - 12 nm of the material. In the case of the photo-emitted electrons, which were generated as the X-rays penetrated 1–5 micrometers of the material, fail to reach the detector due to recapturing or getting trapped in different excited states inside the material itself.

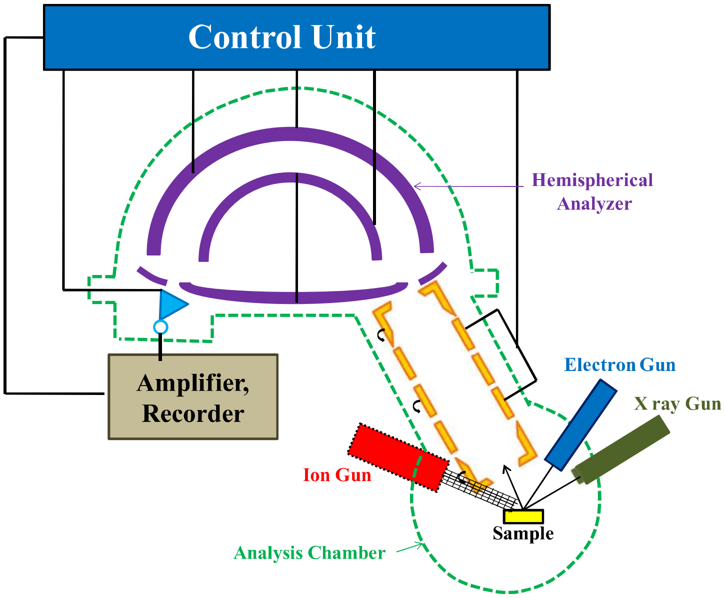

Figure 2.9: Schematic of a XPS instrument

Monochromatic Al Kα X-rays (λ= 8.3386 Å and photon energy of 1486.7 eV) or magnesium X-rays (λ= 9.89 Å with photon energy of 1253.6 eV) are generally produced by diffracting and focusing of non-monochromatic X-rays off a thin quartz disk.

In present study, an ESCA and AES system (SPECS, Surface Nano Analysis GmbH, Germany) equipped with Mg Kα X-ray source and a 150 mm hemispherical analyser, was employed to analyse the oxidation state of iron, oxygen and any sulfur present on the surface of the fresh and spent dispersed Fe_2O_3 catalyst (used for sulfuric acid decomposition reaction for 100 h) as presented in Chapter 3 and 4. Also, the carbon supported Mo_2C electrocatalyst was characterized by XPS as described in chapter 5.

2.3.6 Diffuse Reflectance Ultra Violet-Visible (DRUV-Vis) Spectroscopy

Ultraviolet (200-400 nm) and visible (400-800 nm) radiation with short wavelength, lies between the X-rays and IR radiation of electromagnetic spectrum. ΔE is the energy difference between the ground and excited state orbital. When the energy of the arriving photon is equivalent to ΔE, then the light is absorbed, and an electron from an occupied level is excited from its ground state to vacant higher state. This electronic transition occurs in the UV-visible region of the electromagnetic spectrum [73, 77]. This transition will generally take place between the highest occupied molecular orbital (HOMO) to the lowest unoccupied molecular orbital (LUMO).

UV-Vis spectra tend to be broad in nature due to the fact that vibrational and rotational levels of the molecular orbitals are superimposed upon the electronic levels as shown in Figure 2.10.This limits utility of this technique in identifying materials, however, it is found to be more suitable for quantitative investigations of species in solutions.

In UV-Vis reflectance spectroscopy of solids (shown in Figure 2.11) two types of reflection are encountered. The specular or mirror-like reflection, in which the angles of incidence and angle of reflection are identical and secondly the diffuse reflection from a matte structure which actually serves the basis of reflectance spectroscopy [73]. It is an effective way for obtaining the UV-visible spectra directly on powdered sample resulting from scattering, transmission and absorption interactions. Reflectance is given by: $Reflectance\ (\%) = (I_s/I_r) \times 100$ where I_s is the intensity of the reflected beam and I_r the intensity of a reference standard usually barium sulphate. It is an ideal technique for evaluation of optical and electronic properties of variety of materials such as ceramic powders, films, pigments etc.

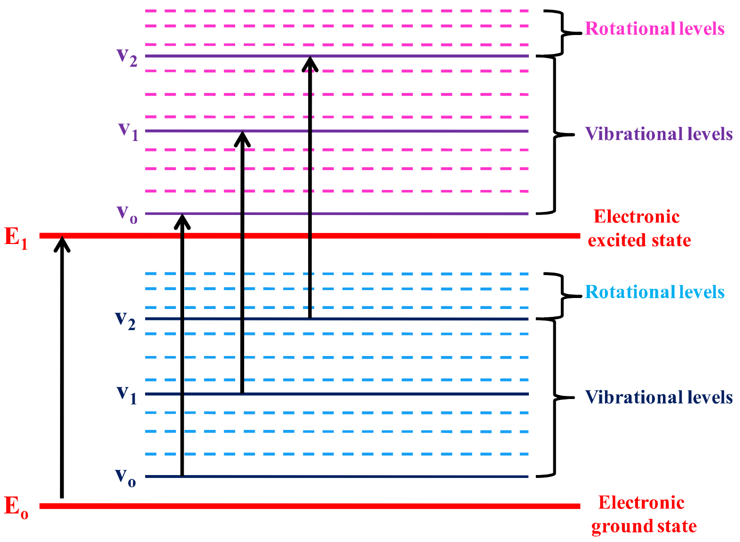

Figure 2.10: Schematic representation of vibrational and rotational levels are superimposed on the electronic levels

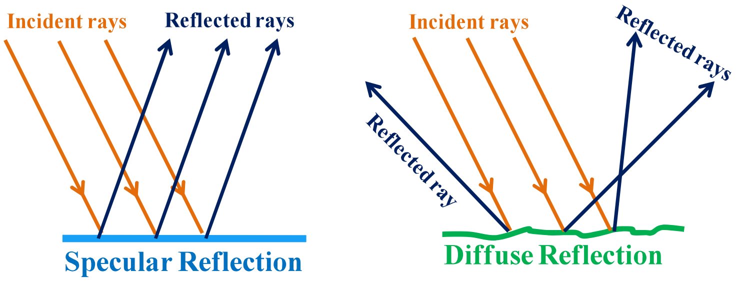

Figure 2.11: Schematic representation of specular reflection on mirror like surface and diffuse reflection from a matte surface

Diffuse Reflectance UV-Vis Spectroscopy involves numerous light-sample interactions. Spectra may exhibit features associated with the transmission and/or reflection (external and/or internal) of UV-Vis radiation. Diffuse reflectance spectra of the dispersed iron oxide on various supports were recorded on a UV-visible spectrometer (JASCO model V-530 spectrophotometer) and analysed in chapter 3.

2.3.7 Temperature Programmed Reduction/Oxidation (TPR/O)

Temperature programmed reduction (TPR) and Temperature programmed oxidation (TPO) are the techniques which are extremely sensitive and particular for redox property of the catalytically active species under reducing or oxidising environment. Since past few years these methods are applicable in study of both supported and unsupported catalysts.

Consider a general reaction between metal oxide MO (M having +2 oxidation state) and hydrogen which can be represented as:

$$MO_{(s)} + H_{2(g)} \rightarrow M_{(s)} + H_2O_{(g)} \text{----------(2.10)}$$

The free energy change for the reduction ΔG° is negative for number of oxides and hence for reduction of these oxides is thermodynamically feasible.

$$\Delta G = \Delta G° + RT \log\left(\frac{P_{H_2O}}{P_{H_2}}\right) \text{----------------(2.11)}$$

In this technique the water vapor is continuously removed from the reaction zone as it is formed. Thus, if P_{H_2O} is adequately low, at higher temperatures it is likely that the term RT log (P_{H_2O} / P_{H_2}) could be sufficiently negative to nullify a positive ΔG°. Hence, it is probable to get TPR profiles for metal oxides at higher reduction temperatures despite of their positive ΔG° values.

The process by which a sphere of metal oxide is reduced in a stream of flowing hydrogen has been explained on the basis of the kinetic studies either by nucleation model or by contracting sphere model [78, 79].

A temperature programmed desorption-reduction-oxidation instrument (make-Thermoquest Italy, model-TPDRO – 1100,) was used for TPD/ TPR/TPO studies. Figure 2.12 represent a typical block diagram of the instrument used. In this instrument analysis is carried out at atmospheric pressure using continuous flow of inert or reactive gases. In a typical TPR experiment the sample is placed in the inner quartz reactor of a quartz reactor system which constitutes of two concentric tubes as shown in Figure 2.12. Before start of actual analysis, the sample is first pretreated under helium flow at 350 °C for 2 h. The reduction profile of the sample is thereafter recorded (cooling the sample after pre-treatment) by heating the sample at a fixed rate under the controlled flow of reactive gas mixture, i.e. 5% H_2 in Argon. A thermal conductivity detector (TCD) is used to observe the variation in composition of reactive gas mixture with time or temperature ramp. Initially when the temperature and no reduction occur a steady baseline is obtained. As the reduction process begins the hydrogen concentration in effluent stream decreases and this change is recorded by TCD. The water formed during reduction process is removed from the carrier gas by using a soda lime trap positioned prior to the detector. Thus, the signal obtained is mainly due to difference in thermal conductivity of the flowing gas due to the consumption of hydrogen for the reduction process. The plot is generally intensity or signal in the TCD with respect to temperature. Peaks reflected in the plot are due to the occurrence of the reduction process and the maxima of the peak attributed to the temperature at which reduction takes place to the maximum extent. The sample is cooled after completion of the analysis. This reduced sample is recovered for ex situ XRD analysis, in order to identify the reduced product. Alternatively, these samples can be used again for recording of a TPO profile. This facilitates the monitoring of the redox process in a particular sample. More than one TPR/TPO band is observed in case of a sample containing more than one kind of reducible species.

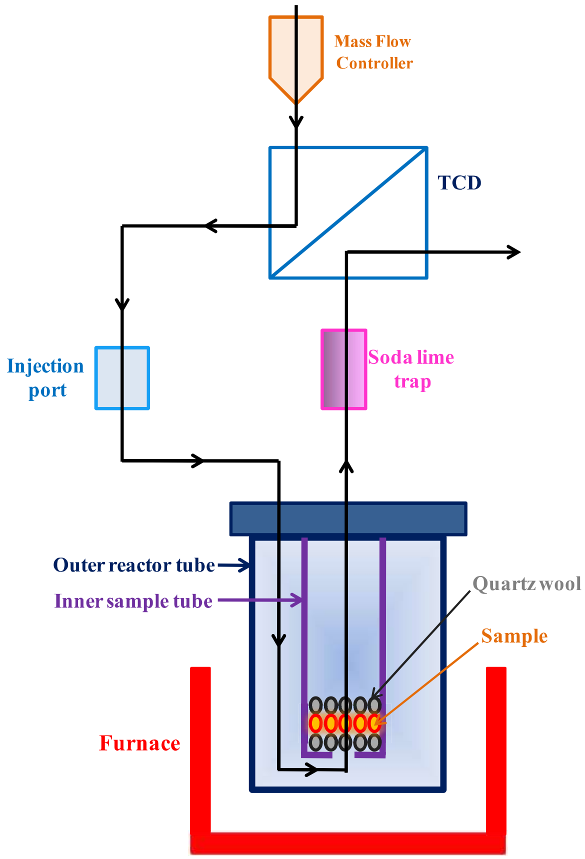

Figure 2.12: Schematic for the TPDRO – 1100 instrument

Redox behavior of the oxide samples viz, Fe_2O_3 dispersed on variable supports towards repeated reduction-oxidation cycles was studied(chapter 3 and 4) by recording temperature programmed reduction/oxidation (TPR/TPO) profiles on a TPDRO-1100 analyzer under the flow of H_2 (5 vol.%) + Ar (for TPR)/O_2 (5 vol.%) + He(for TPO) gas mixtures at a flow rate of 20 ml min^{-1}in temperature range of 25-1000°C for TPR and 25-800°C for TPO at a heating rate of 6°C min^{-1}. Initially the samples were pretreated at 350°C for about 2.5 h in helium, before recording the first TPR run.

2.3.8 Scanning Electron Microscopy (SEM)

Interaction of a finely focused electron beam with matter (specimen) leads to several phenomena such as: (i) emission of secondary electrons (SE) (ii) back-scattering electrons (BSE) and (iii) transmission of electrons etc. which are depicted in Figure 2.13.

In Scanning Electron Microscopy, the signals generated from the surface of the sample by secondary and back-scattered electrons are detected. Scanning microscope comprises of the following systems: (i) electron optical system, (ii) specimen stage, (iii) display and recording system and (iv) vacuum system.

In SEM technique [80], the electrons from the electron source are focussed across the surface of the sample. The electrons reflected from the surface and emitted secondary electrons, provide a map of the surface topography of the sample, which is quite useful in determining the particle size, crystal morphology, magnetic domains, surface defects etc. A varied array of magnifications can be achieved, the finest resolution being about 2 nm. If the material is non-conducting then a coating of gold or graphite is needed to inhibit charging of the surface. In scanning electron microscopy, the elements in the sample also emit characteristic X-rays, which can be separately detected by a silicon-lithium detector. These X rays provides both qualitative and quantitative analysis of the elements present (for elements $Z > 11$) in the sample. This technique is known as energy dispersive analysis of X-rays (EDAX or EDX).

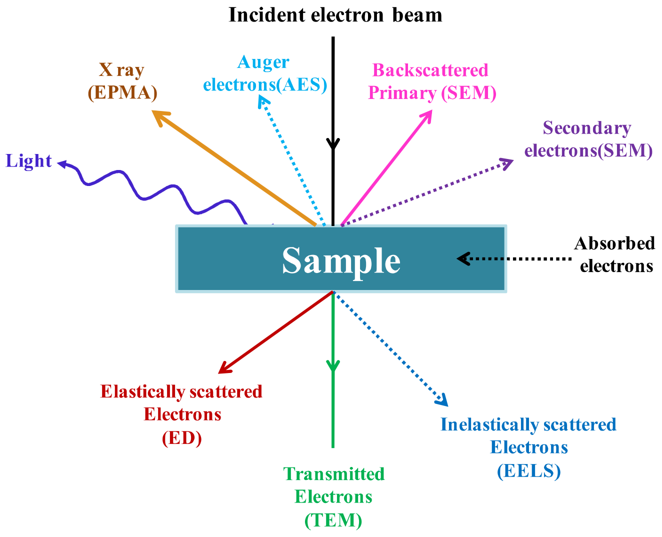

Figure 2.13 Depiction of different phenomena occurring on interaction of electron beam with a solid sample

This technique of Scanning Electron Microscopy (along with EDX) was used to study the microstructure evolution (grain size, porosity, etc.) of the calcined metal oxide particles before and after use as a catalyst for sulfuric acid decomposition and also electrocatalyst which were assembled in MEA for aqueous SO_2 electrolysis. The instrument used was a Scanning Electron Microscope**,** Mirero, Korea, model- AIS2100. Conductive gold coating was applied on the sintered metal oxide samples to overcome the surface charge accumulation using 6” d.c. sputtering unit, model 6-SPT, manufactured by M/s. Hind High Vacuum, Bangalore.

The dispersed iron oxide catalyst was imaged by SEM as described in chapter 4.

2.3.9 Transmission Electron Microscopy (TEM)

Transmission Electron Microscopy (TEM) is used to reveal the morphology of particles which could detect particles upto 1 nm or even lower in case of High resolution TEM. In TEM, a beam of highly focused electrons is directed towards a thin sample where the highly energetic incident electrons on interaction with the atoms in the sample, produces characteristic radiation and thus provide the necessary information for characterization of various materials. Information is obtained in two ways such as imaging mode via transmitted electrons and diffraction mode due to the diffracted electrons. The image mode provides the information regarding micro-structural features whereas the diffraction mode is used for crystallographic information. The transmission electron microscopes are generally operated at voltages as high as 200 kV with a magnification of 300000 X. If the main objective is to resolve the finest possible details in specially prepared specimens, it is advantageous to use the shortest possible wavelength illumination (i.e., high voltage), an objective lens with very low aberrations and a microscope with extremely high mechanical and electrical stabilities, since high resolution requires both high instrumental resolving power and high image contrast. This special technique is termed as high-resolution transmission electron microscopy (HR-TEM) [81].

Low resolution transmission electron microscopy (TEM) images were collected with a Philips CM 200 microscope operating at an accelerating voltage of 200 kV. High resolution TEM (HR-TEM) images were taken with a FEI-Tecnai G-20 microscope operated at 200 kV. The samples were prepared by ultrasonicating the finely ground samples in ethanol and then dispersing on a carbon film supported on a copper grid. Electron micrographs presented in this study are bright field images.

A pin-shaped cathode heated up by passing the current produces the ray of electrons (Figure 2.14). A high voltage under ultra-high vacuum accelerates the electrons to the anode. The accelerated ray of electrons passes a drill-hole at the bottom of the anode. The lens-systems consist of an arrangement of electromagnetic coils. A condenser first focuses the ray and then it allows the ray to pass through the object. The object consists of a thin (< 200 nm), electron transparent, evaporated carbon film on which the powder particles were dispersed. After passing through the object, the transmitted electrons are collected by an objective. Thereby an image is formed, which is subsequently enlarged by an additional lens system. The images formed thereby are visualized on a fluorescent screen or it is documented on a photographic material.

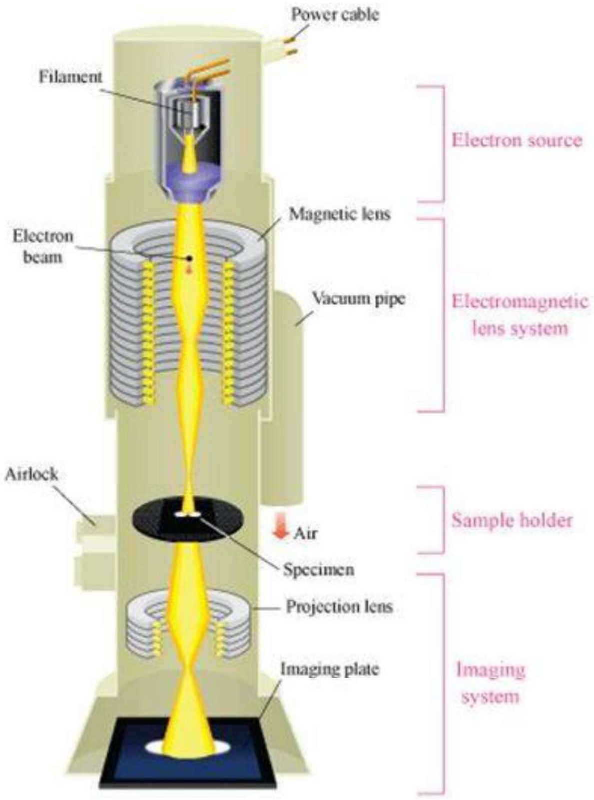

Figure 2.14: Schematics representation of instrumentation of Transmission Electron Microscopy (http://slideplayer.com)

The technique was used to characterize the synthesized supported iron oxide samples in terms of their morphological features of primary particles like shape, size, size distribution and extent of aggregation. Also, the metal oxide dispersion, particle size was analysed for both fresh and used catalysts using this technique, as described in the chapters 3 and 4.

2.3.10 Evolved Gas Analysis (EGA)

To investigate the species formed on the catalyst (iron oxide dispersed on various supports) during sulfuric acid decomposition reaction, the spent catalyst was analyzed by TGA-FTIR (chapter 3) and TGA- QMS techniques (chapter 4). Simultaneous analysis of evolved gases either by Infrared spectroscopy or by Quadrupole Mass spectrometry, while the thermogravimetric analysis of sample is underway is widely employed technique in catalyst characterization. A FTIR coupled to the TG-DTA (Model No.: Tensor, Bruker) was used in one of the study. Typically, the spent catalyst samples (used for sulfuric acid decomposition reaction) were heated in the temperature range of 400-1000 °C at a heating rate of 10 °C/min and the evolved gases were analyzed by FTIR. In another study, QMS coupled to a TG-DTA (model-SETSYS Evolution-1750, SETARAM) was employed [82-83]. It is easier to identify the emitted vapors at different temperatures and understand the underlying mechanism. Evolved gas analyzer hyphenated with a Thermogravimetry set up helps to identify the gases evolved as the decomposition of the species present on the spent catalysts (used for sulfuric acid decomposition reaction). These thermal studies gave an idea about the relative stability of these species thus helping us in proposing a reaction scheme.

2.3.11 Inductively Coupled Plasma- Optical Emission Spectroscopy (ICP-OES)

ICP-OES (Inductively coupled plasma - optical emission spectrometry) is a method for elemental analysis using plasma and a spectrometer [84]. It’s highly reliable, multi-element analytical technique and it’s extensively used for routine researches along with specific analysis purposes. The basic design of the ICP-OES instrument is shown in Figure 2.15. The sample is obtained in the solution form for analysis and is led by a peristaltic pump through a nebulizer into a spray chamber. The aerosols formed are allowed into an argon plasma which is generated at the end of a quartz torch with the help of a water-cooled induction coil through which a high-frequency alternate current flows. As a result, an alternate magnetic field is induced which accelerates electrons into a circular trajectory. During collision between the argon atom and the electrons, ionization occurs and results in extremely hot plasma (6000-7000 K). In the torch desolvation, atomization and ionization of the sample takes place. Electron reaches a higher "excited" state due to taking up of the thermic energy. Light (photons) is released when the electrons relaxes to ground state. Every element has their specific emission spectrum. By means of an Echelle grating, a prism, and a focusing mirror, these emitted photons in various frequencies are captured instantaneously on a CCD chip (Charged Coupled Device).

In our study the elemental composition of the dispersed iron oxide samples (chapters 3 and 4), the Vulcan carbon supported Pt electrocatalyst and the molybdenum carbide samples (chapter 5) were analyzed by this technique.

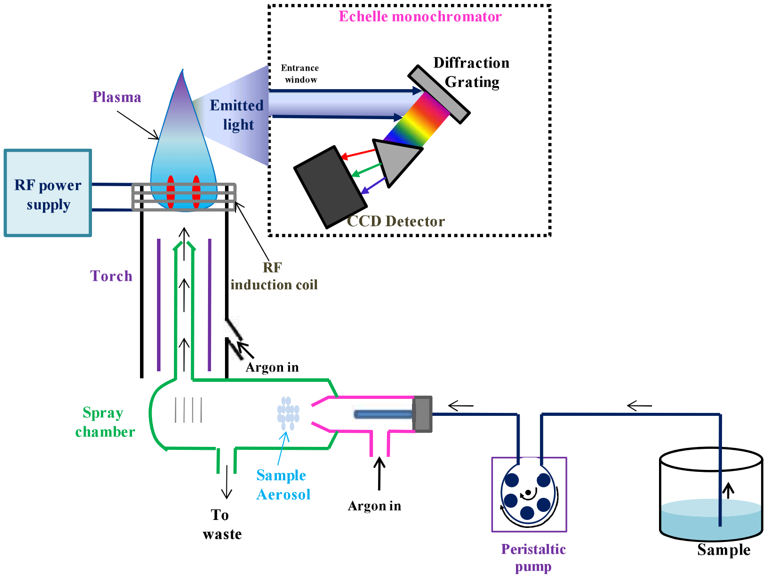

Figure 2.15: Basic Design of ICP-OES instrument

2.3.12 Energy Dispersive X-Ray Fluorescence (EDXRF)

It is one of the simplest, most accurate and most economic analytical methods for the determination of the chemical composition of various types of materials [85]. It can analyze wide-range of elements, from sodium (11) to uranium (92), with detection limits at the sub-ppm level. It can also measure concentrations of up to 100% easily and simultaneously. The atoms in the sample material are excited by X-rays emitted from an X-ray source or a radioisotope and the specific X-ray fluorescence signals emitted by the atoms after the photoelectric ionization are measured simultaneously in a fixed mounted semiconductor detector or sealed gas-proportional counter. The radiation intensity of each element signal relates to the concentration of the element in the sample, which is estimated internally from a stored set of calibration curves. Since the dissolution of silica supported iron oxide samples was found to be intricate while preparing its solution for ICP-OES analysis, EDXRF was preferred for elemental compositional analysis of the iron oxide samples dispersed on variable supports as depicted in chapter 3, 4 and 6.

2.3.13 Catalytic Activity Evaluation for Sulfuric Acid Decomposition

The catalytic reactor designed and developed for evaluation of catalytic activity for sulfuric acid decomposition is discussed here in details. For the lab study, a continuous, flow through fixed-bed quartz reactor with 30 cm length and I.D. of 0.8 cm fabricated in quartz as shown in Figure 2.16 was employed. A syringe pump equipped with a 50 ml glass syringe was filled with concentrated sulfuric acid (98 wt.%, sp.gr = 1.84) and was used for controlled injection of acid (0.05 ml min^{-1}) into the preheater zone maintained at 400°C to produce acid vapors. These vapors were then carried by a high purity N_2 carrier to a quartz catalytic reactor housed inside a controlled electrically heated furnace at high temperature. A condenser along with a liquid collector with tap was fitted downstream. The gaseous products formed were passed through a NaOH solution and then it was vented out.

The catalytic activities of Fe_2O_3 dispersed on various supports prepared by different methodologies were evaluated in this experimental setup and is discussed in chapter 3 and 4. In a typical experiment, the powder samples 0.2 g was packed between the beds of quartz wool into the reactor at room temperature and then fixed it in the heating zone of the catalytic furnace. The carrier gas, nitrogen (HP) was allowed to flow at a fixed rate of 40 ml min^{-1} and then the furnace temperature was raised to primary reaction temperature of 650 °C for a time interval of 1 h. Sulfuric acid (98 wt.%) was then allowed to flow into the system (27.6 g acid g^{-1} h^{-1}) using a syringe pump. At first it reaches along with the carrier to the pre-heater, where vaporization of acid occurs and later decomposed to SO_2, O_2 and H_2O across the catalyst bed. The SO_3, which remains unreacted recombines with H_2O in the condenser downstream and gets collected as a liquid solution. The gaseous products - SO_2 and O_2, along with carrier N_2 were then allowed to pass through NaOH solution, where SO_2 was trapped and the other gases are vented out. Product SO_2 was analyzed by measuring the decrease in concentration of NaOH solution by titration with oxalic acid solution. Also, the sulfuric acid collected downstream of the reactor (i.e., unreacted sulfuric acid) for the definite time interval was determined by chemical titration with standardized NaOH solution. The percentage conversion of sulfuric acid to sulfur dioxide was calculated based on the product yield of SO_2 and is given by,

$$Percentage\ SO_2\ Yield = \frac{No.of\ moles\ of\ SO_2\ produced}{No.of\ moles\ of\ H_2SO_4\ in\ feed} \text{ X } 100\text{----------}(2.12)$$

The catalytic activities were evaluated in the range of 650 °C to 900 °C with an interval of 50°C and hold time was 2h at each measuring temperature.

Ex-situ analysis of the spent sample was studied to check any deactivation, poisoning and prediction of the most likely mechanism of the acid decomposition reaction.

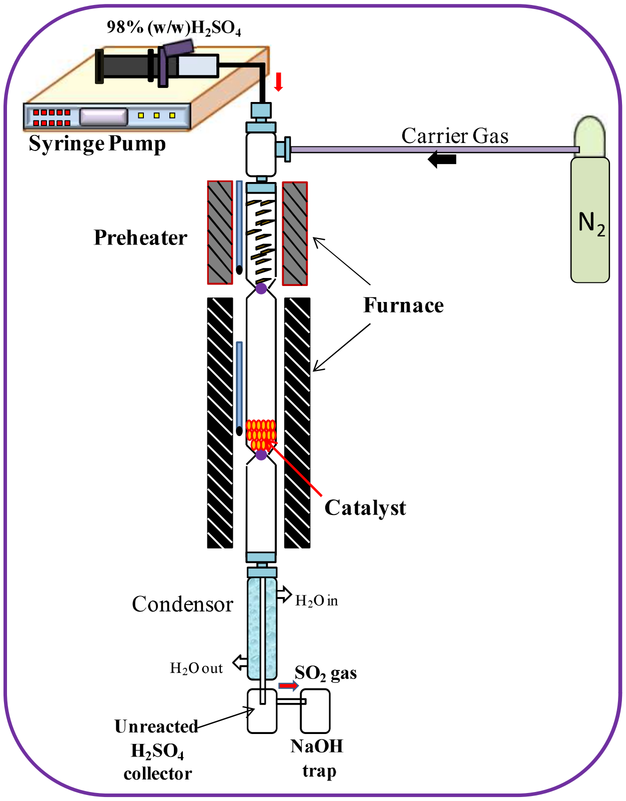

Figure 2.16: Schematic representation of the setup used for H_2SO_4 decomposition reaction

For demonstration of sulfuric acid decomposition with concentrated solar irradiation, a 1.8 m solar dish was employed in the terrace of our building. The photograph of the solar dish holding the reactor at the focus point has been shown in Figure 2.17. The complete experimental set-up for carrying out continuous flow solar thermal sulfuric acid decomposition is shown in Figure 2.18. During operation, the receiver reactor described above was positioned such that the quartz window of the reactor coincided with the focal plane of the 1.8 m diameter dish. 98 wt.% concentrated sulfuric acid was introduced at a constant flow rate of 0.5 mL/min with the help of a syringe pump into the inlet of the solar receiver-reactor. Sulfuric acid vaporization, dehydration and decomposition were achieved within the receiver-reactor at the catalyst zone. The iron oxide based catalyst functioned as catalyst and also absorber of the heat for carrying out solar thermal sulfuric acid decomposition.

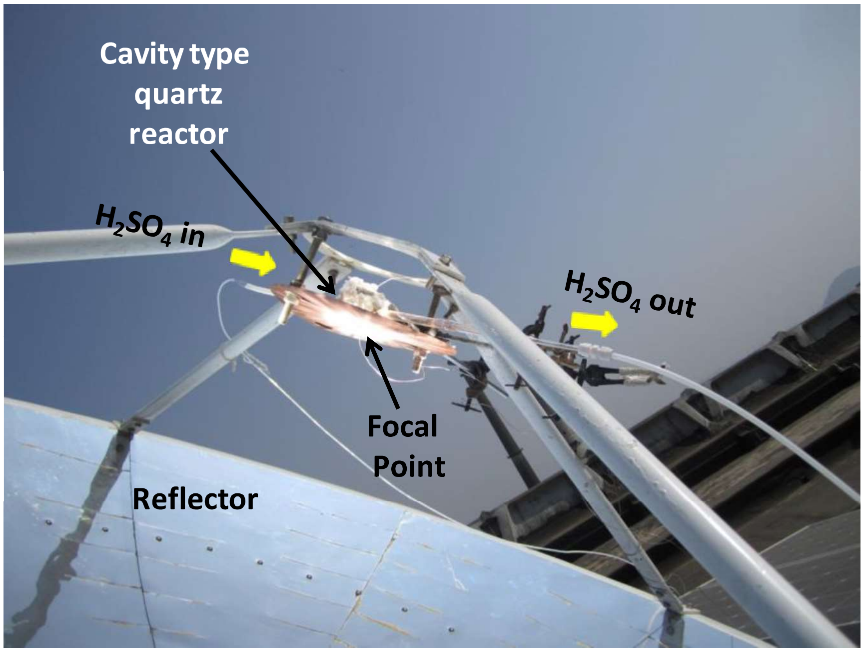

Figure 2.17: Photograph of the solar dish with the reactor held in the heating zone

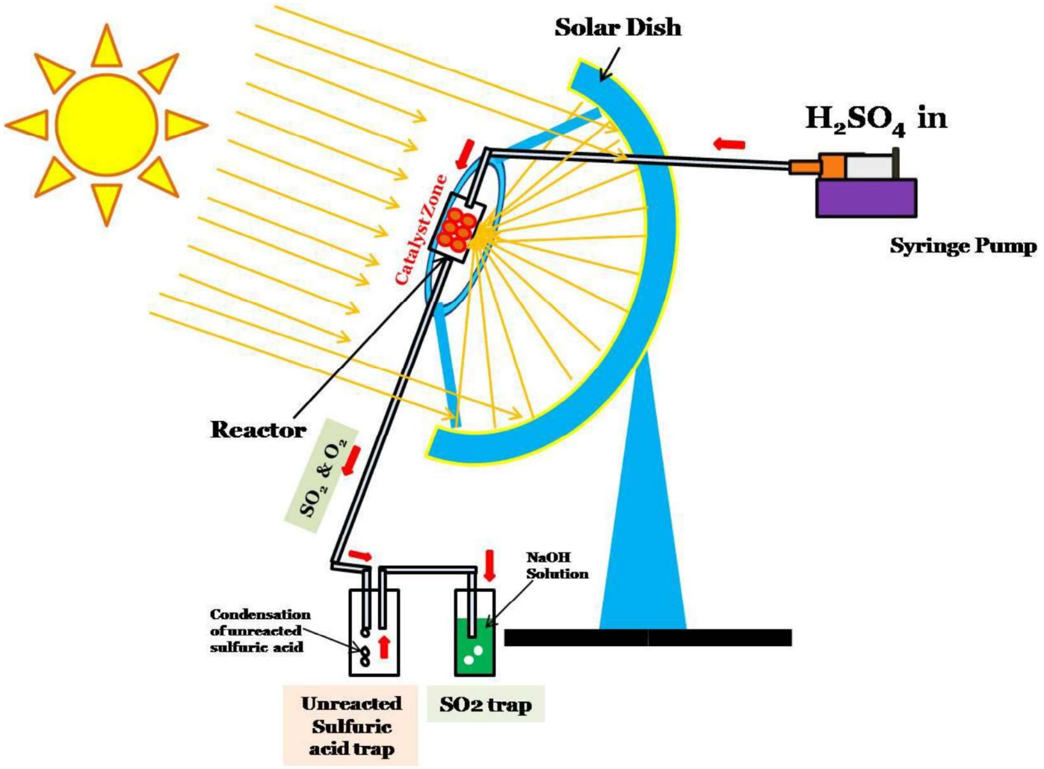

Figure 2.18: Schematic for solar thermal sulfuric acid decomposition reaction

A cavity type configuration of the solar reactor was developed for carrying out solar thermal sulfuric acid decomposition reaction using solar concentrator. The transverse and the top view of the cavity type solar receiver-reactor are shown in Figure 2.19. It consisted of a double walled quartz cylindrical tube with the volume in between the walls vacuum sealed to minimize heat losses. Further, during operation, the outside wall of the cavity was surrounded by alumina wool. The lower surface of the cavity was a flat quartz plate which served as a window for entry of concentrated solar irradiation. To achieve the vaporization, dehydration and then catalytic decomposition of sulfuric acid as discussed earlier a quartz cylindrical tube was placed within the cavity. 2g of the catalyst (10-20 mesh) loaded within the tube in the region of the cavity. The catalyst was held in position by plugging quartz wool from both sides. One end of the tube served as the inlet for sulfuric acid while other end served as an exit for products of decomposition which was realized within the tube.

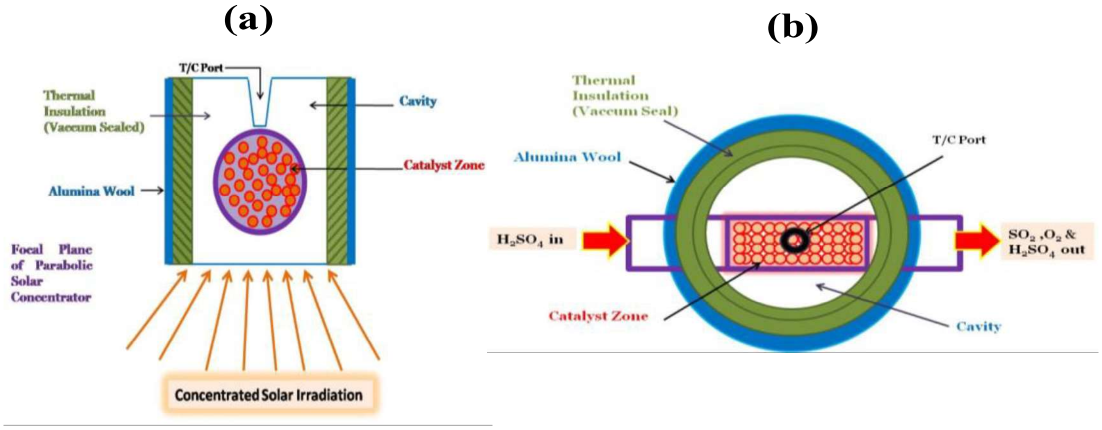
(a)

(b)

Figure 2.19: Schematic representation of the cavity type reactor

2.3.14 Electrochemical Measurements

A potentiostat allows us to regulate the potential of the working electrode. The potential of working electrode is measured with respect to a constant-potential reference electrode which is connected to the working electrode via a high-impedance potentiometer. The current passing between the auxiliary electrode and the working electrode is recorded using an ammeter. Modern potentiostats include waveform generators which allows application of time-dependent potential profile to the working electrode.

A single cell PEM type aqueous SO_2 electrolyser was designed, fabricated and used to evaluate the performance of the 4 cm^2 area MEA as shown in Figure 2.20. All the electrochemical experiments were carried out by the Biologic Scientific Instrument Potentiostat/Galvanostat (VSP-2). The MEA was then sandwiched between the gas diffusion layers, followed by electrically conducting flow field having thickness 3 mm. The serpentine grooves (1 mm width) engraved on the flow field provided the pathway for the anolyte and catholyte. Finally, the Perspex plate with 10 mm thickness were used as the pressure plates having holes for washers and bolts torqued to about 5-7 Nm that compress the cell to prevent from leakage. The face of the pressure plates are provided with two holes containing Teflon inserts which were sealed to the pressure plates. The SO_2 purged in the water reservoir is connected to the inlet of the PEM type electrolyzer. The anolyte then traverses through the grooved channel, where it undergoes oxidation reaction on contact with anode catalyst to produce sulfuric acid and hydrogen ions. The sulfuric acid passes through the outlet and collected in another reservoir. The H^+ ions produced on the anode side migrates to the cathode end and gets reduced to produce hydrogen gas. The electrocatalyst was characterized by cyclic voltammetry and then its polarization studies were performed using SO_2 saturated deionized water which was allowed to pass through the anode.

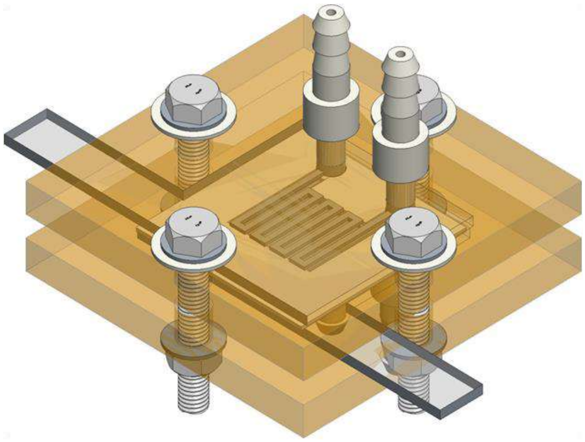

Figure 2.20: Diagrammatic representation of the single cell PEM type electrolyzer

The half-cell hydrogen evolution reaction for supported Molybdenum carbide samples was performed in three electrode configuration (Figure 2.21) with Pt as the counter electrode, saturated calomel electrode (SCE) as the reference electrode and the Pt/C deposited on GC as the working electrode in a Biologic Scientific Instrument Potentiostat/Galvanostat (VSP-2). The electrochemical characterization was performed by measuring the cyclic voltammetry in 0.5 M H_2SO_4 after purging N_2 for 0.5 h. Polarization measurements for hydrogen evolution reaction was carried out in 0.5 M H_2SO_4.

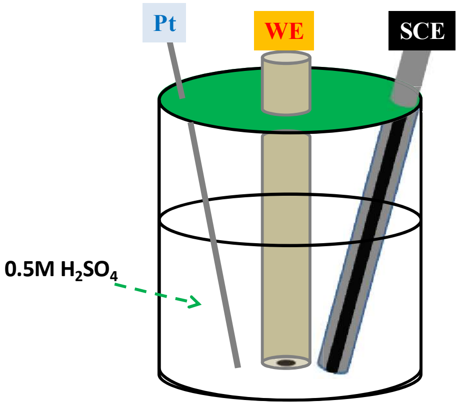

Figure 2.21: Diagrammatic representation of the three electrode system used for HER study

Linear Sweep Voltammetry

In this technique a linear potential sweep is applied to working electrode while simultaneously recording the current flowing through the circuit. Here, a signal generator produces a voltage sweep at a constant rate from E_i to E_f and a potentiostat applies this potential wave to the working electrode. The scan direction can be positive or negative and the sweep rate can possess any constant value: Sweep rate = dE/dt

The features of the linear sweep voltammogram recorded depends on the rate of the electron transfer reaction(s), the chemical reactivity of the electroactive species and the voltage sweep rate.

Oxidation or reduction of species appears as a peak or trough in the current signal at the potential at which the species oxidizes or reduces. The current is a direct measure of rate of electron exchange through electrode-electrolyte boundary. If this rate overpasses the rate at which the oxidizing or reducing species could diffuse from the bulk of the electrolyte to the surface of the electrode, then the current reaches a plateau or exhibits a peak.

LSV was performed during aqueous SO_2 electrolysis while optimizing the electrolyzer as well as, for evaluation of Pt/VC (20 wt.%) is described in chapter 5.

Cyclic Voltammetry

A cyclic voltammogram is generated when a linear potential sweep is applied to the working electrode. During the course, the potential is swung back and forth past the formal potential, E°, of an anolyte and the resultant current flows through the electrode that either oxidizes or reduces the anolyte. The magnitude of this current is equivalent to the concentration of the anolyte in solution, and this enables cyclic voltammetry (CV) to be a very useful tool in an analytical determination of concentration. The current density obtained after normalizing the current to the surface area is then plotted against the applied potential to get a cyclic voltammogram. A peak in the measured current is seen at a potential that is characteristic of any electrode reaction taking place. It is often used to study a variety of redox processes, to determine the stability of reaction products, the presence of intermediates in redox reactions, electron transfer kinetics, and the reversibility of a reaction [86].

The CV was performed for carbon supported Pt samples as well as for Mo_2C samples to ensure stability of the electrode material and this work is also depicted in chapter 5.

Potentiodynamic Electrochemical Impedance Spectroscopy (PDEIS)

This technique acquires ac and dc responses of an electrochemical interface in a single potential scan by investigating the electrochemical interface with streams of mutually coordinated wavelets. PDEIS virtual spectrometer program acquires a potentiodynamic impedance spectrum by a common potentiostat connected to a computer with ADC/DAC interface. The object is placed in a three-electrode electrochemical cell and the spectra are generally recorded in bidirectional potential scans, which give supplementary information on the extent of reversibility of different constituent processes that impact to the frequency response of a non-stationary electrochemical interface. Generally the data obtained by electrochemical impedance spectroscopy (EIS) is explained graphically by a Bode plot or a Nyquist plot [87].

Nyquist diagram helps to evaluate the charge transfer resistance, double layer capacitance and ohmic resistance. The exchange current density can also be determined by the impedance of a redox reaction for $\eta = 0$. Nyquist diagrams are generally made of several arcs for reactions more complex than redox reactions and with mass-transfer limitations.

The EIS was studied for molybdenum carbide samples to investigate the different mode of resistance observed in the series of the samples synthesized (Chapter 5).

Chapter 3: Comparative evaluation of iron oxide dispersed on different metal oxide supports for sulfuric acid decomposition reaction

---

3.1 Introduction

Sulfuric acid decomposition reaction is common to all sulfur based thermochemical cycles and is the most energy demanding step. The reaction comprises following elementary reactions.

$Sulfuric\ acid\ vaporisation: H_2SO_4(l) = H_2SO_4(g)\ (\sim 337\ °C)$--------------(3.1)

$Sulfuric\ acid\ dehydration: H_2SO_4(g) = SO_3(g) + H_2O(g)\ (> 450\ °C)$--------(3.2)

$Sulfur\ trioxide\ decomposition: SO_3(g) = SO_2(g) + 0.5O_2(g)\ (800 - 900\ °C)$ -----(3.3)

$Net\ Reaction: H_2SO_4(l) = SO_2(g) + 0.5O_2(g) + H_2O(g)\ (800 - 900\ °C)$----------------(3.4)

Amongst them, except the later reaction, they are just dehydration reaction and are kinetically quite sound in comparison to the later which could be only paced up for higher efficiency at equilibrium in lower temperature when employed with a suitable catalyst. Different types of catalysts including Pt supported on various supports like Al_2O_3, TiO_2, CeO_2, ZrO_2 have been widely reported for this energy-intensive reaction. To substitute the noble metal based catalyst metal oxides have also been employed [37-39]. A number of benefits are observed with the modified Fe_2O_3incomparison to Pt/Al_2O_3 catalyst. The doped Fe_2O_3 seems to have a superior catalytic activity with Pt/Al_2O_3 and even stability was found to be better [87-88]. The chromium as a dopant stabilized the catalyst particle by reducing the agglomeration on the extended term operation at 800 °C. Copper ferrite also proved to be a compatible catalysts having for sulfuric acid decomposition with high activity [38]. These results ameliorated us to examine other category of Fe_2O_3 based catalysts such as supported Fe_2O_3 [91].

So, it is very clear that Fe_2O_3 and its different diverse modified forms have been employed to catalyze high temperature sulfuric acid decomposition. The modifications were carried out with an aim to adapt their catalytic properties viz. better structural forms, improvised morphology, enhanced redox properties finally to attain superior catalytic activity and stability. The alteration of Fe_2O_3 were attempted through a wide variety of approaches viz. doping Fe_2O_3 [89], dispersing Fe_2O_3 on supports [34, 87-88, 92], forming mixed oxide compounds like spinel ferrites [38,39,93] etc. Doped Fe_2O_3 was found to be more active and stable than Fe_2O_3 [89], and spinel ferrites bulk [38-39] or supported [93] exhibited promising catalytic activity. Among the dispersed Fe_2O_3 or other metal oxide catalysts - Al_2O_3 [94-95], SiO_2 [96-98] and silicon carbide [98-101] supports have been exploited. In this chapter the study of exploration of Fe_2O_3 nanoparticles supported on SiO_2, ZrO_2, CeO_2 and TiO_2 for their catalytic properties has been discussed [90]. Fe_2O_3 was dispersed on variable supports by equilibrium adsorption method which is a modified form of the deposition-precipitation method [90, 92, 102-104].The conventional method for the synthesis of dispersed catalyst is impregnation (either wet or incipient) but in the case of strong interaction between the support and the precursor, the impregnation process is fast and the rate of diffusion of the precursor within the pores becomes crucial. This leads to inhomogeneous distribution of the precursor and consequently non-uniform distribution of the dispersed phase. To surmount this issue alternative methods are employed and in our study, we have utilized equilibrium adsorption method [90]. The prepared catalysts were subjected to compositional, textural, structural and morphological characterization by inductively coupled plasma-atomic emission spectroscopy (ICP-AES), N_2-adsorption-desorption isotherms, powder X-ray diffraction, Mössbauer spectroscopy, Fourier Transform Infrared Spectroscopy (FTIR), Diffuse reflectance ultraviolet-visible spectroscopy (DRUV-Vis), X-ray photoelectron spectroscopy (XPS) and Transmission Electron Microscopy (TEM).This enabled us to determine the variation in physical and chemical properties of the dispersed Fe_2O_3 phase in supported samples arising out due to variance in support. The catalytic activity evaluation was carried out in an indigenously fabricated flow through quartz catalytic reactor. After the activity analysis, ex-situ structural and thermal investigations on the spent catalyst were carried out. An attempt was made to establish structure-property-activity correlation by analysis of the catalytic activity, fresh and spent catalyst characterization outcomes. Establishing such a structure-property-activity correlation facilitated recognizing the aspects which might be responsible for increasing or decreasing catalyzed reaction rates. These results would ease the rational design of catalytically active Fe_2O_3 based formulations for sulfuric acid decomposition and even other high temperature reactions.

3.2 Experimental:

3.2.1 Preparation of Iron Acetyl Acetonate Precursor

Fe(III) acetylacetonate, the precursor for Fe_2O_3, was prepared by adding ferric chloride solution into an aqueous solution of sodium acetylacetonate in 1:3 molar ratio with continuous stirring. The red colored Fe(III) acetylacetonate precipitate was allowed to settle overnight and then filtered through Buchner funnel. Solid obtained was dried in an air oven (~80 °C) overnight. The purity of the sample was verified by melting point measurement.

3.2.2 Synthesis of Iron Oxide Based Catalysts

Using iron acetyl acetonate as the precursor, iron oxide was dispersed over commercial support materials i.e. CeO_2, TiO_2, ZrO_2 and SiO_2.Equilibrium adsorption method was employed for dispersion as shown in Figure 3.1and explained in details in the chapter 2 [39-42]. In brief, iron oxide to the extent of 15 wt.% with respect to the support was loaded sequentially with 5 wt.% dispersion in each step. The multistep dispersion included synthesis of 5 wt%. as-prepared material, followed by further loading on the 5 wt. % to obtain the 10 wt% Fe_2O_3/support and then finally 15 wt. %. In each step the precursor solution (iron acetyl acetonate dissolved in 1:1-water:1-propanol mixture) was added to an ammoniacal suspension (0 °C and pH 10) of support or Fe_2O_3/support (as per the case). The precipitate thus formed in every step was allowed to settle overnight followed by filtration and calcination at 500 °C for 4 h. The 500 °C calcined 15 wt.%Fe_2O_3/support sample was finally heated at 1000 °C for 5 h in air.

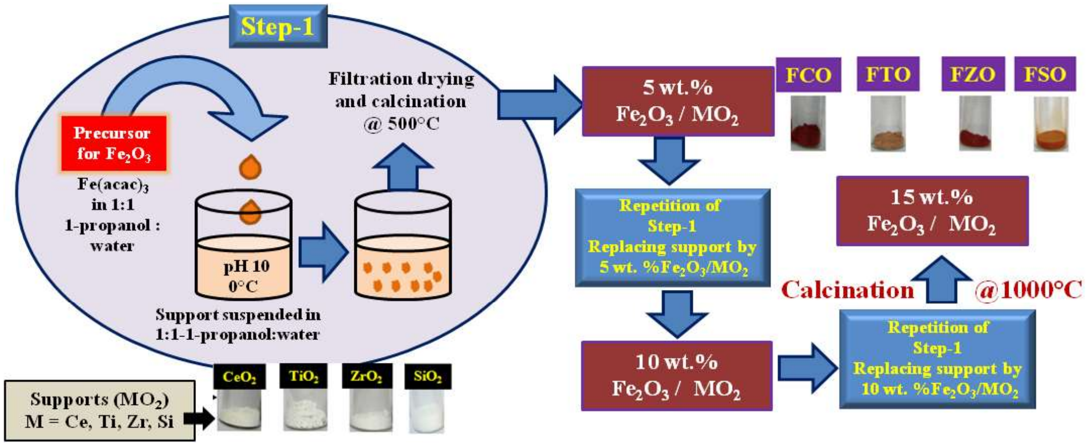

Figure 3.1: Schematic representation of synthesis of dispersed samples

3.2.3 Characterization of the Catalysts

ICP-OES technique was employed to evaluate the Fe_2O_3 content in each catalyst by microwave digestion of the powders in conc. HNO_3-HCl (aqua regia). The powder XRD patterns of the samples were recorded by Philips X'Pert pro X-ray diffractometer using Cu K_α radiation (λ= 1.5418 Å) at 40 kV and 30 mA. Room temperature Mössbauer spectra of all the samples were obtained in a spectrometer operated at constant acceleration mode in transmission geometry. ^{60}Co in Rh matrix of strength 10 mCi was employed as the source [50].The calibration of the velocity scale was carried out using iron metal foil. The outer line width of calibration spectra was 0.29 mm/s. The Mössbauer data was analyzed using a Win Normos site fit program. The redox properties of the samples as a function of temperature were determined by measuring the temperature programmed reduction (TPR) using gas mixtures of 5% hydrogen in argon for TPR in TPDRO-1100 analyzer (Thermo Quest, Italy). The samples were pretreated at 350 °C in helium for 3 h prior to each run. To study the surface characteristics X-ray photoelectron spectra (XPS) of each sample was recorded in a spectrometer (SPECS, Surface Nano Analysis GmbH, Germany) using Mg-K_α X-rays (hν =1253.6 eV) as the primary source of radiation with an overall energy resolution of the instrument of about 0.7 eV. The corrections for charging effect were made with the help of a C 1s signal appearing at 284.5eV. The morphological features were analyzed by recording the High resolution TEM (HR-TEM) images in a FEI-Tecnai G-20 microscope operating at 200 kV. To understand the nature of stable species produced on the catalyst during decomposition of sulfuric acid, the spent catalyst samples were heated in the temperature range of 400-1000 °C at a heating rate of 10 °C/min in a TG-DTA thermobalance (Model No.: STA 409 PC Luxx, Netzsch) and the evolved gases were analyzed by a FTIR coupled to the TG-DTA (Model No.: Tensor, Bruker).

3.2.4 Catalytic Activity Evaluation

A flow through quartz catalytic reactor (schematically shown in Figure 2.16) used in our earlier studies was employed for the evaluation of catalytic activity of all the dispersed samples. At a constant flow rate of 0.05 mlmin^{-1} concentrated sulfuric acid (98 wt.%) was pumped into a quartz preheater held at 450 °C using a 50 ml syringe pump. Liquid sulfuric acid was converted to sulfur trioxide and steam by vaporization and dehydration (Eqn 3.1-3.2) within the preheater. N_2 gas at a flow rate of 40 ml min^{-1} carries this gas mixture into the catalyst (0.2 g) zone where the temperature was maintained between 600-900 °C employing a PID temperature controller. Sulfur trioxide decomposed into sulfur dioxide and oxygen (Eqn. 3.3) within the catalyst zone. At the outlet of the catalytic reactor the unreacted sulfuric acid condenses within the condenser, which was collected while the sulfur dioxide formed was trapped in sodium hydroxide solution and its concentration was estimated by titrimetry. The catalytic activity was quantified by the extent of SO_2 yield defined as:

$$Percentage\ SO_2\ Yield = \frac{No.of\ moles\ of\ SO_2\ produced}{No.of\ moles\ of\ H_2SO_4\ in\ feed}\ \mathrm{X}\ 100\ \text{--------}(3.5)$$

The catalytic performance of all the Fe_2O_3/MO_2 catalysts (20-40 mesh; ASTM) were measured as a function of temperature between 600-900 °C at a WHSV of 27 g acid g^{-1} h^{-1}. Each catalyst was pre-treated at 500 °C for 2 h at N_2 flow rate 40 mlmin^{-1} prior to catalytic activity evaluation. Equilibrium conversion was attained by holding the system for an hour at each set temperature before carrying out the analysis and measurements were carried out till a reproducible result was obtained at each temperature. Percentage SO_2 yield was calculated according to Eqn. 3.5. The catalyst after the activity measurement was recovered and characterized to analyze its properties.

3.3 Results and discussions:

3.3.1 Composition and Texture Analysis

The sample name, abbreviation, calcination temperature and phases identified for all the Fe_2O_3 dispersed samples on ZrO_2, CeO_2, TiO_2 and SiO_2 are listed in Table 3.2. Henceforth in this article the samples will be denoted by their abbreviation. The expected iron content and the actual content as derived from ICP-OES studies, the N_2-BET surface area of the samples are also listed in Table 3.2. The iron content determined experimentally was found to be slightly less than the expected composition. The surface area of SiO_2 supported sample was highest while those of other samples were lower most probably due to lower surface area of these supports.

Table 3.2 Abbreviation, composition, phase identification and textural characteristics of the samples

Sample	**Calcination temperature**	**Abbreviation**	**Phases identified**	**Fe wt.% (Expected 10.5)**	**N_2 BET Surface Area (m^2/g)**
ZrO_2 support	500 °C for 3 h	-	Baddeleyite	-	19
CeO_2 support	500 °C for 3 h	-	Fluorite	-	1.4
TiO_2 support	500 °C for 3 h	-	Anatase	-	8.9
SiO_2 support	500 °C for 3 h	-	Crystabolite	-	249.5

Fe_2O_3(15. wt.%)/ZrO_2	1000 °C for 5 h of FZO15-500	FZO	α-Fe_2O_3 haematite dispersed over Baddeleyite ZrO_2	9.7	3.8
Fe_2O_3(15. wt.%)/CeO_2	1000 °C for 5 h of FCO15-500	FCO	α-Fe_2O_3 haematite dispersed over Fluorite CeO_2	9.9	2.1
Fe_2O_3(15. wt.%)/TiO_2	1000 °C for 5 h of FTO15-500	FTO	pseudo-brookite Fe_2TiO_5 dispersed on rutile TiO_2	8.5	1.7
Fe_2O_3(15. wt.%)/SiO_2	1000 °C for 5 h of FSO15-500	FSO	ε- Fe_2O_3 (major),α,γ-Fe_2O_3 (minor)dispersed on crystabolite SiO_2	9.8	145

3.3.2 Structural Analysis by Powder X-ray Diffraction and Mössbauer Spectroscopy

The powder X-ray diffraction (XRD) patterns of all the prepared samples calcined at 1000 °C are shown in Figure 3.2. The support ZrO_2, CeO_2, TiO_2 and SiO_2 were initially calcined at 500 °C before Fe_2O_3 dispersion and their XRD patterns exhibited baddeleyite (Monoclinic crystal system, Space Group $P2_1/c$ (14) ICSD No. 18190), fluorite (Cubic Crystal system, Space Group Fm-3 m (225), ICSD No. 72155), anatase (Tetragonal crystal system, Space Group $I4_1/a$ md (141), ICSD No. 9852),) and crystabolite (tetragonal crystal system, Space Group: $P4_12_12$ (92), ICSD No. 47219) phases respectively.

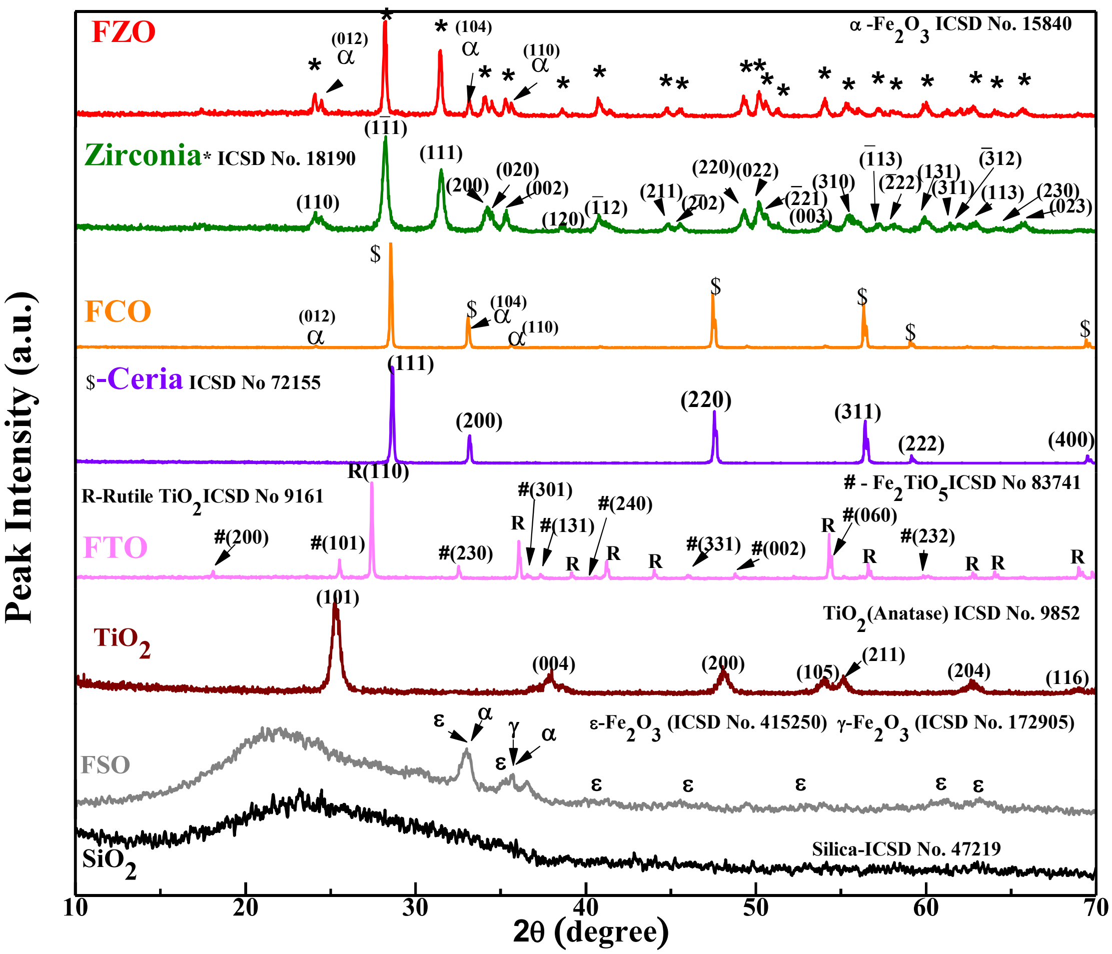

Figure 3.2: Powder XRD patterns of each support and the synthesized dispersed samples

Fe_2O_3 can exist in four different polymorphic forms: α-Fe_2O_3 (mineral name: hematite, corundum type, trigonal crystal system, space group $R\bar{3}c$ (167)), β-Fe_2O_3 (bixbyite type, cubic crystal system, space group $Ia\bar{3}$ (206)), γ-Fe_2O_3 (mineral name maghemite, spinel structure with disordered vacancies, cubic crystal system, space group $Fd\bar{3}m$ (227), or alternate structures), and ε-Fe_2O_3 (isostructural with κ-Al_2O_3, orthorhombic crystal system, space group $Pna2_1$(33)) [90]. In FZO and FCO peaks were observed at 2θ values of 24.1, 33.1, 35.6, 49.5, 54.1, 62.5 and 64.1 corresponding to (012), (104), (110), (024), (116), (214) and (300) planes of α-Fe_2O_3 (ICSD No.

15840) in addition to the peaks corresponding to its support phase i.e. CeO_2 and ZrO_2. But for FTO sample no peaks due to any phases of Fe_2O_3 were present instead peaks due to a new phase of pseudo-brookite Fe_2TiO_5 (ICSD No. 36183) were observed. The pseudobrookite Fe_2TiO_5 crystallizes in orthorhombic structure (mineral name: pseudobrookite, orthorhombic crystal system, space group *Cmcm* (63)). A familiar structural attribute of mixed oxide titanates is the presence of BO_6 moieties (B = Ti, In, Nb, Ta, etc.) [105-106]. Similarly, in Fe_2TiO_5, the crystallographic structure consists of randomly distributed and edge shared TiO_6 and FeO_6 octahedral. The lattice structure possesses two octahedral cationic sites, 4c (Wyckoff position) and 8f and the distribution of Fe^{3+} and Ti^{4+} in these sites widely varies depending upon the preparation conditions and particle size [103].In FTO another structural variation as compared to others was the complete transformation of support phase titania from anatase to rutile due to the calcination step at 1000 °C. In the case for SiO_2 support, Fe_2O_3 crystallized predominantly in ε-phase (ICSD No. 415250) after calcination at 1000 °C [90]. The schematic representation of the iron oxide and titanate phases present in the dispersed phases as derived from the ICSD database are shown in Figure 3.3.

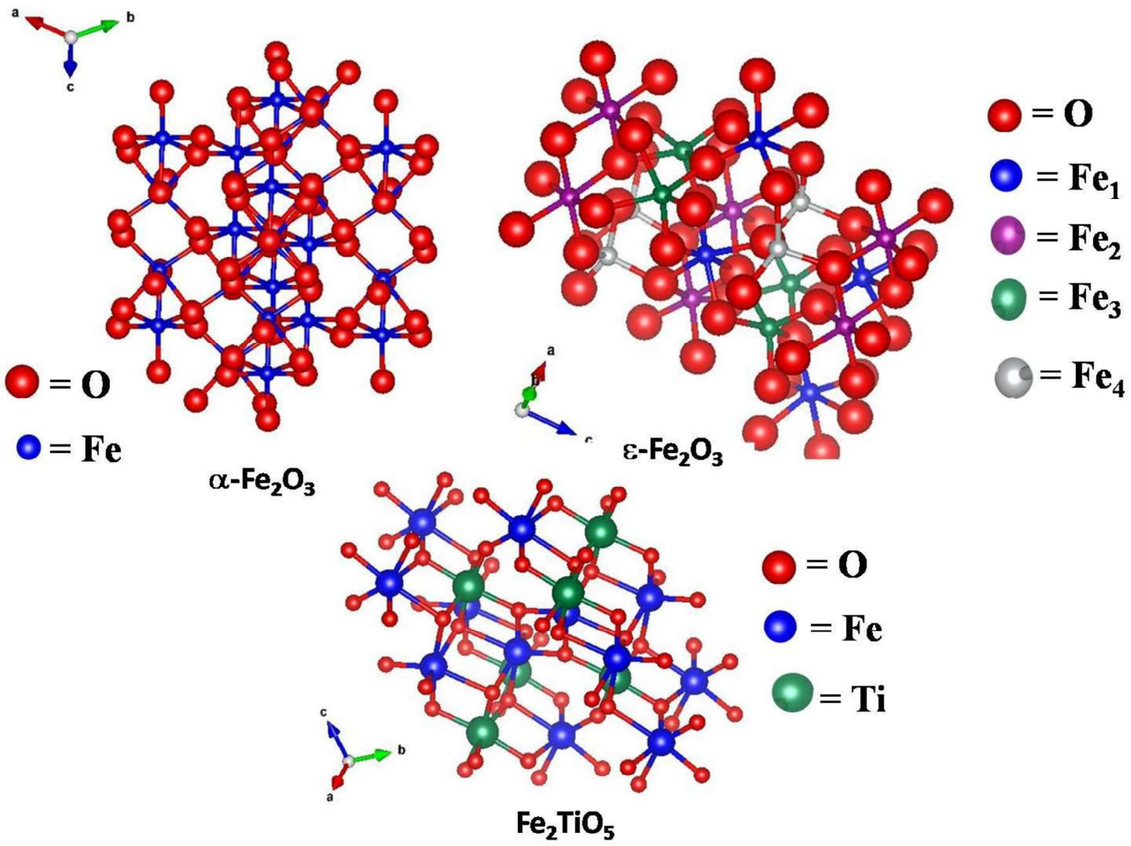

Figure 3.3: Schematic representation of the iron oxide phases evolved over various supports

The room temperature Mössbauer spectra of all the four dispersed iron oxide samples calcined at 1000 °C are shown in Figure 3.4 and the Mössbauer parameters are listed in Table 3.3. FCO exhibits a sextet with isomer shift (δ), quadrupole splitting (Δ), and hyperfine field (H_{hf}) values of 0.357 mm/s, -0.216 mm/s and 51.61 Tesla. These values are consistent with α-Fe_2O_3 phase [38, 90, 107-109]. FZO sample in addition to a sextet exhibits a paramagnetic doublet. The sextet with relative area (R_A) 94.4% (δ =0.36 mm/s, Δ = -0.206, H_{hf} = 51.72) belongs to α-Fe_2O_3 phase whereas the doublet with R_A = 5.6 % appeared due to the presence of minor quantities of paramagnetic γ-Fe_2O_3 phase [90,107].The minor amount of γ-Fe_2O_3 remained undetected in its XRD pattern. We can attribute these differences to better sensitivity of ^{57}Fe Mössbauer spectroscopy for Fe as compared to powder X-ray diffraction. The FTO Mössbauer spectrum can be fitted with two symmetric doublets of Fe_2TiO_5. Orthorhombic Fe_2TiO_5 is having two crystallographic Fe sites, 8f and 4c, so two components were observed in the Mössbauer spectrum [110]. The assignment of the doublets for two different Fe sites has been done based on the values of Δ and R_A values. The value of Δ and R_A are higher for 4c site in Fe_2TiO_5 [106]. It has been proposed that the Fe^{3+} ions have a slight preference for 4c sites, whereas Ti^{4+} ions have preference for 8f sites, but as pointed out earlier the distribution widely varies with preparation method and particle size [110-111]. However, in our sample, we find from the relative area of the Mössbauer spectrum that the Fe^{3+} distribution in the two sites are almost equal (51.5 % and 48.5 % for 4c and 8f sites). Thus, Fe^{3+} does not seem to have any preference for either site in a dispersed Fe_2TiO_5 system. The values of δ for all three samples are in the range of 0.3-0.392 mm/s which corresponds to high spin Fe^{3+}. In the case of FSO three sextets due to ε-Fe_2O_3 (although structure has four non-equivalent Fe^{3+} sites two close sextets could not be distinguished), one sextet due to α-Fe_2O_3 and a doublet attributed to γ-Fe_2O_3 [90].

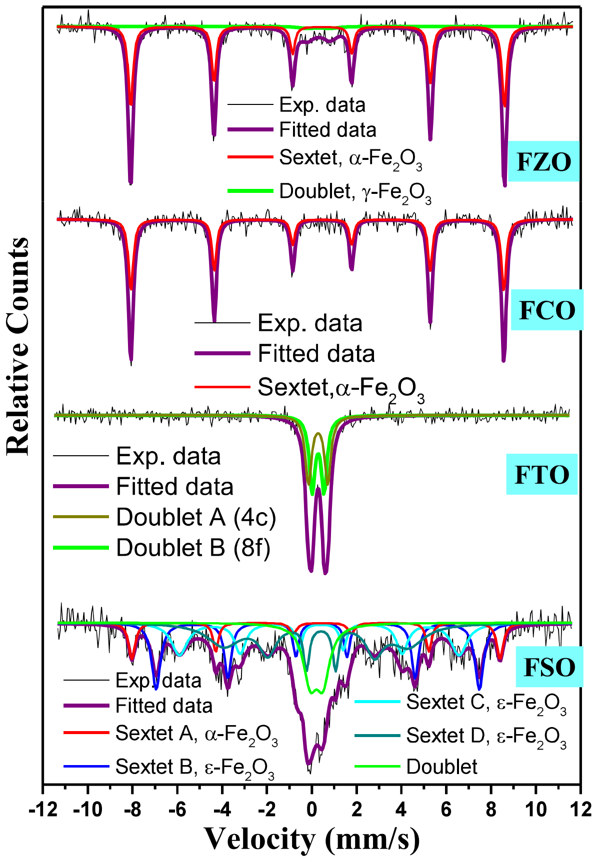

Figure 3.4: Room Temperature Mössbauer spectra of the dispersed catalysts on different supports calcined at 1000 °C

Table 3.3The hyperfine field values (Hhf), isomer shift (δ), quadrupole splitting (Δ), linewidth (Γ) of Fe^{3+} ions for 15 wt.% Fe_2O_3 dispersed on SiO_2, CeO_2,TiO_2 and ZrO_2 heated at 1000 °C derived from Mössbauer spectrum, recorded at room temperature. Fitting quality (χ^2), Isomer shift values are relative to Fe metal foil. Quadrupole splitting for magnetic sextet $\Delta(M) = (\Delta_{12}-\Delta_{56})/4$.

Sample	**Iron Sites (Fe^{3+})**	**Relative area (R_A) %**	**Outer Line width (Γ) mm/s**	**Isomer shift (δ) mm/s**	**Quadrupole splitting (Δ) mm/s**	**Hyperfine field (H_{hf}) Tesla**	**Fitting quality (χ^2)**
FZO	Sextet	94.4	0.255±0.015	0.360±0.002	-0.206±0.004	51.72 ± 0.015	1.17042
	Doublet	5.6	0.863±0.18	0.300±0.002	1.0174±0.105	----	
FCO	Sextet	100	0.246 ±0.014	0.357±0.002	-0.216±0.004	51.61 ± 0.015	1.20178
FTO	Doublet A (4c)	51.5	0.34±0.03	0.392±0.004	0.862±0.04	-----	1.07452
	Doublet B (8f)	48.5	0.316±0.03	0.395±0.003	0.531±0.03	----	
FSO	Sextet A - α-Fe_2O_3	11.6	0.4± 0.2	0.327±0.02	-0.28±0.04	50.93 ± 0.15	0.86109
	Sextet B - ε-Fe_2O_3	21.6	0.31±0.07	0.349±0.014	-0.17±0.03	44.72 ± 0.13	
	Sextet C - ε-Fe_2O_3	21.6	0.347±0.11	0.376±0.03	-0.09±0.06	38.69 ± 0.3	
	Sextet D - ε-Fe_2O_3	28.8	0.313±0.07	0.30±0.06	-0.23±.13	25.50±0.55	
	Doublet (γ-Fe_2O_3)	16.4	0.736±0.06	0.212±0.02	0.57±0.03	--	

From the above structural investigations using powder x-ray diffraction and Mössbauer spectroscopy it is evident that in spite of similar synthetic procedure employed for the dispersion of Fe_2O_3 on different supports the composition, phase and crystallinity widely varied depending upon the nature of support. On SiO_2, ZrO_2 and CeO_2 the composition of the dispersed phase was Fe_2O_3 while in TiO_2, Fe_2TiO_5 mixed metal oxide was produced. The driving force for formation of Fe_2TiO_5 instead of Fe_2O_3 could be the lattice matched structures of Fe_2TiO_5 and anatase TiO_2 [105]. In the first three supports Fe_2O_3 was precipitated as the dispersed phase because the reaction between the support and Fe_2O_3 was not facile for formation of any mixed phase. Instead, in the case of FTO, during calcination at 1000 °C Fe_2TiO_5 was crystallized due to the kinetically rapid reactivity between the Fe_2O_3 and TiO_2 phases owing to lattice-matched structures of Fe_2TiO_5 and anatase TiO_2. Again, in FCO and FZO, α-Fe_2O_3 was crystallized upon calcination, whereas ε-Fe_2O_3 phase evolved over SiO_2 support [90].

3.3.3 FTIR and DR-UV-Vis Spectra Analysis

FTIR spectra of each support - ZrO_2, CeO_2, TiO_2 and SiO_2 along with their catalytically active forms after attempted Fe_2O_3 dispersion are displayed in Figure 3.5. Such a study would facilitate understanding of the microstructural modifications occurring in the support phase on dispersion and also the nature of bonding created in the dispersed phase. The peak positions and their assignments are listed in Table 3.4. Peaks at 413, 449, 512, 577, 663 and 747 cm^{-1} characteristic of monoclinic phase of ZrO_2 were observed in pure zirconia support [112]. On Fe_2O_3 dispersion the peak positions were shifted to slightly higher values probably due to microstructural changes that occurred on the stepwise loading, calcinations and Fe_2O_3 dispersion. However, a prominent change in peak shape and intensity was observed at 579 cm^{-1}. A weak shoulder at ~ 577 cm^{-1} in ZrO_2 was transformed to an intense peak at ~ 579 cm^{-1} in FZO due to the presence of Fe-O stretching vibration overlapping at the same region [18, 89]. In contrast to multiple peaks for M-O (metal-oxygen) vibrations in low symmetry monoclinic ZrO_2, the high symmetry cubic CeO_2 support exhibits only one intense broad hump extending from 550 cm^{-1} to 400 cm^{-1}, which can be assigned to characteristic Ce-O vibrations in CeO_2 crystal [113]. In FCO a shoulder appeared at 538 cm^{-1} due to Fe-O stretching and another at ~ 473 cm^{-1} due to Fe-O-Fe deformation [18, 89]. Although α-Fe_2O_3 structure consist of only one equivalent Fe^{3+} site in the lattice and hence single type of FeO_6 octahedral with defined Fe-O distances (Fe-O bond distances for α-Fe_2O_3 marked in the schematic representation of structure in Figure 3.6) but based on the support the dispersed α-Fe_2O_3 have quite different Fe-O bond characteristics as observed from the FTIR spectra. The Fe-O-M bonds that might be created at the interface of Fe_2O_3 and MO_2 support also modify the structure and the extent of modification varies with the nature of metal M (MO_2), which is reflected as different peak characteristics in their FTIR spectra. In TiO_2 anatase support two broad peaks centered at 680 cm^{-1} and 529 cm^{-1} were observed due to Ti-O bending vibrations [114-116]. In FTO, the presence of Fe_2TiO_5 dispersed phase and transformation of the anatase support to rutile modified the FTIR spectrum significantly. Both the bands present in the support shifted to lower wavenumber region to 670 cm^{-1} and 505 cm^{-1}. An additional band appeared at ~ 420-400 cm^{-1}. Further, the 670 cm^{-1} band extended into an intense tail towards higher wavenumber region probably due to the presence of fundamental vibrations of Fe_2TiO_5 [117]. For SiO_2, peaks at 469 and 1111 cm^{-1} appeared due to Si-O-Si bond vibrations while the band at 800 cm^{-1} corresponds to vibrations associated with [SiO_4] tetrahedron [118-119]. In FSO an additional peak appeared at ~ 609 cm^{-1} appeared. This peak could be assigned to Fe-O stretching vibrations in ε-Fe_2O_3 lattice. An interesting feature is that the peak due to Fe-O stretching appears at a much higher wavenumber for ε-Fe_2O_3 in FSO than α-Fe_2O_3 in FCO/FZO. This can be attributed to considerable difference in bond strengths and consequent bond lengths of Fe-O in the two different crystalline Fe_2O_3 structures. ε-Fe_2O_3has some Fe-O bonds which are much shorter than the Fe-O bonds in α-Fe_2O_3 (evident from the Fe-O bond distances in the FeO_6 octahedral in α-Fe_2O_3 and for three FeO_6 octahedral and one FeO_4 tetrahedral in ε-Fe_2O_3 shown in the ball-stick model of the two polymorphs in Figure 3.6) and thus the band emerge at a higher wave number for the epsilon phase.

Table 3.4 List of FTIR peaks and their assignments

Support	**Peak position (cm^{-1})**	**Assignment**	**Catalyst**	**Peak position (cm^{-1})**	**Assignment**
ZrO_2	413 449 512 577 663 747	Zr-O vibrations	FZO	427 450 522 579 670 688 745	Zr-O vibrations
				579	Fe-O vibrations
CeO_2	550-400 (broad)	Ce-O vibrations	FCO	550-400 (broad)	Ce-O vibrations
				473	Fe-O-Fe deformation
				538	Fe-O stretching
TiO_2	680 (broad)[a] 529 (broad)[b] a and b merged	Ti-O bending vibrations	FTO	670 (broad)[a] 515 (broad)[b] a and b merged 420-400 (broad)	Ti-O bending vibrations
				Intense tail below 670	Vibrations of Fe_2TiO_5
SiO_2	472	Si-O-Si bond vibrations	FSO	472	Si-O-Si bond vibrations
				609	Fe-O stretching
	807	vibrations associated with [SiO_4] tetradedron		806	vibrations associated with [SiO_4] tetradedron
	1111	Si-O-Si bond vibrations		1108	Si-O-Si bond

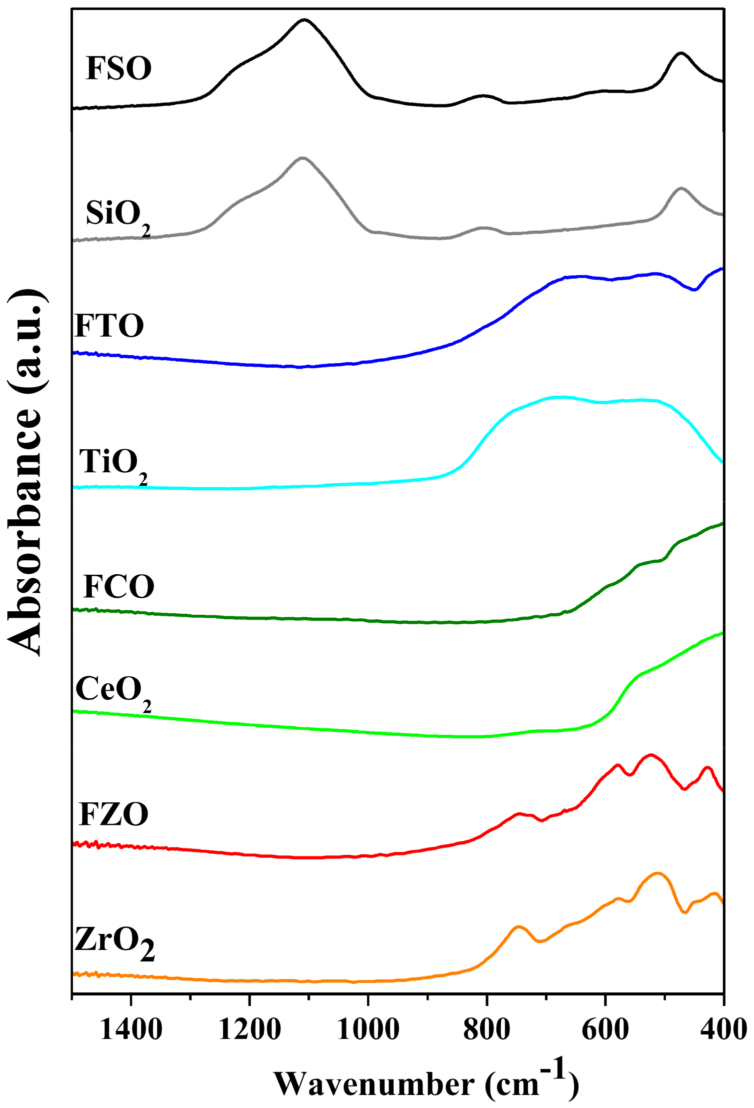

Figure 3.5: FTIR spectra of each support and the dispersed samples

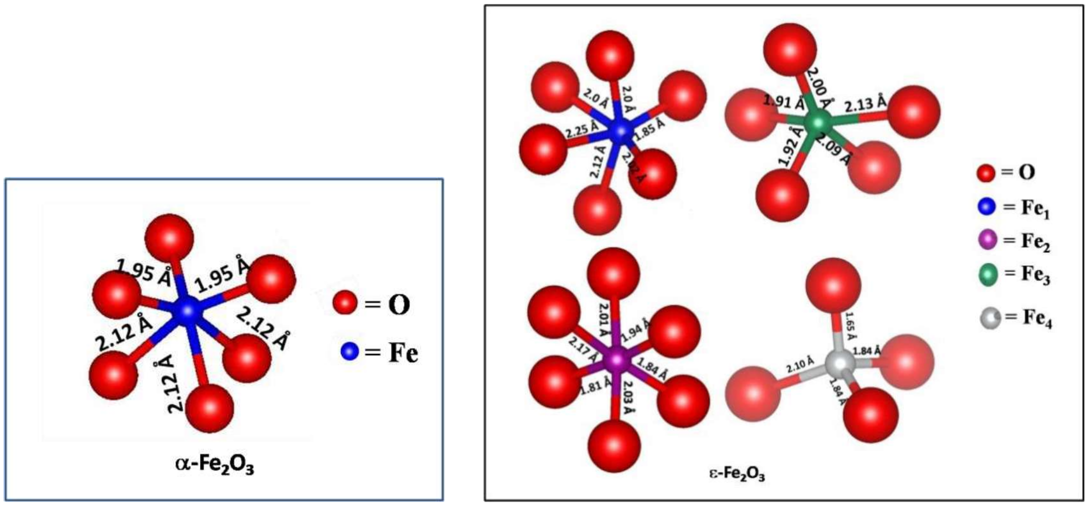

Figure 3.6: Representative Fe-O bond distances in the FeO_6 octahedra and FeO_4 tetrahedral present in α-Fe_2O_3 (ICSD No. 15840) and ε- Fe_2O_3 (ICSD No. 415250).

The Diffuse Reflectance Ultra Violet Visible (DR-UV-Vis) spectra of the prepared hetero structures provided valuable information regarding the microstructural variations in the dispersed iron oxide species present in the samples. From the DR-UV-Vis spectra shown in Figure 3.7, it can be stated, that the UV-Vis absorption for all the samples begins from ~ 205 nm and exhibit a broad absorption extending with prominent intensity well into the visible region. This broad absorption can be attributed to the band gap transition from valence band to conduction band of the crystalline phases of oxides of iron. The absorption spectra for FZO and FCO are almost similar due to the existence of α-Fe_2O_3 phase in these samples and correspondingly similar band structure. In these samples an intense absorption maxima is observed peaking at ~ 550 nm which begins to diminish reaching the minima at ~ 745 nm with a pronounced absorption shoulder at ~ 650 nm. Further, the absorption again increases and a peak appears at ~ 850 nm. FSO exhibits a slightly dissimilar spectrum due to the presence of Fe^{3+} in a different structural environment (ε-phase) than FCO or FZO (α-phase). FSO also displays broad absorption spectra in the visible region but there is a continuous decrease in intensity of absorption from the ~ 520 nm peak without any further intensity increase in the lower energy region. In contrast to the above, the DR-UV-Vis spectrum of FTO was found to be quite different. Mössbauer spectra confirmed that for all the 1000 °C calcined samples the bulk iron is in 3+ oxidation state which for a low spin state have a ground state configuration of $[t_{2g}]^5$ (spectroscopic term - T_{2g}). Any inter-configuration transition is nominal due to the weak spin-orbit coefficient of Fe^{3+} [120-121]. According to Tanabe-Sunago diagram Fe^{3+} in octahedral surrounding can exhibit four d-d transitions:

$^2T_{2g} \rightarrow {}^4T_{1g}$ **(Spin Forbidden)**
$^2T_{2g} \rightarrow {}^4T_{2g}$ **(Spin Forbidden)**
$^2T_{2g} \rightarrow {}^2T_{1g}$ **(Spin allowed)**
$^2T_{2g} \rightarrow {}^2E_{g}$ **(Spin allowed)**

The common feature in all the samples were presence of two weak shoulders over the broad absorption band, one at ~ 220 nm and another at ~ 260 nm. The 220 nm shoulder can be assigned to electron transfer from the free electron pair of oxygen atom (from surface water or OH groups) to the t_{2g} or e_g empty iron orbitals [120].The higher shoulder located higher is probably due to d-d transitions in Fe^{3+} [121]. The rest of the DR-UV-Vis spectra vary depending upon the nature of Fe^{3+} present in the sample.

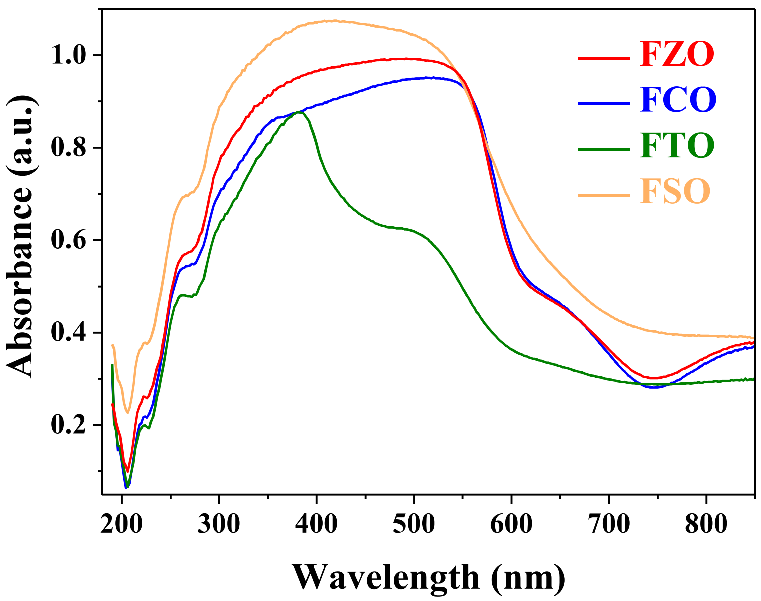

Figure 3.7: DR-UV-Vis spectra of the dispersed Fe_2O_3 samples which are calcined at 1000 °C

3.3.4 Redox Properties Determined by Temperature Programmed Reduction (TPR)

As we can observe from Eqn. 1.8 that sulfur trioxide decomposition, the catalytic step, is a redox reaction, the redox property of the catalyst is bound to impart a vital role with respect to functioning of the catalyst during the reaction. The first cycle TPR profiles of the synthesized catalysts are shown in Figure 3.8 while the powder XRD patterns of the residue obtained after reduction are shown in Figure 3.9. FZO and FCO exhibit TPR patterns typical for α-Fe_2O_3 which generally shows three major peaks corresponding to three reduction steps: Fe_2O_3 to Fe_3O_4 at ~ 400 °C, Fe_3O_4 to FeO at ~ 600 °C and finally FeO to Fe metal at ~ 720 °C, respectively [16]. In FZO the corresponding peak positions were obtained at ~ 450 °C for the first reduction while the second and the third reduction peaks merged and exhibited a peak at ~ 582 °C along with a prominent shoulder at ~ 640 °C. FCO exhibited similar attributes but peaks/shoulders shifted to higher temperature positions and appeared at ~ 473 °C, ~ 600 °C and ~ 690 °C. It is thus evident that although α-Fe_2O_3 crystallized over both ZrO_2 and CeO_2, the reducibility in case of ZrO_2 supported sample was obviously better as compared to CeO_2. In the powder XRD patterns of the residue obtained after TPR (Figure 3.9) we could observe metallic Fe peaks indicating the complete reduction of iron oxide. The mixed oxide Fe_2TiO_5 in FTO was found to be more stable in reducing atmosphere and exhibited one reducing peak at ~ 700 °C. The powder XRD of the residue obtained after TPR pointed the presence on metallic Fe and $FeTiO_3$, suggesting strong interactions between the Fe and Ti components in the mixed oxide or dispersed phase-support which inhibited complete reduction. In the case of FSO, the reduction of ε-Fe_2O_3 dispersed on SiO_2 was found to be entirely different from others. Multiple reduction peaks located at 425, 552 and 729 °C probably due to three reducing paths: Fe^{3+} to Fe^{2+} (with fayalite- Fe_2SiO_4 formation), Fe_2O_3 to FeO and Fe_2O_3/FeO to Fe [90,104]. In fact, the powder XRD of the reduced sample (Figure 3.9) indicated the presence of both metallic Fe and Fe_2SiO_4. The extent of reduction was found to be lower in case of FSO due to reduction restrain imparted by the support SiO_2 owing to strong SiO_2-Fe_2O_3 interactions [90]. Thus, although ease of reducibility was found to be higher in α-Fe_2O_3 dispersed over ZrO_2 and CeO_2 the thermal stability towards reduction was higher in the case of FSO and FTO owning to strong interactions between ferric oxide and support in the case of SiO_2 and TiO_2 inhibiting complete reduction.

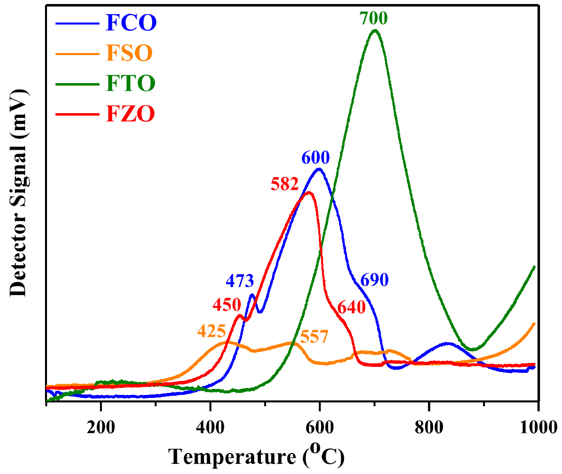

Figure 3.8: Temperature Programmed Reduction profiles of all the synthesized samples

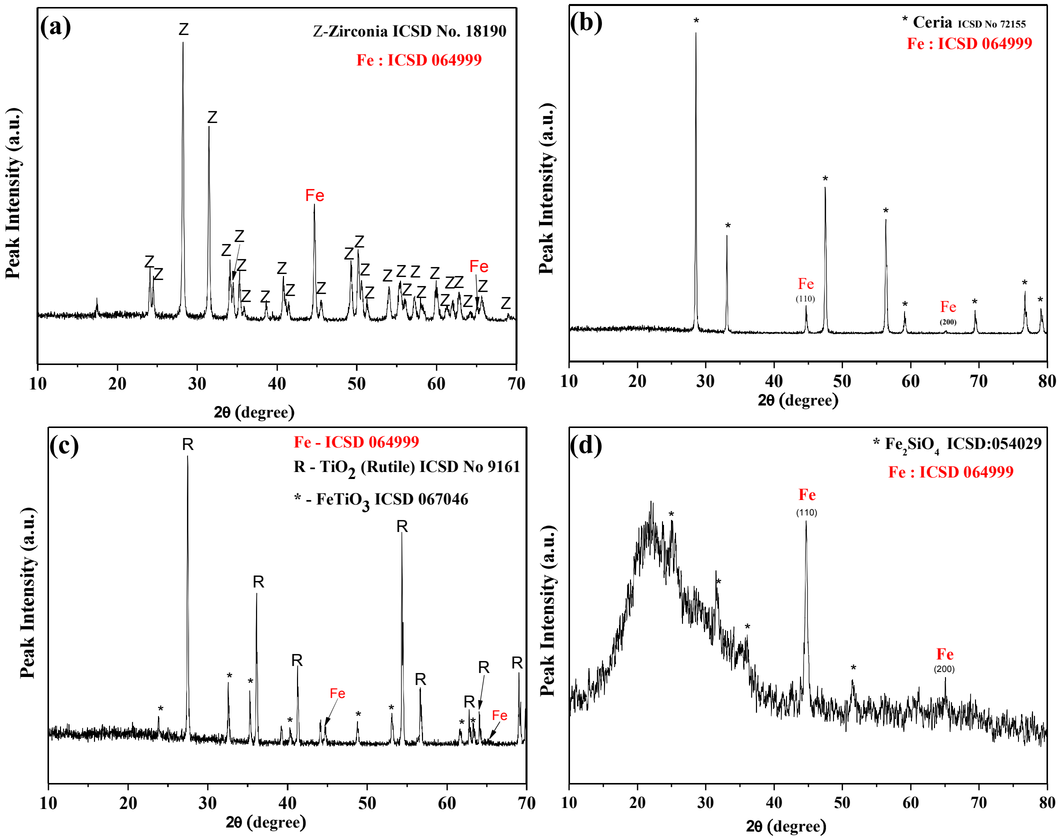

Figure 3.9: XRD patterns of the residues after studying Temperature Programmed Reduction of the catalyst samples

3.3.5 Surface Analysis by X-ray Photoelectron Spectra

The X-ray photoelectron spectra (XPS) and its analysis provided useful surface features. The Fe2p and O1s spectra for all the prepared catalysts are shown in Figure 3.10.The binding energy values observed for Fe2p$_{3/2}$ and O1s and that for each support metal (M of MO$_2$, M= Zr, Ce, Ti and Si) in each sample are listed in Table 3.5. The Fe2p spectra for all the samples exhibited two peaks due to Fe2p$_{3/2}$ and Fe2p$_{1/2}$ with separation of ~ 13.6 eV between them typical for Fe^{3+} [90, 122]. The O1s spectra of the samples however are complicated due to surface oxide ion non-equivalence. The O1s peak maxima appeared at binding energy values of 529.6, 529.8, 529.6, and 532.7 eV for FZO, FCO, FTO and FSO which agreed well with the reported values of O^{2-} present in support phases ZrO$_2$, CeO$_2$, TiO$_2$ and SiO$_2$ [123].In SiO$_2$ the BE appeared at a higher value because of the presence of numerous surface hydroxyl groups or silanol moieties (Si-O-H). In each case, the O1s peak was asymmetric which could be deconvoluted into three components and oxygen for the dispersed and support phases could easily be distinguished. The three components consisted of a central major contribution from oxide ions from the support, a lower binding energy contribution from oxo-anion of the dispersed ferric counterpart while chemisorbed oxides appeared at a higher binding energy [90]. Interestingly, the O1s peak appearing at the lowest B.E. value due to oxo-anion of iron seems to vary in position and shape. This chemical shift confirms that the local chemical environment around the oxide ion in the ferric oxide based dispersed phase varied on the surface. Moreover, the support MO$_2$ imparts significant divergence from ideal iron oxide structures through M-O-Fe bonds and consequently the chemical environment around surface oxide ions vary. The XPS peaks due to core level photoelectron emission from the support metal M (M = Zr, Ce, Ti and Si) are shown in Figure 3.11. The Ce3d region exhibited six peaks not because of multiple oxidation states instead due to mixing of Ce4f and O2p states during the primary photoemission process [123,124]. Due to such phenomenon two sets of multiplets are obtained – designated as u and v in Figure 3.11, which can be assigned to $Ce3d_{3/2}$ and $Ce3d_{5/2}$ respectively. The corresponding electronic configuration for each $3d_{3/2}$ peaks can be assigned as, u1: $Ce3d^9\ 4f^2\ O2p^4$, u2: $Ce3d^9 4f^1\ O2p^5$ and u3: $Ce3d^9 4f^0\ O2p^6$ - all due to Ce^{4+}. The core level Zr3d spectrum showed well resolved asymmetric spin-orbit components with a separation of ~ 2.1 eV between them.The peak position of $Zr3d_{5/2}$ at 181.5 eV was characteristic of Zr^{4+} [125]. The Ti2p spectrum exhibited asymmetric spin-orbit coupled $2p_{3/2}$ and $2p_{5/2}$ peaks with a separation of 5.7 eV confirming the presence of Ti^{4+} [125]. The binding energy of the Si2p peak was ~ 103.2 eV characteristic of Si^{4+} [90,125]. The XPS pattern for each support metal ion M confirmed that they are present in their highest oxidation state (Zr^{4+}, Ce^{4+}, Ti^{4+} and Si^{4+}).

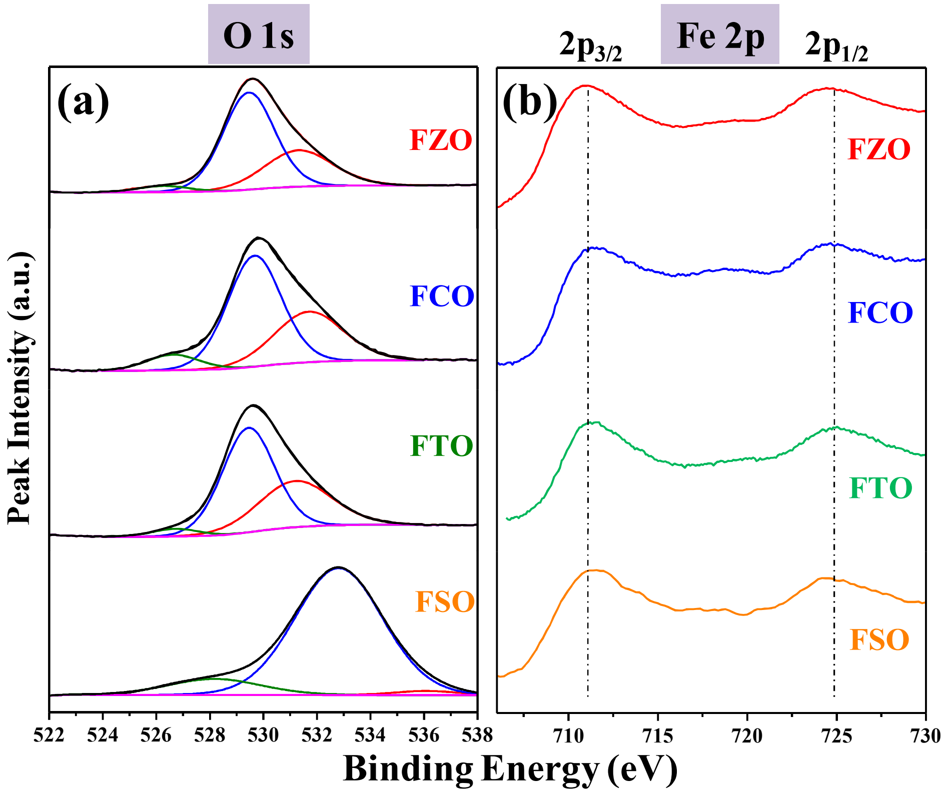

Figure 3.10: X-ray photoelectron spectra of the samples dispersed on different supports

(a) O1s (b) Fe

Table 3.5 XPS core level binding energies of the Fe_2O_3/MO_2 (M = Zr, Ce, Ti and Si) samples

Sample	**Binding Energy(eV)**					
	O$_{1s}$	**Si 2p$_{3/2}$**	**Ti 2p$_{3/2}$**	**Zr3d$_{5/2}$**	**Ce 3d$_{5/2}$**	**Fe 2p$_{3/2}$**
FZO	529.6	--	--	181.5	--	710.9
FCO	529.8	--	--	--	897.6	711.4
FTO	529.6	--	458.1	--	--	711.3
FSO	532.6	103.5	--	--	--	711.5

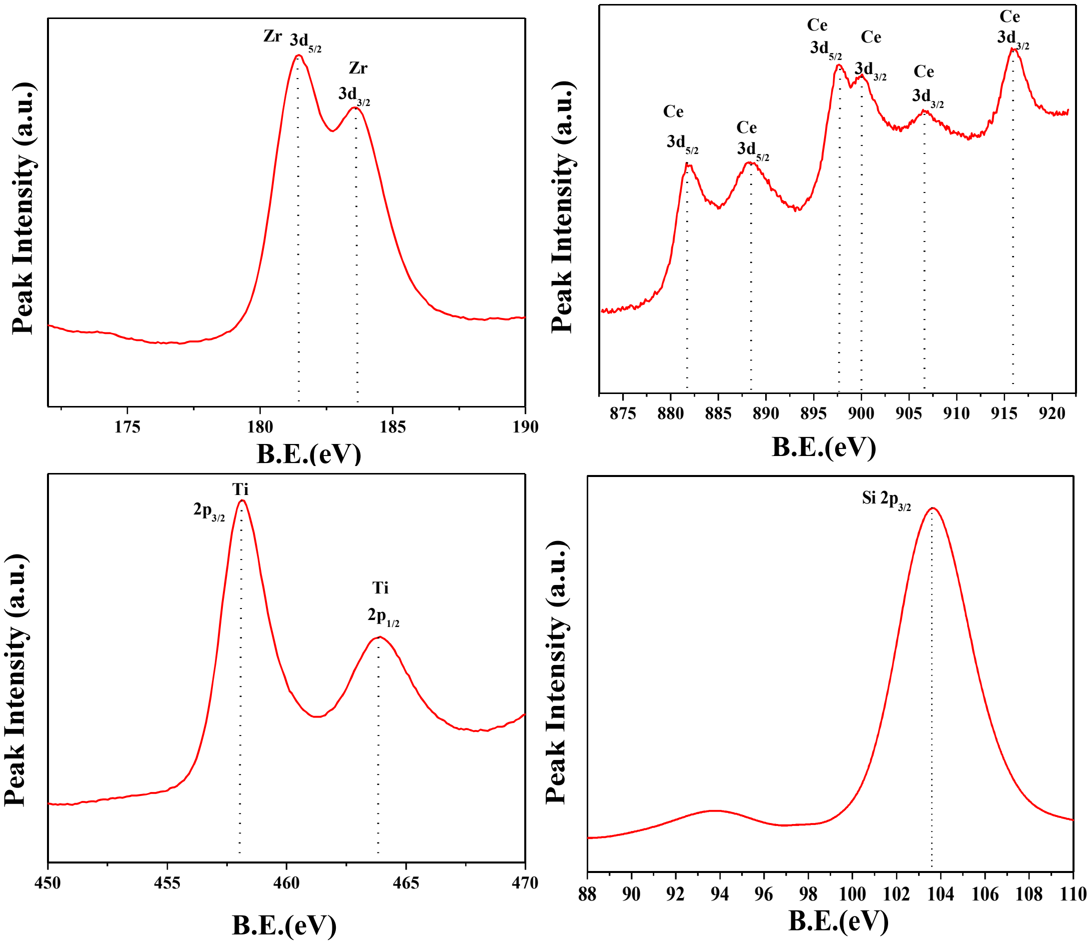

Figure 3.11: X-ray photoelectron spectra of the (a) Zr 3d (b) Ce 3d (c) Ti 2p (d) Si 2p in FZO,FCO, FTO and FSO respectively.

3.3.6 Transmission Electron Microscopy

The transmission electron microscopy (TEM) images of the samples are shown in Figure 3.12. It is evident from the figure that iron oxide of uniform size is homogeneously dispersed over the support phase in SiO_2 while the dispersion in CeO_2 was found to be inhomogeneous with varied particle size and shape. In FTO, the Fe_2TiO_5 dispersion is not visible instead the TiO_2 agglomerated particles are observed. In the case for ZrO_2 proper dispersion was not visible. For this purpose the STEM image of the sample was recorded along with EDX spectra. The STEM image of FZO is shown in Figure 3.13 (a) and the EDX spectra of the marked region in red square (1) is given in Figure 3.13(b) which confirmed the surface presence of Fe, Ti and O. But to understand the surface coverage, the K-level X-ray emission along the red line (1) was recorded and shown in Figure 3.13(c). It is obvious from the line distribution that Fe_2O_3 is distinctly covered over ZrO_2 grains. It is evident from the above that the surface features are found to vary extensively depending upon the type of support although same methodology of preparation has been adopted. Homogeneous dispersion was obtained for high surface area SiO_2 support, non-uniform distribution was found in the case of low surface area CeO_2, while STEM-EDX indicated distinct coverage of Fe_2O_3 over ZrO_2.

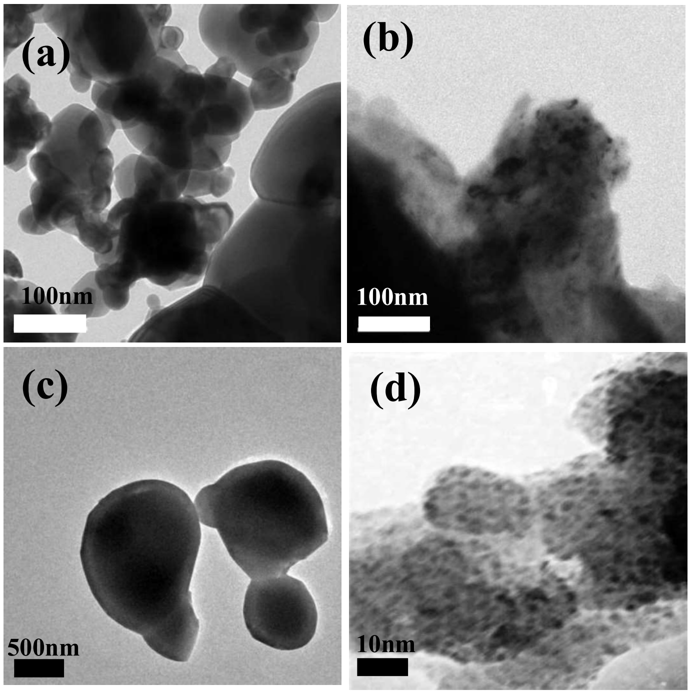

Figure 3.12: Transmission electron microscope (TEM) images of the Fe_2O_3/MO_2; M = (a) Zr, (b) Ce, (c) Ti and (d) Si samples

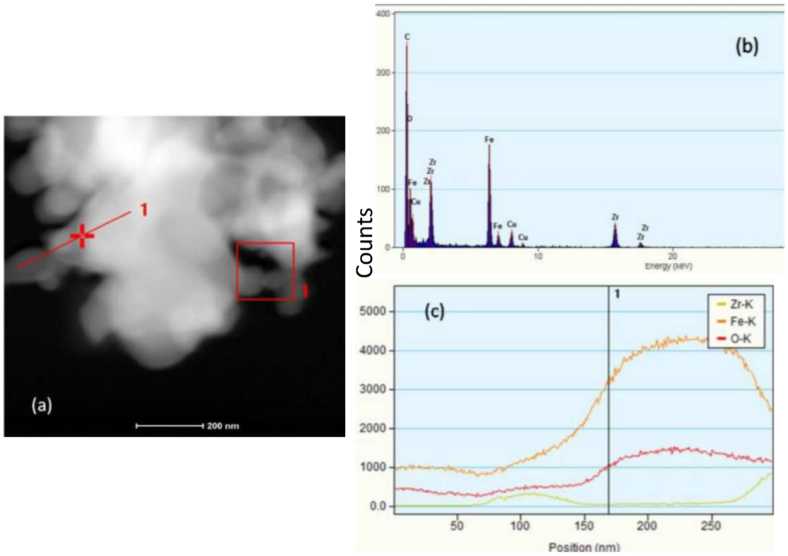

Figure 3.13:(a) STEM image of FZO and (b) EDX pattern of the selected region (square 1) and (b) distribution of Fe, Zr and O along the line (line 1) based on the corresponding K-level X-ray emission

3.3.7 Catalytic Activity Evaluation

The temperature dependent catalytic activity for sulfuric acid decomposition (Eqn. 3.4) in the temperature range of 600°C to 900 °C of all the prepared samples calcined at 1000 °C at a WHSV of 27 g acid g^{-1} catalyst h^{-1} are shown in Figure 3.14a. The SO_2 yield values were successfully reproduced twice within the experimental error limits. For all the samples the SO_2 yield as determined from Eqn. 3.5 was found to increase with an increase in temperature which was due to increased kinetics at higher temperatures. A maximum SO_2 yield was obtained at 900 °C for each sample which was found to be ~ 91.5%, 82.6%, 86.3% and 87.5% for FSO, FTO, FZO and FCO respectively. As shown in Figure 3.14 the order of SO_2 yield at a low temperature of ~ 750 °C was observed to follow the order FSO > FTO > FZO > FCO. As described in the introduction section sulfuric acid decomposition reaction is the heat extraction step in solar/nuclear thermochemical cycles for hydrogen generation. It is generally proposed to be accomplished at ~ 900 °C depending upon the temperature of the coolant in the nuclear reactors or intermediate heat exchangers in solar thermal heliostat field. On this basis the order of usefulness of each catalyst can vary depending upon the operational temperature. However, at the highest recording temperature of 900 °C the SO_2 yield was found to be comparable for all the catalyst (Figure 3.14).

Sulfuric acid dehydration to sulfur trioxide (SO_3) (Eqn. 3.2) is kinetically fast and instantaneously reaches at 100 % conversion on reaching the thermodynamically feasible temperature while the decomposition of SO_3 (Eqn. 3.3) is kinetically controlled [90]. Each catalyst seems to improve the kinetics of this SO_3 decomposition and can be considered to be an irreversible first-order reaction depending upon the concentration of SO_3. Applying the integral method of reaction analysis as done by Kondamudi and Upadhyayula, an attempt was made to determine the activation energy for the reaction in presence of the various catalysts by using the Arrhenius rate equation [94]:

$$ln\{ln(1|(1-X))\} = ln\left[A_o \frac{W}{F_{SO_3}}\right] - \frac{E_a}{R}\frac{1}{T} \text{----------------------(3.6)}$$

The plot of ln{ln[1/(1-X)} vs 1/T provided us the activation energies from the above equation (shown in Figure 3.14b) and were found to be 83.5 kJmole^{-1} for FSO, 108.4 kJmole^{-1} for FTO, 153.9 kJmole^{-1} for FZO and 198.3 kJmole^{-1} for FCO. Thus, substantial catalytic performance is observed for FSO and FTO followed by FZO and least catalytic activity by FCO.

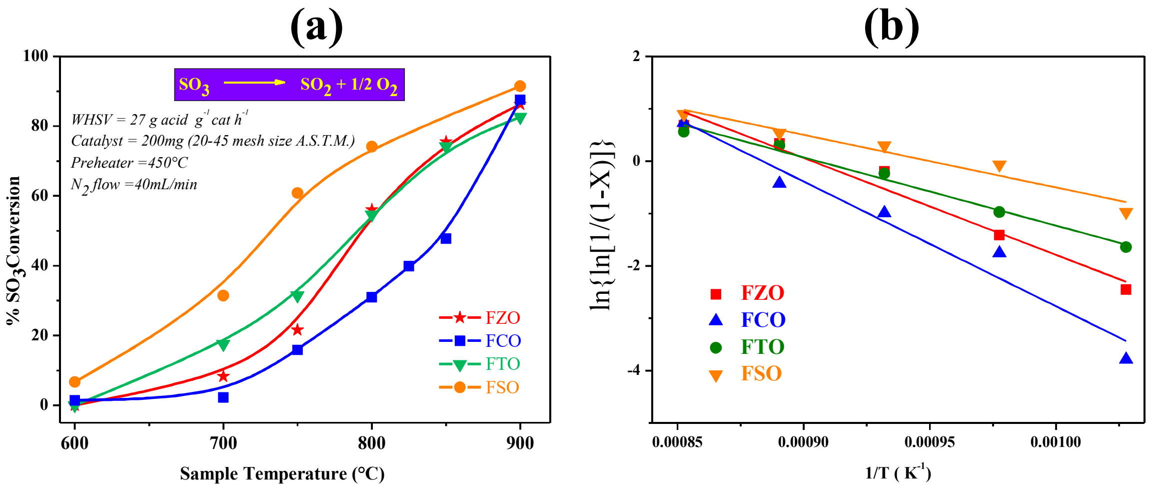

Figure 3.14(a) Effect of temperature on the catalytic activity and (b) Arrhenius plot of FZO, FTO, FCO and FSO samples for sulfuric acid decomposition reaction

3.3.8 Mechanistic Investigations and Role of Support:

The catalytic activity trend as observed from the above measurements could be co-related with the structure, morphology or other specific properties of the catalyst if we have proper understanding of the functioning of the catalyst via intermediates i.e. idea regarding the mechanism of the reaction. Generally *in-situ* techniques (*in-situ*-FTIR etc) [126] are employed to exactly determine the reaction intermediates but due to high operational temperature and corrosive environment we have to adopt an indirect approach. It has been discussed from the mechanistic investigation in our previous articles that sulfuric acid decomposition most probably proceeds over oxide catalysts by the formation and decomposition of the corresponding sulfates [14, 34, 84-85]. Moreover, a similar sort of mechanism was found to be operational over supported iron oxide catalyst viz. Fe_2O_3/SiO_2 as discussed in our last article [86]. If sulfates are considered as an intermediated in supported iron oxide catalyst a concerted mechanism of sulfate formation and decomposition can be suggested. For this purpose, each support material and the catalysts were sulfated in the catalyst zone of the flow through quartz catalytic reactor (shown in Figure 2.16) at 500 °C for 15-20 minutes with a N_2 flow (40 mlmin^{-1}) and sulfuric acid pumping (0.05 mlmin^{-1}). The sulfated support and catalysts were investigated as an attempt to recognize if sulfates can act as intermediates and consequently determine the most probable mechanism.

The powder XRD patterns of the sulfated supports and catalysts are shown in Figure 3.15. It is evident from the figure that sulfation has been accomplished in ZrO_2, CeO_2 and TiO_2 while SiO_2 remained unsulfated.

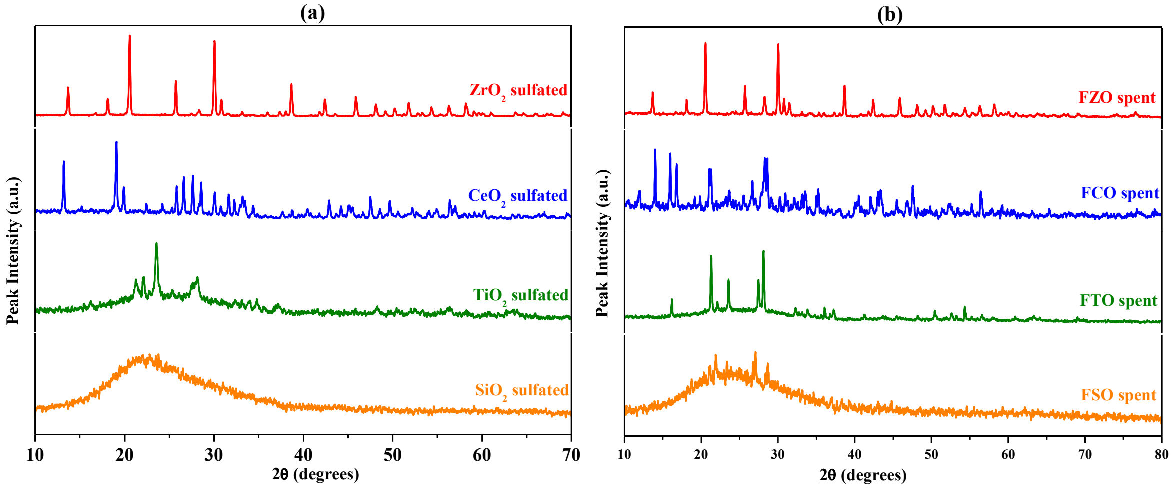

Figure.3.15: XRD patterns of the (a) sulfated support and (b) sulfated catalysts

The DTG pattern of the sulfated support is shown in Figure 3.16a. The thermal decomposition of sulfated zirconia support occurs to regenerate the oxide in a single step, in addition to the low-temperature water removal peaks at 147 °C and 282 °C. The peak at 727 °C corresponds to the conversion of zirconium sulfate to zirconia (Eqn 3.7) [127-128].

$$Zr(SO_4)_2 \rightarrow ZrO_2 + 2SO_2 + O_2 \text{------------} (3.7)$$

Cerium sulfate instead decomposes in two steps for its complete conversion to ceria (Eqn. 3.8-3.9) via the formation of the adduct $CeO_2.Ce(SO_4)_2$ and consequently two peaks are evident – the first one at 516 °C due to the formation of the adduct (Eqn 3.8) and another at 811 °C due to the decomposition of the adduct (Eqn. 3.9)[129].

$2Ce(SO_4)_2 \rightarrow CeO_2.Ce(SO_4)_2 + 2SO_2 + O_2$----------------(3.8)

$CeO_2.Ce(SO_4)_2 \rightarrow 2CeO_2 + 2SO_2 + O_2$ -------------------(3.9)

$Net\ Reaction: 2Ce(SO_4)_2 \rightarrow 2CeO_2 + 4SO_2 + 2O_2$-----------------(3.10)

Titania forms titanium oxysulfate in presence of sulfuric acid vapors and it exhibited peaks in its DTA decomposition pattern, primarily due to the water removal and sulfate decomposition producing titania. The major peak appeared at 624 °C.

$TiOSO_4 \rightarrow TiO_2 + SO_2 + 0.5O_2$-----------------(3.11)

Interestingly SiO_2 remained unsulfated under the same conditions as evident from the corresponding powder XRD (no difference in XRD pattern of SiO_2 support and sulfated support) and TG-DTA patterns (no weight loss or any exothermic/endothermic peaks).

The catalysts which were sulfated under similar conditions as that of the support were investigated for thermal decomposition and the DTG patterns are shown in Figure 3.16b. The decomposition profiles of the catalysts and the corresponding support varied considerably. The sulfated FZO catalyst exhibited a similar DTG pattern as that of support but a shoulder appeared between 600- 660 °C region. The main peak can be ascribed to the zirconium sulfate decomposition while shoulder can be attributed to the thermal decomposition of sulfate of the dispersed iron sulfate. The spent FCO displayed an additional peak at ~ 650 °C as compared to its bare sulfated support decomposition, which can be attributed to the decomposition of the sulfate of iron dispersed on CeO_2. Further, the CeO_2 support decomposition temperatures shifted from 516 and 811 cm^{-1} to lower temperatures of 509 and 794 °C for the two peaks due to cerium sulfate decomposition. In FTO a single peak could be detected probably due to mixed sulfate decomposition (ferric sulfate and titanium oxysulfate) at ~ 650 °C. For FSO two lower temperature peaks appeared (~ 126 °C & 256 °C). The first peak was due to moisture loss but assignment of the second peak was difficult and might be ascribed to SO_3/SO_2 removal from weakly held surface sites. A prominent peak at 640 °C can be attributed to the dispersed iron sulfate decomposition.

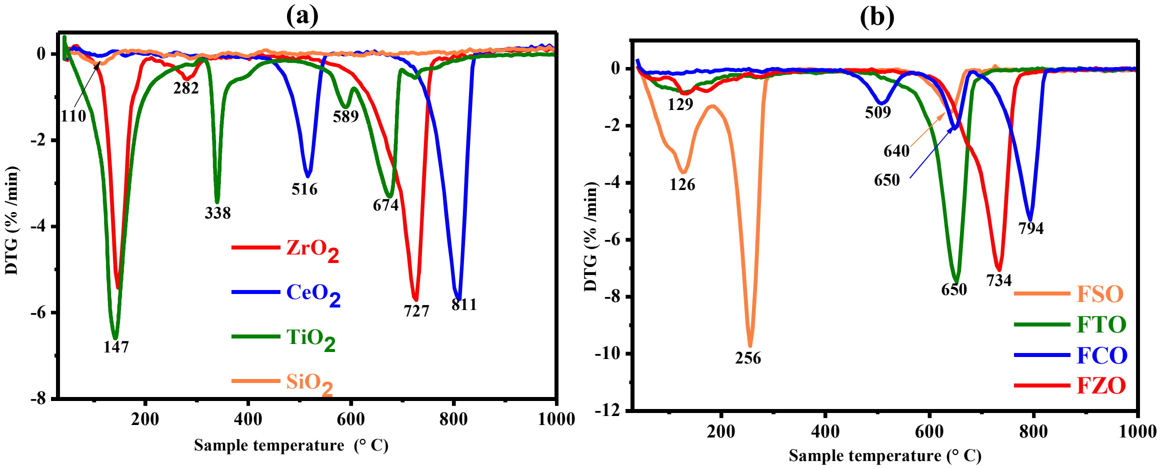

Figure 3.16: DTG patterns of (a) sulfated supports and (b) the sulfated catalyst samples

From the investigations of the sulfate decomposition profiles of the support and catalyst a probable decomposition mechanisms that might be operating can be proposed for individual catalysts and are shown in

Figure 3.17. For each catalyst at high temperature, the active ferric oxide species loses surface oxygen to form the non-stoichiometric oxide with surface oxygen vacant sites, but the dispersed ferric counterpart varies as α-Fe_2O_3 in FZO and FCO, Fe_2TiO_5 for FTO and ε-Fe_2O_3 in the case of SiO_2. These sites act as the active site for chemisorptions of SO_3 molecule forming the corresponding sulfate. The sulfate decomposes producing SO_2 and regenerating the active dispersed oxide. But, for every catalyst the support is also sulfated with the exception of SiO_2. For FSO the crystal structure of dispersed phase was ε-Fe_2O_3, having uniform dispersion, active phase (Fe_2O_3) sulfation but no support sulfation. Here, the role of SiO_2 was to provide stability to the uniformly dispersed nanoparticulate Fe_2O_3 phase [90]. It itself remained inert towards sulfation but provided active sites for sulfated Fe_2O_3 for lower temperature decomposition (640 °C). In FTO the mixed phase Fe_2TiO_5 was formed with sulfation of both active phase and support with a common decomposition peak temperature of 650 °C. Again, for FZO and FCO, α-Fe_2O_3 active phase was dispersed and was sulfated along with support with sulfate decomposition temperatures of ~ 650 °C for dispersed phase and 734 °C and 794 °C for sulfated support.

If we consider the catalytic sulfuric acid decomposition at 900 °C proceeding through the mechanistic pathway as described in Figure 3.17, then it is obvious that both dispersed phase and support undergoes metastable sulfate formation (sulfate decomposition temperature in DTG well below 900 °C for each support/dispersed component) which immediately decomposes to regenerate the oxide catalyst and support. At this temperature the sulfate decomposition step for every catalyst are kinetically fast and comparable rendering comparable SO_2 yield at 900 °C. At low temperature of ~ 750 °C the sulfate decomposition does not proceed fast, instead becomes rate determining. The iron sulfate decomposition for FSO was lowest (640 °C) and there was no support sulfation and decomposition yield was maximum. For FTO, FZO and FCO both support and active phase were sulfated and the decomposition temperature of the ferric part was comparable (~ 650 °C). The order of activity followed the temperature of decomposition of the support part (FTO ~ 650 °C, FZO ~ 734 °C and FCO ~ 794 °C). It is thus obvious that support plays a crucial role in the catalytic decomposition of sulfuric acid over dispersed iron oxide. If the sulfate decomposition temperature of the ferric component is less superior yield is obtained. Otherwise, the support performs a vital task of participating in the reaction mechanism and its ease of decomposition dominates the reaction yield at low temperature. Stable support sulfates seem to impart a retarding effect to the progress of the reaction at lower temperatures. Thus, the sulfate decomposition step acts as the rate determining for the overall reaction and even facile support sulfate decomposition facilitate the decomposition.

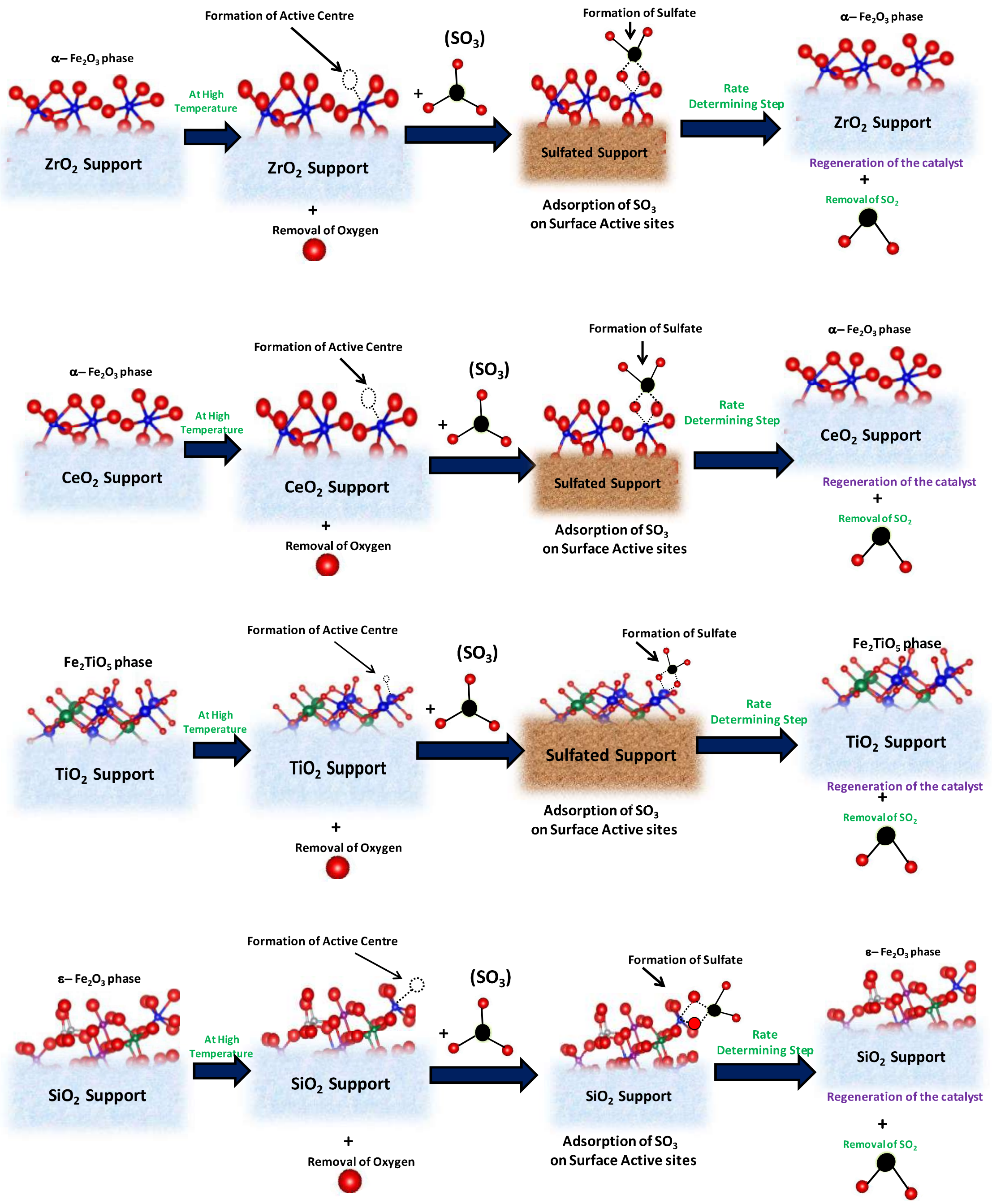

Figure 3.17: Schematic representation of the most probable reaction mechanism proposed for sulfuric acid decomposition reaction.

3.4 Conclusion:

Dispersed iron oxide based catalysts on CeO_2, ZrO_2, TiO_2 and SiO_2 were successfully prepared using an adsorption-equilibrium method. The support was found to play a key role on the nature of active species that evolved. CeO_2 and ZrO_2 yielded α-Fe_2O_3 dispersed phase while ε-Fe_2O_3 was formed over SiO_2 and interestingly a mixed oxide Fe_2TiO_5 phase crystallized in the case of TiO_2 support. Strong interaction between ferric oxide and support was observed in the case of SiO_2 and TiO_2 which stabilized the ferric component and inhibited its complete reduction in TPR studies. The microstructure as observed from TEM images were found to vary considerably for the samples with uniform dispersion in case of SiO_2, non-uniform coverage for CeO_2 while homogeneous surface coverage of Fe_2O_3 over the ZrO_2 support. The catalytic activity at 750 °C was found to follow the order: $Fe_2O_3/SiO_2 > Fe_2TiO_5/TiO_2 > Fe_2O_3/ZrO_2 > Fe_2O_3/CeO_2$ while comparable at 900 °C. The sulfated catalysts and supports were investigated for thermal decomposition of the sulfate species which was found to be intimately related to the catalytic activity. The reducibility of iron oxide in ceria and zirconia supported catalyst was found to be better in case of latter and this phenomenon could be attributed to the stronger Fe_2O_3-CeO_2 interaction. The catalytic activity of these catalysts for sulfuric acid decomposition reaction, however, depended largely on the stability of surface sulfate species that again is dependent on the nature of support. Thus, there exists active component-support interaction which plays crucial role on the catalytic properties. The most promising catalyst Fe_2O_3/SiO_2 is further evaluated in more details and discussed in the next chapter.

Chapter 4: Investigations on sulfuric acid decomposition reaction over silica supported iron oxide catalysts: Effect of preparation methodology and loading

4.1 Introduction

With an aim to develop better catalyst for overcoming the issues faced with the bulk catalyst on using as the rate enhancer for the most energy demanding sulfuric acid decomposition reaction step amongst the sulfur-based thermochemical cycle, dispersed catalyst was chosen as a suitable contender. The preparation, characterization and the activity evaluation of the dispersed iron oxide on different supports has been very well explained in the chapter 3. The hypothesis of dispersing the active component i.e. Fe_2O_3 on a stable support was to bring out the promising constituent in the most efficient manner to achieve greater efficiency for the prior mentioned chemical reaction. In the previous chapter 3, the study on role of different support for the iron oxide in the sulfuric acid decomposition reaction showed up the best with SiO_2 as the ideal support. In this chapter, the effect of loading of the active component on the activity parameter was envisaged to find out the optimal loading required. Apart from that, description of the effect of different methodologies to bring about the dispersion of the Fe_2O_3 on the silica support and their characterization along with activity evaluation will be discussed in this particular chapter.

4.2 Experimental

4.2.1 Preparation of 5, 10, 15 and 20 wt.% Fe_2O_3/SiO_2 Catalysts

The immobilization of Fe_2O_3 phase on SiO_2 (Evonik, Aeroperl 300/30) was carried out by an adsorption-equilibrium method or more appropriately by adsorption on SiO_2 and simultaneous hydrolysis of Fe(III) acetylacetonate as described schematically in Figure 4.1 [102-104]. In brief, SiO_2 was well dispersed in 1-propanol by magnetic stirring and the pH of the solution was adjusted to 10 by adding NH_4OH. The temperature of this solution was maintained ~ 0 °C by cooling with ice. A Fe(III) acetylacetonate solution was prepared with appropriate stoichiometry (so that the final product yields 5 weight % Fe_2O_3 in SiO_2) in a 1:1 water and 1-propanol mixture (solution A). Solution A was then added dropwise to the ice cooled solution of SiO_2 in NH_4OH. The mixed solution was aged overnight, filtered, the product washed several times with water and ethanol and dried in an air oven at 100 °C overnight. This is the Fe_2O_3 (5 wt.%)/SiO_2 as synthesized (FSO5as) product. The product was first calcined at 500 °C for 4 h in air (FSO5-500) and then appropriately treated to either obtain the Fe_2O_3 (5 wt.%)/SiO_2 (FSO5) catalyst or synthesize higher Fe_2O_3 content compositions as shown in Figure 4.1.

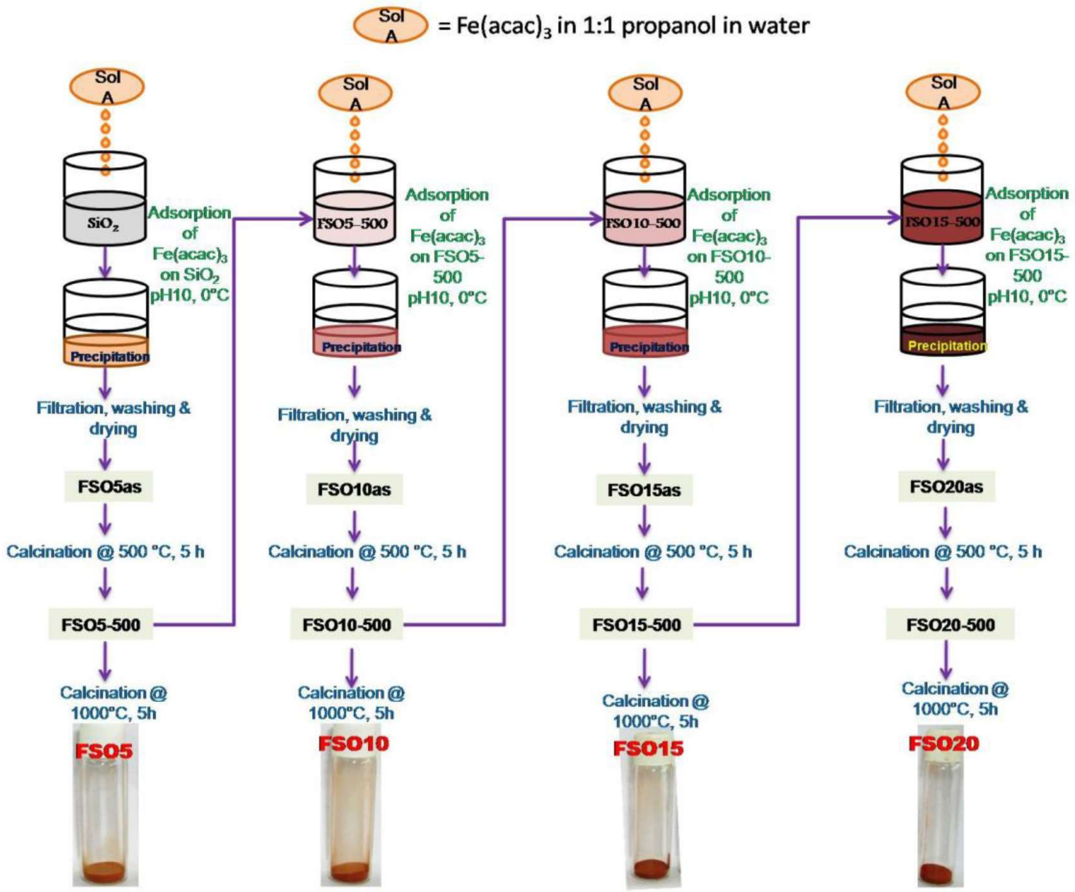

Figure 4.1: Schematic representation of the preparation method of Fe_2O_3/SiO_2 catalyst with varying composition

To prepare the Fe_2O_3 (5 wt.%)/SiO_2 sample, the 500 °C calcined sample (FSO-500) was further heated at 1000 °C for 5 h to get the final product (FSO5). To synthesize the Fe_2O_3 (10 wt.%)/SiO_2 sample, the above method was repeated by replacing SiO_2 with the 500 °C calcined Fe_2O_3 (5 wt.%)/SiO_2 sample (FSO5-500) as shown in Figure 4.1. Similarly to prepare the Fe_2O_3 (15 wt.%)/SiO_2 sample, Fe_2O_3 (10 wt.%)/SiO_2 was used instead of SiO_2 and so on. The final product in each case was calcined at 1000 °C for 5 h to yield the functional catalyst. Heating rates for the calcination steps were maintained at 5 °C min^{-1}.These catalysts, hereafter, are referred as FSOX, where, X represents the weight percent of iron oxide in the dispersed sample.

4.2.2 Preparation of Fe_2O_3/SiO_2 Catalysts by Polyol, Wet Impregnation and Solvothermal Route

In order to overcome the complexity of the preparation method observed in equilibrium adsorption method efforts were made to seek for uncomplicated dispersing technique. So the dispersed samples were further prepared in three more methods such as polyol, wet impregnation and solvothermal treatment as shown in Figure 4.2. In case of polyol method iron acetyl acetonate was refluxed with silica in ethylene glycol solution for 6 h at 180 °C in presence of urea as a hydrolysing agent. The precipitate was allowed to stand overnight and later it was filtered through Buchner funnel. After drying in air oven for 4h the solid product was obtained. In wet impregnation method the iron acetyl acetonate dissolved in 1-propanol was added in to the silica support with continuous stirring, later it was dried. In solvothermal treatment method the precursor for iron oxide i.e. iron acetylacetonate, dissolved in 1- propanol was dropped into silica suspended 1-propanol solution whose pH was maintained @10 using NH_4OH. The solution mixture was heated in an autoclave at 150 °C for 6h; after allowing settling the precipitate overnight the solid product was obtained after filtration which was dried in air oven for 4h.

Finally, the dried solid precipitate was calcined at 500 °C for 4 h and later calcined at 1000 °C in air for 5 h.

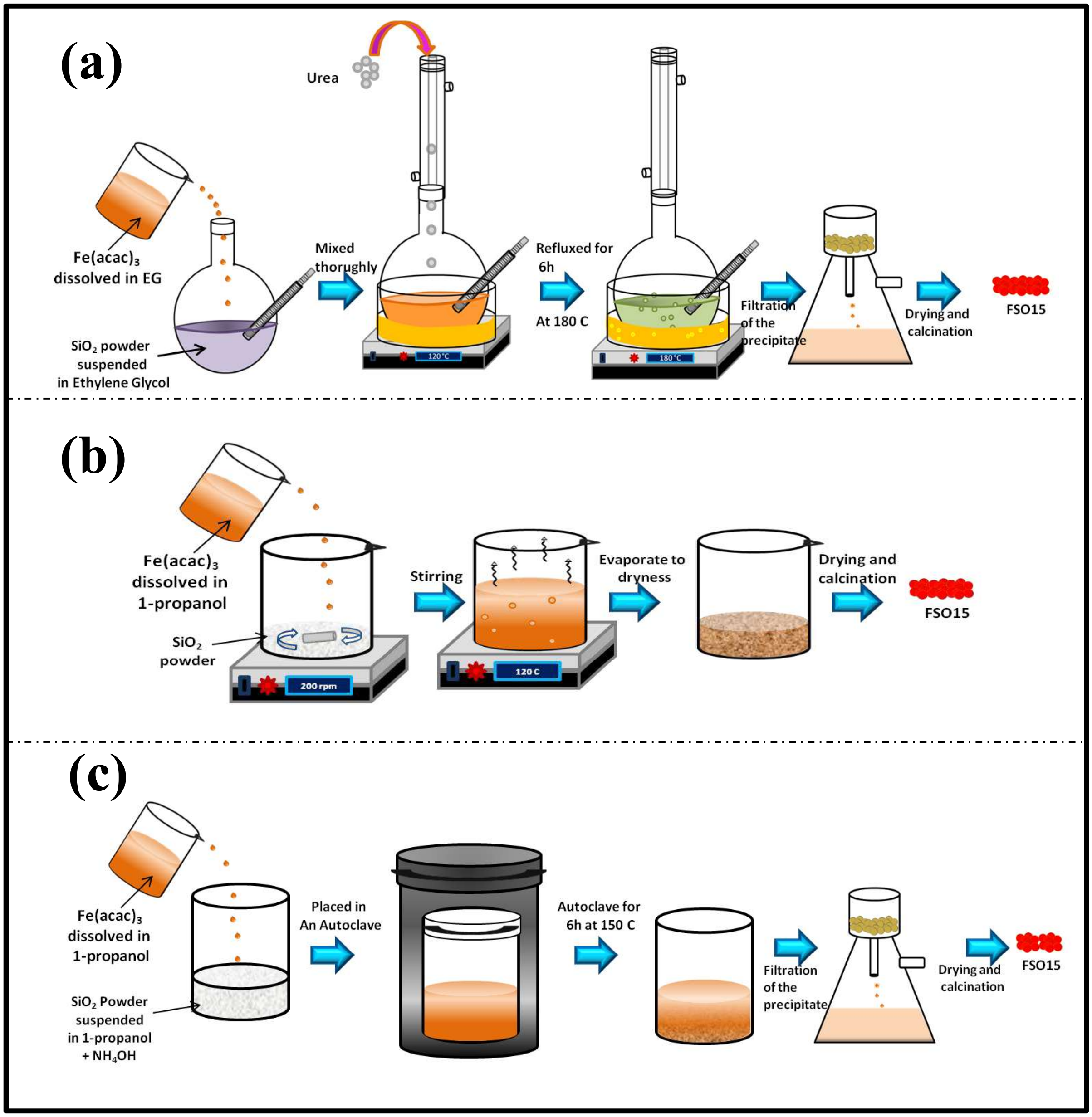

Figure 4.2: Schematic representation of the preparation method of Fe_2O_3/SiO_2catalyst (a) Polyol (b) Wet impregnation (c) Solvothermal Routes

4.2.3 Fresh and Spent Catalyst Characterization

The Fe_2O_3 content in each of the Fe_2O_3/SiO_2 catalysts was estimated using ICP-AES technique after microwave digestion of the powders in conc. HNO_3-HCl (aqua regia). The powder

XRD patterns were recorded on a Philips X'Pert pro X-ray diffractometer using Cu $K_\alpha$radiation (λ= 1.5418 Å) at 40 kV and 30 mA. Micromeretics ASAP-2020 surface area analyzer was employed for measurement of N_2-BET surface area, pore size distribution and pore volume by recording the N_2-adsorption-desorption isotherms. The pore size distribution and pore volume was determined from desorption isotherm using the BJH method. Room temperature Mössbauer spectra of all the samples were obtained using a spectrometer operating in constant acceleration mode in transmission geometry. The source employed was Co in Rh matrix of strength 50mCi. The calibration of the velocity scale was carried out using iron metal foil. The outer line width of calibration spectra was 0.29 mm/s. The Mössbauer data was analyzed using a least square fitting programme. The redox properties of the samples as a function of temperature were determined by measuring the temperature programmed reduction/oxidation (TPR/O) using gas mixtures of 5% hydrogen in argon and 5% oxygen in helium for TPR and TPO respectively in TPDRO-1100 analyzer (Thermo Quest, Italy). The samples were pretreated at 350 °C in helium for 3 h prior to each run. The morphological features were analyzed by recording the High resolution TEM (HR-TEM) images in a FEI-Tecnai G-20 microscope operating at 200 kV. The spent catalyst was also analysed by XPS, SEM, HRTEM and Mössbauer spectroscopy to identify the morphological and structural changes arising out due to the 100 h catalytic operation in sulfuric acid decomposition reaction. To understand the nature of stable species produced on the catalyst during decomposition of sulfuric acid, the spent catalyst sample was heated in the temperature range of 400-1000 °C at a heating rate of 10 °C/min in a TG-DTA thermobalance and the evolved gases were analyzed by a QMS coupled to the TG-DTA, (SETSYS Evolution-1750, Setaram).

4.2.4 Catalytic Activity Measurements

The catalytic activities of all the dispersed samples were evaluated in a flow through quartz catalytic reactor (shown in Figure 2.16). Concentrated sulfuric acid (98 wt.%) was loaded in a 50 ml syringe and injected into a quartz preheater at a flow rate of 0.05 mlmin^{-1} held at 450 °C. In the preheater liquid sulfuric acid is converted to sulfur trioxide and steam by vaporization and dehydration. To carry this gas mixture into the catalyst zone N_2 gas was used as a carrier at a flow rate of 40 ml min^{-1}. In the catalyst zone, sulfur trioxide decomposition occurs to produce sulfur dioxide and oxygen. 200 mg of the catalyst was loaded in the catalyst zone and the temperature of the zone was maintained with a temperature controller. After exiting from the catalytic reactor, the products along with the unreacted reactants proceeds to the condenser where unreacted sulfuric acid is condensed and the sulfur dioxide is later trapped in a sodium hydroxide solution and measured using chemical titrimetric methods. The catalytic activity was quantified by the extent of SO_2 yield defined as:

$$Percentage\ SO_2\ Yield = \frac{No.of\ moles\ of\ SO_2\ produced}{No.of\ moles\ of\ H_2SO_4\ in\ feed}\ \text{X}\ 100\text{----------}(4.1)$$

The catalytic activity of all the Fe_2O_3/SiO_2 catalysts (40-80 mesh; ASTM) was measured as a function of temperature between 700-900 °C at a WHSV of 27 g acid g^{-1} h^{-1}. Prior to each run the catalyst was degassed at a temperature of 500 °C for 2 h at a N_2 flow rate of 40 ml min^{-1}. To achieve equilibrium the catalyst was held at each temperature for 30 mins and then measurement was initiated. Several measurements were made in ~ 2 h duration kept at each temperature.FSO15 exhibited highest temperature dependent catalytic activity as discussed in details later. Further, to get a quantitative measure of the diffusion limitation in the most active catalyst composition, the SO_2 yield was evaluated at 800 °C with FSO15 catalyst for three different catalyst particle sizes 45-80 mesh, 20-45 mesh and 10-20 mesh. Finally, to determine the stability of the most active catalyst, a 100 h time on stream performance for sulfuric acid decomposition was evaluated for the FSO15 (20-45 mesh) and the catalyst was recovered and spent catalyst characterized.

4.3 Results and Discussions

4.3.1 Effect of Loading

4.3.1.1 Efficacy of the Method of Preparation

The immobilization of Fe_2O_3 on SiO_2 was carried out by the adsorption equilibrium method as shown in Figure 4.1 [98-100], which involved drop wise addition of Fe(III) acetylacetonate (Solution A) to an ice cooled alkaline solution (precipitant) of suspended SiO_2. The chemical process involved the hydrolysis of the Fe(III) acetylacetonate (catalyst precursor) into Fe-hydroxide (the precipitate). The insoluble precipitate is immobilized (adsorbed) onto the support which is generated slowly in solution (equilibrium), and subsequently its concentration is raised homogeneously. Under vigorous agitation of the suspended SiO_2 solution, a rapid distribution of the precipitant-precursor is ensured and precipitation occurs homogeneously while hydrolysis of the bulky precursor at low temperature ensures slow generation of the precipitate. To analyze the complete hydrolysis of iron acetylacetonate and immobilization of iron oxide species, the thermo-gravimetric analysis of the Fe(III) acetylacetonate ($Fe(acac)_3$), the as-synthesized 5 wt. % sample (FSO5as) and the 500 °C calcined sample (FSO5-500) was recorded and the TG pattern is shown in Figure 4.3. The Fe(III) acetylacetonate undergoes thermal decomposition with onset of weight loss at ~ 170 °C. The decomposition products were analyzed by recording the FTIR spectra of the evolved gases *in-situ*. The evolution of CO_2 and acetone was observed at 305 °C and 597 °C respectively (Figure 4.4) which is in agreement with reported literature [126]. The as-synthesized and the calcined 5 wt. % Fe_2O_3 samples did not undergo any appreciable thermal weight loss phenomenon and neither any gas was detected in the outlet by FTIR, confirming the completion of hydrolysis of iron acetylacetonate.

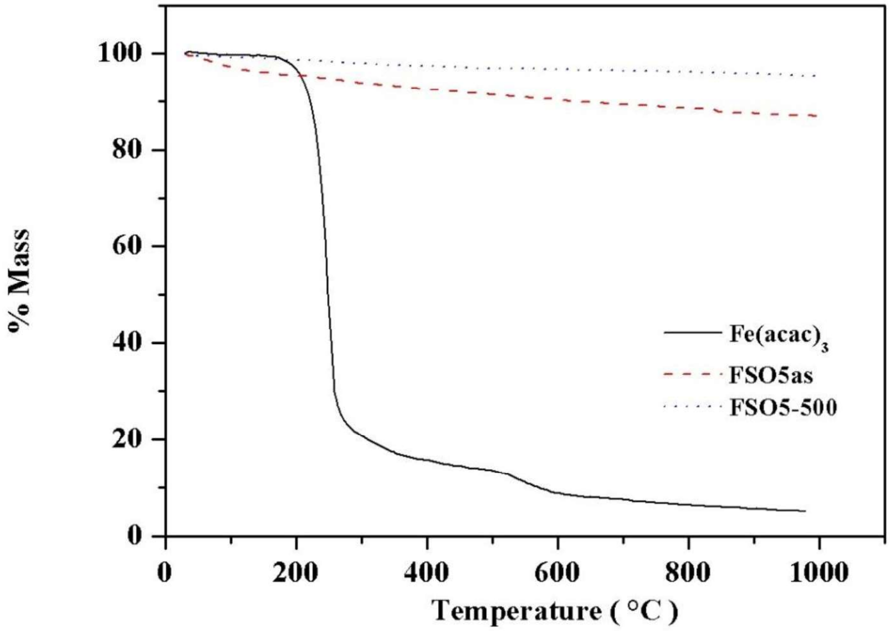

Figure 4.3: Thermogravimetric profile of the Fe(acac)$_3$, the as-synthesized Fe_2O_3(5 wt.%)/SiO_2 and FSO5

To further confirm this aspect it was observed that the FTIR spectra of Fe(III) acetylacetonate showed characteristic peaks due to Tris(2,4-pentanedionato) Iron [131], while, no presence of acetyl acetonate species were observed in the 500 °C calcined sample (FSO5-500) or even in the as-synthesized 5 wt.% dispersed sample (FSOas) (Figure 4.5). Moreover, in FSOas and FSO5-500 a shoulder appears due to the presence of Fe-O bond stretching in iron oxides [89]. This, not only confirms the complete hydrolysis of the Fe(III) acetylacetonate but also formation of iron-oxygen species in the as-synthesized product. Thus, the effectiveness of this process for the preparation of dispersed Fe_2O_3nanoparticles is established.

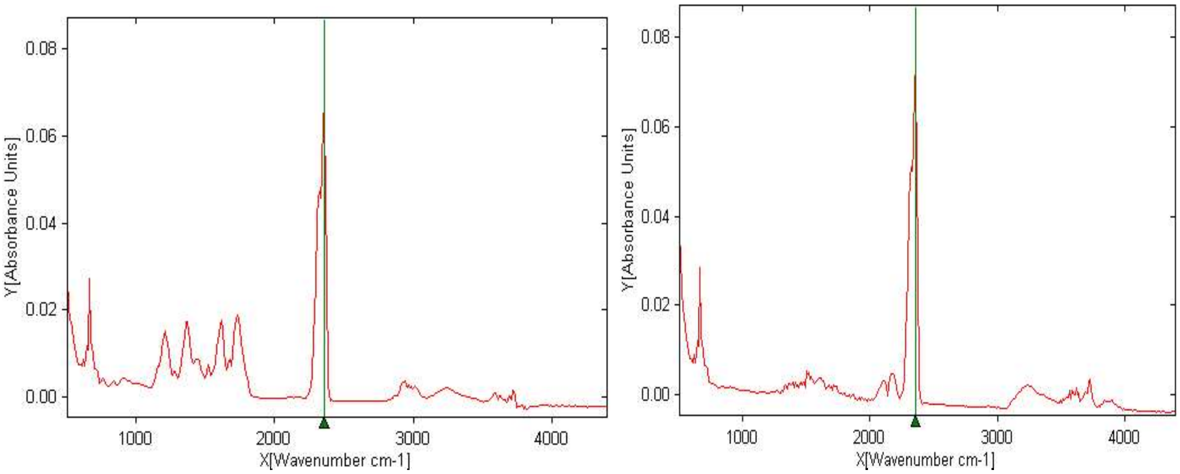

Figure 4.4: The FTIR spectra of the evolved gas as decomposition product of Fe(acac)$_3$ at 305 °C and 597 °C respectively

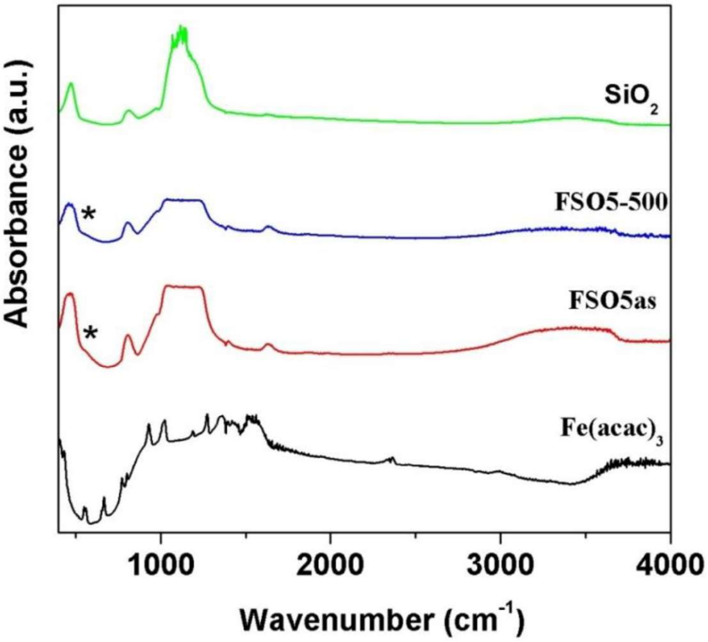

Figure 4.5: FTIR spectra of Fe(III) acetylacetonate(Fe(acac)$_3$), as-synthesized Fe$_2$O$_3$(5 wt.%)/SiO$_2$ (FSO5as) and the 500 °C calcined Fe$_2$O$_3$ (5 wt. %)/SiO$_2$ (FSO5-500) and silica. * indicates the shoulder due to the presence of Fe-O bond stretching

4.3.1.2 Textural Properties of the Catalyst

The composition of the samples synthesized, their abbreviation and the actual amount of Fe_2O_3 (w/w) dispersed on SiO_2 catalysts as determined by elemental composition analysis using ICP-AES technique are listed in Table 4.6. It is evident from Table 4.6 that the samples synthesized contain almost the expected amount of Fe_2O_3, with the exception of the highest composition, where a lower amount of Fe_2O_3 is deposited than expected. A probable cause for such a phenomenon might be that an optimum concentration of Fe_2O_3 on SiO_2 might have reached and excess iron species was unable to get incorporated within the SiO_2 matrix.

Table 4.6 Sample composition of Fe_2O_3 dispersed on SiO_2 with weight percentage (w/w) in parenthesis, sample abbreviation, N_2-BET surface area, pore size and pore volume of the samples

Nominal Sample Composition	**Sample Abbreviation (1000 °C calcined)**	**Actual Composition (ICPOES)**	**N_2-BET Surface Area**	**Pore Size**	**Pore Volume**
Fe_2O_3 wt. % on SiO_2		**Fe_2O_3 wt. % on SiO_2**	**(m^2/g)**	**nm**	**cm^3/g**
SiO_2	SiO_2		249.5	26.9	1.8
Fe_2O_3(5%)/SiO_2	FSO5	4.6	147.6	28.5	1.3
Fe_2O_3(10%)/SiO_2	FSO10	9.8	120.0	29.5	1.1
Fe_2O_3(15%)/SiO_2	FSO15	14.0	99.6	31.8	0.9
Fe_2O_3(20%)/SiO_2	FSO20	17.6	100.9	26.9	0.8

4.3.1.3 N_2 Adsorption-Desorption Isotherm

Table 4.6 also lists the N_2-BET surface area, pore size and pore volume of the samples. As can be seen from the Table 4.6, the BET surface area drops down drastically from 249.47 m^2/g for bare SiO_2 to 147.61 m^2/gas 5 wt. %Fe_2O_3 is deposited on it. This drastic decrease is mainly due to coupled effect of the calcination steps at 500 °C and 1000 °C and the deposition of Fe_2O_3 on SiO_2 surface, thus Fe_2O_3 blocking the surface sites of SiO_2. On further dispersion of the active component Fe_2O_3, on the SiO_2 substrate, a progressive decrease in surface area is observed. Only in the case for the extreme composition FSO20, there is no further decrease in the surface area. The above result possibly signifies that the Fe_2O_3 is well deposited on the surface sites of SiO_2 and a maximum dispersion is probably reached at ~ 15 wt.%.

The N_2 adsorption-desorption isotherm and the pore size distribution plots for these samples (Figure 4.6) exhibits Type-IV isotherm with hysteresis, typical of mesoporous character. It is thus evident that the mesoporosity is retained in all the samples. The pore volume also exhibits a similar trend as surface area and a progressive decrease in its value is observed with an increase in Fe_2O_3 content. Interesting feature is seen in the case of pore size of the samples. Bare SiO_2 exhibits a pore size of ~ 26.9 nm. The pore size increased gradually as Fe_2O_3 was deposited on the SiO_2 surface signifying incorporation of Fe_2O_3 moieties inside the pores and its consequent enlargement to accommodate the nanosized Fe_2O_3 particles. This trend continues till 15 wt.% dispersed samples where a maximum value of pore diameter of ~ 31.8 nm is observed. Thus maximum dispersion of Fe_2O_3 within the pores of SiO_2 took place for the 15 wt. % dispersed sample leading to maximum pore opening. The pore size for FSO20 reverted back to 26.9 nm, a suggestion of Fe_2O_3 agglomeration and enhanced precipitation outside the pore structure of the support. The result indicates that significant amount of Fe_2O_3 remains confined within the mesoporous network of SiO_2 matrix till FSO15. But beyond this composition, Fe_2O_3 mostly precipitates outside the pores of SiO_2 and also agglomerates of Fe_2O_3 blocked the pore openings, since the pore volume, on the contrary, decreased further than FSO15. However, we can conclude from the above studies that the porous network of SiO_2 undergoes significant deformation on the Fe_2O_3 immobilization and the degree of distortion directly depends on the extent of Fe_2O_3 deposited.

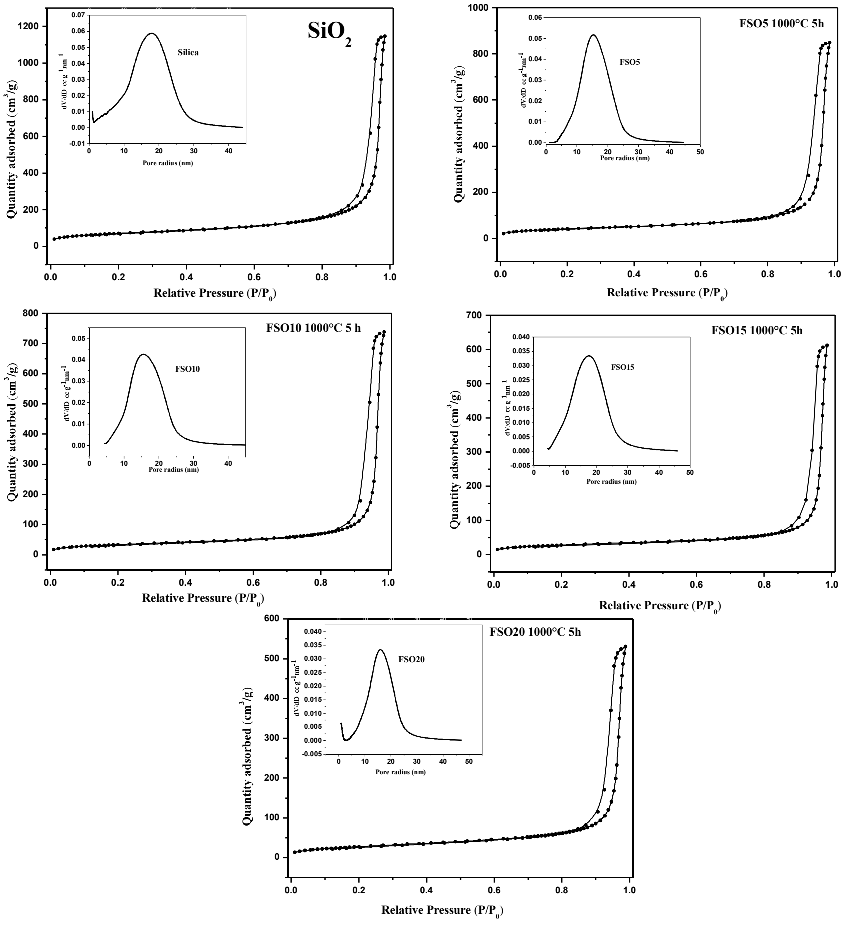

Figure 4.6: N_2 adsorption-desorption isotherm of all the 1000 °C calcined Fe_2O_3/SiO_2 samples along with SiO_2

4.3.1.4 Phase Identification by Powder XRD and Mössbauer spectroscopy

Fe_2O_3 is a well-known polymorph existing in four different crystalline forms: α-Fe_2O_3 (mineral name: hematite, corundum structure, space group $R\bar{3}c$(167)), β-Fe_2O_3(bixbyite structure, space group $Ia\bar{3}$(206)), γ-Fe_2O_3 (mineral name maghemite, spinel structure with disordered vacancies, space group $Fd\bar{3}m$(227), or alternate structures), and ε-Fe_2O_3 (isostructural with κ-Al_2O_3, space group $Pna2_1$(33)) [132-133]. Determination of the Fe_2O_3 phase in a dispersed sample like ours is rather difficult due to its low content and nanocrystalline nature. In fact, structural studies related to phase transformations of Fe_2O_3 dispersed on SiO_2 as a function of temperature is a demanding topic in view of its vast application and separately investigated in recent times [108,132-135]. Phase identification in our Fe_2O_3/SiO_2 dispersed samples was first attempted by recording and analyzing the powder XRD patterns. The powder-XRD patterns of all the 1000 °C calcined samples are shown in Figure 4.7.The support SiO_2 exhibits a broad hump centered at peak position $2\theta \sim 22$ degrees (mineral name: crystabolite, tetragonal crystal system, Space Group: $P\ 4_12_12$ (92), ICSD No. 47219). Peaks due to Fe_2O_3 were not clearly visible in FSO5 probably due to the low iron oxide phase content. In higher Fe_2O_3 containing samples broad peaks due to various phases appeared. In FSO10 peaks due to ε-Fe_2O_3 phase (orthorhombic crystal system, ICSD No. 415250) were present. In FSO15 and FSO20, minor peaks due to α- and γ- Fe_2O_3 were also visible. The 100 % peak of ε-Fe_2O_3 (ICSD No. 415250); γ-Fe_2O_3 (ICSD No. 172905) and α-Fe_2O_3 (ICSD No. 15840) appeared at peak positions $2\theta = 33.05$, 35.6 and 33.2 degrees respectively. In all the above three samples the peak due to the ε-Fe_2O_3 phase was most prominent and intense signifying that this phase has the major contribution in the 1000 °C calcined samples.

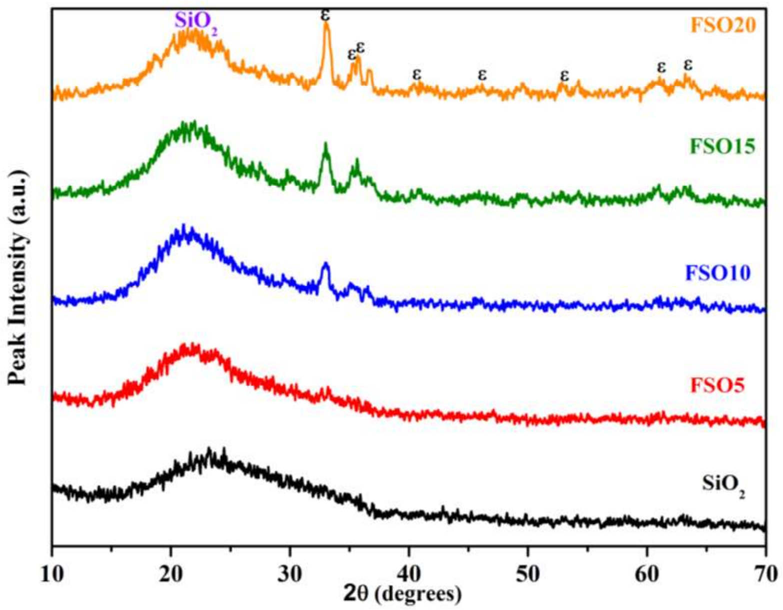

Figure 4.7: Powder XRD patterns of the silica support and 1000°C calcined Fe_2O_3/SiO_2 samples

The crystal structures of the three different polymorphs identified in our sample are shown in Figure 4.8. In our earlier study with bare Fe_2O_3 nanoparticles we obtained α-Fe_2O_3 as the lone crystalline phase upon calcination at 750 °C [89]. In this study, the intensity pattern of powder XRD suggests that this phase might be present in minor quantity. It is one of the most common and the most thermally stable polymorph of Fe_2O_3 and is generally produced by thermal decomposition of a wide variety of iron (II) and iron (III) compounds and also by thermal transformations of other iron oxide polymorphs [134-135]. From Figure 4.8 it is evident that it comprises of a hexagonal close-packed array of oxide ions with ferric ions occupying two-thirds of the octahedral interstices giving rise to eight cations in the first neighbor sphere. Thus all the Fe sites are equivalent. Its rhombohedral unit cell contains six formula unit with lattice parameters of a = 5.036 Å and c = 13.749 Å [16, 89, 108,134-135]. The other common Fe_2O_3 phase is the γ-Fe_2O_3 or maghemite which is also present in minor amounts in the 1000 °C calcined samples. Generally, the lower temperature nanometer sized stable phase is the γ-Fe_2O_3phase and it exhibits superparamagnetism in nanoparticle form [108,135-136]. It exhibits a cubic crystal structure (a = 8.351 Å) of an inverse spinel type with cationic vacancies either randomly distributed (space group $Fd\bar{3}m$) or an ordered vacancy structure (space group $P4_332$ and/or $P4_132$). Thus, Fe occupies two non-equivalent sites. In the current study ε-Fe_2O_3 was obtained as the major phase. This Fe_2O_3 phase is orthorhombic and not as common as the above two with very rare natural occurrence and is generally obtained as an intermediate phase (with intermediate structural features) during the thermal transformation of cubic spinel γ-Fe_2O_3 nanostructured phase to a rhombohedral corundum α-Fe_2O_3 polymorph when dispersed over SiO_2 [128-131]. ε-Fe_2O_3 exhibits an orthorhombic crystal structure with a space group of $Pna2_1$ and lattice parameters a = 5.072 Å, b = 8.736 Å, c = 9.418 Å. The structure consists of three nonequivalent anion (A, B and C) and four cation (Fe1, Fe2, Fe3 and Fe4) positions. Fe4 is tetrahedrally coordinated, while Fe1, Fe2, Fe3 are octahedrally coordinated [108]. Anyways, controlled synthesis of ε-Fe_2O_3 alone is a tough task and is currently being studied by gaining control over the kinetics of γ-Fe_2O_3 to ε-Fe_2O_3 transformations [134-135].

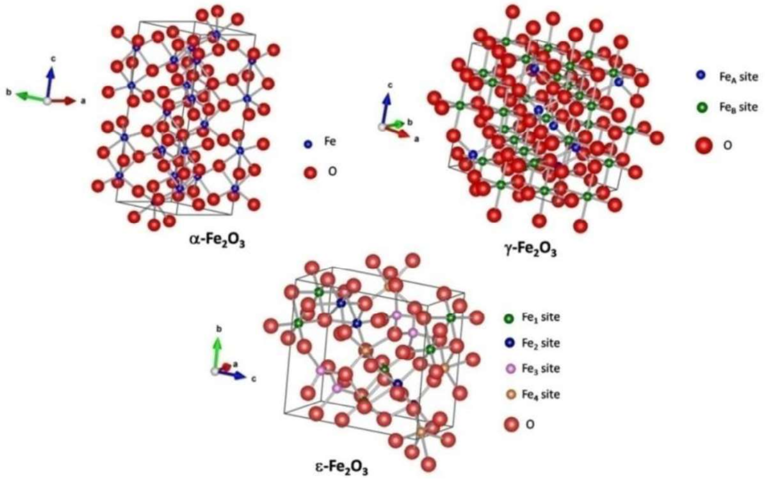

Figure 4.8: Schematic representation of the unit cell of the three polymorphs of Fe_2O_3 obtained in our study viz. α- Fe_2O_3, γ-Fe_2O_3 and ε-Fe_2O_3 employing ball and stick model.

^{57}Fe Mössbauer spectroscopy is a unique method to distinguish and identify different structural forms, amorphous or nanostructured Fe_2O_3 particles [38, 108, 137]. In order to determine the oxidation state of Fe, structure of the oxide and extent of nanocrystallinity, the room temperature Mössbauer spectroscopy was studied for FSO10, FSO15 and FSO20 and the spectra is shown in Figure 4.9 .The values of different Mössbauer parameters are given in the Table 4.7 and 4.8. The room temperature Mössbauer spectra of samples calcined at 1000 °C can be fitted with four sextets (Zeeman splitting patterns) and a superparamagnetic doublet. The identification of different phases of iron oxide is done based on the values of Isomer shift (δ), Quadrupole splitting (Δ) and Hyperfine field values (H_{hf}). α-Fe_2O_3 exhibits only one sextet (sextet A) due to the octahedrally placed Fe at equivalent 12c crystal sites. It exhibits the following room temperature hyperfine parameters - isomer shift (δ) Fe (isomer shift related to metallic iron) ~ 0.329-0.396 mm/s, Quadrupole splitting (Δ) of ~ - 0.22-0.28 mm/s, and Hyperfine field (H_{hf}) of ~ 51 T. The other three sextets, B (Fe_1 and Fe_2), C (Fe_3) and D (Fe_4) belong to ε-Fe_2O_3 phase. Although,ε-Fe_2O_3 consist of four non-equivalent Fe sites, two of the three octahedral sites overlap due to close values of Hyperfine field [108] and is difficult to distinguish in our spectra. The Hyperfine field values differentiates the octahedral sites (Fe1, Fe2 & Fe3, H_{hf}~ 45 & 39 Tesla) from the tetrahedral site (Fe4, H_{hf}~ 25 Tesla). The doublet belongs to superparamagnetic γ-Fe_2O_3 phase [108,137-138]. Hence, the observed Mössbauer spectra are due to contribution of all three phases of iron oxide. The relative area of the three phases as calculated from the area under the curve was found to be: ε-Fe_2O_3 (~74.5%) >α-Fe_2O_3 (16.7%) >γ-Fe_2O_3 (8.8%) for FSO20 sample.

Thus, in accordance with powder XRD results, the major phase in the samples is found to be present in ε-Fe_2O_3 form.

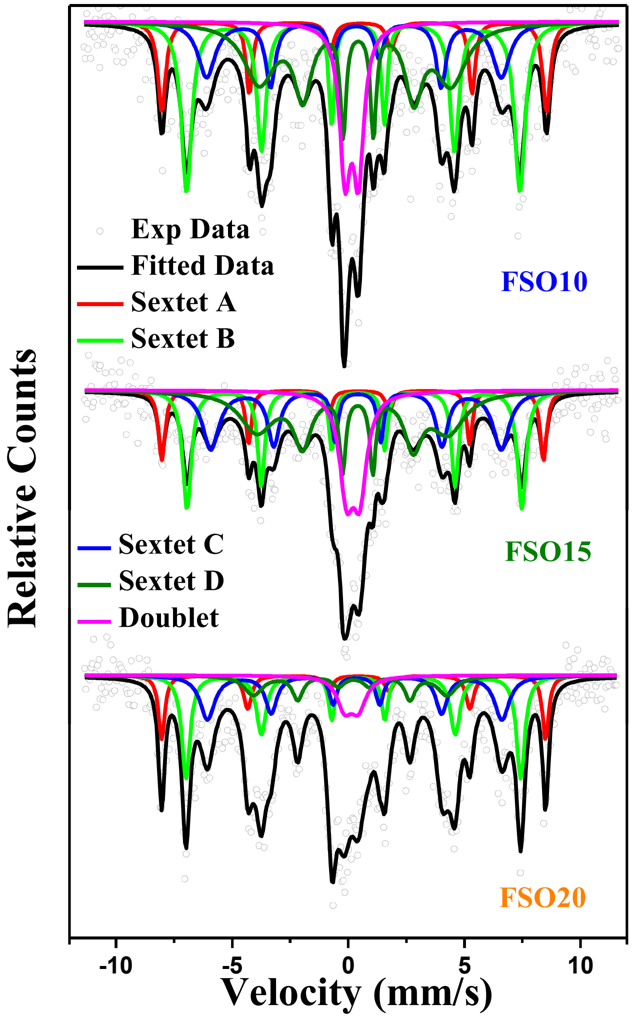

Figure 4.9: Room Temperature Mössbauer spectra of the dispersed Fe_2O_3 samples calcined at 1000 °C for 5 h.

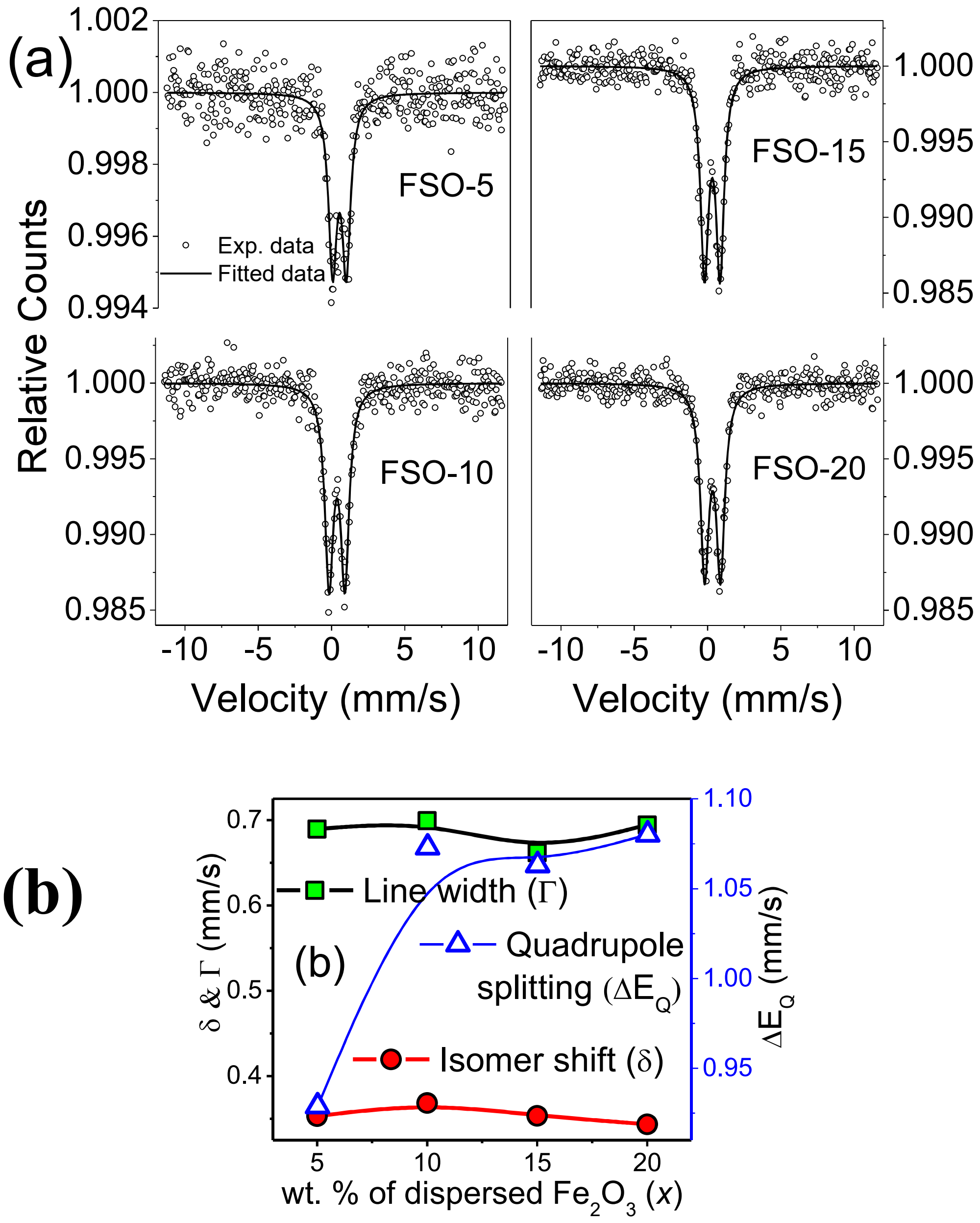

Figure 4.10:(a) RT Mössbauer spectra of Fe_2O_3/SiO_2 calcined at 500 °C. (b) Variations in δ,ΔEQ and Γ of superparamagnetic doublet.

It is pertinent to mention here that the room temperature Mössbauer spectra of all the dispersed samples calcined at 500 °C exhibited a single superparamagnetic doublet mostly due to the existence of γ-Fe_2O_3 nanoparticles dispersed over SiO_2 (Figure 4.10). The single doublet represents γ-Fe_2O_3 nanoparticles in which long range magnetic ordering is absent. This clearly authenticates the fact that till 500 °C calcination, Fe_2O_3 dispersed on SiO_2 exist only in γ-phase. Further, the variation in isomer shift (δ), quadrupole splitting (Δ), line width (Γ) as a function of Fe_2O_3 content are shown in Figure 4.10. Quadrupole splitting values increased with increasing Fe_2O_3 content, indicating an increase in distortion as shown in Figure 4.10 and as found earlier the distortion do not further increase for the 20 wt. % dispersed samples. The line width (Γ) was found to lie between 0.662 – 0.699 mm $s^{-1}$for all compositions due to presence of particles in the nanometer range. Thus, the ε-Fe_2O_3 in our sample could be the stable intermediate produced in our sample during the structural transformation of γ-Fe_2O_3 to α-Fe_2O_3.

Table 4.7 The isomer shift (δ), quadrupole splitting (Δ), linewidth (Γ) of Fe^{3+} ions for x.Fe_2O_3/SiO_2 nanocomposites (x = 5%, 10, 15, and 20 wt.% calcined at 500 °C) derived from Mössbauer spectra, recorded at room temperature. For the paramagnetic doublet, the paramagnetic doublet, the quadrupole splitting $\Delta E_Q = e^2qQ/4$ (separation between two resonance lines of doublet)

Composition (Wt % of Fe_2O_3)	**Iron Sites Doublet (Fe^{3+}) Spm**	**Line width (Γ) mm/s ±0.02**	**Isomer shift (δ) mm/s ±0.007**	**Quadrupole splitting (ΔE_Q) mm/s ±0.01**	**Fitting quality (χ^2)**
5	γ-Fe_2O_3	0.689	0.353	0.929	1.00
10	γ-Fe_2O_3	0.699	0.368	1.073	0.92
15	γ-Fe_2O_3	0.662	0.353	1.063	0.87
20	γ-Fe_2O_3	0.694	0.343	1.080	0.89

Table 4.8 The hyperfine field values (Hhf), isomer shift (δ), quadrupole splitting (Δ), linewidth (Γ) of Fe^{3+} ions for x.Fe2O3/SiO2 nanocomposites (x =10, 15 and 20 wt.% heated at 1000 °C) derived from Mössbauer spectrum, recorded at room temperature. Fitting quality Chi^2≅ 1. Quadrupole splitting for magnetic sextet Δ(M) = (Δ$_{12}$-Δ$_{56}$)/4.

Composition (Wt % of Fe_2O_3)	**Iron Sites Phase (Fe^{3+})**	**Relative area (R_A) %**	**Line width (Γ) mm/s**	**Isomer shift (δ) mm/s**	**Quadrupole splitting (Δ) mm/s**	**Hyperfine field (H_{hf}) Tesla**
10	Sextet A -α-Fe_2O_3	14.81	0.42±0.19	0.40±0.02	-0.28±0.04	51.37±0.15
	Sextet B - ε-Fe_2O_3	25.90	0.31±0.07	0.32±0.02	-0.21±0.03	44.52±0.15
	Sextet C - ε-Fe_2O_3	21.50	0.46±0.18	0.29±0.03	-0.09±0.07	39.30±0.39
	Sextet D - ε-Fe_2O_3	26.88	0.30±0.001	0.33±0.07	-0.19±0.13	25.62±0.54
	Doublet (γ-Fe_2O_3)	10.91	0.57±0.06	0.15±0.02	0.57±0.03	---
15	Sextet A -α-Fe_2O_3	11.33	0.38± 0.2	0.33±0.02	-0.28±0.04	50.94±0.13
	Sextet B - ε-Fe_2O_3	21.18	0.30±0.08	0.35±0.015	-0.17±0.03	44.72±0.11
	Sextet C - ε-Fe_2O_3	21.79	0.34±0.11	0.38±0.02	-0.09±0.05	38.75±0.247
	Sextet D - ε-Fe_2O_3	29.42	0.310±0.074	0.30±0.06	-0.24±.13	25.50±0.57
	Doublet (γ-Fe_2O_3)	16.28	0.73±0.07	0.20±0.02	0.57±0.03	--
20	Sextet A -α-Fe_2O_3	16.7	0.45±0.14	0.37±0.01	-0.22 ±0.03	51.59 ±0.07
	Sextet B - ε-Fe_2O_3	27.7	0.34 ±0.05	0.36 ±0.02	-0.22±0.03	45.01 ±0.07
	Sextet C - ε-Fe_2O_3	25.3	0.41±0.09	0.34±0.02	-0.07±0.04	39.58 ±0.18
	Sextet D - ε-Fe_2O_3	21.5	0.63±0.26	0.19 ±0.04	-0.15 ±0.07	26.08 ±0.26
	Doublet (γ-Fe_2O_3)	8.8	0.80±0.097	0.16 ±0.03	0.60 ±0.06	--

4.3.1.5 Surface Features from X-ray Photoelectron Spectroscopy

The X-ray photoelectron spectra of the dispersed Fe_2O_3 samples calcined at 1000 °C revealed crucial surface features. XPS is a surface sensitive technique in which the analytical volume is confined to approximately five monolayers [136]. Thus, the XPS spectra and its analysis provided information about surface or near surface elemental composition in our samples. The atom percent of each element as determined from the survey scan of our samples using Casa XPS package are listed in Table 4.9. The Fe content was found to be much lower (~ 10 % of the desired value with respect to bulk composition) than expected for the three samples FSO5, FSO10 and FSO15. This clearly confirms our previous finding from N_2 adsorption desorption isotherms that the majority of Fe_2O_3 nanoparticles are immobilized within the porous network of SiO_2 [122,139-140]. On the contrary, the surface Fe content in FSO20 sample was found to abruptly increase to more than 30 % of the expected value indicating that with higher concentrations of Fe_2O_3, the phenomenon of nanoparticle restriction within support pores, as observed for lower concentrations are reduced. Above a certain concentration of Fe, the Fe_2O_3 phase gets deposited outside the SiO_2 mesoporous structure. Thus, 15 wt. % Fe_2O_3 may be regarded as the optimum loading in SiO_2 to obtain dispersed Fe_2O_3/SiO_2 composition with maximum Fe_2O_3 confined within pores. The Fe2p spectra of the four samples are shown in Figure 4.11(a). For all the samples the $Fe2p_{3/2}$ peak appears at a binding energy of ~ 711 eV with a separation of ~ 13.6 eV from the $Fe2p_{1/2}$ peak characteristic of Fe^{3+} [89, 122]. Whatever little Fe was detected could be fitted into two peaks - one at ~ 710.6 eV due to Fe^{3+} present in Fe-O-Fe linkages while, another at a higher BE value of ~ 712.8 eV can be attributed to Fe^{3+} bound to the SiO_2 support i.e. in Fe-O-Si linkages. Interesting pattern was observed in the case for O1s spectra shown in Figure 4.11 (b). The O1s peak could be deconvoluted into three peaks - the main peak having a BE value of ~ 532.5 eV in all the samples attributed to O^{2-} present in the major oxide component i.e. SiO_2 matrix, a lower intensity peak at the highest BE values between 533.5-534.5 eV assigned to chemisorbed surface oxygen or surface adsorbed water or hydroxyl moieties [141-142], while another minor peak appeared at much lower binding energy values (527 eV to 529 eV). This low intensity peak progressively increased in intensity as we moved from FSO5 to FSO20 indicating that the peak could be assigned to O^{2-} present in dispersed Fe_2O_3. Further, this peak also displayed a shift in position from ~ 527 eV in case of lower Fe_2O_3 containing compositions viz. FSO5, FSO10 and FSO15 to ~ 529 eV for FSO20, which could probably be attributed again to decreased strain in Fe_2O_3 nanoparticles in FSO20 due to precipitation of phase outside the pores. The Si2p X-ray photoelectron spectra of fresh samples calcined at 1000°C is shown in Figure 4.11 (c) which confirms the presence of Si in 4+ state.

Table 4.9 The atom percent of each element determined from the survey scan of XPS spectrum of Fresh samples.

Sample	**Fe %**		**Si%**		**O%**	
	Theoretical	**Experimental**	**Theoretical**	**Experimental**	**Theoretical**	**Experimental**
FSO5	1.22	0.22	32.32	30.76	66.46	69.02
FSO10	2.36	0.29	31.36	30.78	66.27	68.93
FSO15	3.44	0.40	30.54	29.12	66.03	70.48
FSO20	4.44	1.51	29.59	29.78	65.95	68.71

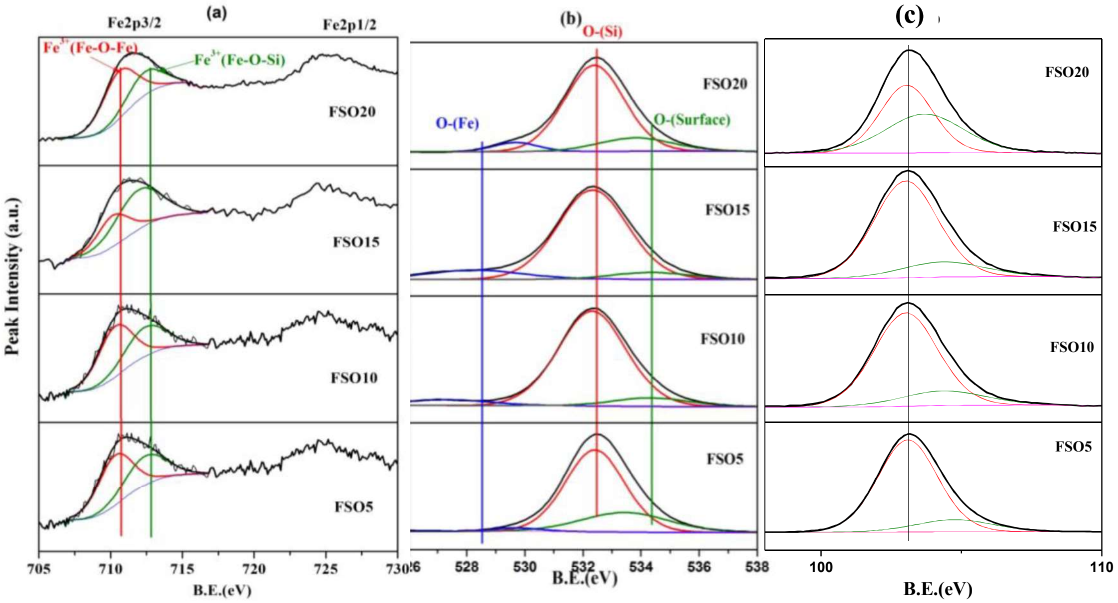

Figure 4.11: X-ray photoelectron spectra of (a) Fe2p and (b) O1s (c)Si-2pof the Fe_2O_3/SiO_2 samples calcined at 1000°C

4.3.1.6 Redox Properties of the Catalyst Investigated by TPR/TPO

The redox properties of the Fe_2O_3/SiO_2 samples were investigated by recording the temperature programmed reduction (TPR)/oxidation (TPO) cycles. The first cycle TPR profile of all the samples calcined at 1000 °C are plotted in Figure 4.12. The support SiO_2 was found to be non-reducing (as seen in Figure 4.12) under the TPR experimental conditions. Thus, in the dispersed sample all the peaks correspond to the reduction of the dispersed Fe_2O_3 phase. An obvious feature in the TPR profiles was that the extent of reduction increased with an increase in Fe content i.e. the area under the curve which corresponds to the amount of hydrogen consumed increased [143], as we moved from FSO5 to FSO20. This signifies that the availability of catalyst Fe_2O_3 increases with increase in loading. All the samples show mainly three peaks - two lower temperature (300-600 °C) major peaks which were merged and a higher temperature (650-750 °C) minor peak. The peak maxima (i.e. the temperature at which maximum hydrogen was consumed) for the merged first and second peaks appeared at ~ 430 °C and ~ 500 °C respectively for the three lowest Fe_2O_3 content samples. The third peak or hump appeared at ~ 680 °C. Further, it can be noticed that the peak maxima for all the three peaks move to a considerably higher temperature for FSO20 which implies inferior reducibility of FSO20 than other three. Since in FSO5, FSO10 and FSO15, Fe_2O_3 is mainly immobilized within the SiO_2 pores while in FSO20 in major amount outside the pore as a composite, the reducibility of the FSO20 sample is found to be weaker. Better immobilization in lower percentage (upto 15 wt.%) have stabilized the nanoparticles of Fe_2O_3 in SiO_2 and better reducibility (in terms of lower reduction temperature) is achieved. On the contrary, precipitation of considerable amount of Fe_2O_3 outside pores as a composite could not stabilize the nanoparticles and poorer reducible samples were obtained. Again, among the low weight percent dispersion having similar reduction profile, FSO15 possesses better reducing capabilities by virtue of highest Fe_2O_3 content and consequently largest area under the reducing peak.

It is reported that reduction of bulk Fe_2O_3 takes place successively in three steps, first due to Fe_2O_3 to Fe_3O_4, then Fe_3O_4 to FeO and finally reduction of FeO to Fe with the ratio of the three reduction peak areas of 1:2:6 [89]. However, in our earlier study with bulk Fe_2O_3 two peaks were observed, a smaller peak at a lower temperature (~520 °C) due to the first reduction step and a larger peak at higher temperature (~815 °C) owing to the merging of second and third reduction steps [89]. The Fe_2O_3/SiO_2 samples in this study show significantly different reduction profiles. This, dissimilar behavior in reduction profiles of dispersed Fe_2O_3 as compared to bulk implies that different reduction mechanism exists. One suggestion given earlier by Gervasini et al for Fe_2O_3/SiO_2 catalysts was that hydrogen reduces dispersed iron oxide to three different final products due to three reducing paths: (i) Fe^{3+} to Fe^{2+} (with fayalite-Fe_2SiO_4 formation), (ii) $Fe_2O_3$to FeO and (iii) Fe_2O_3 to Fe [104]. Thus, complete reduction of Fe_2O_3 is inhibited due to the adherence of Fe_2O_3 with SiO_2 matrix or more specifically SiO_2-Fe_2O_3 interactions i.e. presence of Fe-O-Si linkages as observed in XPS.

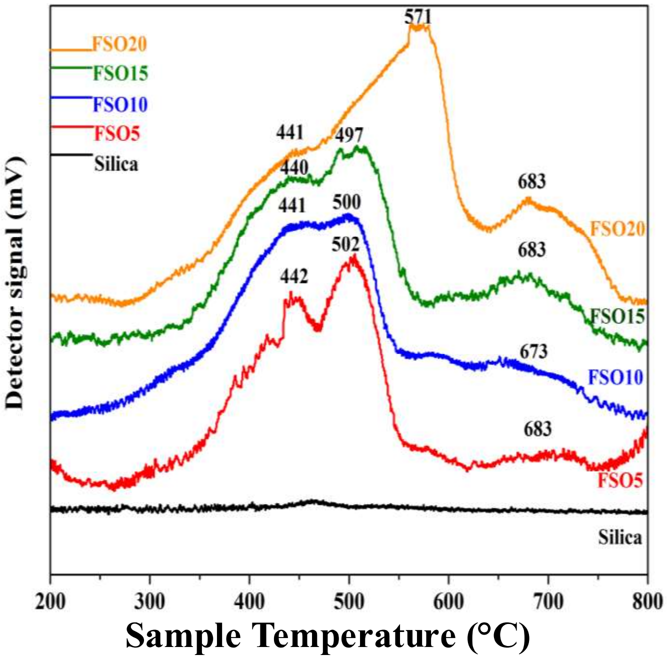

Figure 4.12: Temperature Programmed Reduction profiles of first cycle of the individual Fe_2O_3/SiO_2 samples calcined at 1000°C

To further investigate this aspect, successive three TPR cycles were carried out for all the samples with an oxidation step in between two successive TPR cycles. The first reduction cycle is found to be much meager than the second cycle, probably due to the effect of adhered silica matrix which hinders the complete reduction of iron oxide. The three successive cycles for FSO15 samples are shown in the Figure 4.13. It is evident that the intensity of the reduction band increases in the second cycle for every sample and then remains almost constant. Since the amount of reducible Fe_2O_3 is constant for a particular sample in all cycles, this behavior observed in multi cycling cannot be interpreted unless we consider the strong Fe_2O_3–SiO_2interactions. In the first cycle silica acts as inhibitor for the reduction, and a sluggish reduction profile of Fe^{3+} to Fe^0 is observed i.e. Fe_2O_3 is partly reduced to Fe, FeO and also Fe_2SiO_4. But in subsequent cycles (interspersed with TPO), the Fe_2O_3 phase gets segregated out and a lesser inhibited (or enhanced) reduction of Fe_2O_3 was observed. Evidently, TPR also supports the presence of strong support-active phase interactions or Fe-O-Si linkages as interpreted in the XPS observations. These Fe-O-Si linkages will be instrumental for stabilizing the Fe_2O_3 nanoparticles over SiO_2 during catalytic operation.

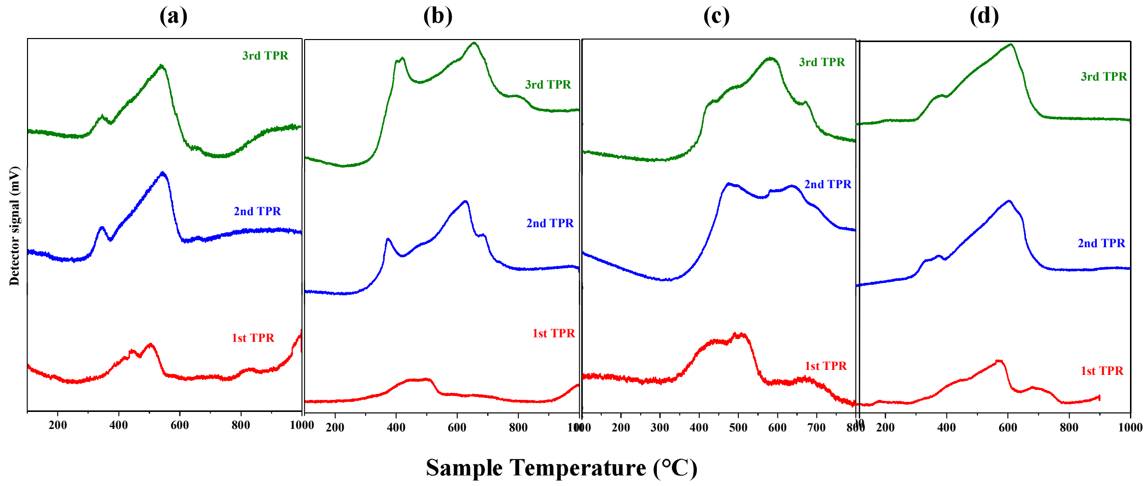

Figure 4.13: Temperature Programmed Reduction pattern of successive cycles of (a) FSO5 (b) FSO10 (c) FSO15 and (d) FSO20 samples

4.3.1.7 Compositional Superiority of 15 wt.% Fe_2O_3 on SiO_2

The structural and redox properties clearly indicate a better prospect of FSO15 sample as catalyst with respect to the other compositions. In this work the deposition of Fe_2O_3 phase was done in succession i.e. FSO5 was prepared first and on that sample further Fe_2O_3 was deposited to form the FSO10 and so on. A limit was probably reached for FSO15 in which case we noticed several advantageous properties. Firstly, the pore size for FSO15 was found to be maximum for the same base SiO_2 support among all the samples. A plausible cause for the increase in pore size of SiO_2 on Fe_2O_3 deposition was that, as progressive dispersion was attempted to increase Fe_2O_3 concentration in support SiO_2, the deposition prompted destabilization of the SiO_2 porous structure to certain extent to accommodate the increased amount of Fe_2O_3 particles within pores. This reached a maxima for the 15 wt.% dispersed sample beyond which the SiO_2 was unable to accommodate any further Fe_2O_3 within the pores and thus an increased amount of Fe_2O_3 deposited outside the pores and the sample formed a combination of Fe_2O_3/SiO_2 dispersed system and SiO_2-Fe_2O_3 nano-composite. This plausible phenomenon was supported by our surface area, pore size distribution and XPS observations. Further, TPR studies clearly suggested better redox properties for FSO15 although FSO20 contained higher content of reducible species. So, for a dispersed catalyst system, there is always an optimum amount of the active component (Fe_2O_3) that could be properly dispersed on a porous support (SiO_2) which is neither too small nor too large.

4.3.1.8 Morphological Features of the Catalyst Studied by TEM

The transmission electron microscopy images of the Fe_2O_3 (15 wt.%)/SiO_2 sample calcined at 500 °C and 1000 °C are shown in Figure 4.14 and is clearly evident that the support SiO_2 particles are spherical with particle size in the range of ~ 40-60 nm diameter. The small dots marked by arrows could be noticed in the Figure 4.14(a) which might be attributed as Fe_2O_3. However, to visualize the shape and size of the Fe_2O_3 nanoparticles dispersed on SiO_2, HRTEM images showing the presence of the particles in form of fringes were obtained (Figure 4.14 (b)). Crystalline nanoparticles, with varied shape, some spherical with 2-3 nm diameter, some oval with 2-5 nm size, some rectangular having size less than 5 nm length are found to be embedded on the surface of amorphous SiO_2 in the 500 °C sample. Inset in Figure 4.14(b) showed a magnified view of the region marked in image. The inset shows typical lattice spacing of 0.25 nm, corresponding to the (311) plane of γ-Fe_2O_3. The same sample after calcination at 1000 °C, yielded Fe_2O_3 nanorods dispersed on amorphous SiO_2. From Figure 4.14(c) presence of nanorods with typical width of 5 nm could be noticed. These nanorods adhered together to form crystalline rods of larger width of the order of 10 nm or 15 nm. The (111) plane of ε-phase is evident along the nanorods with lattice spacing of ~ 0.39 nm from the magnified view of the selected area in Figure 4.14(d). Such a considerable modification in morphological properties of dispersed Fe_2O_3 particles is due to simultaneous agglomeration and phase transformation from γ to ε-Fe_2O_3. These TEM results confirmed the phase evolution of Fe_2O_3 nanoparticles immobilized in SiO_2 as inferred from the results of the XRD and Mössbauer spectroscopic studies. Further, the size and shape of the Fe_2O_3 nanoparticles observed under TEM seems to be highly depended on its crystal phase. The phase of Fe_2O_3 again depends on the calcination temperature and nature of support (SiO_2 in our case). To the best of our knowledge, ε-Fe_2O_3 nanorods dispersed on SiO_2 is employed as catalyst for high temperature sulfuric acid decomposition reaction for the first time.

The above findings would be highly useful for the rational design of Fe_2O_3 based heterogeneous nanocatalysts, as catalytic properties are highly depended on not only the size but also shape of the nanocrystals [144]. In such kind of morphology driven nanocatalysis, the desired catalytic activity and selectivity can be realized by tuning the shape, that is, the exposed crystal facets, of a nanocrystal catalyst. By our current efforts, we exhibit how the size, shape of Fe_2O_3 nanocrystallites depended on the produced crystal phase which again is depended on the temperature of calcination. This phenomenon can effectively lead us to pathways for the design of iron oxide shape selective catalysts which can promote catalyst conversions and might also be highly selective for particular reactions wherever applicable. Specifically, metal oxide nanorods have been found to be highly active for various reactions over their counterparts having identical composition but dissimilar morphology [144-146]. In our reaction, the primary aim is not selectivity instead catalytic activity and stability which we will investigate by determining the high temperature catalytic properties.

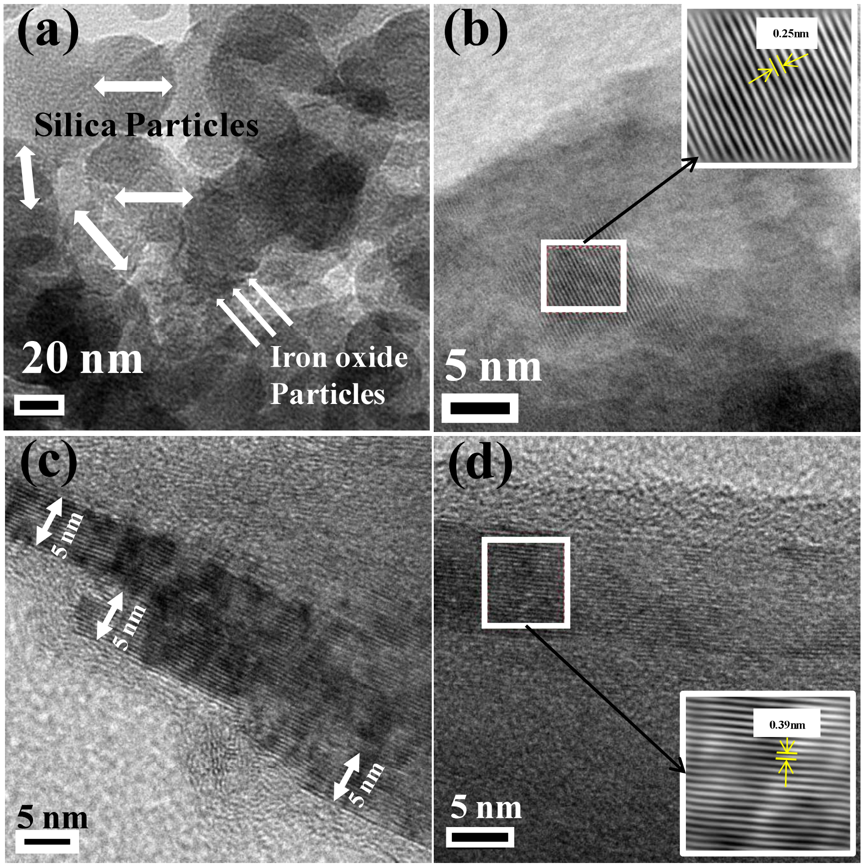

Figure 4.14:(a) Low resolution (b) High Resolution TEM images of FSO15-500 fresh sample with magnified image of the selected area (c) and (d) High Resolution TEM images of the FSO15 sample

4.3.1.9 Catalyst Performance

The catalytic activities in the temperature range of 700-900 °C at a WHSV of 27 g acid g^{-1}catalyst h^{-1} of all the dispersed samples of 45-80 mesh were evaluated and are shown in Figure 4.15(a). The SO_2 yield increased with an increase in temperature for all the samples which is due to kinetic factors [89]. Throughout the entire temperature range it is observed that the catalytic activity increases from FSO5 to FSO10 due to an increase in Fe content, then a significant increase for FSO15 and finally a drop in SO_2 yield for the extreme sample FSO20. FSO15 exhibited the highest activity throughout the entire temperature range. A maximum SO_2 yield of 92 % at 900 °C was achieved over the FSO15 sample. As we move from FSO5 to FSO20, the Fe_2O_3 content gradually increases and accordingly FSO20 is expected to exhibit the highest catalytic activity. But, earlier we established that 15 wt.% dispersion was the optimum Fe_2O_3 content to achieve maximum confinement within pores, optimum dispersion and best reducibility and hence it showed maximum catalytic activity. The FSO20 sample, on the other hand suffered from deposition outside pores and consequently poorer reducibility. FSO5 and FSO10 were also sufficiently active but the Fe_2O_3 content was not sufficient enough on the surface to convert maximum possible SO_3 molecules to the product according to thermodynamic predictions. Based on the above findings it can be established that FSO15 is the superior catalyst with optimum amount of Fe_2O_3 content. So, further investigations were carried out with this composition to verify its practical applicability as a high temperature thermally stable catalyst viz. checking pore diffusion limitations with larger sized catalyst particles, long term catalytic property evaluation, evaluation of structural and morphological stability after long term operation.

Under practical conditions in an enhanced scale [89] the catalyst to be used is in a macro particulate form. In the above tests the catalyst used was in powder form (80-45 mesh). For larger sized particles the diffusion of the gaseous reactants (and products) through the pores of the catalyst to reach (or go away from) an active site easily become rate limiting. To get a quantitative measure of this diffusion limitation, the SO_2 yield was evaluated at 800 °C for three different catalyst particle sizes 45-80 mesh, 20-45 mesh and finally 10-20 mesh. The result obtained is plotted in Figure 4.15(b). It is evident that the SO_2 yield decreases from ~ 79 % for the smallest particle fraction to ~ 60 % for the largest fraction of the catalyst. As the mesh fraction of the catalyst decreases i.e. the particulate size increases, SO_2 yield decreases. This data gives us a quantitative estimate as to what extent the catalytic activity decreases as we employ bigger size granules.

Long-term stability evaluation is mandatory before proposing a nanosized catalyst as a potential candidate for any high-temperature reaction as it essentially determines its thermal stability under actual reaction conditions. We earlier found Pt/Al_2O_3 as thermally unstable in the long term catalytic evaluation due to agglomeration of Pt nanoparticles [88] and also Fe_2O_3 undergone sintering to a certain extent in 100 h under similar condition [89]. A 100 h time on stream performance for sulfuric acid decomposition was evaluated for FSO15 (20-45 mesh) and is plotted in Figure 4.15(c). The catalyst shows sufficient stability with a decrease in SO_2 yield from ~ 70 % to ~ 60 % after 100 h operations at a WHSV of 27 g acid g^{-1} cat h^{-1}.

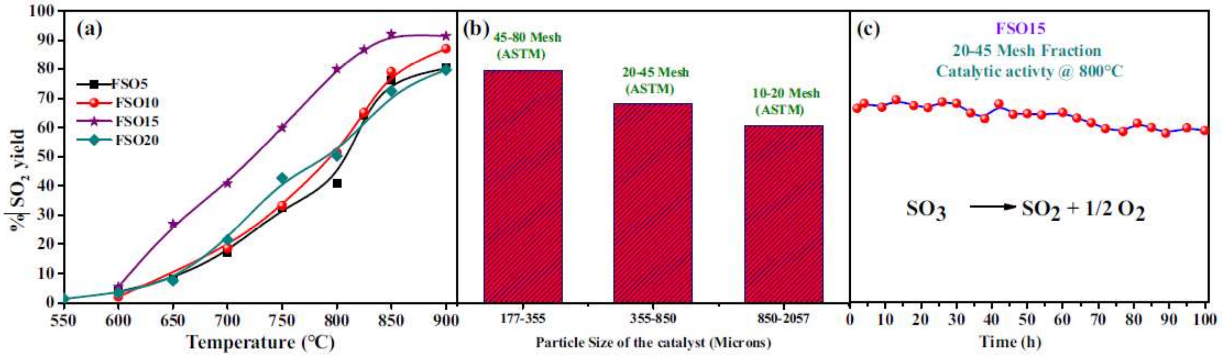

Figure 4.15(a) Temperature dependent activity profiles as a function of temperature of all the samples calcined at 1000°C (b) The SO_2 yield as a function of mesh fraction of the FSO15 sample((c) catalytic activity of FSO15 (20-44 mesh) sample used in sulfuric acid decomposition reaction for 100 h time on stream at 800 °C. In all cases a WHSV of 27 g acid g^{-1} catalyst h^{-1} was maintained.

4.3.1.10 Ex-situ Characterization of the 100 h Spent Catalyst

Post 100 h run the FSO15 catalyst was characterized ex-situ for changes in morphology, structure, oxidation state to investigate the mechanistic aspects. This would help us in identification of the catalytic properties that would play a key role in enhancing or decreasing rates. Further, ex-situ catalyst characterization post activity measurements would also enumerate the reasons that might have caused the catalytic activity decrease and hence would be able to convincingly indicate regarding catalyst stability and life.

The powder XRD pattern of the fresh and spent FSO15 catalyst used for 100 h is shown in Figure 4.16. It is obvious that the small peaks due to various Fe_2O_3 phases present in the prepared catalyst are no longer visible in the powder XRD pattern of the spent catalyst and only the hump due to SiO_2 exist. Thus, whatever limited long range ordering was present in the prepared nanoparticles were probably lost on 100 h use. The amorphous nature of the support SiO_2 was still preserved.

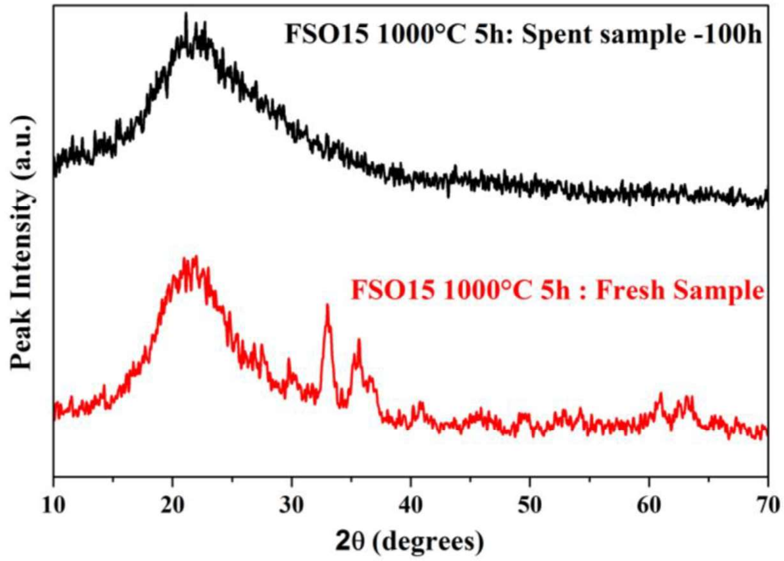

Figure 4.16: Comparison of powder XRD patterns of fresh and spent FSO15 catalyst after 100 h run at 800 °C for sulfuric acid decomposition reaction

The room temperature Mössbauer spectrum of the spent catalyst sample shows a single symmetric paramagnetic doublet as shown in Figure 4.17. In order to conclusively confirm the presence of any magnetic sextet due to ordering Fe^{3+} ions we have recorded the Mössbauer spectrum at higher velocity scale (± 11.5 mm/s) but no such sextet was observed at room temperature in the Mössbauer spectrum. Thus the magnetic ordering present in the prepared sample was completely lost due to 100 h catalytic exploitation. Thus, the Mössbauer data supports our XRD findings. The values of Mössbauer parameters; isomer shift (δ), quadrupole splitting (ΔE_Q) and line width (Γ) are found to be 0.455 mm/s, 0.531 mm/s and 0.276 mm/s, respectively. These results gave us strong evidence regarding the nature of Fe species present in the spent sample. For amorphous iron (III) oxides, the values of δ and ΔE_Q are found to be in the range of δ ~ 0.33-0.34 mm/s and ΔE_Q ~ 1.01-1.11 mm/s [147-148]while the same for anhydrous iron (III) sulfate in the paramagnetic state at room temperature were found to be 0.49 mm/s and 0.29 mm/s, respectively relative to natural α-Fe foil [149]. Vaughan *et al* observed δ = 0.39 mm/s and ΔE_Q = 0.6 mm/s for $Fe_2(SO_4)_3$ at atmospheric temperature and pressure [150]. Thus the Mössbauer study provides a strong indication that the Fe present in the sample is in the form of sulfate although its crystallinity might be poor.

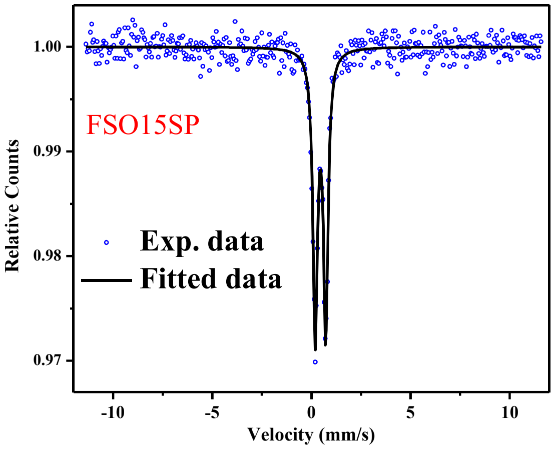

Figure 4.17: Room Temperature Mössbauer spectrum of FSO15 sample after 100 h run as catalyst for sulfuric acid decomposition reaction

The XPS pattern of the spent catalyst was also reordered and analyzed. The surface elemental composition as determined from the XPS spectra is listed in Table 4.10 for fresh FSO15 and used catalyst. An obvious outcome on 100 h use is the appearance of considerable amount of sulfur in addition to Si, O and Fe present in fresh catalyst (Table 4.10). The chemical nature of this sulfur was confirmed from the XPS spectra (Figure 4.18a) where we see that the S2p peak appears at ~ 169 eV. This sulfate peak could be deconvoluted into three peaks, a major peak at ~ 169.4 eV due to ferric sulfate [89] another at ~ 168 eV due to Fe-sulfate attached with support SiO_2 i.e. the sulfated Fe in Fe-O-Si linkages and finally a minor peak at ~ 171.6 eV which is assigned to weakly adsorbed SO_2 on SiO_2 surface/pores [151-152]. The elemental Fe content which was ~ 11 % of the theoretical content of Fe concentration in fresh catalyst reduced to ~ 8 % in the spent catalyst, considering all the Fe_2O_3 being sulfated in the spent catalyst (Table 4.10). The most probable cause for this reduction in Fe content as compared to the fresh catalyst can be ascribed to formation to its surface sulfate species and thus Fe being masked. The Fe2p XPS pattern of the spent catalyst as compared with the fresh one is shown in Figure 4.18b. The peak due to Fe2p appears to be quite broader than fresh catalyst and thus can be deconvoluted into four peaks - a low BE peak due to Fe^{2+}, two due to Fe^{3+} in Fe_2O_3 (one Fe-O-Fe and other Fe-O-Si) and another at highest BE due to Fe^{3+} in its sulfate [89]. The O1s spectra of the fresh and spent catalyst shown in Figure 4.18c shows that the major peak due to O^{2-} in SiO_2 retains its position at ~ 532.5 eV, whereas a peak due to O^{2-} in Fe-sulfates appears at higher binding energy (531 eV) as compared to the O^{2-} in Fe_2O_3 in the fresh catalyst. The peak due to presence of chemisorbed oxygen/hydroxyl groups and adsorbed water is much broader in the spent catalyst.

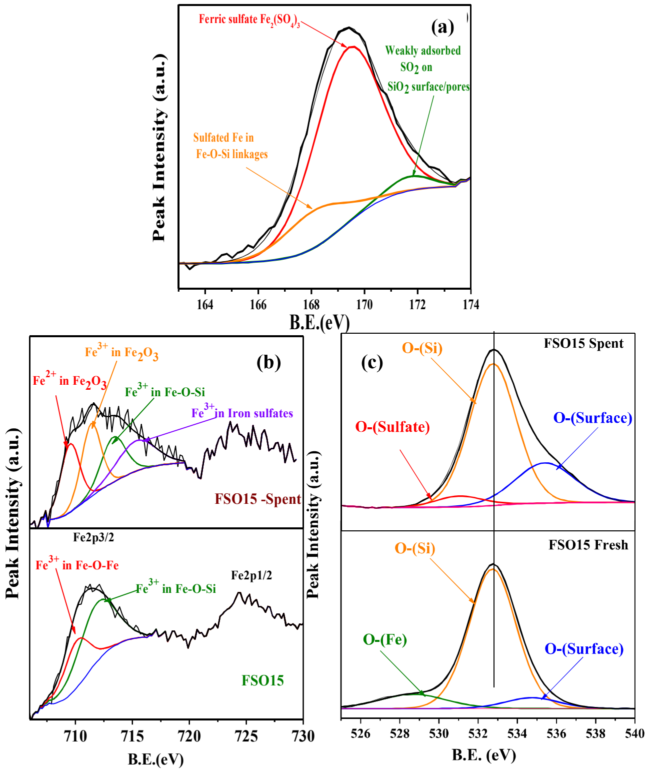

Figure 4.18: (a) S2p X-ray photoelectron spectra of 100h spent catalyst (b) Comparative Fe2p and (c) comparative O1s X-ray photoelectron spectra of fresh and spent catalyst after use for 100h at 800°C for sulfuric acid decomposition reaction

Table 4.10 The atom percent of each element as determined from the survey scan of XPS spectrum of spent sample after 100h.

Sample	**Fe %**		**Si%**		**O%**		**S%**	
	Theory	**Exp.**	**Theory**	**Exp.**	**Theory**	**Exp.**	**Theory**	**Exp.**
FSO15 fresh	3.44	0.40	30.54	29.12	66.03	70.48	----	----
FSO15 spent	2.85	0.24	25.19	26.95	67.68	66.65	4.28	6.15

4.3.1.11 Mechanistic Aspects

The spent catalyst was also subjected to thermogravimetry-evolved gas analysis (TG-EGA) experiments, where the evolved gases from the sample when it was heated in a programmed mode were analyzed by a QMS. Figure 4.19 shows the profile of the intensity of evolved gas, having mass number 64 (SO_2), in the temperature range of 250-900 °C. A small peak is observed at very low temperatures ~ 220 °C, which was never encountered in our earlier studies with ferrites [38] or iron oxides [89] or Pt/Al_2O_3 [88]. This can be explained by the desorption of surface adsorbed or weakly adsorbed SO_2 species (observed in XPS) within the mesoporous network of SiO_2. A sharp and a prominent peak appears at a peak maxima of ~ 645 °C which can be attributed to the decomposition of iron-sulfate species, since iron sulfate decomposes producing sulfur dioxide and metal oxide [89]. A very broad peak appeared at a further higher temperature with peak SO_2 evolution at ~ 850 °C. The nature of this sulfate can be ascribed to the iron sulfates which are formed at the Fe_2O_3-SiO_2 interface or at Fe-O-Si linkages and since these Fe-O species are attached to Si-O moieties the decomposition of the corresponding sulfate is considerable hindered. The evolution of SO_2 from the surface sulfate species corroborates our prior assumption [89] of concerted phenomenon of surface sulfate formation and decomposition as the most probable mechanism of the reaction.

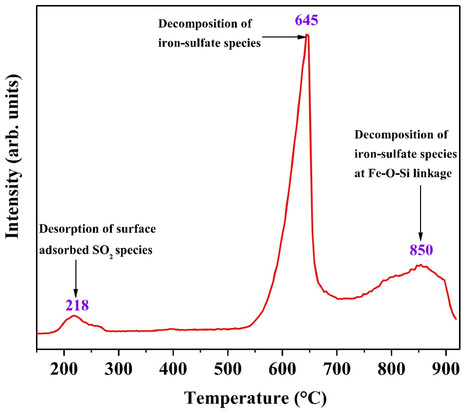

Figure 4.19: Evolved gas analysis for mass number 64 as a function of temperature in mass spectrometer of the spent catalyst

The proposed most probable mechanism is schematically shown in Figure 4.20. Oxygen vacancies usually exist on the Fe_2O_3 nanoparticles at the high operating temperature by desorption of oxygen. This thermal oxygen evolution reaction requires proper functioning of the Fe^{3+}/Fe^{2+} redox couple in Fe_2O_3/SiO_2 catalyst. The appearance of Fe^{2+} in the XPS of the spent catalyst supports the importance of the redox phenomenon of the Fe-species during catalytic use. Subsequent step is the formation of Fe-sulfate by chemisorption of SO_3 on these oxygen vacant sites and both the free Fe (Fe-O-Fe) and SiO_2 linked Fe (Fe-O-Fe) are sulfated [89]. This step is followed by the crucial sulfate decomposition yielding the product SO_2 and regenerating the metal oxide back. According to the TG-EGA results it is imperative that only the free Fe-sulfate decomposes at temperatures below 850 °C generating SO_2. The participation of the higher temperature decomposing sulfates or the mixed Fe-Si sulfates are probably meager instead their role is mostly to impart stability to the Fe_2O_3 nanoparticles. In our study the catalytic activity of the samples at 850 °C followed the order FSO15>FSO10>FSO5>FSO20. As, the concentration of active Fe_2O_3 species increases from FSO5 to FSO15 and the dispersion are retained the catalytic activity increases progressively. But, in FSO20 although there was an increase in Fe_2O_3 concentration the redox property was found to be inferior and so was the catalytic activity. From the proposed most probable mechanism it is evident that facile sulfate decomposition and redox properties (i.e. easy working of Fe^{2+}/Fe^{3+} couple) are crucial factors for determining reaction rates. In FSO20 the redox properties was found to be inferior as compared to other compositions. Thus, in case of Fe_2O_3/SiO_2 just by increasing the Fe_2O_3 content the redox and catalytic properties cannot be increased indefinitely, instead there exist an optimum concentration till which the dispersion will be proper yielding stable nanoparticles with superior redox and catalytic properties. Again, the nanoparticle stability is imparted in Fe_2O_3/SiO_2 by the Fe_2O_3-SiO_2 interactions i.e. the presence of Fe-O-Si linkages. To examine the extent of this stability the 100 h spent catalyst was also analyzed by transmission electron microscopy.

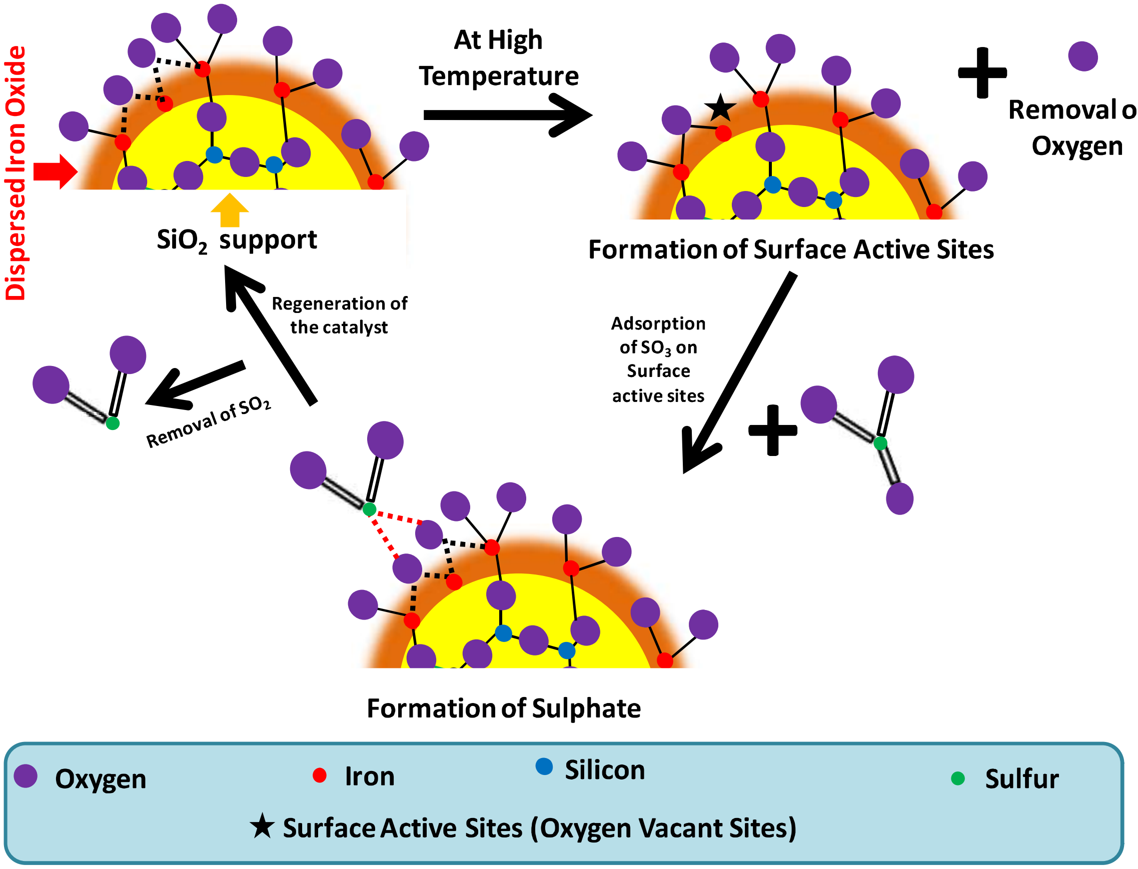

Figure 4.20: Schematic representation of the most probable reaction mechanism proposed for sulfuric acid decomposition over silica supported iron oxide catalyst

4.3.1.12 Morphological Modifications on Catalytic Use

The low resolution TEM image of the spent sample indicates that the size and shape of SiO_2 particles are intact even after 100 h use at 800 °C. The HRTEM of the spent catalyst samples unambiguously exhibits the presence of amorphous spherical nanoparticles of ~ 8-10 nm size well distributed over the SiO_2 particles. As can be seen from the image (Figure 4.21a) the crystalline nature of the ε-Fe_2O_3 as was observed in the fresh particles are completely lost which was further confirmed by the broad halo in the SAED pattern of the spent catalyst (Figure 4.21b). The entire morphology gets modified i.e. the shape, size and crystallinity of the FSO15 sample was found to change on 100 h use. The shape of the particles is almost spherical. The particle size of the amorphous Fe_2O_3 was of the order of ~ 10 nm as observed from the HRTEM images (Figure 4.21). The particle size enhancement in this case is much smaller when compared to an average particle size increase to ~ 150-300 nm from ~ 100 nm in the case of Cr doped Fe_2O_3 used for sulfuric acid decomposition during 100 h operation at a much smaller WHSV of 3.4 g cat g^{-1} cat h^{-1}. This behavior suggests the reorganization of the active component on catalytic use, a phenomenon observed during several other catalysts on use in chemical processes [153-154]. The most probable cause for such a reorganization of the active component may be assigned to the nature of metal oxide-support interaction i.e. Fe_2O_3-SiO_2 interaction and also the nature of reaction environment. Thus, schematically the morphological modifications during the entire course of preparation to catalytic use can be schematically described by Figure 4.22.

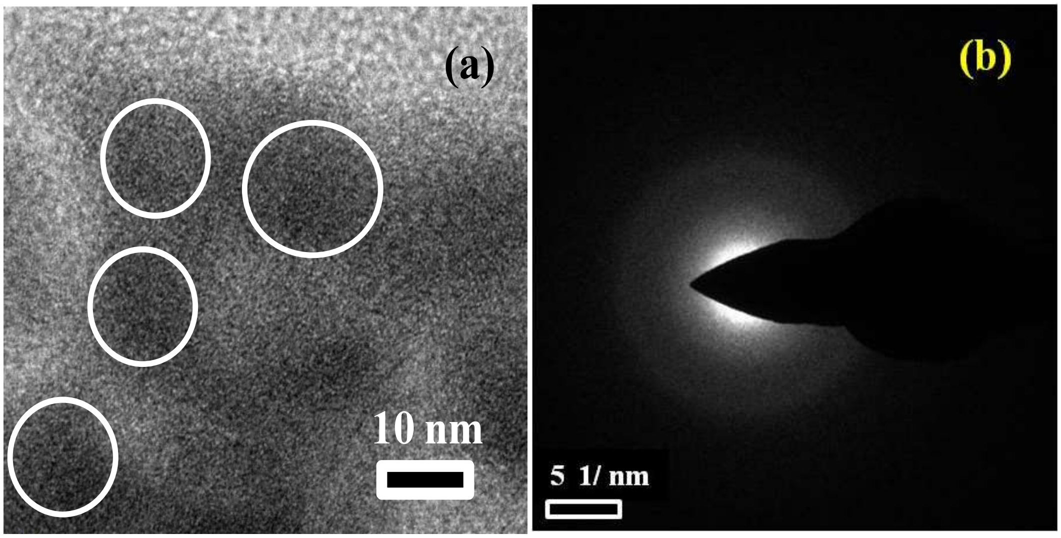

Figure 4.21: (a) High Resolution TEM image and (b) SAED pattern of the of FSO15 sample used for 100 h at 800°C for sulfuric acid decomposition reaction

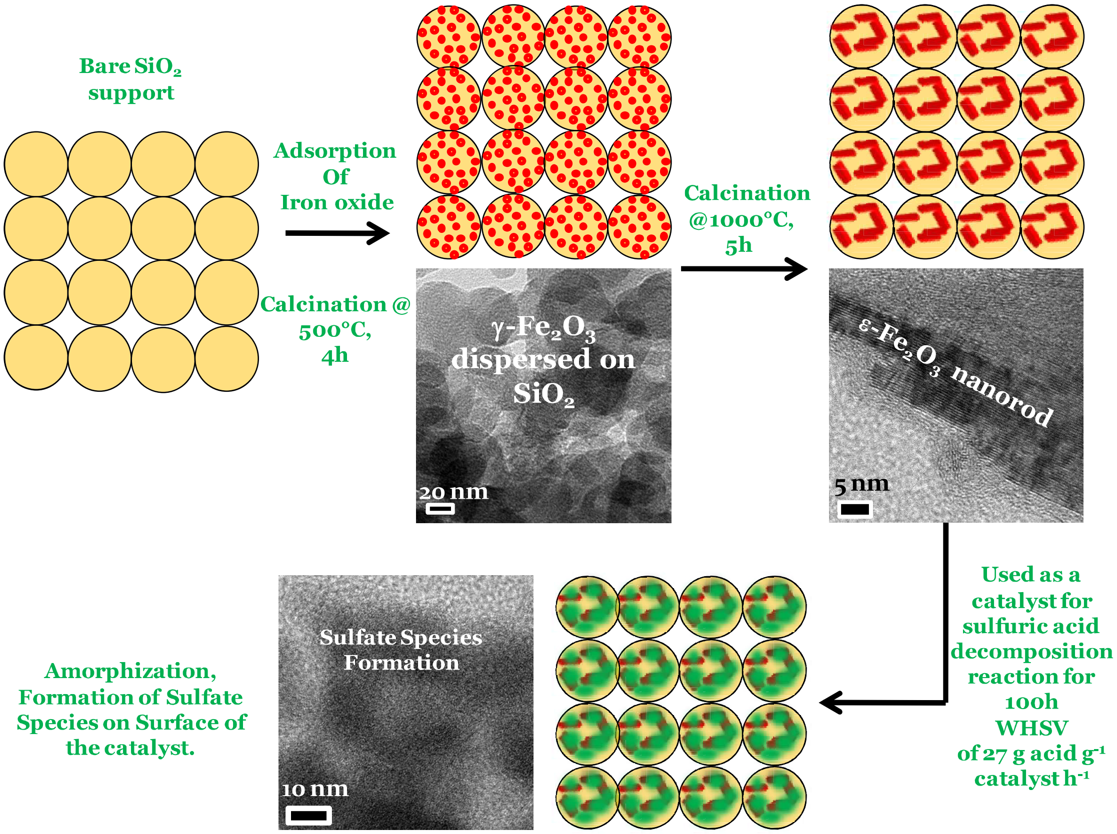

Figure 4.22: Schematic representation of the morphological evolution of FSO15 nanoparticles from preparation to catalytic use

4.3.1.13 Role of Fe_2O_3-SiO_2 Interactions

In recent years it has emerged that enhanced stability and modified physico-chemical properties, even superior catalytic properties can be accomplished in the case of lattice matched support-active phase combinations [130, 155-156] owing to electron density overlap of the support and dispersed phase. In some cases, thermal stability for high-temperature reactions has been attributed to core shell configurations viz. Pt@SiO_2 [157]. In our case of amorphous support and crystalline dispersed phase, we observe interestingly amorphisation and sulfation of dispersed phase. The structure of a heterogeneous catalyst is dynamic, as it adapts to the changes required depending upon the surrounding environment [157]. Thus, the surface morphology, structure and composition get significantly modified in order to adapt to our reaction environment. The sulfation of the Fe_2O_3 is obviously as a result of its involvement in SO_3 decomposition reaction. But, further to this, the participation (sulfation, desulfation and oxygen evolution) of Fe_2O_3 nanoparticles supported over amorphous SiO_2 in the decomposition reaction causes significant reorganization of the active phase Fe_2O_3. The 15 wt.% Fe_2O_3 in SiO_2 yielded composition (FSO15) with superior redox property and catalytic activity but the Fe-O-Si linkages were not able to prevent the loss of crystallinity of the active phase and slight agglomeration of the Fe_2O_3 nanoparticles during rigorous catalytic use at 800 °C under harsh conditions of high temperature, steam, SO_2 and SO_3. But, they are able to stabilize the Fe_2O_3 nanoparticles to a considerable extent so that the catalyst retains significant catalytic activity even after 100 h of active operation at high temperature of 800 °C. These findings provide considerable impetus in the design and probable use of supported metal oxide nanoparticles as catalysts for high-temperature reactions.

4.3.2 Effect of Preparation Method

4.3.2.1 Preparation Methodology:

The active component Fe_2O_3 was dispersed on SiO_2 via three different preparative methods i.e. polyol, wet impregnation and solvothermal treatment as explained in the flow sheet diagram (Figure 4.2). In polyol method, ethylene glycol solution was the solvent as well as hydrolysing agent and iron acetyl acetonate as the precursor for iron oxide. Both the precursor and silica powder were refluxed in ethylene glycol, instigating the dispersion of iron oxide over the silica surface. In wet impregnation method, precursor dissolved in 1:1 1-propanol was added over the silica support. Thus allowing the solution to seep into the pores of the support and then later aging overnight results in dispersion of iron oxide on the support. In solvothermal route iron acetylacetonate initially dissolved in 1:1 1-propanol was heated along with the silica suspended 1:1 1-propanol solution in an autoclave at 150 ° C. The pH of the solution was maintained @ 10 using NH_4OH solution, after autoclaving it yielded in formation of Fe_2O_3 /SiO_2 (15% wt.). The precipitate obtained from all three methods were air dried @120 °C with subsequent calcination @500 °C for 4 h and finally at 1000 °C for 5 h.

4.3.2.2 Compositional Analysis of the Samples:

The abbreviation, the expected and observed composition of Fe_2O_3 (weight %) estimated by Energy Dispersive X-Ray Fluorescence Spectrometry of the samples synthesized are tabulated in Table 4.11. The expected weight % of $Fe_2O_3$was almost near to the experimental results as evident from the listed values in Table 4.11. This indicates no leaching or loss of any iron species during the procedure of dispersing the active component i.e. the iron oxide on the stable support. However, the succession of dispersion of the active component i.e. the presence of iron oxide in the predicted form can be however concluded from the subsequent characterization techniques.

4.3.2.3 N_2 BET Surface Area:

N_2-BET surface areas of the samples are listed in Table 4.11. It is very evident that the BET surface area decreased from 249.47 m^2/gfor bare SiO_2 to ~125 m^2/g for FSP and FSWI samples. However for FSHT sample the surface area observed was ~75 m^2/g. This extreme decrease in surface area of samples in comparison to the support is mainly due to heating action at 500 °C and 1000 °C. The deposition of Fe_2O_3 on SiO_2 facade causes Fe_2O_3 to impede the surface sites of SiO_2.

Table 4.11 Composition, BET surface area, Pore size and Pore volume

SAMPLE	**Preparation Method**	**Sample Abbreviation (1000 °C calcined)**	**Actual Composition (ED XRF)**	**N_2-BET Surface Area**	**Pore Size**	**Pore Volume**
Fe_2O_3 15 wt. % on SiO_2			**Fe_2O_3 wt. % on SiO_2**	**(m^2/g)**	**nm**	**cm^3/g**
SiO_2	Commercial	SiO_2	--	249.5	26.9	1.8
Fe_2O_3 15 wt. % on SiO_2	Polyol	FSP	15.8	122.8	18.5	0.19
Fe_2O_3 15 wt. % on SiO_2	Wet impregnation	FSWI	14.9	126.3	11.2	0.11
Fe_2O_3 15 wt. % on SiO_2	Solvothermal Treatment	FSHT	14.5	74.7	23.6	0.00

4.3.2.4 Powder XRD for Phase Elucidation:

Powder XRD patterns (Figure 4.23) in the 2θ range of 10-70 degrees of the support and that of the synthesized samples calcined at 1000°C i.e. FSP, FSWI and FSHT were recorded and analyzed. The support SiO_2 exhibits a broad hump centered at peak position 2θ ~ 22 degrees (mineral name: crystabolite, tetragonal crystal system, Space Group: P 41212 (92), ICSD No. 47219 (orthorhombic crystal system, ICSD No. 415250) were present. In FSP, peaks corresponding to onlyα-Fe_2O_3 (ICSD No. 15840) were observed whereas in case of FSWI and

FSHT α-Fe_2O_3 was major phase and ε-Fe_2O_3 (ICSD No. 415250) was observed as secondary phase [132-135].

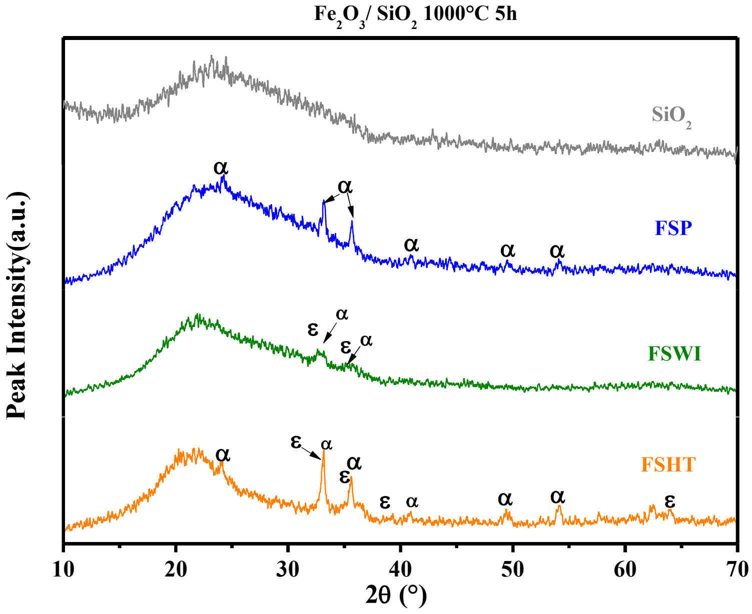

Figure 4.23: XRD pattern of all the fresh samples prepared by different methods

4.3.2.5 X-ray Photoelectron Spectroscopy:

X-ray photoelectron spectroscopy helps in understanding the surface characteristics. Being a surface sensitive technique, it is very useful method especially for dispersed catalysts where the surface morphology plays a key role. The atom percent of each element determined from the survey scan of samples using CASA XPS package are enlisted in Table 4.12.The atom % of Fe for FSP and FSHT was about 15% of the expected value, however the value was nil for FSWI. The Fe component on the surface was found to be lower than the expected theoretical composition, which signifies immobilization of iron oxide nanoparticles into the porous silica in the bulk rather than the surface of the support [122,139-140]. X-ray photoelectron spectra of all the samples calcined at 1000 °C has been illustrated in Figure 4.24.For all the samples the $Fe2p_{3/2}$peak appears at a BE of ~711eV with a separation of ~13.6 eV from the Fe2p$_{1/2}$. The peaks as shown in Figure 4.24a corresponding to Fe could be fitted into two peaks one at ~711eV which is due to Fe-O-Fe linkages whereas the peak at higher value ~712 eV is due to the Fe linked with the silica support. In the case of O1s, peak could be deconvulated into three peaks as represented in Figure 4.24b. For FSP the pattern exactly resembled to previously studied catalyst, with the major peak attributed to oxide ions of silica matrix reflected in the region 532.8eV and the minor peak at 529 eV due to oxide ion bound to the metal and a third minor peak at higher BE value of 536 eV due to chemisorbed oxygen was also evident [140]. However the difference was evident in case of FSWI and FSHT samples. In the case of FSWI sample the three deconvulated peaks at the previously observed BE values, almost had the similar peak area and for FSHT two minor peaks at 530.3 and 532.5 eV along with the major peak at 546 eV was very clearly distinct.

Table 4.12 The atom percent of each element as determined from the survey scan of XPS spectrum of all fresh samples

Sample	**Fe %**		**Si%**		**O%**	
	Theory	**Exp.**	**Theory**	**Exp.**	**Theory**	**Exp.**
FSP	3.44	0.507	30.54	37.473	66.03	62.02
FSWI		-----		14.097		85.903
FSHT		0.465		27.390		72.145

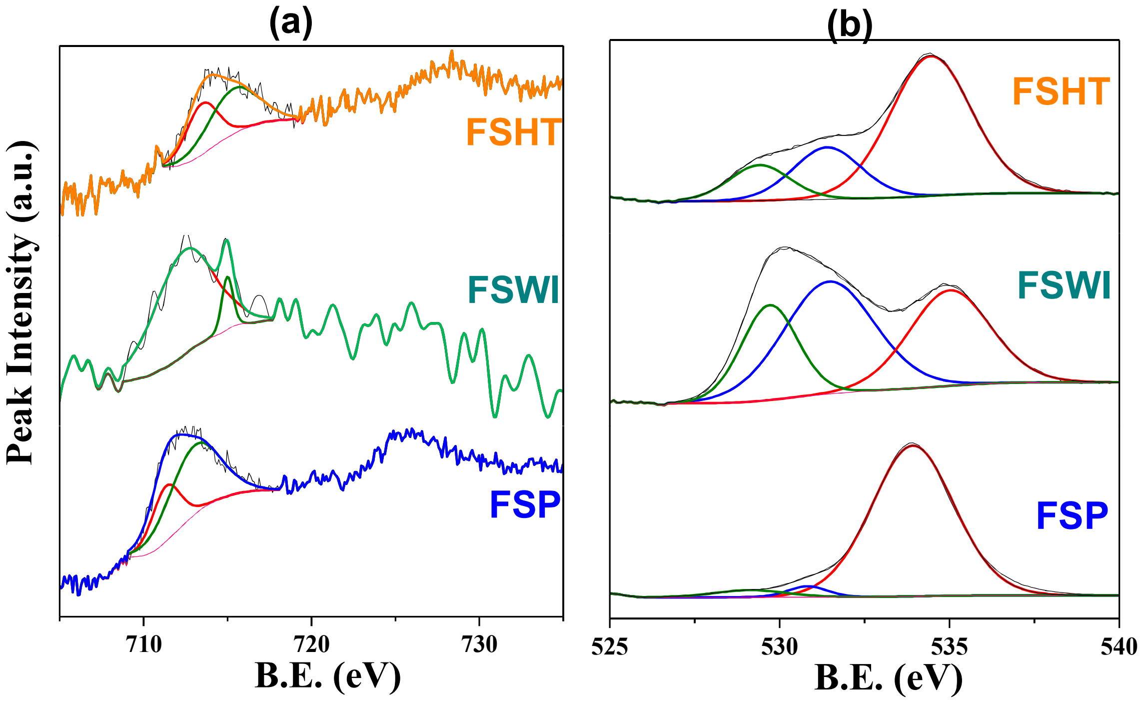

Figure 4.24: X-ray photoelectron spectra of (a) Fe2p and (b) O1s of the Fe_2O_3/SiO_2 samples calcined at 1000°C

4.3.2.6 TPR/TPO to Evaluate the Redox Properties

The redox properties of the samples calcined at 1000 °C were explored by studying Temperature Programmed Reduction (TPR) and Temperature Programmed Oxidation (TPO) cycles. The first cycle TPR of the fresh samples are shown in Figure 4.25.In order to study the effect of reducing and oxidizing nature of the environment over the catalyst, multiple TPR cycles were performed with subsequent Temperature Programmed Oxidation (TPO) in between the two reducing cycles. Three such cycles were studied for all the samples and depicted in Figure 4.25(a).The support i.e. silica does not show any reducing properties under TPR conditions, so the peaks observed in case of samples(FSP, FSWI, FSHT) can be corroborated due to the active Fe_2O_3 phase only [143] . The extent of reduction varied in all three samples, as evident from the area under the curve (Figure 4.25) corresponding to consumption of hydrogen shows the order of reducibility as FSP> FSWI ~ FSHT. The reduction seems to follow a three step reduction phenomena for the conversion of Fe^{3+} to Fe° as discussed earlier in this chapter. The extent of reduction was improved from first TPR cycle to subsequent cycles as noticeable in Figure 4.25(b) in case of FSP, however the reducing pattern observed in other samples were similar in all three TPR cycles. The first reduction cycle of FSP is comparatively poorer than the subsequent two cycles which should be due to the deterring effect of silica matrix. Also the first peak is observed at a higher region i.e. 481 °C with respect to 371 °C in the second and third TPR cycles and the peak attributing to step number 2 and 3 seems to be merged. In FSWI, though the first reduction step representing peak appears to be at the lowest temperature region as shown in Figure 4.25(c), the intensity of the peak is found to be meagre. Also there is a visibility of the two peaks corresponding in the lower temperature region indication of 1st reduction step which is unique in comparison to other samples. The reason for two peaks in the region at 398 °C and 476 °C could be due to the unsupported and supported iron oxides. The 1st reduction peak in the initial TPR cycle also gets shifted to lower region in consecutive cycles which is very similar to the FSP sample. However the intensity of peaks keeps on increasing with the subsequent cycles [90].

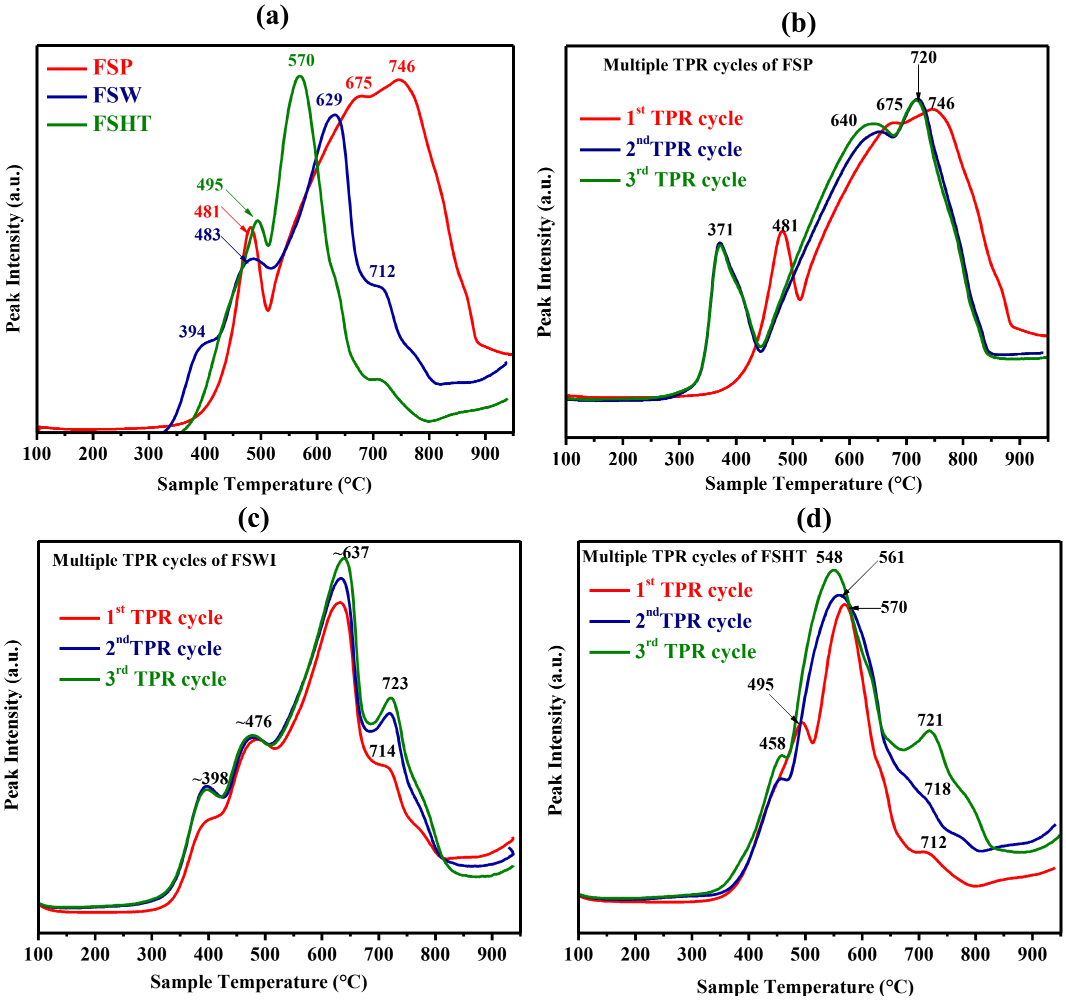

Figure 4.25 (a) TPR plot of 1st cycle of all synthesized samples (b) multiple TPR cycles of FSP (c) multiple TPR cycles of FSWI (d) multiple TPR cycles of FSHT

4.3.2.7 Catalytic Activity for Sulfuric Acid Decomposition Reaction

The catalytic activities of all the samples (20-45 mesh) for sulfuric acid decomposition in the temperature range of 500-900 °C were assessed and depicted in Figure 4.26(a).It is very clearly evident from the figure that the catalytic activity increased with sample temperature which is due to the kinetic parameters. The SO_2 yield was nearly same till 700 °C and above 700 °C the trend observed was FSP > FSWI ~ FSHT. At 750 °C the SO_2 yield of 76.2 % was found to be highest for FSP amongst all three samples. However the SO_2 yield was comparable at 900 °C. Before emphasizing any catalyst as an ideal catalyst for the sulfuric acid decomposition reaction it is indeed essential to study the catalytic activity for long term duration. The catalytic activity of FSP was performed for 100 h at 800 °C and it is shown in Figure 4.26(b). The conversion rate was found to be 79 % and it was nearly constant throughout the 100 h run. The activation energy for the reaction in presence of the various catalysts was evaluated by using the Arrhenius rate equation. The plot of $\ln\{\ln[1/(1-X)\}$ vs $1/T$ provided us the activation energies from the above equation (shown in Figure 4.26c) and were found to be 83.5 $kJmole^{-1}$ for FSEQ, 83.3 $kJmole^{-1}$ for FSP, 109.9 $kJmole^{-1}$ for FSWI and 92.0 $kJmole^{-1}$ for FSHT. The activation energies evaluated exactly followed the trend observed for the catalytic activity of the various catalyst performances in sulfuric acid decomposition reaction.

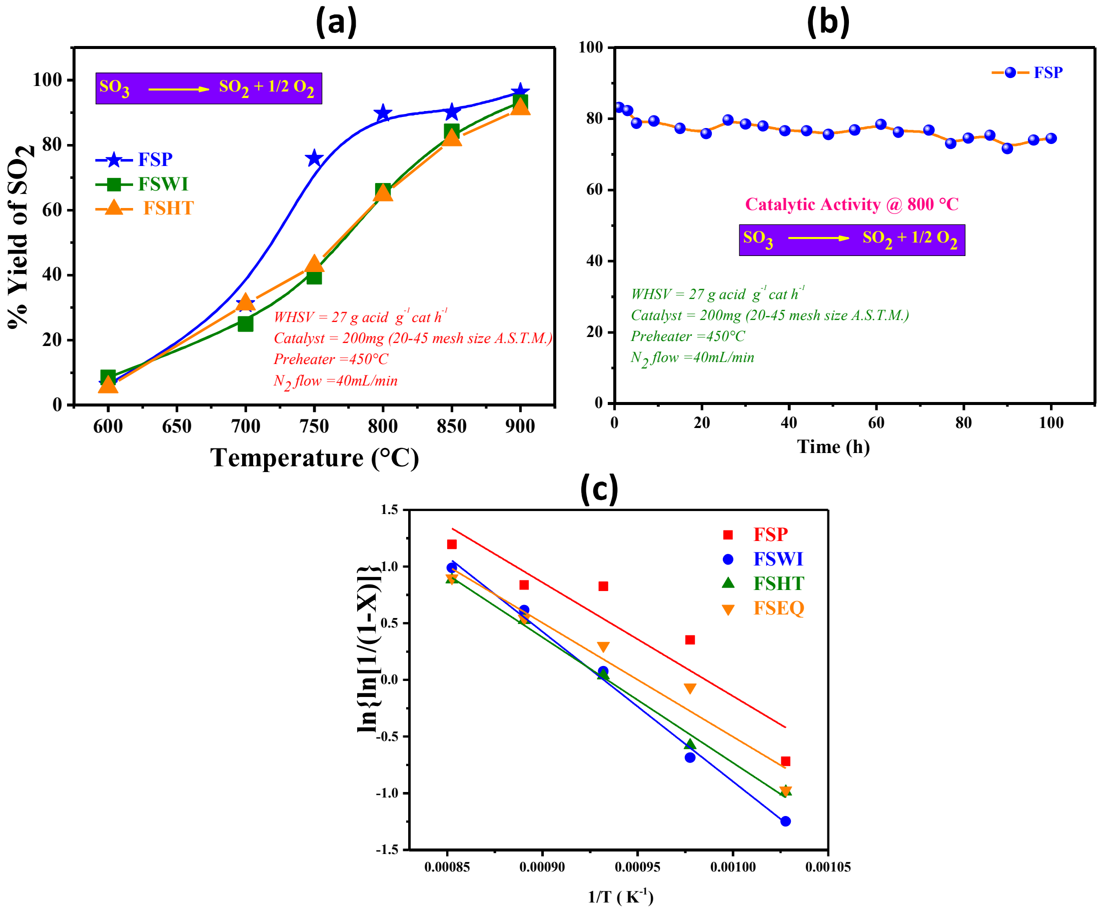

Figure 4.26: (a)Temperature dependent activity profiles as a function of temperature of all samples calcined at 1000°C, (b) Plot of catalytic activity of Fe_2O_3(15 wt.%)/SiO_2 (20-45 mesh) for sulfuric acid decomposition reaction for 100 h time on stream at 800 °C (c) Arrhenius plot

4.3.2.8 Study of the Catalyst Post Evaluation of the Activity:

In order to understand the mechanistic aspects involved during the interaction of the reactant with the sulphuric acid, it is very much essential to get aware about the characteristics of the intermediates which are actually formed in the interspersed steps before proceeding to the product formation. The post activity evaluation of the spent catalysts thus could be a clear evidence to study the nature of the metastable intermediates. The spent samples were collected and characterised by XRD, FTIR, DTG-EGA to understand the modification happening in the used sample. XRD pattern of spent samples are displayed in Figure 4.27(a) and it is very clearly indicative of amorphisation of the sample. The broad hump being visible, along with disappearance of the minor crystalline Fe_2O_3 phases. FTIR spectra shown in Figure 4.27(b) and peaks attributing to Fe-O, Si-O vibrations are very clearly evident even in the spent samples. Thus indicative of the catalyst to be present in the initial form observed during its preparative stage and retaining its structure; thus proving to be a stable catalyst, even under harsh environment. The DTG patterns of all the spent samples are shown in the Figure 4.28. The predicted mechanism as explained in the chapter 3 as well as in the prior explained in this chapter (Figure 4.20) found to be also observed with this series of dispersed iron oxide catalysts which were prepared by different methods. As evident in Figure 4.28 two peaks observed in the region at ~ 115 °C & 235 °C. The first peak can be attributed due to loss of moisture content however the reason for occurrence of peak at ~235 °C is still unclear, but the strong possibility seems to be due to SO_3/SO_2 removal from weakly held surface sites. A prominent peak at 635 °C can be ascribed to the dispersed iron sulfate decomposition.

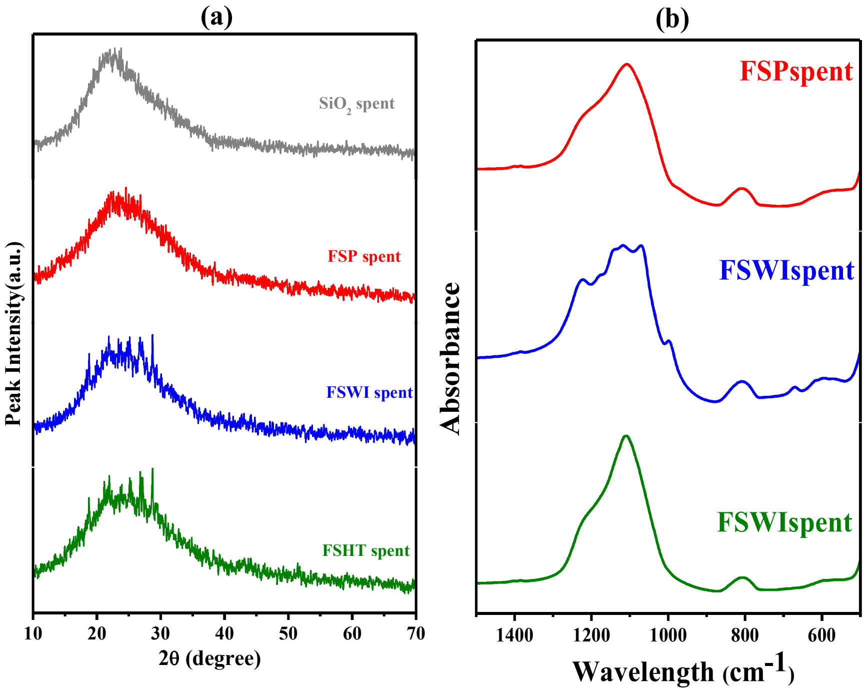

Figure 4.27: (a) XRD pattern (b) FTIR spectra of spent catalyst

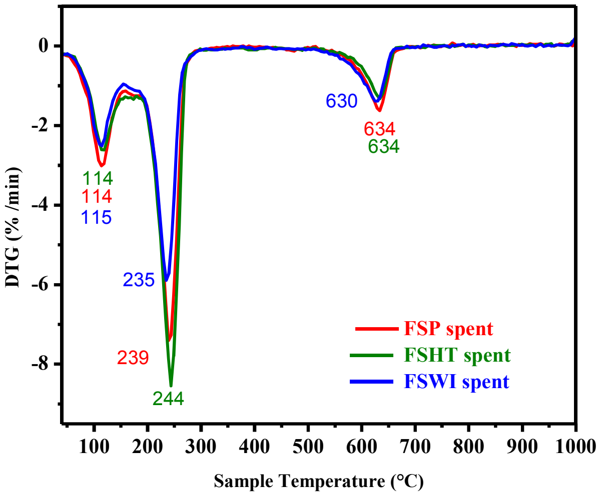

Figure 4.28: DTG pattern of all the spent catalysts after employing for sulfuric acid decomposition reaction.

4.4 Conclusions

Fe_2O_3/SiO_2catalysts were successfully prepared by four different methods viz. equilibrium-adsorption, polyol, solvothermal and wet impregnation. All the catalysts were found to be active and stable for high temperature sulfuric acid decomposition reaction. The FSP sample which was prepared by polyol method had the highest activity for the sulfuric acid decomposition reaction and the trend followed as FSP > FSEQ > FSWI~ FSHT. The high activity can be ascribed to the nanoparticulate nature of the Fe_2O_3 phase which facilitates reducibility of Fe_2O_3 species while active component-support interactions ensure stability of the catalyst during prolonged uses. To optimize the Fe_2O_3 loading on SiO_2 samples having variable compositions (5-20 wt. %) were also prepared and evaluated. The 15 weight percent of Fe_2O_3 on the SiO_2matrix was arrived as the optimum concentration of iron oxide exhibiting maximum pore confinement, superior redox properties and highest catalytic activity. Substantial structural and morphological rearrangements took place in the catalyst during 100 h use, but catalytic activity was retained to reasonable levels. A concerted phenomenon of surface sulfate formation and decomposition was found to be the most probable mechanism for decomposition of sulfuric acid over nanodispersed iron oxide catalyst. The present study will contribute to the design and probable use of supported nanoparticles for high temperature sulfuric acid decomposition reaction.

Chapter 5: Studies on electrocatalyst for SO_2 aqueous electrolysis and its evaluation in PEM based electrolyzer

5.1 Introduction

The hybrid sulfur cycle (Eqn. 5.1-5.3), is a thermochemical water splitting hydrogen generation process involving both thermal sulfuric acid decomposition and electrolysis of aqueous SO_2. We have dealt in details regarding the catalyst development in the thermal sulfuric acid decomposition step in chapter 3 and 4.This chapter specifically deals with the electrocatalyst development and feasibility studies of aqueous SO_2 electrolysis. In aqueous SO_2 electrolysis, the anodic reaction is the oxidation of sulfur dioxide to sulfuric acid (Eqn. 5.4) and the hydrogen evolution reaction occurs at the cathode (Eqn. 5.5).The originally designed electrolyzer comprised two compartments separated by membrane, however with advancement it got modified to membrane electrode assembly (MEA) based compact electrolyzer. Aqueous SO_2 electrolysis can most efficiently be carried out in a PEM based electrolyzer in which the protons generated in the anodic compartment by aqueous SO_2 oxidation migrates across the proton exchange membrane to the cathodic compartment where the proton is reduced and generates gaseous hydrogen as shown in Figure 5.1 [40-47]. The aqueous SO_2 oxidation and the hydrogen evolution reaction (HER) are kinetically slow and require an electrocatalyst to accelerate the processes. The main focus in this chapter is to study the aqueous SO_2 electrolysis process by using a proton exchange membrane based electrolyser. A series of Pt/C electrocatalyst with weight percentages of Pt of 10, 20 and 40 with respect to carbon were prepared by chemical reduction method and were evaluated for the two individual half-cell reactions viz. aqueous SO_2 oxidation (Eqn. 5.4) and hydrogen evolution reaction (HER) (Eqn. 5.5). The catalyst having the optimum loading of Pt was employed as the electrocatalyst in PEM based electrolyzer for fabrication of MEA and tested for aqueous SO_2 electrolysis in the indigenously developed electrolyzer.

With an attempt to replace the noble metal Pt-based catalyst, another series of non-noble metal i.e. molybdenum carbide catalyst supported over the Vulcan carbon was developed which was also studied for HER. The requirement of Pt as electrocatalyst makes the process expensive and thus tremendous efforts have been focused on finding suitable cheaper alternative to Pt for HER. Among the promising candidates mention must be made of MoS_2 [162], Ni_2P [163], MoB [164], Mo_2C [164] and MoN [165] – all having reasonable stabilities in acidic medium under which the PEM based electrolysers operate. Mo_2C has the typical advantage of being a structural analogue to Pt and is considered as an effective electrocatalysts for HER due to their similar d-band electronic density-of-state, high electrical conductivity, and optimal hydrogen-adsorption properties [165].The anchoring of Mo_2C on the carbon support downshifts the d-band center of molybdenum which decreases the hydrogen binding energy. As a consequence, Mo_2C based materials are being extensively examined in recent times targeting improvements in HER catalytic activity. In this chapter we report series of Mo_2C/C electrocatalyst prepared by dispersing Mo_2C over commercially available Vulcan carbon XC-72R by in-situ carburization method [43]. Attempt was made to determine the optimum loading of Mo_2C on the carbon support. The prepared materials were characterized by powder XRD and XPS techniques to understand the crystal structure and surface properties of the compositions. The electrochemical properties were investigated by cyclic voltammetry, linear sweep voltammetry, electrochemical impedance spectroscopy to determine the performance of the electrocatalysts and probable mechanism under operation.

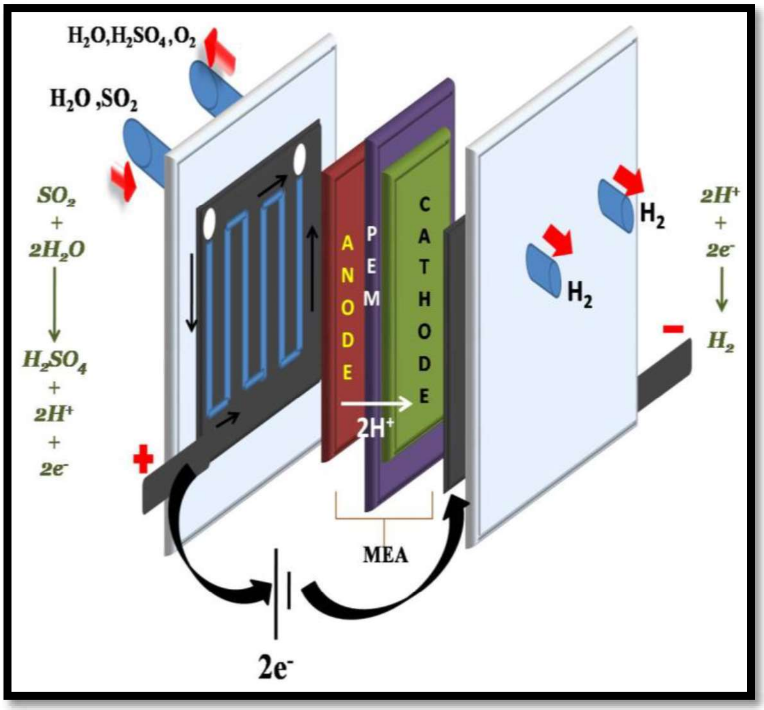

Figure 5.1: Schematic of the PEM based electrolyzer for aqueous SO_2 electrolysis

Hybrid -Sulfur Cycle (Hy-S cycle):

Sulfuric acid decomposition: $H_2SO_4 \leftrightarrow SO_2 + 0.5O_2 + H_2O$ (800 – 900 °C)------ (5.1)

Aqueous SO_2 electrolysis: $SO_2 + 2H_2O \leftrightarrow H_2SO_4 + H_2$ (RT, $E° = 0.158$ V) --------(5.2)

Net reaction: (water splitting) $H_2O \leftrightarrow H_2 + 0.5O_2$--------(5.3)

Electrochemical Steps in Aqueous SO_2 Electrolysis

$SO_2 + 2H_2O \rightarrow H_2SO_4 + 2H^+ + 2e^-$(At Anode)---------------------------- (5.4)

$2H^+ + 2e^- \rightarrow H_2$ (At Cathode)---------------(5.5)

Net reaction: $SO_2 + 2H_2O \leftrightarrow H_2SO_4 + H_2$---------------(5.2)

In the earlier study by Westinghouse cycle, 200 mA/cm^2 was achieved at 0.6V applied voltage, Later 500mA/cm^2 was achieved at 0.6 V potential by Staser etal using gaseous SO_2 [42]. Electrolyzer design included the use of a membrane electrode assembly (MEA) as shown in Figure 5.1

5.2 Experimental

5.2.1 Preparation of Pt/Carbon Electrocatalyst

Vulcan carbon (XC72R) supported Pt in different loadings such as 10, 20 and 40 wt. % was synthesized by chemical reduction method. In chemical reduction, required amount of $H_2PtCl_6.H_2O$ solution was added to an aqueous suspension of carbon (Vulcan-XC72R). To this mixed solution slight excess of sodium borohydride solution was added dropwise with continuous stirring to obtain platinum in metallic state dispersed over carbon. This solution was aged overnight followed by filtration. The product obtained in each case, was washed with water, acetone and then dried in an air oven at 80 °C. These catalysts were characterised by powder XRD and SEM.

5.2.2 Electrochemical Studies for Pt/C

For electrochemical measurements, catalyst inks were prepared by dispersing 5 mg of each of the above samples separately in mixed solution of water and Nafion (5 wt.%). All the electrochemical measurements were performed in three electrode configuration with Pt as the counter electrode, saturated calomel electrode (SCE) as the reference electrode and the Pt/C deposited on GC as the working electrode in a Biologic Scientific InstrumentPotentiostat/Galvanostat (VSP-2). The electrochemical characterization was performed by measuring the cyclic voltammetry in 0.5 M H_2SO_4 after purging N_2 for 0.5 h. Polarization measurements for hydrogen evolution reaction was carried out in 0.5 M H_2SO_4. Also these catalysts were evaluated for aqueous SO_2 electrolysis using three electrode system in SO_2 gas saturated 0.5 M H_2SO_4.

5.2.3 Design and Development and Testing of 4 cm^2 Active Area PEM Based Electrolyser

20 wt. % Pt which was dispersed on Vulcan carbon XC72R by chemical reduction method was chosen as the electrode material for studying the aqueous SO_2 electrolysis in a PEM type electrolyzer [159-161]. The ink was prepared by sonicating the required amount of the Pt/C electrocatalyst in isopropanol: water: Nafion solution mixture. Then the ink was brush coated on the Toray carbon paper of dimension 2×2 cm^2 to obtain loading of 4 mg/cm^2. A set of two such electrocatalyst loaded carbon paper was assembled on either sides of Nafion 117 membrane. Subsequent layers were the hastelloy flow field plate (3 mm thickness) with 1 mm width grooved serpentine channels followed by gold coated copper terminal plate and finally the Perspex pressure plates (Figure 5.6). SO_2 saturated 25% H_2SO_4 was the anolyte solution whereas the catholyte solution used was 25% H_2SO_4. These solutions were stored in a reservoir and then pumped to the respective electrodes using a pump at constant flow rate 15 ml/min as shown in the Figure 5.7. So initially it was allowed to equilibrate by allowing the flow for about 45 minutes by only passing the sulfuric acid (25 %) and then proceeding to flow of SO_2 purged solution for about 15 minutes.

5.2.4 Electrochemical Properties of Mo_2C/C for Hydrogen Evolution Reaction

A series of molybdenum carbide catalysts were attempted to be dispersed on Vulcan carbon having weight percentages of Mo metal equivalent to 10, 20, 30 and 40 with respect to the initial weights of Vulcan carbon employed. The preparation of the samples were carried out by carburization of the Vulcan carbon supported ammonium molybdate $(NH_4)_6Mo_7O_{24}.4H_2O$ as shown in Figure 5.8. Vulcan carbon on supported ammonium molybdate was synthesized by impregnation of the aqueous ammonium molybdate solution over Vulcan carbon. 1 gm of Vulcan carbon and requisite amount of ammonium molybdate was dispersed in water-methanol (1:1) mixture. The mixed solution was stirred for 6 h and then evaporated to dryness on a hot plate. The collected residue using Buchner funnel by filtration through Whatman paper was initially dried in hot air oven for about 2h. Subsequently, the carburization of Vulcan carbon-supported ammonium molybdate of different concentrations was carried out by heating the powdered precursor samples in Ar flow (50mL/min) in a tubular furnace at 800 °C for 2 h. The heating rate was maintained at 10 °C min^{-1}. A reference sample was prepared where the weight ratio of Mo and vulcan carbon taken were maintained at 2:1 and thereafter similar protocol as above was employed. ICP-OES technique was employed to evaluate the Mo content in eachelectrocatalyst catalyst by microwave digestion of the powders in conc. HNO_3-HCl (aqua regia). The powder XRD patterns of the samples were recorded by Philips X'Pert pro X-ray diffractometer using Cu K_α radiation (λ= 1.5418 Å) at 40 kV and 30 mA.To study the surface characteristics X-ray photoelectron spectra (XPS) of each sample was recorded in a spectrometer (SPECS, Surface Nano Analysis GmbH, Germany) using Mg-K_α X-rays (hν =1253.6 eV) as the primary source of radiation with an overall energy resolution of the instrument of about 0.7 eV. The corrections for charging effect were made with the help of a C 1s signal appearing at 284.5eV.

The electrochemical measurements were carried out by using Mo_2C/VC deposited on Glassy Carbon Electrode (GCE) as the working electrode, saturated calomel electrode (SCE) as the reference electrode and Pt as the counter electrode. Catalyst inks were prepared by dispersing each of the above samples separately in water and Nafion (5 wt. %) solution mixture. 5 μl of this ink was then deposited on a GC electrode (3 mm diameter) to prepare the Mo_2C/VC. The electrochemical studies that were carried out included cyclic voltammetry measurements, electro catalytic activity for hydrogen evolution reaction and impedance measurements in the frequency range of Hz. All electrochemical measurements were carried out in 0.5 M H_2SO_4.

5.3 Results and Discussions:

5.3.1 Evaluation of Pt/C Electrocatalyst for Hydrogen Evolution Reaction and Aqueous SO_2 Oxidation

The XRD pattern of the synthesized sample has been shown in Figure 5.2, from the figure the graphitic carbon peak at 2θ ~26° were observed. The peaks reflected at 2θ = 39.8, 46.4 and 67.7° can be attributed to the characteristic peaks of platinum (ICSD no 064917). Thus, it assures the presence of platinum in the metallic state along with graphitic nature of carbon; even after dispersing noble metal on the carbon support. The crystallite sizes of all the catalyst were evaluated using the Scherer equation and it was found to be in the range of ~ 3-5 nm.

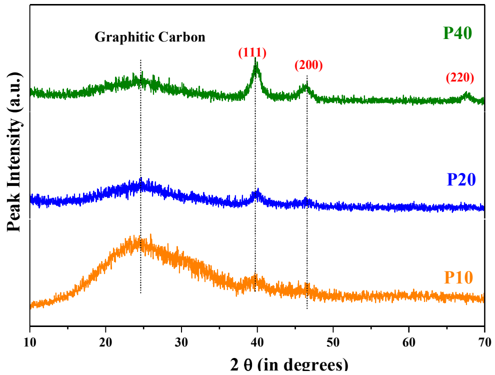

Figure 5.2: XRD pattern of P10, P20 and P40 sample

Cyclic voltammetry was performed by depositing the catalyst on glassy carbon working electrode in 0.5 M H_2SO_4.The Pt loading of the samples P10, P20 and P40 were3.5, 7.1 and 14.2 μg/cm^2.The potentiodynamic curves as seen in Figure 5.3 resembled the shape to those obtained in bulk metals. The cyclic voltammogram exhibits characteristic peaks due to hydrogen adsorption, hydrogen evolution and hydrogen desorption in the respective regions. Further, the peaks due to surface oxide formation, oxygen evolution and surface oxide reduction are also clearly observed. The Electrochemical Surface Area (ECSA) mentioned in Table 5.13 were calculated by integrating the reduction peak of the chemisorbed oxygen from the cyclic voltammograms due to the fact that oxygen desorption charge can be compared with the charge due to hydrogen monolayer desorption charge [158].The charge corresponding to reduction of a monolayer of surface oxide per unit area was considered as 420 μC cm^{-2}. Amongst the series P 20 has the highest surface area. ECSA of the samples prepared varied as P20>P40>P10. Multiple CV run upto 100 cycles for individual electrocatalyst in the range 0.1 to 1.2V vs NHE @ 100mVs^{-1}. It was noted that polarization curves resembled to the initial cycle which ensures its long time stability.

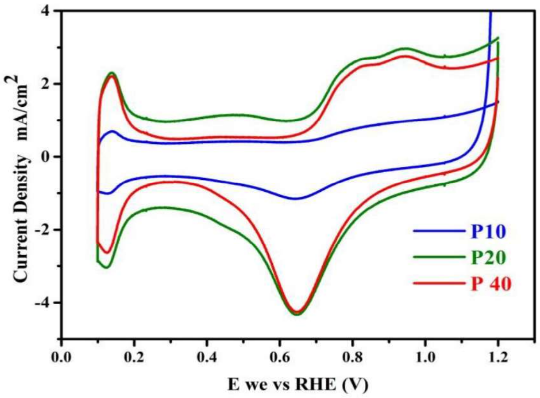

Figure 5.3: Cyclic voltammograms of the samples carried in 0.5M H_2SO_4

Table 5.13: Electrochemical active surface area (ECSA) of the samples

Sample	ECSA(m^2/g)
P10	129
P20	179
P40	141

Activity for (HER) Hydrogen Evolution Reaction of all the samples evaluated in 0.5 M H_2SO_4 is shown in Figure 5.4.From the polarisation curves we can observe that activity of all catalyst for HER showed the trend as P20> P40>P10.

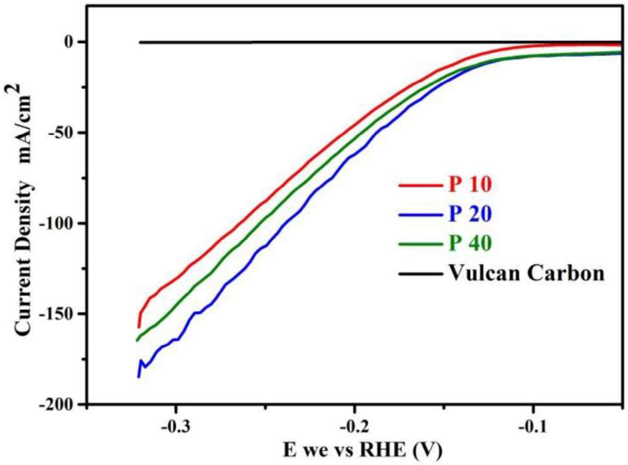

Figure 5.4: Polarization curve of Hydrogen Evolution Reaction of all the samples in 0.5M H_2SO_4

Aqueous SO_2 electrolysis was performed in SO_2 saturated 0.5 M H_2SO_4 by depositing the catalyst on the GCE via preparation of the ink of the respective electrocatalysts. The polarization curve obtained as shown in Figure 5.5. The onset of SO_2 oxidation was observed at 0.75 V with respect to RHE. From the comparative graph it is very evident that the P20 showed better catalytic performance than P40. The current density of P20 (0.45 mA/cm^2)was higher than that observed in the case of P40 samples(0.33mA/cm^2).Thus from all the comparative study it is very clear that P20 sample stands out to be the best electrocatalyst.

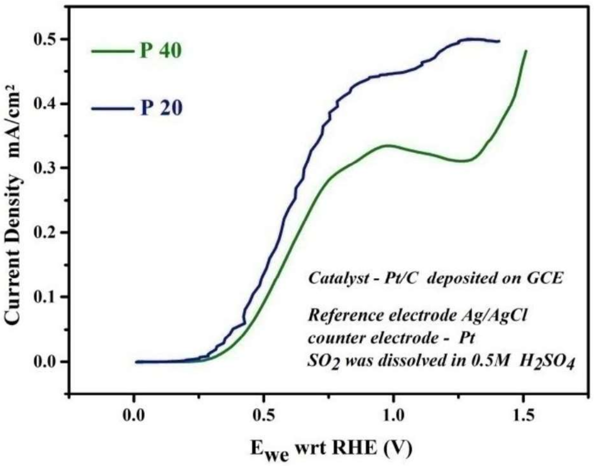

Figure 5.5: Polarization curve of aqueous SO_2 electrolysis in SO_2 saturated 0.5 M H_2SO_4

5.3.2 Testing of Single Cell Electrolyzer

The I-V plot obtained during the aqueous SO_2 electrolysis has been shown in Figure 5.8. At 1 V applied potential 75 mA/cm^2 current density was observed and this value was constant throughout the 2 h analysis.

Figure 5.6: Photograph of single PEM type electrolyzer cell (4 cm^{2}active area)

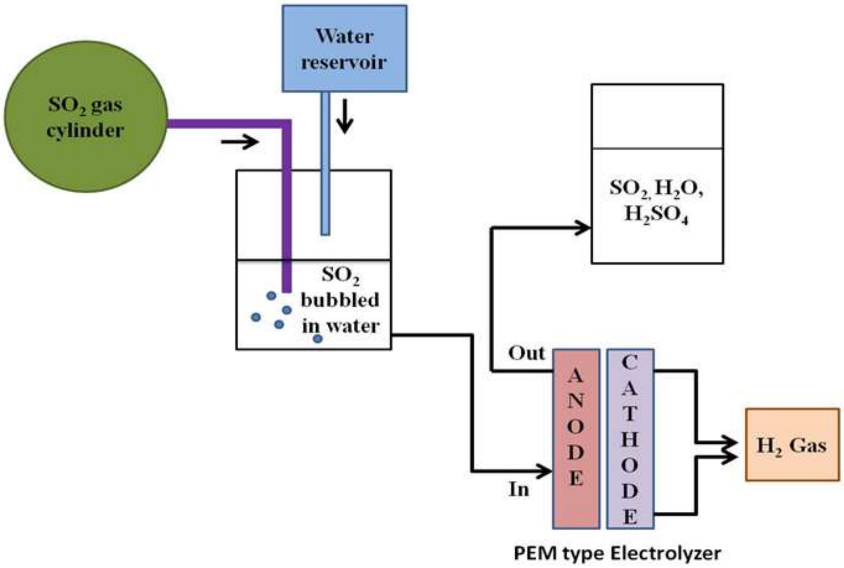

Figure 5.7: Schematics of the set-up used for aqueous SO_2 electrolysis

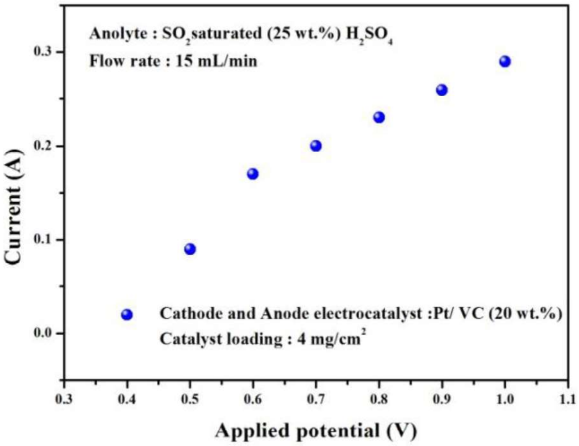

Figure 5.8: I-V Curve of the single cell (4 cm^2 area) assembled by using 20 % Pt/VC XC72R as the electrocatalyst.

Post the evaluation of aqueous SO_2 electrolysis; the catalyst loaded carbon paper was analyzed by XRD technique, shown in Figure 5.9. Sharp peaks observed for both the surfaces at $2\theta = 26$ and 54 degrees which could be attributed to the carbon present in Toray carbon paper.

The characteristics peak due to the metallic platinum observed in the fresh sample was also prominently visible (shown in inset in Figure 5.9).

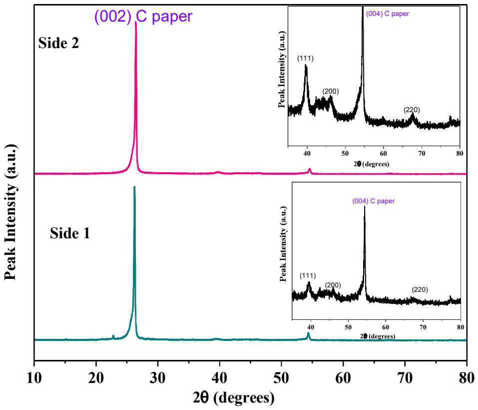

Figure 5.9: XRD pattern of Pt/C loaded on Toray carbon paper post aqueous SO_2 electrolysis

5.3.3 Evaluation of Mo_2C Dispersed on Vulcan Carbon for HER

The abbreviation of the samples used, the expected compositions, the actual composition, the phases obtained from powder XRD patterns and the crystallite size obtained from the (101) peak of Mo_2C phase are listed in Table 5.14. The loading of Mo attempted was 10, 20, 30 and 40 wt. % w.r.t. the initial amount of Vulcan carbon employed. The actual composition was found to be lower as compared to the attempted and the difference kept on increasing as the concentration of Mo was increased.

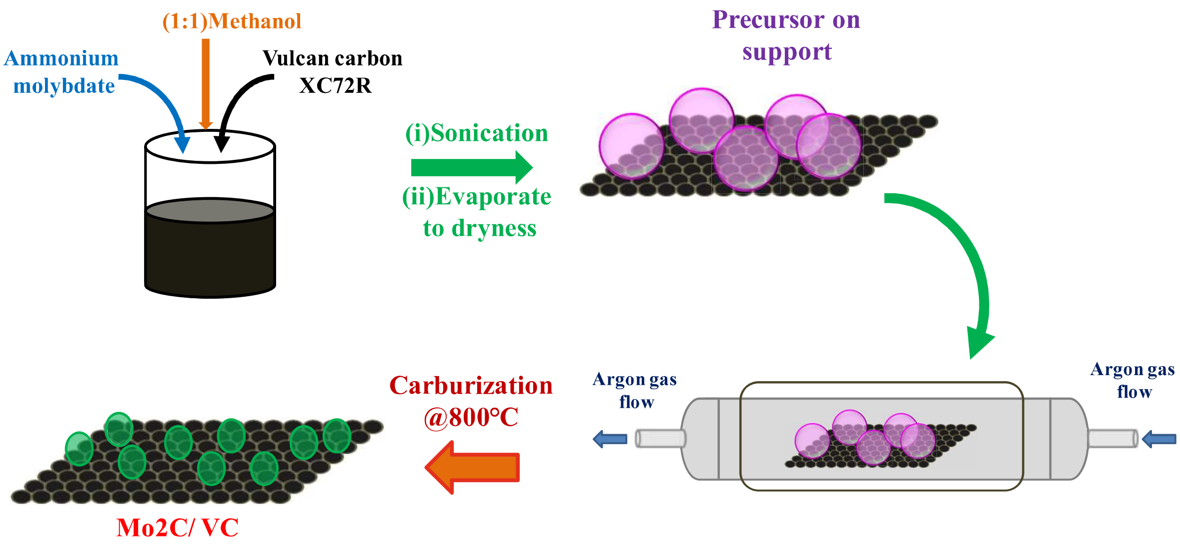

Figure 5.10: Schematic representation of the preparation of Vulcan carbon supported Mo_2C

The TG pattern of the Vulcan carbon supported ammonium molybdate is shown in Figure 5.11. The weight loss at 350 °C can be attributed to the conversion of ammonium molybdate to MoO_3, [166] the weight loss at ~ 600 °C can be ascribed to the conversion of MoO_3 to MoO_2 while the final weight loss at the temperature hold at 800 °C was due to the formation of Mo_2C by solid state reaction between the MoO_2 and carbon support which involves a weight loss. This TG pattern can justify the decrease in the observed Mo content as compared to the expected composition. This is because in each of the weight loss step indicated above there is a possibility in the reaction of carbon support with either moisture or oxygen to yield CO/CO_2.

Table 5.14 The samples synthesized, their abbreviation the molybdenum content, phases as derived from powder XRD and the crystallite size using Scherrer equation

S.No.	Sample	Abbreviation	Expected Mo content wt%	Observed Mo content wt%	Phases present from powder XRD	Crystallite size (nm)
1	10% Mo_2C /VC	MoC_1	10	9.3	Orthorhombic β-Mo_2C and graphitic hump	16.25
2	20% Mo_2C /VC	MoC_2	20	15.8	Orthorhombic β-Mo_2C and graphitic hump	16.7
3	30% Mo_2C /VC	MoC_3	30	20.4	Orthorhombic β-Mo_2C and graphitic hump	20.5
4	40% Mo_2C /VC	MoC_4	40	28.0	Orthorhombic β-Mo_2C and graphitic hump	17.22
5	MoO_2	MO	-	-	Monoclinic MoO_2	41.61
6	VC	VC	-	-	Graphitic hump at 27 degrees	0.59

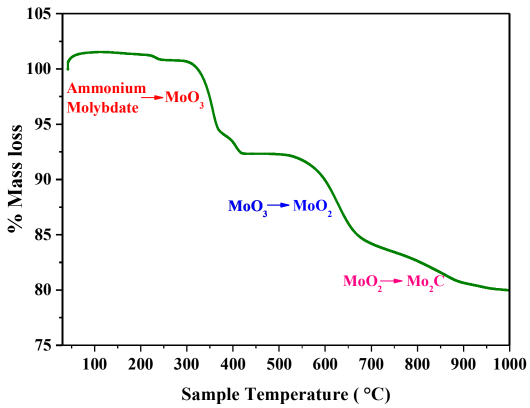

Figure 5.11: TG plot of the precursor ammonium molybdate.

The powder XRD patterns of the samples are shown in Figure 5.12. The vulcan carbon showed the hump characteristic due to graphite at 2θ = 27 degrees. The MO sample prepared by heating ammonium molybdate exhibited peaks characteristic of MoO$_2$ phase. β-Mo$_2$C phase evolved in all the other samples with the 100 % peak appearing at 2θ ~ 39 degrees corresponding to the (101) plane. In the MoC4 sample all peaks due to β-Mo$_2$C are distinct and are marked

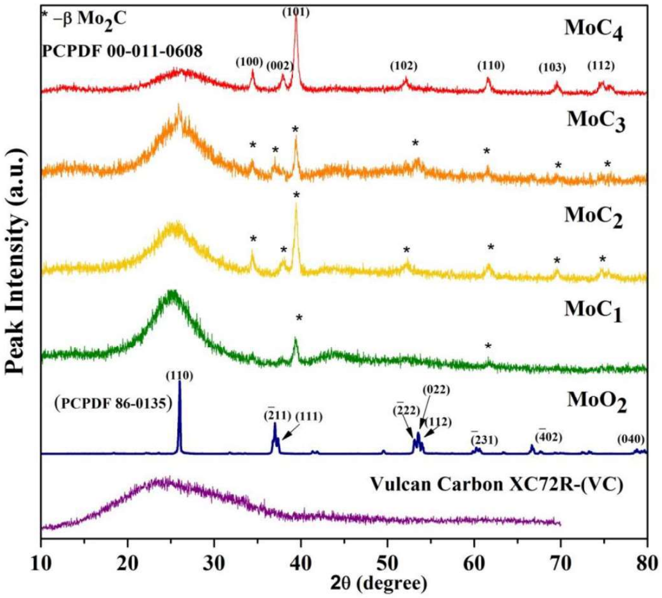

Figure 5.12: Powder XRD patterns of each synthesized unsupported samples along with unsupported sample calcined at 800°C and Vulcan carbon

The X-ray photoelectron spectra (XPS) of the Mo3d and C 1s of the prepared samples are shown in Figure 5.13. XPS or ESCA (Electron spectroscopy for chemical analysis) is a surface analysis tool in which the analytical volume restricted to approximately five monolayers [167]. Thus, the XPS patterns of the samples provided information about surface chemical state. It is evident from Figure 5.13(a) that Mo exist in multiple oxidation states Mo^0, Mo^{2+}, Mo^{4+} and Mo^{6+} as revealed by deconvolution of the Mo 3d peak [168]. The 3d5/2 peak for Mo^0, Mo^{2+}, Mo^{4+} and Mo^{6+} appears at BE values of ~ 227.8, 228.5, 229.5 and 233 eV [122,169].The Mo of low valency (Mo^0, Mo^{2+}) are generally active while that of Mo^{4+} and Mo^{6+} appearing due to presence of surface MoO_2 and MoO_3 because of aerial oxidation of the carbides are inactive [166]. It is evident from Figure 5.13 that the content of lower valent state of Mo increases in intensity from MoC1 to MoC2 to MoC3 but in MoC4 the intensity of the low valent Mo decreases. Thus, the active low valent Mo is most predominant in MoC3 among all the samples. The C1s spectra can be deconvulated into a graphitic, carbidic and carbon having adsorbed oxygen (organic) and is shown in Figure 5.13(b).

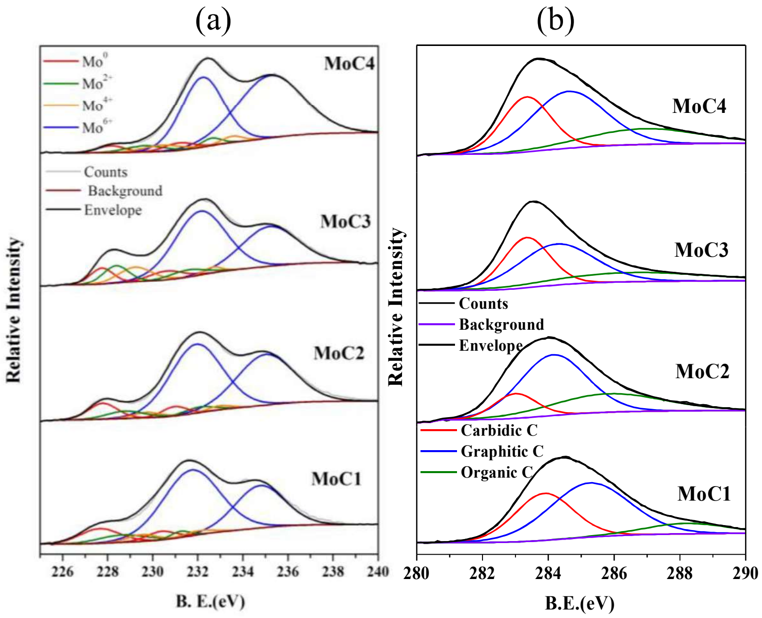

Figure 5.13: (a) XPS plot of Mo 3d and (b) XPS plot of C for MoC1, MoC2 , MoC3 and MoC4 samples.

The electrocatalytic performances of the prepared electrocatalysts and that of Pt (20 wt.%)/VC having similar loading for hydrogen evolution reaction are shown in Figure 5.14 which represents the LSV curves at 2 mVs^{-1} of each sample in 0.5 M H_2SO_4. It is evident from the figure that all the electrocatalysts are active for HER in acidic media. The current densities exhibited by each sample at overpotential of 0.4 mV are as follows: MoC1, MoC2, MoC3 and MoC4 are 9.44, 17.26, 19.04 and 6.44 mA/cm^2 resp. The trend in increase in electrocatalytic activity is according to an increase in the active component the α–Mo_2C phase, upto a concentration of 30 wt. % of Mo wrt initial carbon beyond which again the electrocatalytic activity decreases. Thus, the optimum loading of the active α-Mo2C phase is 30 wt.% of Mo wrt initial vulcan carbon taken.

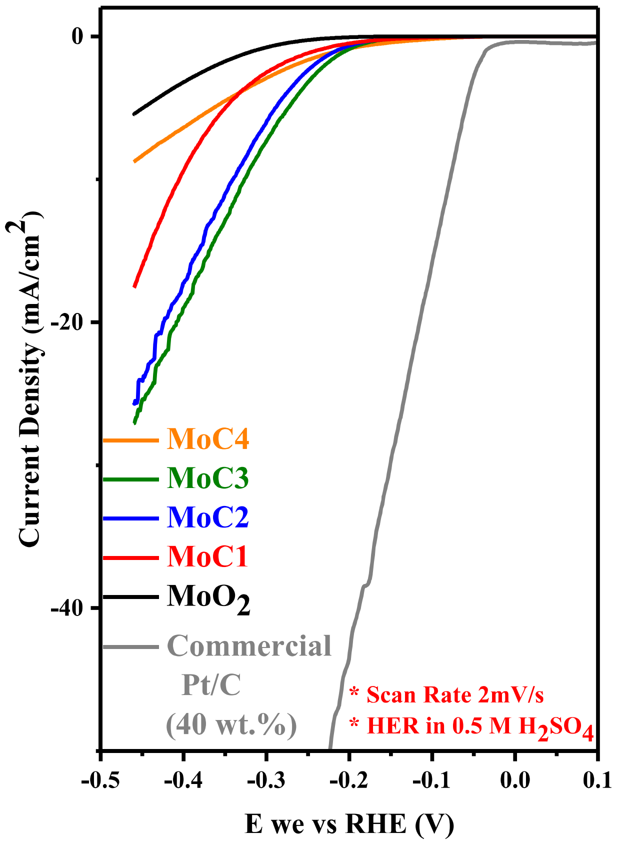

Figure 5.14: Polarisation curves of carbon supported samples (MoC1, MoC2, MoC3, MoC4), unsupported sample (MoO_2), Vulcan carbon and commercial Pt (40 wt.%) in 0.5M H_2SO_4 (scan rate 2mV per s)

The Tafel plots which are useful in delineating the predominant HER reaction mechanism are shown in Figure 5.15 [162]. The corresponding Tafel slopes and the exchange current densities are listed in Table 5.15. It is well known that the HER reaction, a multistep one, proceeds via the reaction mechanism shown in Figure 5.16. [162]. In the discharge or Volmer step adsorbed hydrogen atoms are generated by simultaneous electron transfer and proton adsorption at electrode surface. These adsorbed species could evolve gaseous hydrogen by either or a combination or two different mechanisms. In Heyrovsky or ion + atom reaction hydrogen evolution occurs by the simultaneous transfer of a second electron and proton at the first adsorbed hydrogen atom site. Alternatively, a second adsorbed hydrogen atom generated by Volmer reaction reacts with the first one on the electrode surface to evolve hydrogen a process named as combination or Tafel reaction. For Pt generally a low Tafel slope is obtained as it is established that HER occurs via the Volmer - Tafel mechanism as also in our case. On the other hand, higher Tafel slopes for the dispersed α-Mo_2C samples suggest operation of the Volmer-Heyrovsky mechanism.

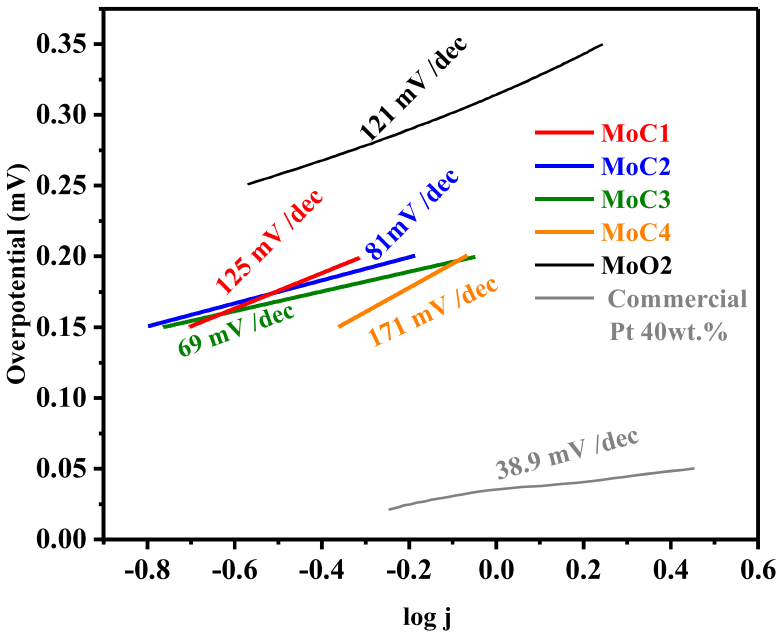

Figure 5.15: Tafel plots for the HER over carbon supported samples (MoC1, MoC2, MoC3, MoC4), unsupported sample (MoO_2), Vulcan carbon and commercial Pt (40 wt.%) in 0.5M H_2SO_4

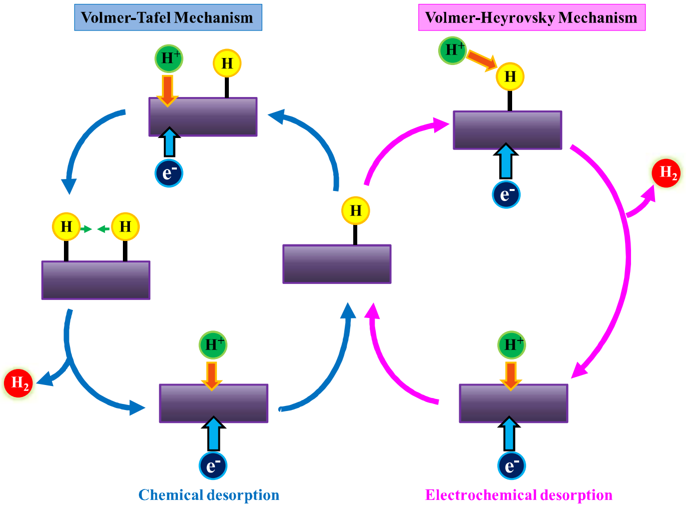

Figure 5.16: Schematic representation of the reaction mechanism for multistep HER.

Table 5.15 Electrochemical properties - Tafel slope and exchange current density

S.No.	**Abbreviation**	**Tafel Slope (mVdecade^{-1})**	**Exchange Current density J$_0$ (mA/cm2)**
1	MoC_1	125.1	1.25 x 10^{-2}
2	MoC_2	81.5	2.3 x 10^{-3}
3	MoC_3	69.6	1.2 x 10^{-3}
4	MoC_4	171.3	5.75 x 10^{-2}
5	MO	121.5	2.5 x 10^{-3}
6	VC	145.2	8.55 x 10^{-3}
7	Pt	38.5	0.135

However, the values of Tafel slope decreases from MoC1 to MoC2 to MoC3 indicating that the proton transfer and electron discharge kinetics improve as the Mo2C content in the electrocatalyst increases. The lowest Tafel slope appears for the MoC3 (~69 mVdecade^{-1}) with an exchange current density of 1.2x10^{-3} mAcm^{-2} suggesting that the kinetics of proton transfer and electron discharge are faster as compared to others. Again, with further increases in Mo2C concentration the kinetics again decreases.

The electrochemical active surface areas of the dispersed Mo_2C samples were evaluated by an indirect cyclic voltammetry method by measuring the electrochemical double layer capacitance (C_{dl}) as discussed elsewhere [166-169]. In this method the double layer capacitance current of each sample is estimated by recording the cyclic voltammetry of each sample at different scan rates as shown in Figure 5.17. This current was then plotted against the respective scan rate from which the slope represented the double layer capacitance.

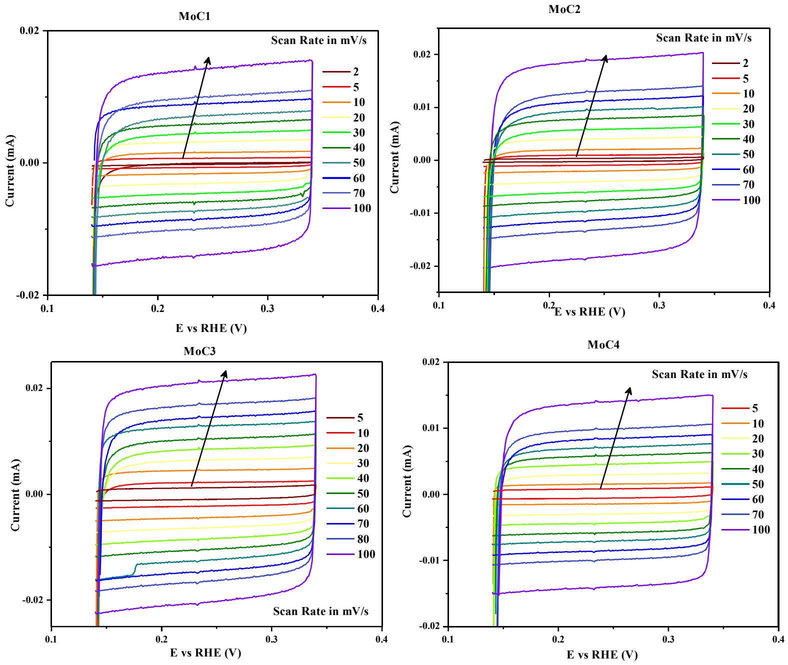

Figure 5.17: Cyclic voltammograms for MoC1, MoC2, MoC3, and MoC4 in 0.5M H_2SO_4 at variable scan rates.

From Figure 5.18, it is very clearly evident that the double layer capacitance of MoC3 is the highest (2.92 mFcm^{-2}) in comparison to MoC1 (1.98 mFcm^{-2}), MoC2 (2.62 mFcm^{-2}) and MoC4 (1.96 mFcm^{-2}). This clearly reflects MoC3 to be having the highest electrochemically active surface area with respect to other compounds prepared in this series. Thus, suggesting to be having porous structure and fine particle size which could provide with more active sites for hydrogen evolution reaction (HER) and thus enhancing HER activity.

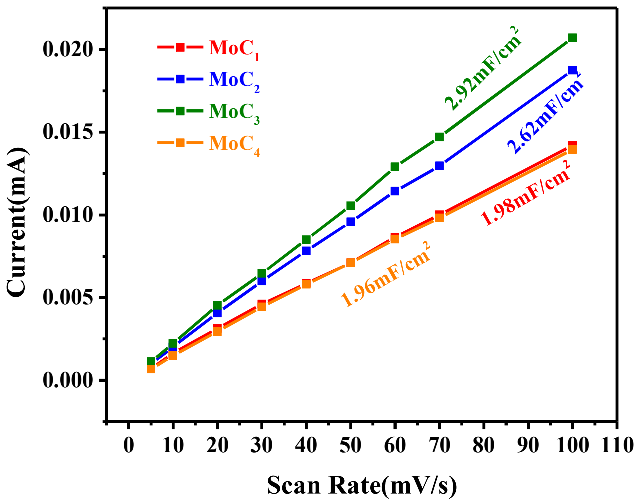

Figure 5.18: Capacitive current based on scan rate at overpotential 250mV for MoC1, MoC2, MoC3, and MoC4

The electrochemical impedance spectroscopic analysis was studied in the overpotential range of 50 to 300 mV in the frequency region 100000 Hz to 0.1 Hz. A two time-constant model was employed to describe the response of the hydrogen evolution reaction on rough electrode surfaces. The model comprised of a series resistance (R_s) which is in series with two parallel branches, out of which one is related to the charge transfer process ($C_{d1} – R_{ct}$) and the second one is related to the surface porosity (C_{d2}- R_p). Here the Rs comprises of various components such as resistance in the wiring, resistance in carbon black, resistance due to carbide and the solution resistance. The Nyquist plot at variable overpotentials in the range 50 to 300 mV as shown in the Figure 5.20, from which the charge transfer resistance is determined and its dependency on the overpotential is very well evident from the Figure 5.19. It is evident that the charge transfer process in most facile in MoC3 sample which is in accordance with the HER activity and ECSA results. However, it is obvious from Fig. 5.20 that the charge transfer resistances are highly dependent on the value of the overpotential at which EIS measurements are made for each electrocatalyst.

Thus, the above study reveals that Mo_2C/Vulcan carbon is an efficient system as a non-noble based electrocatalyst for HER reaction. However, the loading of Mo plays a crucial role as the β-Mo_2C phase is the electroactive dispersed component. The HER activity increases as the Mo content in the sample increases upto 20 wt.% and then decreases. Thus there is an optimum concentration of Mo_2C that provides the electrocatalyst most effective in terms structure, surface composition and electrochemical properties viz. electrochemical active surface area and charge transfer resistance. It is established in this study that 20 wt. % Mo loading in Mo_2C/C is optimum for achieving highest electroactivity for HER.

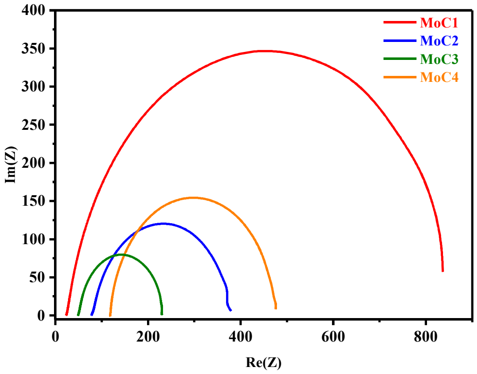

Figure 5.19: Nyquists plot of carbon supported samples (MoC1, MoC2, MoC3, MoC4) recorded at 250mV overpotential in 0.5M H_2SO_4

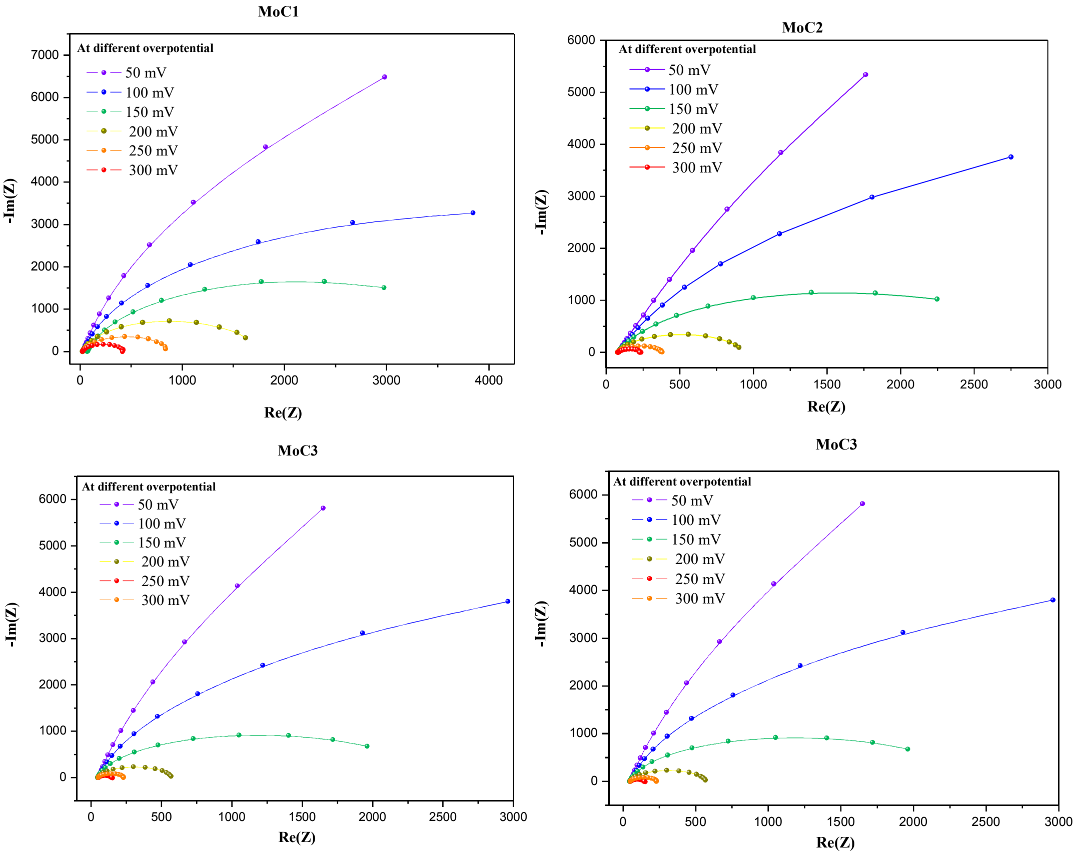

Figure 5.20: Nyquist plot of MoC1, MoC2, MoC3 and MoC4 at different overpotentials in 0.5 M H_2SO_4

5.4 Conclusion:

A series of Pt/C electrocatalyst was successfully prepared by chemical reduction method, characterized and their electrochemical properties tested for hydrogen evolution reaction and aqueous SO_2 oxidation. 20 wt. % Pt was found to be the most effective and thus was employed for the fabrication of a membrane electrode assembly along with Nafion-117 and conducting carbon papers, having 4 $mgcm^{-2}$ of electrocatalyst loading. A single cell PEM based aqueous SO_2electrolyser was designed, fabricated and tested with the MEA and a current density of ~75 $mAcm^{-2}$ was achieved at 1 V. As an attempt to investigate non noble metal based electrocatalyst for the HER reaction, a series of molybdenum carbide electrocatalysts dispersed on carbon with varying Mo content has been successfully synthesized by carburization of ammonium molybdate dispersed Vulcan XC72R. As the Mo content increased the HER activity increased upto 20 wt. % of Mo, which showed the highest activity. The 20 wt. % Mo sample possessed favorable surface properties, exhibited the highest electrochemical active surface area and minimum charge transfer resistance. It is established that 20 wt. % Mo is optimum for achieving highest electroactivity for HER among the samples investigated with ~ 9 to 20 wt. % of Mo.

Chapter6: Demonstration of solar thermochemical sulfuric acid decomposition in a cavity type reactor

6.1 Introduction

It is about few decades, strategy has been set up to converted concentrated solar energy into a useful form of energy.[171-175] Chemical fuels provides with the advantages of being transportable as well as storable for extended periods of time. This point is important because energy demand is rarely synchronous with or geographically matched to incident solar radiation. The production of solar fuels for the transportation sector is considered to be one amongst in the future applications. Solar thermal and thermochemical approaches naturally and work at high temperatures wherein the entire solar spectrum is exploited. Thus a thermodynamically favorable path to solar power and fuel production with high energy conversion efficiencies and, consequently, economic competitiveness could be provided.

Sun is an ultimate source of heat which is equivalent to 5800 K as observed at the point of origin. However, due to geometrical intricacies from sun to earth causes unwanted dilution which thus leaves up to $1kW/m^2$ heat flux reaching the earth terrestrial [176]. Higher solar radiative fluxes with comparatively reduced thermal losses can be brought about using optical concentration devices. Such devices have reflecting surfaces with larger surface area and which could collect the incident solar radiation and concentrate on to a receiver. The solar field is generally designed for direct normal irradiation (DNI) of solar irradiation; hence the Sun Belt region (±40 °) is mostly considered for this application. The regions with high level of humidity and / or aerosol are hardly preferred for concentrating solar power. The solar concentrating technologies primarily used in pilot and commercial level are parabolic trough collectors, linear Fresnel reflector systems, dish-engine systems or central receiver systems (Power towers)[177-178]. The schematic representation of such concentrating systems is illustrated in Figure 6.1.Parabolic trough and linear Fresnel are 2-D concentrating systems that concentrate the incident solar radiation onto a solar receiver which is mounted along the focal line by one-axis tracking mirrors. Such systems best suited for centralized power generation at dispatchable markets with a Rankine steam turbine/generator cycle. Central Receivers, 3-D concentrating systems focusses the incident solar radiation onto a solar receiver mounted on top of a tower by means of a large paraboloid that is isolated into a field of two-axis tracking heliostats. This type of systems is preferred in dispatchable markets and integration into advanced thermodynamic cycles or thermochemical processes. Dish-Engine systems are smaller 3-D two-axis tracking parabolic concentrators which the incident solar radiation onto a Stirling engine or Brayton mini-turbine mounted at the focal point.

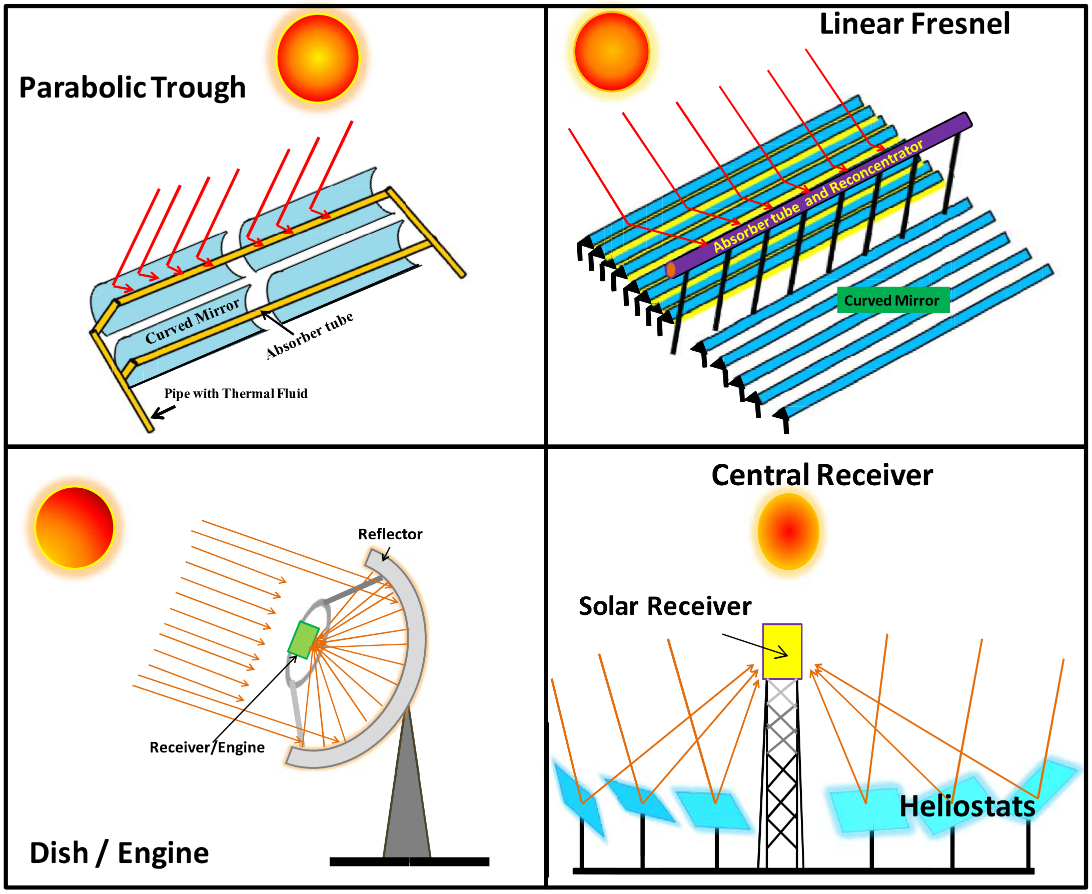

Figure 6.1: Schematics of the four solar concentrating technologies currently applied at commercial CSP plants: parabolic trough collectors, linear Fresnel reflector systems, dish–engine systems, and power towers—also known as central receiver systems

Solar receiver traps the incident solar radiation concentrated by reflector systems utilizing cavities, black painted tube panels or volumetric porous structures. Mostly the solar receiver used is a single unit for optimal utilization of the energy thus inflicting high availability and durability. On the basis of geometrical construction the design of the receiver can be defined in two different forms such as external and cavity type receivers.The cavity-receiver consists of a small aperture into a well-insulated enclosure containing the absorber through which the incident concentrated solar radiation enters. Such cavities are held angularly and then used in north/south-field layouts.

However, external receivers can be cylindrically shaped for surround heliostat fields. Irradiation on receivers could be directly or indirectly performed. Fluids or particle streams exposed directly to the concentrated solar radiation are utilized in case of the direct irradiation. For such pressurized applications necessitated a transparent window. In the case of indirectly irradiated receivers absorbing surfaces exposed to the concentrated solar radiation are used to conduct the heat across the walls to the thermal fluid.

In order to convert solar radiation into a chemical fuel such as hydrogen is an engineering challenge. The thermochemical conversion of solar radiation to hydrogen via a high-temperature water-splitting cycle can be brought as illustrated in the schematics shown in Figure 6.2. Solar thermochemical processes utilizes concentrated solar radiation as the energy source of high-temperature process heat to drive endothermic reactions. Thermochemical cycles for the generation of hydrogen from water consist of a series of chemical reactions which splits water to produce hydrogen and oxygen separately at much lower temperatures than required for the direct thermal decomposition of water. [12] Water splitting into hydrogen and oxygen is achieved via chemical reactions using intermediate products which are recycled. The sum of all the reactions is equivalent to the dissociation of a water molecule. The primary energy source to drive the cycle can be provided by the concentrated solar heat.Such high solar radiation fluxes obtained by the concentrating solar power devices can allow the conversion of solar energy to thermal reservoirs upto1500 K and above which are needed for the more efficient thermochemical cycles. Details of the hybrid Sulfur thermochemical cycle have been explicitly explained in the introduction chapter. In this cycle, sulfuric acid decomposition reaction is the key highest temperature step which utilizes the high-grade heat from a nuclear reactor or a solar concentrator to generate SO_2 and O_2. The SO_2 is utilized in a subsequent electrolysis step to produce hydrogen and sulfuric acid is regenerated. [90] In the present chapter, the designing, fabrication and testing of a quartz reactor to demonstrate the utilization of concentrated solar energy for catalytic decomposition of sulfuric acid which requires a temperature of 800 °C and above has been discussed briefly.

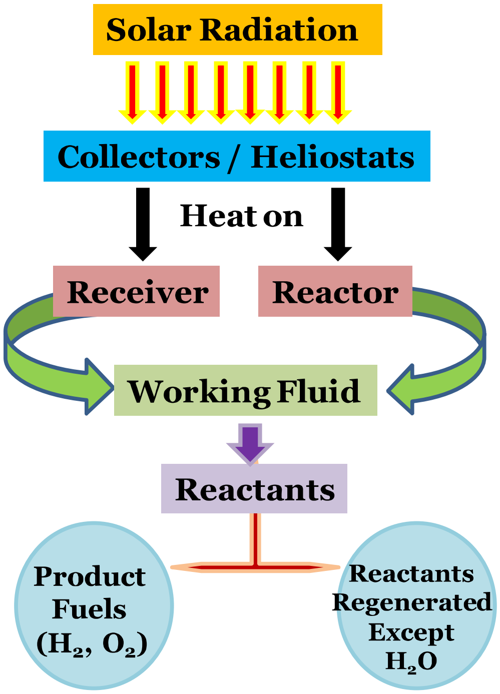

Figure 6.2: Schematic of the conceptual representation of the solar thermochemical processes.

6.2 Experimental:

The sulfuric acid decomposition comprises of the following two reactions in series:

H_2SO_4 (g) = H_2O (g) + SO_3 (g) (~ 450 °C)--------------(6.1)

SO_3 (g) = SO_2 (g) + 0.5 O_2 (g) (~ 800 - 900 °C)----------(6.2)

Sulfuric acid can be decomposed to its anhydride SO_3 with or without a catalyst, while the decomposition of SO_3 has been established to be a catalytic reaction. [89-90] For carrying out solar thermal sulfuric acid decomposition both the reactions are required to be carried out using concentrated solar heat. Thus, the design of the solar reactor should have provision for vaporization, dehydration and then catalytic decomposition of sulfuric acid utilizing the solar heat received from a solar concentrator. Thus there is a need to develop receiver reactor which would be capable to accomplish all the above three processes in a single zone utilizing concentrated solar energy. Solar reactors for highly concentrated solar systems usually feature cavity-receiver configurations, i.e. a well-insulated enclosure with a small aperture to let in concentrated solar radiation. Because of multiple internal reflections, the fraction of the incoming energy absorbed by the cavity greatly exceeds the surface absorbance of the inner walls. As the ratio of the cavity's characteristic length to the aperture diameter increases, the cavity-receiver approaches a blackbody absorber. Hence, for our application, we chose a cavity type configuration of the solar reactor [175]. The transverse and the top view of the cavity type solar receiver-reactor are shown in Figure 2.19. It consisted of a double-walled quartz cylindrical tube with the volume in between the walls vacuum sealed to minimize heat losses. Further during operation the outside wall of the cavity was surrounded by alumina wool. The lower surface of the cavity was a flat quartz plate which served as a window for entry of concentrated solar irradiation. To achieve the vaporization, dehydration and then catalytic decomposition of sulfuric acid as discussed earlier a quartz cylindrical tube was placed within the cavity as shown in Figure 2.19. $Fe_{1.8}Cr_{0.2}O_3$ catalyst [89] and Fe_2O_3/SiO_2 (15wt.%) [90] which were found earlier to be an active and stable catalyst for the above reaction was chosen as the catalyst for studying the above reaction. 2g of the catalyst (10-20 mesh) was individually studied on separate occasions and loaded within the tube in the region of the cavity. The catalyst was held in position by plugging quartz wool from both sides. One end of the tube served as the inlet for sulfuric acid while other end served as an exit for products of decomposition which was realized within the tube.

Previously the activity of chromium doped Fe_2O_3 was studied for the sulfuric acid decomposition reaction in the similar quartz flow through tube reactor and proved it to be a suitable catalyst. Hence this commercially obtained $Fe_{1.8}Cr_{0.2}O_3$ was tested in the cavity type reactor. The performance of Fe_2O_3/SiO_2 (15wt. %) catalyst amongst the dispersed catalyst for the sulfuric acid decomposition reaction was proved to be the best in the chapter3. In order to envisage the same catalyst 5 g lot was prepared by the most suitable method i.e. the polyol method as explained in the chapter 4. Iron acetyl acetonate was the precursor for iron oxide and commercial silica was used as the support. 2 g of the catalyst with the mesh size of 10-20 was used and studied for solar thermochemical sulfuric acid decomposition reaction.

With an aim to demonstrate sulfuric acid decomposition with concentrated solar irradiation, a 1.8 m solar dish was employed in the terrace of our building. The photograph of the solar dish holding the reactor at the focus point has been shown in Chapter 2, Figure 2.17. The complete experimental set-up for carrying out continuous flow solar thermal sulfuric acid decomposition is shown in Chapter 2, Figure 2.18. During operation, the receiver reactor described above was positioned such that the quartz window of the reactor coincided with the focal plane of the 1.8 m diameter dish. 98 wt.% concentrated sulfuric acid was introduced at a constant flow rate of 0.5 mL/min with the help of a syringe pump into the inlet of the solar receiver-reactor. Sulfuric acid vaporization, dehydration and decomposition were achieved within the receiver-reactor at the catalyst zone. The iron oxide based catalyst functioned as catalyst and also absorber of the heat for carrying out solar thermal sulfuric acid decomposition. The unreacted sulfuric acid coming out of the reactor was condensed and collected, while the SO_2 produced was trapped in a known concentration of NaOH solution. Analysis of the reactants and products were carried out by chemical titrimetric method.The catalytic activity was quantified by the extent of SO_2 yield defined as:

$$Percentage\ SO_2\ Yield = \frac{No.of\ moles\ of\ SO_2\ produced}{No.of\ moles\ of\ H_2SO_4\ in\ feed}\ X\ 100 \text{-------------} (6.3)$$

The temperature at the heating zone was measured using the thermocouple. Temperature at the quartz window surface was maintained in the range of ~ 800 °C.

6.3 Results and Discussions:

The successful preparation of Fe_2O_3/SiO_2 (15wt. %) was confirmed from XRD study of the uncalcined sample along with sample calcined at 500 and 1000 °C. The XRD pattern shown in Figure 6.3 confirms the formation of Fe_2O_3 dispersed over the silica support in the case of sample obtained after calcinations at 1000 °C.

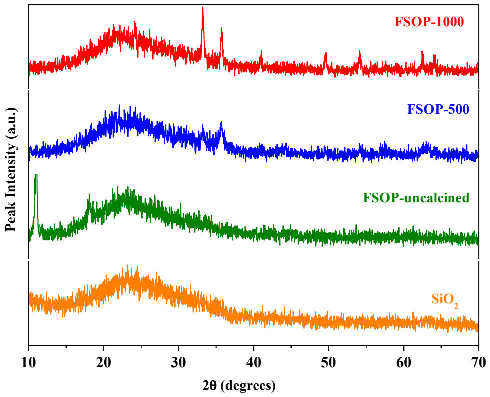

Figure 6.3: XRD pattern of the synthesized Fe_2O_3/SiO_2 (uncalcined and calcined) along with the SiO_2 support

The support SiO_2 exhibited a broad hump centered at peak position 2θ ~ 22 degrees (mineral name: crystabolite, tetragonal crystal system, Space Group: P 41212 (92), ICSD No. 47219 (orthorhombic crystal system, ICSD No. 415250). Also peaks reflected at 2θ ~24.1, 33.1, 35.6, 49.5, 54.1, 62.5 and 64.1 corresponding to (012), (104), (110), (024), (116), (214) and (300) planes of α-Fe_2O_3 (ICSD No. 15840) were observed.

The catalytic activities were performed for both the catalysts $Fe_{1.8}Cr_{0.2}O_3$ and Fe_2O_3/SiO_2 (15wt. %) successfully. The weight hourly space velocity (WHSV) of sulfuric acid was maintained at 28 g acid/gcat/h. A maximum SO_2 yield of 38 % was obtained for $Fe_{1.8}Cr_{0.2}O_3$ which was studied during summer May 2017, when the temperature at the reactor point could be achieved upto 900 °C. In the case of Fe_2O_3/SiO_2 (15wt. %) maximum SO_2 yield of 40 % was obtained, however the temperature of 750 °C could only be achieved post-monsoon season (October 2017). During the above experiment conducted for 100 min a variation of SO_2 yield within 10 % was observed. This variation can be attributed to the local changes in temperature of the catalyst zone due to minor manual errors in solar tracking. Post evaluation of the activity the samples were analyzed by ex-situ analysis.

6.4 Conclusions:

Concentrated solar radiation is used as the energy source of high-temperature process heat for the thermal production of solar power and chemical fuels. For realisation of solar thermal sulfuric acid decomposition a quartz receiver-reactor was designed and developed. Testing of this reactor was then carried out using concentrated solar heat from a 1.8 m diameter dish. Sulfuric acid decomposition was successfully achieved using the solar receiver reactor. Similar reactor design fabricated with efficient absorber material viz. SiC can be exploited in future. Also, issues related to tracking system could be overcome if automatic tracking system is implemented, which would minimize the technical errors while focussing the solar radiation at the receiver.

Chapter 7: Conclusion and scope of future work

This study was initiated with an objective to develop suitable functional materials such as catalysts, electrocatalysts, and membrane electrode assembly etc. for the thermochemical hydrogen generation via Hybrid-Sulfur cycle (HyS cycle). Accordingly, work on development of dispersed iron oxide catalyst for sulfuric acid decomposition step and Pt/C and Mo_2C electrocatalysts for aqueous SO_2 electrolysis step of the HyS cycle was undertaken. Attempts were made to utilize solar heat for the sulfuric acid decomposition reaction. Necessary quartz reactors for sulfuric acid decomposition reaction and proton exchange membrane (PEM) based electrolyzer for aqueous SO_2 electrolysis was also developed indigenously. With detailed characterization of both fresh and spent catalysts mechanistic aspects of sulfuric acid decomposition process were elucidated. Following are the salient features of the work:

Studies on Sulfuric Acid Decomposition Reaction

- Iron oxide, the active component for sulfuric acid decomposition reaction was first dispersed on silica support to optimize its content to maximize its catalytic performance. These studies have established 15 wt% Fe_2O_3loading to be the optimum. Subsequently, dispersed iron oxide samples with 15 wt.% Fe_2O_3loading were also prepared employing different oxide supports viz., SiO_2, TiO_2, CeO_2 and ZrO_2.

- The catalytic activity for the acid decomposition at 750 °C was found to follow the order: Fe_2O_3/SiO_2> Fe_2TiO_5/TiO_2> Fe_2O_3/ZrO_2> Fe_2O_3/CeO_2 while at 900 °C, they were found to be comparable.
- Influence of preparation methods like polyol, wet-impregnation, solvothermal and equilibrium-adsorption on the catalyst performance in temperature range of 500 -900 °C was also evaluated in detail. The Fe_2O_3 (15 wt.%)/SiO_2 samples prepared by polyol method exhibited highest activity for the sulfuric acid decomposition reaction and the activity trend at 800 °C was found to be as follows: Polyol> equilibrium-adsorption > wet-impregnation ~ solvothermal.
- No appreciable deterioration in the catalyst performance during 100 h run for sulfuric acid decomposition reaction at 800 °C was observed over Fe_2O_3 (15 wt.%)/SiO_2catalyst.
- Catalytic properties of the dispersed iron oxide samples were found to be dependent on nature of support, structure, morphology and the redox properties of iron oxide phase.
- The most probable mechanism of sulfuric acid decomposition over dispersed iron oxide catalyst was established via ex-situ characterization of fresh and spent catalyst and it involved formation and decomposition of sulfate species.
- Solar thermal sulfuric acid decomposition employing concentrated solar heat from a 1.8 m diameter dish and in-house developed quartz receiver-reactor was successfully demonstrated. A maximum SO_2 yield of 38 % was achieved with Fe_2O_3 (15wt. %)/SiO_2catalyst at WHSV of ~ 28 g acid/gcat/h, when the temperature of quartz receiver-reactor was in range 750-850 °C.

Studies on Aqueous SO_2 Electrolysis

- A series of Pt/C electrocatalysts with varying platinum content (10-40 wt%) were successfully prepared by chemical reduction method and their electrochemical properties were tested for hydrogen evolution reaction and aqueous SO_2 oxidation reaction. Amongst these, catalyst containing 20 wt. % Pt was found to be the most effective.
- A single cell PEM based aqueous SO_2 electrolyzer (4 cm^2 active area) was designed, fabricated and tested with the membrane electrode assembly (MEA) comprising of the most active Pt/C elctrocatalyst.A current density of ~75 $mAcm^{-2}$ was achieved at a cell voltage of 1 V.
- As a non-noble metal based electrocatalyst, molybdenum carbide electrocatalysts dispersed on carbon with varying Mo content (10-40 wt%)were synthesized and evaluated for hydrogen evolution reaction (HER). Among these electrocatalysts, sample with 20 wt% Mo content exhibited maximum electroactivity for the hydrogen evolution which was attributed to favorable surface properties, highest electrochemical active surface area and minimum charge transfer resistance of the electrocatalyst.

Scope for Future Study

Our study has established the dispersed iron oxide catalysts on silica support as an effective catalyst for sulfuric acid decomposition reaction however, for practical applications the desired catalyst form will be in porous granular/extrudates forms. Thus, there is ample scope to prepare the dispersed catalyst in suitable form for engineering scale application of Hybrid-sulfur process. Similarly, there is big scope to synthesize and utilize the non-noble metal based electrocatalysts for aqueous SO_2 electrolysis step of the Hybrid-sulfur cycle.

References:

[1] X.Cao, Resources Policy 29 (2004) 61–67.

[2] U.F. Akpan, G.E. Akpan, Int.J Energy Economics and Policy 2 (2012) 21–33.

[3] K.B. Tokarska, N.P. Gillett, A.J. Weaver, V.K. Arora, M. Eby, The climate response to five trillion tonnes of carbon, (2016) 1–6. doi:10.1038/NCLIMATE3036.

[4] Hydrogen Energy and Fuel cells in India- A way forward, Ministry of New and Renewable Energy, Government of India, New Delhi June, 2016.

[5] M. Balat, Potential importance of hydrogen as a future solution to environmental and transportation problems, 33 (2008) 4013–4029.

[6] I. Dincer, C. Acar. Int. J. Hydrogen Energy. (2014).

[7] K. Zeng, D. Zhang. Sci. 36 (2010) 307–326.

[8] Atsushi Tsutsumi, ENERGY CARRIERS AND CONVERSION SYSTEMS – Vol. I - Thermodynamics of Water Splitting

[9] Report on Hydrogen Production in India, Ministry of New and Renewable Energy, Government of India, New Delhi June, 2016.

[10] Z. Ping, W. Laijun, C. Songzhe, X. Jingming.Renew. Sustain. Energy Rev. (2017) 1–11.

[11] C. Sattler, M. Roeb, C. Agrafiotis, D. Thomey.Sol. Energy. (2017).

[12] T. Kodama, N. Gokon. Chem. Rev.107 (2007) 4048–4077.

[13] D. Yadav, R. Banerjee, Renew. and Sust. Energy Reviews,54 (2016) 497-532

[14] L.C. Brown, J.F. Funk, S.K. Showalter, General Atomics, April 2000

[15]V. Barbarossa, S. Brutti, M. Diamanti, S. Sau, G. De Maria.Int. J. Hyd. Energy. 31 (2006) 883–890.

[16] A.M. Banerjee, M.R. Pai, K. Bhattacharya, A.K. Tripathi, V.S. Kamble, S.R. Bharadwaj, S.K. Kulshreshtha. Int. J. Hyd. Energy. 33 (2008) 319–326.

[17] B. Wong, R.T. Buckingham, L.C. Brown, B.E. Russ, G.E. Besenbruch, A. Kaiparambil, R. Santhanakrishnan, A. Roy,Int. J. Hyd. Energy. 32 (2007) 497–504.

[18] US3888750 patent, Westinghouse Electric Corp., Electrolytic decomposition of water.(1975)

[19] W. A Summers, M. B. Gorensek, M. R. Buckner. Proceedings of GLOBAL 2005 (2005) 97

[20] I. V Dulera, R.K. Sinha, High temperature reactors, J. Nucl. Mater. 383 (2008) 183–188.

[21] H. Production, Non-Electric Applications of Nuclear Power : Seawater Desalination , Hydrogen Production, (2007) 16–19.

[22] A.T.-R. H. Cunping, Sol. Energy. 78 (2005) 632–646.

[23] D. Schwartz, R. Gadiou, G. Prado. Ind. Engg. Chem. Res. 39(2000) 2183–2189.

[24] S.Upadhyayula,A.Bhaskarwar, K.Kondamudi, P.Damraju, B.Bhargava, S.Bannerjee, Process for conversion of sulfur trioxide and hydrogen production, Indian Patent Application no.: 201611014896.

[25]S.Upadhyayula,A.Bhaskarwar, K.Kondamudi, P.Damraju, B.Bhargava, S.Bannerjee, Catalyst composition for conversion of sulfur trioxide and hydrogen production process, Indian Patent Application no: 201611014898.

[26] A. Noglik, M.R. Ã, C. Sattler, R. Pitz-paal. Int. J. Energy Res.(2009) 799–812.

[27] J. Park, J. Hyun, H. Jung, K. Jung. Int. J. Hydrogen Energy. 39 (2013) 54–61.

[28] S. Noh, S. Young, Y. Gun, K. Jung, Int. J. Hydrogen Energy. 39 (2014) 4181–4188.

[29] Y.S. Kim, H.C. No, J.Y. Choi, H.J. Yoon. Int. J. Hydrogen Energy. 38 (2013) 3537–3544.

[30] J. Park, H. Kim, Y. Kim Nuc. Engg. Tech. 40 (2008) 233–238.

[31] J. Park, Y. Chun, J. Chang. J. Nuclear Mater. 362 (2007) 268–273.

[32] H.A. Khan, K.D. Jung Catal. Letters. 147 (2017) 1931-1940.

[33] D.M. Ginosar, L.M. Petkovic, A.W. Glenn, K.C. Burch.Int. J. Hydrogen Energy.32 (2007) 482–488.

[34] L.M. Petkovic, D.M. Ginosar, H.W. Rollins, K.C. Burch, P.J. Pinhero, H.H. Farrell. App. Catal. A. 338 (2008) 27–36.

[35] B.M. Nagaraja, K.D. Jung, B.S. Ahn, H. Abimanyu, K.S. Yoo Ind. Engg.Chem. Res. 4 (2009) 1451–1457.

[36] S.N. Rashkeev, D.M. Ginosar, L.M. Petkovic, H.H. Farrel. Catal. Today, 139 (4) (2009), 291-298.

[37] J.H. Norman, K.J. Mysels, R. Sharp, D. Williamson. Int. J. Hydrogen Energy, 7 (7) (1982), 545-556.

[38] A.M. Banerjee, M.R. Pai, S.S. Meena, A.K. Tripathi, S.R. Bharadwaj, Int. J. Hydrogen Energy. 36 (2011) 4768–4780.

[39] D.M. Ginosar, H.W. Rollins, L.M. Petkovic, K.C. Burch, M.J. Rush. Int. J. Hydrogen Energy. 34 (2009) 4065–4073.

[40] M.B. Gorensek, J.A. Staser, T.G. Stanford, J.W. Weidner Int. J. Hydrogen Energy. 34 (2009) 6089–6095.

[41] J.A.O. Brien, J.T. Hinkley, S.W. Donne, S. Lindquist. Electrochem.Acta. 55 (2010) 573–591.

[42] J.A. Staser, J.W. Weidner. J. Electrochem. Soc. (2009) 836–841.

[43] P.W.T. Lu, R.L. Ammon,J. Electrochem. Soc. 127 (1980) 2610.

[44] D. Stolten, D. Krieg, Alkaline Electrolysis This document appeared in Alkaline Electrolysis – Introduction and Overview, 78 (2010).

[45] S.N. Laboratories, Membrane Development for Hybrid Sulfur Electrolysis at High Temperatures Sandia National Laboratories Sulfur-Iodine versus Hybrid Sulfur Cycle.

[46] J. Staser, J.W. Weidner, J. Staser, R.P. Ramasamy, P. Sivasubramanian, Electrochem. Solid State Lett.11(2007) 1–4.

[47] F. Jomard, J.P. Feraud, J.P. Caire. Int. J . Hyd. Energy. 33 (2008) 1142–1152.

[48] S. Motupally, A.J. Becker, J.W. Weidner, J. Electrochem. Soc. 147 (2000) 3171–3177.

[49] A.J. Appleby, B. Pinchon. Int. J. Hydrog. 5 (1980) 253–267.

[50] M. Elvington, D.T. Hobbs, Close out report for HyS electrolyzer component development work at Savannah River National (2010).

[51] B.D.Struck, R.Junginger, H.Neumeister, B.Dujka.Int. J . Hyd. Energy. 7 (1982) 43–49.

[52] J.L.H. Langer. J. Appl. Electrochem. 25 (1995) 353–357.

[53] L.B. C Quijada, FJ Huerta, Emilia Morallón, JL Vázquez Electrochim. Acta. 45 (2000) 1847–1862.

[54] Q. Zhao, M. Hou, S. Jiang, S. Wang, J. Ai, L. Zheng, Z. Shao. RSC Adv. 6 (2016) 80024–80028.

[55] W.-F. Chen, J.T. Muckerman, E. FujitaChem. Commun. 49 (2013) 8896.

[56] M. Romero, A. Steinfeld.Energy Environ. Sci. 5 (2012) 9234.

[57] M.S.. William V Knowles, Michael O. Nutt. Catal. Prep. Sci. Eng., Florida, (2007) 254.

[58] F. Fiévet, R. Brayner. Springer London, London,(2013) 1–25..

[59] C. Cheng, F. Xu, H. Gu. New J. Chem. 35 (2011) 1072.

[60] H. Dong, Y.-C. Chen, C. Feldmann, Green Chem. 17 (2015) 4107–4132.

[61] J. Haber, J.H. Block, B. Delmon. Pure Appl. Chem. 67 (1995) 1257–1306.

[62] G. Demazeau, J. Chem. Sci. 65 (2010) 999–1006.

[63] A.R. West, Solid State Chemistry and its Applications, Wiley- India, (2003).

[64] T. Stephen. US Patent.US 8,158,094 B2,Apr. 17, 2012.

[65] P. Ghosh, Preparation of Nanomaterials, (module 9;lecture 2) 1–23.

[66] B. Bladergroen, H. Su, S. Pasupathi, V. Linkov, Overview of Membrane Electrode Assembly Preparation Methods for Solid Polymer Electrolyte Electrolyzer, in: V.L. and J. Kleperis (Ed.), Electrolysis, InTechOpen, 2012.

[67]B. D. Cullity, “Elements of X-ray diffraction”, Addison-Wilson Publishing Comp. Inc., USA (1959).

[68] H. P. Klug and L. E. Alexander, “X-ray diffraction procedures”, Wiley-Interscience Publication, New York (1974).

[69] L. V. Azaroff and M. J. Buerger, “The Powder Method in X-ray Crystallography”, McGraw-Hill Book Comp., New York (1958).

[70]S. Brunauer, P. Emmett and E. Teller, J. Amer. Chem. Soc., 60 (1938) 309.

[71]Mössbauer Spectroscopy Group, Royal Society of Chemistry (RSC) website, Introduction to Mössbauer Spectroscopy Part 1 (2010)

[72]Mössbauer Spectroscopy Group, Royal Society of Chemistry (RSC) website, Introduction to Mössbauer Spectroscopy Part 2 (2010)

[73]A. Skoog in Principles of instrumental analysis, 3rd Edition, Saunders Golden Sunburst

Series, Orlando (1985) 315

[74] W. F. Pickering in Modern analytical chemistry, Marcel Dekker, Inc., New York, p. (1971) 153

[75]An Introduction to Surface Analysis by XPS and AES, J.F.Watts, J.Wolstenholme, published by Wiley & Sons, (2003) Chichester, UK, ISBN 978-0-470-84713-8

[76]Handbook of X-ray Photoelectron Spectroscopy, J.F.Moulder, W.F.Stickle, P.E.Sobol, and K.D.Bomben, published by Perkin-Elmer Corp., 1992, Eden Prairie, MN, USA

[77]C. N. Banwell and E. M. McCash, Fundamentals of Molecular Spectroscopy, 4th Edition, Tata McGraw Hill Publishing Company Ltd. New Delhi (1995).

[78]S. D. Robertson, B. D. McNicol, J. H. De Baas, S. C. Kloet and J. W. Jenkins, J. Catal., 37 (1975) 424.

[79] T. Uda, T. T. Lin and G. W. Keulks, J. Catal. 62 (1980) 26.

[80]R. W. Cahn, P. Haasen and E. J. Kramer, “Material Science and Engineering: Characterisation of Materials”, VCH Publisher Inc., New York (1991).

[81]D. B. William and C. B. Carter, “Transmission Electron Microscopy”, Plenum Press, New York (1996).

[82] D.F. Shriver, P. W. Atkins, Shriver & Atkins’ Inorganic Chemistry, 4th edition, Oxford University Press, Oxford (2006) 189-190.

[83] A. R. West, Basic Solid State Chemistry, 2nd Edition, Wiley, London, (2001) 203-210.

[84]P.W.J.MBoumans. Inductively coupled plasma emission spectroscopy. Part II: applications and fundamentals. Volume 2,John Wiley and Sons,New York, NY

[85] R. Van Grieken, A. Markowicz,Handbook of X-ray Spectrometry (2001) Marcel Dekker Inc.,New York.

[86]A. J. Bard and Larry R. Faulkner, *Electrochemical Methods: Fundamentals and Applications*,:2nd ed. Wiley (2001)New York

[87]A. Lasia, Electrochemical Impedance Spectroscopy and its Applications. Modern Aspects of Electrochemistry,Springer, 143-248

[88]A. M.Banerjee, M. R.Pai, R.Tewari, N.Raje, A. K.Tripathi, S. R.Bharadwaj, D Das. Appl Catal B: Env 162 (2015)327-37.

[89]A. M.Banerjee, A. R.Shirole, M. R.Pai, A. K.Tripathi, S. R.Bharadwaj, D.Das, P. K.Sinha. Appl Catal B: Environ 127 (2012)36-46.

[90] A.Nadar,A. M.Banerjee, M. R.Pai, S. S.Meena, R. V.Pai, R.Tewari, S. M.Yusuf, A. K.Tripathi, S.R.Bharadwaj. App Catal B: Environ 217 (2017)154-168.

[91] T.H.Kim, G.T.Gong, B.G.Lee, K.Y.Lee, H. Y.Jeon, C. H.Shin, H.Kim, K. D.Jung.Appl Catal A: Gen 305 (2006) 39-45.

[92] S.Bennici, A. Auroux, C.Guimon, A.Gervasini. Chem Mater 18(2006) 3641-50.

[93]L.N.Yannopoulo, J.F.Pierre. Int J Hyd Energy 9(1984)383-390.

[94] K.Kondamudi, S.Upadhyayula. Int J Hyd Energy 37(2012)3586-94.

[95]H.Abimanyu, K. D.Jung, K. W.Jung, J.Kim, K. S Yoo. Appl Catal A: General 343 (2008) 134-41.

[96]T. Kawada, H.Yamashita, Q.Zheng, M.Machida.Int J Hyd Energy 39 (2014) 20646-51.

[97] T.Kawada, A. Ikematsu, T.Tajiri, S.Takeshima, M.Machida. Int J Hyd Energy 40 (2015)10726-33.

[98] H.Yang, Y.Zhang, J.Zhou, Z.Wang, J.Liu, K.Cen. Int J Hyd Energy 41(2016) 3339-48.

[99] H.Yang, Y.Zhang, J.Zhou, Z.Wang, J.Liu, K.Cen. Int J Energy Res 40 (2016) 1062-72.

[100] A.Giaconia, S.Sau, C.Felici, P.Tarquini, G.Karagiannakis, C.Pagkoura, C.Agrafiotis, A. G.Konstandopoulosc, D.Thomey, L. de Oliveira, M.Roeb, C.Sattler. Int J Hyd Energy 36 (2011) 6496-509.

[101] G.Karagiannakis, C. C.Agrafiotis, C.Pagkoura, A. G.Konstandopoulos, D.Thomey, L de Oliveira, M.Roeb, C.Sattler. Int J Hyd Energy 37(2012) 8190-8203.

[102] J.A.Schwarz, C.Contescu, A.Contescu. Chem. Rev 95 (1995) 477-510.

[103] S.Bennici, A. Auroux, C.Guimon, A.Gervasini.Chem Mater 18 (2006) 3641-50.

[104] A. Gervasini, C.Messi, P.Carniti, A.Ponti, N.Ravasio, F.Zaccheria.JCatal 262 (2009)224–34.

[105] A. M.Banerjee, M. R.Pai, A.Arya, S. R.Bharadwaj. RSC Adv 5(2015)61218-61229.

[106] M. R.Pai, A. M.Banerjee, A. K.Tripathi, S. R.Bharadwaj.Fundamentals and Applications of the Photocatalytic Water Splitting Reaction. S. Banerjee and A. K. Tyagi, editors. In:

Functional Materials: Preparations, Processing and Applications, USA: Elsevier (2012) 579-606.

[107] R.Ghosh, L.Pradhan, Y.Priyabala Devi, S. S.Meena, R.Tewari, A.Kumar, S.Sharma, N. S.Gajbhiye, R. K.Vatsa, B. N.Pandey, R. S.Ningthoujam. J Mater Chem 21(2011)13388-98.

[108] R.Zboril, M.Mashlan, D.Petridis. Chem Mater14(2002) 969-82.

[109] K.Sharma, S.Singh, C. L.Prajapat, S.Bhattacharya, Jagannath, M.R. Singh, S. M.Yusuf, G. P.Kothiyal. J Magn Magn Mater 321(2009)3821–8.

[110] G.Seitz, N.Penin, L.Decoux, A.Wattiaux, M.Duttine, M.Gaudon. Inorg Chem 55(2016) 2499-2507.

[111] W. Q. Guo, S.Malus, D.H.Ryan, Z.Altounian. J Phys: Condens Matter 11 (1999) 6337-46.

[112] N. T.McDevitt, W. L.Baun.J American Ceramic Soc 47(1964)622-4.

[113] M.Srivastava, A. K.Das, P.Khanra, Md. E.Uddin, N. H.Kim, J. H.Lee. J Mater Chem A, 1(2013)9792-9801.

[114] F.Liu, K.Asakura, H.He, Y.Liu, W.Shan, X.Shi, C.Zhang.Catalysis Today 164(2011) 520-7.

[115] K. V.Bineesh, D. K.Kim, D. W. Park.Nanoscale 2(2010)1222-8.

[116] T.C.Jagadale, S.P.Takale, R.S.Sonawane, H. M.Joshi, S. I. Patil, B. B.Kale, S. B.Ogale. J Phys Chem C 112 (2008) 14595-602.

[117] M.Enhessari, M.Kargar Razi, L.Etemad, A.Parviz, M.Sakhaei. J Exp Nanosci 9(2014) 167-176

[118] G. Q.Xu, Z. X.Zheng, W. M. Tang, Y. C.Wu. J. Lumin 124(2007) 151-156.

[119] N.Selvi, N. Padmanathan, K. Dinakarand, S.Sankar. RSC Adv 4 (2014)55745-51.

[120] A.Jitianu, M.Crisan, A.Meghea, I.Rau, M.Zaharescu. J Mater Chem 12(2002)1401-7.

[121] A. B. P.Lever.Inorganic Electronic Spectroscopy. Amsterdam: Elsevier; 1984.

[122] C. D.Wagner, W. M.Riggs, L. E.Davis, J. F.Moulder, G. E.Muilenberg. Handbook of X-Ray Photoelectron Spectroscopy. Eden Prairie, MN: Perkin-Elmer Corporation; 1979.

[123] B. M. Reddy, A. Khan, Y. Yamada, T. Kobayashi, S. Loridant, J. C. Volta. J Phys Chem B107(2003)11475-84.

[124]A. Bensalem, F. Bozon-Verduraz, M. Delamar, G. Bugli. Appl Catal A: General 121(1995)81-93.

[125] Thermo Scientific XPS.http://xpssimplified.com/elements/

[126] M.R.Pai,A.M. Banerjee, K.Kartha, R.V.Pai, V.S.Kamble, S.R.Bharadwaj.J Phys Chem B 114(2010)6943–53.

[127] H. Tagawa . Thermochimica Acta 80(1984)23-33.

[128] C. A. Strydom,G. Pretorius.Thermochimica Acta 223(1993)223-32.

[129]M. R. Udupa. Thermochimica Acta 57(1982)377-381.

[130] F. Jasim, I. Hamid, Thermochim. Acta 93 (1985) 65–68.

[131] NIST webbook available online at: http://webbook.nist.gov.

[132] S. Sakurai, A. Namai, K. Hashimoto, S. Ohkoshi, J Am. Chem. Soc. 131 (2009)18299–18303.

[133] P. Brazda, J. Kohout, P. Bezdicka, T. Kmjec, Cryst. Growth Des 14 (2014)1039–1046.

[134] L. Machala, J. Tucek, R. Zboril, Chem. Mater. 23 (2011) 3255–3272.

[135] J. Tucek, R. Zboril, A. Namai, S. Ohkoshi, Chem. Mater. 22 (2010) 6483–6505.

[136] R. Kellner, J.-M. Mermet, M. Otto, M. Valcarcel, H.M. Widmer, Surface andinterface analysis, in: J.M. Mermer, M. Otto, M. Valcarel (Eds.), AnalyticalChemistry: A Modern Approach to Analytical Science, Wiley-VCH, Weinheim, 2004, pp. 897–951 (chapter 27).

[137] R.M. Cornel, U. Schwertmann, The Iron Oxides. Structure, Properties,Reactions and Uses, Wiley, VCH, Weinheim, 1996.

[138] T.P. Braga, A.N. Pinheiro, W.T. Herrer, Y.T. Xing, E. Baggio-Saitovitch, A.Valentini, J. Mater. Sci. 46 (2011) 766–773.

[139] A.H. Lu, J.J. Nitz, M. Comotti, C. Weidenthaler, K. Schlichte, C.W. Lehmann, O.Terasaki, F. Schuth, J. Am. Chem. Soc. 132 (2010) 14152–14162.

[140] Z. Wu, W. Li, P.A. Webley, D. Zhao, Adv. Mater. 24 (2012) 485–491.

[141] J. Bao, X. Zhang, B. Fan, J. Zhang, M. Zhou, W. Yang, X. Hu, H. Wang, B. Pan, Y.Xie, Angew. Chem. Int. Ed. 54 (2015) 7399–7404.

[142] S. Wang, W. Shi, C. Lu.Anal. Chem. 88 (2016) 4987–4994.

[143] A.M. Banerjee, M.R. Pai, Jagannath, S.R. Bharadwaj, Thermochim. Acta 516(2011) 40–45.

[144]K. Zhou, Y. Li, Angew. Chem. Int. Ed. 51 (2012) 602–613.

[145] X. Xie, Y. Li, Z. Liu, M. Haruta, W. Shen, Nature 458 (2009) 746–749.

[146] Y. Li, W. Shen, Chem. Soc. Rev. 43 (2014) 1543–1574.

[147] N. Heiman, N. Kazama, J. Appl. Phys. 50 (1979) 7633.

[148] C. Cannas, G. Concas, A. Falqui, A. Musinu, G. Spano, G. Piccaluga, J. Non-Cryst.Solids 286 (2001) 64–73.

[149] L. Machala, R. Zboril, A. Gedanken, J. Phys. Chem. B 111 (2007) 4003–4018.

[150]A.R. Champion, R.W. Vaughan, H.G. Drickamer, J. Chem. Phys. 47 (1967) 2583.

[151] J.A. Rodriguez, T. Jirsak, S. Chaturvedi, M. Kuhn, Surface Sci. 442 (1999)400–412.

[152] J.A. Rodriguez, T. Jirsak, A. Freitag, J.Z. Larese, A. Maiti, J. Phys. Chem. B 104(2000) 7439–7448.

[153] N.J. Divins, I. Angurell, C. Escudero, V. Pérez-Dieste, J. Llorca, Science 346(2014) 6209.

[154] A. Locatelli, C. Sbraccia, S. Heun, S. Baroni, M. Kiskinova, J Am. Chem. Soc. 127(2005) 2351–2357.

[155] X. Jin, L. Dang, J. Lohrman, B. Subramaniam, S. Ren, R.V. Chaudhari, ACS Nano 7(2013) 1309–1316.

[156] J. Treu, T. Stettner, M. Watzinger, S. Morkötter, M. Döblinger, S. Matich, K.Saller, M. Bichler, G. Abstreiter, J.J. Finley, J. Stangl, G. Koblmüller, Nano Lett.15 (2015) 3533–3540.

[157] S.H. Joo, J.Y. Park, Chia-Kuang Tsung, Y. Yamada, P. Yang, G.A. Somorjai, Nat.Mat. 8 (2009) 126–131.

[158] A.Capon,R. Parsons, J. Electroanal.Chem.,65(1975) 285

[159] S. A. Grigoriev, V. I. Porembsky, V. N. Fateev, Int J Hydrogen Energy 31 (2006) 171-175.

[160] J. A. O’Brien, J.T. Hinkley, S. W. Donne, S-E Lindquist, Electrochemical Acta 55(2010) 573-591.

[161] R. J. Kriek, J. Rossmeisl, S. Siahrostami and M. E. Bjorketun. Phys.Chem.Chem.Phys. 16 (2014) 9572-9579.

[162] D.Merki, X.Hu. Energy Environ. Sci. 4(2011)3878-88.

[163] E.J.Popczun, J.R.McKone, C.G.Read, A.J.Biacchi, A.M.Wiltrout, N.S.Lewis, RE Schaak J. Am. Chem. Soc. 135 (2013) 9267−70.

[164] H.Vrubel, X.Hu, Angew.Chem.124 (2012) 12875–78.

[165] L Ma, LRL Ting, V Molinari, C Giordano, BS Yeo. J. Mater.Chem.A 3 (2015) 8361-68.

[166] W.F.Chen, S Iyer, K Sasaki, C.H.Wang, Y Zhu, J.T.Muckerman, E Fujita. Energy Environ. Sci. 6 (2013) 1818-26.

[167] Y.J.Tang, M.R.Gao, C.H.Liu, S.L.Li, H.L.Jiang, Y.Q.Lan, M Han, S.H.Yu. Angew.Chem. Int. Ed. 54(2015)12928–32.

[168] M.C.Weidman, D.V.Esposito, Y.C.Hsu, J.G.Chen. J. Power Sources 202(2012) 11– 17.

[169] KRobert, M Jean-Michel, O Matthias, V Miguel, WH Michael, Chapter 27, Surface and Interfacial Analysis ISBN 978-3-527-30590-2 - Wiley-VCH, Weinheim.

[170] H.Lin, N.Liu, Z.Shi, Y.Guo, Y.Tang, Q.Gao. Adv. Funct. Mater.26 (2016) 5590–98.

[171] Pifre, Nature 21(1882), 503–504.

[172] J. Ericsson, Nature 38 (1888) 321.

[173] A. Eneas, US Pat.670 (1901) 917.

[174] F. Shuman, Sci. Am.109 (1913) 350.

[175] G. Francia, Sol. Energy 12 (1968) 51–64.

[176] Solar Power Plants, ed. C. J. Winter, R. L. Sizmann and L. L. Vant-Hull, Springer-Verlag, Berlin, 1991.

[177] M. Romero and J. Gonz_alez Aguilar, Energy & Power Generation Handbook, ed. K. R. Rao, ASME Three Park Avenue, New York,NY 10016-5990, USA, 2011, ch. 3.

[178] D. Mills, Sol. Energy 76(2004) 19–31.